GRAPHENE, NANOTUBE & ORGANIC MATERIALS COMPOSITES FOR TRANSPARENT CONDUCTOR AND ELECTRICAL DEVICE APPLICATIONS

Yue Chau (Garen) Kwan

School of Physical and Mathematical Sciences

A thesis submitted to the Nanyang Technological University
in partial fulfilment of the requirement for the degree of
Doctor of Philosophy

2016

Dedicated to
My wife and my new life
the close of a chapter
and the start of something new

Remember
Trust in the Lord
Stay hungry, stay foolish

and that
Fortune favours the bold

Acknowledgements

I would like to thank the Economic Development Board and Robert Bosch (SEA) Pte Ltd for providing the money and the opportunities that have made this work possible. It was an interesting confluence of circumstances that allowed me to embark on a PhD away from the hospices of the university and the experience has been both intellectually fulfilling and experientially exciting.

My greatest thanks to Prof. Alfred Huan for taking me as your PhD & FYP student despite your exceptionally busy schedule as Head of the PAP division when I was an undergraduate and your current role of Executive Director at the Institute of High Performance Computing. It has been a privilege to have been trained by you and I hope to be retain the spirit of philosophy towards research in my future endeavours. I will remember your methods of questioning into the topic and relentless pursuit for the truth of the matter.

Thank you Dr. Ng Ging Meng, Dr. Suresh Palale, Dr. Christoph Treutler, Dr. Patrick Poa, Dr. Grace Wang and Dr. Walter Daves for your individual contributions towards making this thesis a possibility. In chronological order, thank you Dr. Treutler for listening to me explain my FYP project during the interview, deciding to take me into the organization anyway and for your kind almost fatherly way of managing the department of CR/RTC1-AP. Thank your Dr. Poa for the allocation of the GO topic to me when there was a need to change topics, I hope that I have met and exceeded the expectations that you had for this topic. A big thank you to Dr Ng. for your supervision and guidance through the course of this work, the countless hours spent with me in discussions about the topic, manuscript and patent work is much appreciated. Thank you Dr. Daves and Dr. Wang for helping me push the patent application through. Particularly, thank you Dr. Daves for helping with the interface problems when we were trying to communicate with the departments in Germany. Finally, thank you Dr. Palale for seeing me through the last leg of this endeavour. Your thoughtful comments on this thesis and the support that you have given for the completion of this work is appreciated.

Thank you Prof. Sum for including me as one of your group. The support provided that I received from just being part of the group has been a wonderful blessing. Thank you Dr. Chen Shi for your discussions on the XPS work, your experience in the area was a great help to me. Thank you Le Quang Luan for spending your internship with me, I hope you are pleased with the outcome of the process. Thank you Ms. Sharon Chia for testing my ideas for the ridiculous experiment that turned out to be such a success.

To my wonderful wife, this phase of my life is finally over, Praise the Lord! Your patience has paid off and your husband is no longer a student. Thank you for growing with me, for helping me to keep my sanity, for being my beautiful wife, for being the support that I needed when times were just too difficult, for being understanding and for nights that we played DOTA2 just because I was not in the mood to do any work. You are indeed God's blessing to me and now that this is done we can begin work on our next goal, together.

I thank God for the fortunate confluence of events that allowed me to be born in the country of Singapore, for it is here that my mind could be developed into the tool that it is today. It is with humility that I recognize the fact that there are many other people in the world that have the same intellectual capabilities that I do, but not the opportunities that I have been presented with. My accomplishments today are equal parts my doings and that of circumstances that were entirely beyond my control in the first place. So thank You for your blessings.

Contents

Abstract

Heralded as the next miracle material, graphene oxide (GO) has the potential to be used in a variety of next generation devices. However, there are still gaps in the fundamental knowledge on this material and even now, a canonical model of GO has not been developed. The two aims of this thesis are to support the development of the canonical model by studying the O $1s_{1/2}$ spectra of GO and to develop the use of reduced GO for electronic device applications.

Here, the identities of peaks in the O $1s_{1/2}$ spectrum were identified by chemical and mathematical analysis and the fabrication processes were made environmentally friendly and industrially scalable by the use of ascorbic acid for low temperature reduction of GO and ultrasonic spray coating for large area deposition respectively in transparent conducting electrodes (TCE). Further to this, the conductive character of reduced GO was also utilized in a bilayer device design with phthalocyanines for a NO_2 sensing application.

The binding energy of O $1s_{1/2}$ electrons in the carbonyl, carboxyl, hydroxyl and epoxy functional groups were found to be 530.9, 532.3, 533.1 & 534.4 eV respectively. With this information, metastability in GO was understood to result in the preferential formation of the carboxyl functional group, which cause vacancies in the graphene flake and are difficult to remove, during the thermal reduction of GO. This was estimated to occur between the temperatures of 543 & 561 K and

it is recommended that thermal reduction methods keep below this temperature range.

A TCE with a figure of merit of 189.9 was fabricated when GO reduced by ascorbic acid was used in conjunction with silver nanowires (AgNW) in a bilayer TCE. The reduced GO over layer was observed to retard AgNW degradation caused by capillary instability and this was achieved by protecting the surface of the nanowire from oxygen. This reduced surface diffusion of the silver atoms and extended the lifetime of the nanowires. Finally, a new bilayer gas sensing device utilizing phthalocyanines on reduced GO was described and tested. The bilayer design improved device currents, with no loss in normalized sensitivity and a theoretical model that was developed to describe it.

In summary, a deficiency in the literature of GO was identified & solved and this finding will be a useful tool in the development of a canonical model for GO. The identification of the O $1s_{1/2}$ peaks of the different functional groups will also aid in the characterization of reduced GO with low C/O ratios, typically found in highly reduced GO. The main challenges preventing the widespread use of GO in electronic devices were identified to be device design and fabrication techniques. GO is a versatile material platform which can be used in a variety of applications, but a deep understanding of both GO properties and the properties of complementary materials is required so that the right device design can be employed to harness the desirable characteristics of these materials. Future work will focus on the development of the canonical model, consider methods of increasing the FOM of TCEs fabricated using reduced GO, confirm the stability of the bilayer device and expand the use of GO into other devices.

List of Figures

List of Tables

Glossary

E_g	Band gap
2D	Two-dimensional
2DEG	Two-dimensional electron gas
AA	Ascorbic Acid
AFM	Atomic Force Microscope
AgNW	Silver Nanowire
AJ	Ajayan (Theoretical model of GO)
APTES	3-aminopropyltriethoxysilane
B.E.	Binding Energy
C/O	Carbon to Oxygen ratio in XPS
CAE	Constant Analyzer Energy
CNT	Carbon Nanotube
Conc.	Concentration
CPD	Contact Potential Difference
CRR	Constant Retard Ratio
CVD	Chemical Vapour Deposition
DAU	Data Acquisition Unit
DNA	Deoxyribonucleic Acid
EFGO	Edged-Functionalized Graphene Oxide

GLOSSARY

FET	Field Effect Transistor
FLG	Few Layered Graphene
FOM	Figure of Merit
FWHM	Full Width at Half Maximum
GF	Graphene Fibre
GO	Graphene Oxide
HOMO	Highest Occupied Molecular Orbital
ITO	Indium doped Tin Oxide
LK	Lerf-Klinowski (Theoretical model of GO)
LUMO	Lowest Unoccupied Molecular Orbital
MD	Molecular Dynamical
Me	Metal
MPc	Metal Phthalocyanine
NiPC	Nickel Phthalocyanine
NiPC(OBu)$_8$	Nickel(II) 1,4,8,11,15,18,22,25-octabutoxy-29H,31H-phthalocyanine
NMP	N-methyl-2-pyrrolidinone
OD	Oxidative Debris
PVD	Physical Vapour Deposition
R	Resistance
RGC	Relative Gradient Change
SEM	Scanning Electron Microscope
Sens.	Sensitivity of device calculated from the gradient of the RGC against analyte concentration graph.
TCE	Transparent Conducting Electrode
TGA	Themo-gravimetric Analysis

VASP	Vienna Ab-initio Simulation Package
XPS	X-ray Photoelectron Spectrometry
ZnPC	Zinc Phthalocyanine
ZPE	Zero-point energy

1

Introduction

1.1 Graphene

1.1.1 Discovery of Graphene

The term graphene first appeared in an article published in 1991, and the first patent application containing this term in 1994[1,2]. However, no further patent applications were made on this topic in the 6 years that followed[3]. While it was not the main subject of research in the years following 1991, the term graphene was known to the scientific community and was commonly used to describe the mono-layer carbon lattice that occurs in graphite. It was also used in a review to describe the material that is folded to form carbon nanotubes (CNT) and as a constituent layer of the naturally occurring few layered by-product formed during the fabrication of CNTs by hydrogen arc discharge[4,5]. Despite knowledge of its existence, MLG was assumed to be unstable at ambient conditions and would not be characterized until 2004 by Berger *et al.*[6].

The measurements were made on MLG that was epitaxially grown on the (0001) surface of 6H-SiC by thermal decomposition. Berger *et al.* showed that MLG had n-type carrier densities of 3.6×10^{12} cm^{-2} per sheet, carrier mobilities of up to 1100 cm^2/Vs and, by the demonstration of Shubnikov-de Haas oscillations, that the electrons formed a two-dimensional electron gas (2DEG).

However, it was the isolation and study of FLG, derived by micro-mechanical cleavage in the same year that marked the beginning of the era of two-dimensional

(2D) materials research[7]. Later in 2005, MLG was characterized by Novoselov *et al.* and they showed that carrier concentrations in graphene were as high as 10^{13} cm^{-2} per sheet with associated mobilities of between 2000 and 5000 cm^2/Vs[8]. In a subsequent article in Nature, the presence of a 2DEG in graphene was confirmed and the anomalous half-integer filling factors of the quantum Hall effect in graphene was identified by Geim *et al.*[9] For their 'ground breaking experiments regarding the two-dimensional material graphene', the researchers were jointly awarded the Nobel Prize in Physics in 2010[10].

Of equal importance to the understanding of graphene's electronic structure were the observation of the Berry's phase and half-integer quantum Hall effect by Zhang *et al.*Interestingly, this article was published in the same volume of the same journal *and* immediately after the above mentioned Geim *et al.* article[11]. While substrate effects on MLG had yet to be accounted for, these results combined to show that the high carrier mobility in graphene could potentially be used in electronic devices.

In the decade following 2004, there was an exponential increase in the amount of research effort spent in characterizing the material and incorporating it into matrices and devices. Fig. 1.1 shows how the explosion in research effort led to a 100× increase in the number of graphene related articles and patents[3].

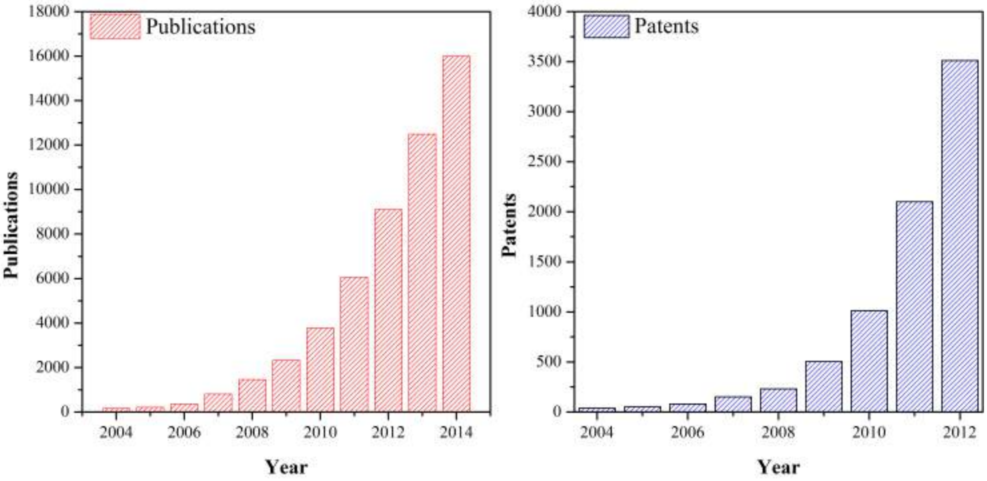

Figure 1.1: Histograms of publications in scientific journals and patents with graphene as a topic or keyword since 2004.

1.1.2 Key Developments of Graphene

As a unique material with many ideal electronic properties, it appeared that graphene had the potential of being a silicon replacement in electronic devices[12]. Additionally, despite the success of using micro-mechanical cleavage to isolate individual graphene flakes for scientific research, it quickly became clear that this was not an ideal method of obtaining graphene for industrial applications Several fundamental obstacles inherent in the usage of the material had to first be overcome and the main difficulties faced by the researchers included and were not limited to[12,13]:

- Difficulty in transferring films to target medium
- Low throughput and non-scalable method of graphene production by micro-mechanical cleavage
- Small maximum size and non-consistent shape of flakes
- Properties were highly dependent on production method
- Difficulty in dispersal over large areas

In the following sections, key scientific findings in the area of graphene characterization and the state of the art of graphene production are highlighted.

1.1.2.1 Identifying Graphene

The 2-dimensional unit cell of graphene has sides of length 2.46 Å and a two-atom basis set, consisting of 2 inequivalent carbon atoms, positioned at a separation of 1.42 Å. Using this carbon-carbon separation, a, as a unit length, the primitive lattice vectors can be given as

$$\begin{array}{lllllllll} \hat{\boldsymbol{a}} & = (& \frac{3}{2} & \hat{\boldsymbol{x}} & + & \frac{\sqrt{3}}{2} & \hat{\boldsymbol{y}} &) & a \\ \hat{\boldsymbol{b}} & = (& -\frac{3}{2} & \hat{\boldsymbol{x}} & + & \frac{\sqrt{3}}{2} & \hat{\boldsymbol{y}} &) & a \end{array}$$

The unit cell is completed by placing carbon atoms at atomic positions

$$\begin{array}{lcl} \boldsymbol{r_1} & = & (0\ ,\ 0) \\ \boldsymbol{r_2} & = & \frac{1}{3}\,\hat{\boldsymbol{a}} + \frac{2}{3}\,\hat{\boldsymbol{b}} \end{array}$$

Repeating this unit cell in the $\hat{\boldsymbol{a}}$ and $\hat{\boldsymbol{b}}$ directions, reveals the familiar hexagonal structure of graphene, as shown in Fig. 1.2 and this is the basis upon which the theoretical framework of graphene is formulated. Fundamental calculations on models made with the introduction of linear defects has shown that these defects cause electron scattering[14]. Additionally, by stacking it in the $\hat{\boldsymbol{z}}$ direction to form trilayer graphene it was shown that the stacking order (ABA or ABC) affects the resulting band structure at the K-point in reciprocal space[15].

Graphene sheets are typically difficult to observe under a light microscope due to its mono-atomic thickness. At a thickness of 3.35 Å per layer and with an optical absorbance value, that is related to the fine structure constant (α), of 2.3 % per layer, its presence could only be detected optically by deposition onto a 300 nm thick silicon oxide layer[16–20].

This technique makes use of the interference between the incident and reflected light at the air-SiO_2 and the SiO_2-Si interfaces, where an increase in the optical path length induced by a change in SiO_2 thickness, or in this case by the presence of a monolayer of graphene, can be observed as a colour change on the SiO_2 surface[21]. While the presence of and number of layers of graphene can be estimated by this optical technique, one would use X-ray photoelectron spectroscopy and/or Raman spectroscopy to give additional information regarding the chemical and electronic make-up of the deposited graphene sample.

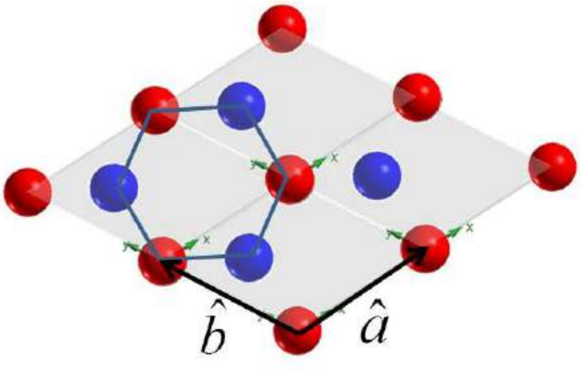

Figure 1.2: Depiction of 4 units of the graphene unit cell. The vectors $\boldsymbol{a}$ & $\boldsymbol{b}$ are the primitive lattice vectors, the red carbon atoms are positioned at $\boldsymbol{r_1}$, the blue carbon atoms at $\boldsymbol{r_2}$ and the hexagon is drawn in for emphasis.

Electrical Conductivity of Graphene

As was shown in Fig. 1.2, forming the familiar hexagon shaped bonds in graphene requires each carbon atom to form a chemical bond with its 3 nearest neighbour atoms. In an ideal graphene monolayer, every cabon atom is sp^2 hybridized and each carbon atoms forms 3 σ and 1 π bond with the neighbouring atoms[22,23].

Electrons from these π bonds are responsible for electrical conductivity in graphene and under ideal conditions, carrier mobilities were measured at up to 200,000 cm^2/Vs, the highest carrier mobility recorded in any known material[24,25].

However, the conductivity of graphene is limited by the low intrinsic carrier concentration of the material[25]. On top of this, electrical conductivity of the material is also affected by the presence of defects and vacancies in the carbon basal plane[26]. In order to maximise the conductivity of graphene, methods must be employed to eliminate defects and vacancies and to increase the carrier concentration while minimising any impact these modifications might have on carrier mobility in the graphene sheet.

X-ray Photoelectron Spectroscopy of Graphene

The binding energy of the C $1s_{1/2}$ electron depends on the hybridization of the carbon atom and sp^2 hybridized electrons typically have a lower binding energy than sp^3 hybridized electrons[27,28]. In the X-ray photoelectron spectroscopic study of graphene, the C $1s_{1/2}$ electron is expected to have a binding energy of 284.7 eV, a value derived from the binding energy of an electron in the same orbital in highly oriented pyrolytic graphite[29]. Any deviation from this value is attributed to changes in the chemical make-up of the sample as demonstrated in the XPS spectra of graphene oxide (GO) shown in Fig. 1.3[30].

Furthermore, the technique of XPS can also be used to probe the number of layers of graphene deposited; Rollings *et al.* showed that a sample of MLG could be differentiated from a sample of trilayer graphene through careful analysis of the intensity of the substrate peaks[17]. However, since the C $1s_{1/2}$ electrons have an escape energy of about 1 keV in XPS measurements, these electrons will have an attenuation length of about 25 Å[31,32]. Since the information depth is estimated to be 3 times the electron attenuation length, XPS characterization of a graphene sample typically gives information about the material up to 7.5 nm below the material-vacuum interface[33].

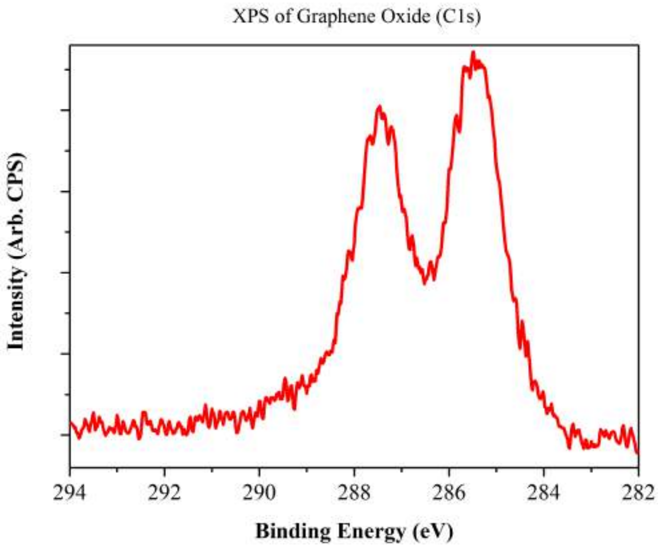

Figure 1.3: Typical XPS spectrum of the C $1s_{1/2}$ electrons in GO. The C $1s_{1/2}$ electrons in sp^2 hybridized carbon atoms would form the peak at 284.7 eV while the remainder are from sp^3 hybridized carbon atoms with binding energy shifts due to the presence of neighbouring oxygen functional groups.

This is supported by the work of Jablonski and Zemek who developed the technique of multiline-analysis to study the thickness of a nickel over-layer on a silicon substrate and showed that they could measure the thickness of over-layers of up to 7.2 nm[34]. In a similar fashion, Seah *et al.* developed a technique that made use of the effective attenuation length to identify the thickness of SiO_2 on a silicon substrate. In their work, they found that SiO_2 over-layer thicknesses of up to 7.8 nm could be reliably quantified with an associated error of ±0.4 nm[35–41].
From energetic considerations, the C $1s_{1/2}$ electrons collected in XPS experiments typically have attenuation lengths similar to that of electrons collected from Si 2s orbitals, and though not yet done, the above methods could no doubt be adapted for use in the XPS study of graphene[42]. Layering graphene on silicon substrates and applying the above techniques of multiline analysis or electron attenuation length on the detected Si 2s signal could in theory allow thickness measurements of graphene over-layers of up to 7.5 nm.

Raman Spectroscopy of Graphene

Raman spectroscopy of graphene is shown in Fig. 1.4 and is commonly used to characterize sp^2 hybridized electrons in a variety of materials. It can give information about the (i) vibrational properties, (ii) crystallographic properties, (iii) physical properties, (iv) presence of dopants and (v) dimensionality of the carbon atoms present, *i.e.* 0D fullerenes, 1D carbon-nanotubes, 2D graphene and 3D graphite[43–46].

Analysis of the resulting Raman spectra with theoretical understanding of the Raman process and material under study allow precise information to be obtained. For example, as was shown by Ferrari *et al.*, one can tell if MLG, FLG or graphite is present in the sample by analysing the the G′ band (also known as the 2D band), which occurs at ~2700cm^{-1} in the Raman spectra[47]. As shown in Fig. 1.4. From the figure, beginning with MLG and increasing the number of layers causes (i) the formation of a secondary peak features at a higher and lower wavelengths, (ii) widening of the overall peak, (iii) diminished relative intensity of the initial graphene 2D peak and (iv) an increase in the intensity of the peak at higher wavelengths. While the quantitative values associated with the above observations are dependent on the excitation energy, the qualitative changes remain independent of the excitation energy, making Raman spectroscopy an excellent tool in determining the number of layers of graphene present in the sample.

1.1.2.2 Production of Graphene

There are a many methods of producing graphene and the production method severely affects the quality of the resulting material. Ideally, graphene produced by any method should have large physical dimensions, be mono-crystalline, be formed without grain boundaries and have tunable thickness or number of layers. The large physical size is required for applications in industrial processes, while the property of mono-crystallinity is essential for the material to maintain its superior carrier mobilities. Thickness control is also required as it has a direct impact on the transparency and conductivity of the resulting film.

At present, large area graphene with high electrical conductivity can be produced by chemical vapour deposition (CVD) on copper in a roll to roll setup[48]. Graphene produced by this method was monolayer with an intrinsic sheet resistance of 500 $\Omega/\Box$ which fell to 125 $\Omega/\Box$ with an associated optical transmittance

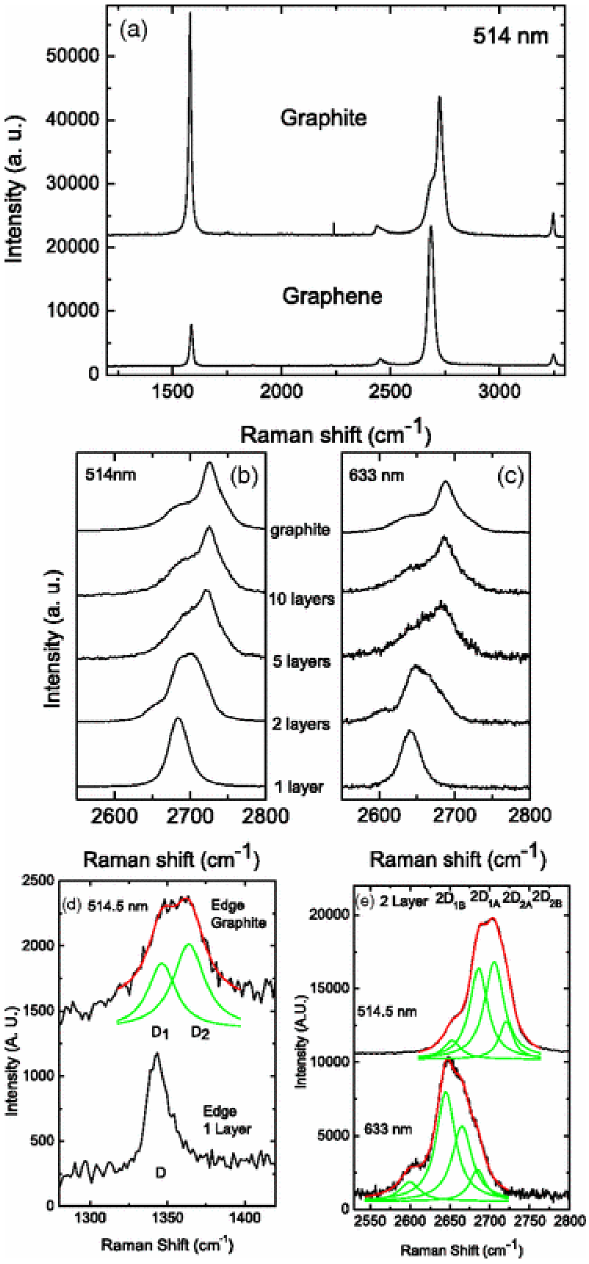

Figure 1.4: (a) Comparison of Raman spectra of graphite and graphene using a 514 nm excitation. Change in the spectra of graphene with increasing layers under (b) 514 nm & (c) 633 nm excitation. (d) Comparison of the D-peak in graphene and graphite using 514 nm excitation. (e) Bilayer graphene under 514 & 633 nm excitation.

Reprinted with permission from reference [47]. Copyright 2006 by the American Physical Society.

of 2.9 % through the monolayer after it was doped with gold chloride. While these impressive results showed that MLG could be produced repeatably and reliably over large areas, the material's sheet resistance was not low enough to make it an indium tin oxide (ITO) replacement.

While it is possible to stack MLG to get FLG, the layers tend to have interlayer spacings and the films have less reliable physical properties as a result of this. The problem of large interlayer spacings in layer-by-layer stacked FLG can be overcome by using nickel as a substrate, however, this method incurs a new problem of non-homogeneous substrate coverage[49–51]. Typical coverage of the graphene on the nickel substrate consists of islands of about 10 μm in diameter and the number of graphene layers in these islands varied between one and three layers. This severely affects the homogeneity of FLG produced and greater control over the growth characteristics of FLG are required.

1.1.2.3 Solvent Soluble Graphene

Graphene is poorly soluble in most solvents and and is generally not easily deposited onto surfaces of arbitrary shape and size. It was first shown to be appreciably dispersible in N-methyl-2-pyrrolidinone (NMP) by Hernandez *et al.* and through improvements in the technique of dispersion, the concentration of MLG was increased from 0.01 to 2.0 mg/ml[52–54]. However, if FLG can be used in the target application, concentrations of graphene in NMP can reach values as high as 20 mg/ml[54].

Besides organic solvents, graphene flakes can be suspended in water if a surfactant is present. By pre-mixing a surfactant and water solution and subjecting the solution to ultrasonication in the presence of graphite powder, suspensions of graphene in water at concentrations of up to 1 mg/ml can be produced[55]. However, compared to CVD grown graphene, solvent dispersed graphene exhibits smaller flake sizes and the presence of foreign molecules in the vicinity of the graphene flakes reduces and increases graphene's optical and electron conductivities respectively[56].

While the flat layer of graphene produced by CVD is ideal for use in most electronic applications, the same cannot be said for graphene based surface coatings.This can be understood from the theory of solubility of graphene in a solvent which will be briefly outlined here[52].

Enthalpy of Mixing

Considering first an isolated mass of graphite powder (M_G) with thickness T_1 and area A_1, the number of flakes present (N_1) is given by

$$N_1 = \frac{M_G}{\rho_G T_1 A_1}, \tag{1.1}$$

where ρ_G is the density of graphite.

The enthalpy of mixing requires the following energy values:

i. separating the graphene sheets to infinity

$$E_1^{G-\infty} = N_1 \left[2 \cdot \left(\frac{T_1\, A_1}{t\, A} \right) A - 2\, A_1 \right] E_{Sur}^{graphite} \tag{1.2}$$

where t and A are the thickness and area of individual graphene sheets and $E_{Sur}^{graphite}$ is the effective graphite surface energy

ii. separating the solvent molecules to infinity

$$E_1^{sol-\infty} = V_{sol}\, E_{coh}^{sol} - A_1^{sol}\, E_{sur}^{sol} \tag{1.3}$$

where E_{coh}^{sol} is the solvent cohesive energy, E_{sur}^{sol} is the solvent surface energy and A_1^{sol} is the external surface area of the solvent

iii. making graphene flakes

$$E_2^{G} = N_2 \left[2 \cdot \left(\frac{T_{flake} A_2}{t\, A} \right) A - 2\, A_2 \right] E_{sur}^{graphite} \tag{1.4}$$

where N_2 is the actual number of flakes in the final dispersion, and in a manner similar to Equation (1.1), T_{flake} and A_2 are the thickness and area of these flakes

iv. bringing the solvent molecules together and leaving voids to accommodate the graphene flakes

$$E_2^{sol} = V_{sol} E_{coh}^{sol} - A_2^{sol} E_{sur}^{sol} - A^{G-sol} E_{sur}^{sol} \qquad \text{and} \tag{1.5}$$

v. the interfacial energy associated with placing graphene flakes in these voids

$$E_2^{G-sol} = 2 A^{G-sol} E^{G-sol} = 2\, N_2 \cdot 2\, A_2\, E^{G-sol} \tag{1.6}$$

The enthalpy of mixing is then given by

$$\Delta H_{Mix} = E_1^G + E_1^{sol} - \left(E_2^G + E_2^{sol} + E_2^{G-sol}\right) \tag{1.7}$$

By substitution of Equation (1.2) through (1.6) and assuming that the external surface area of the solvent remains constant ($A_2^{sol} \approx A_1^{sol}$) and that flakes in the graphite powder are thicker than those in the dispersion ($T_1 >> T_{flake}$), Equation (1.7) becomes

$$\Delta H_{mix} \approx 2\,\frac{M_G}{T_{flake}\,\rho_G}\left[E_{sur}^{sol} - 2\,E^{G-sol}\right] \tag{1.8}$$

Substituting $\phi = M_G/(\rho_G V_{mix})$ to represent the volume fraction of graphite with V_{mix} as the volume of the mixture and approximating $E^{G-sol} \approx \sqrt{E_{sur}^G\,E_{sur}^{sol}}$, the above equation becomes

$$\boxed{\frac{\Delta H_{mix}}{V_{mix}} \approx \frac{2}{T_{flake}}\left(\delta_G - \delta_{sol}\right)^2 \phi} \tag{1.9}$$

where we also substituted $\delta_i = \sqrt{E_{sur}^i}$.
In this form, the relationship between ΔH_{mix} and the solvent energy is such that

- ΔH_{mix} is minimized when $\delta_G = \delta_{sol}$
- larger flakes reduce the enthalpy of mixing
- larger mixing volumes increases the enthalpy of mixing.

1.1.2.4 Graphene Derivatives

The limitations of intrinsic monolayer graphene as well as scientific curiosity has led to the development of many techniques that change the nature of the graphenic material. One technique alters the physical dimensions of the graphene flake to form a nanoribbon, as shown in Fig. 1.5(a). This results in the formation of a band gap in graphene, of which the size of this band gap depends on the width of the ribbon and edge type[57–59]. Alternatively, by attaching heteroatoms such as hydrogen to form graphane, Fig. 1.5(b), or functional groups to existing carbon atoms changes could be made to the properties of the material[60]. A third method involves the substitution of carbon atoms in the basal plane and atoms for this modification method include boron and nitrogen as shown in Fig. 1.5(c)[61–64].

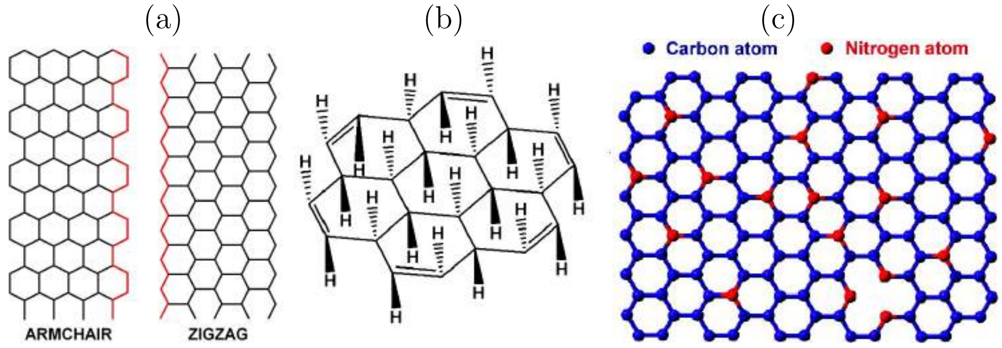

Figure 1.5: (a) Example of graphene nano-ribbons with armchair or zigzag edges. (b) Graphane, an example of graphene with heteroatoms attached. (c) Nitrographene, graphene with substituted nitrogen atoms.

Reprinted with permission from reference [65]. Copyright 2009 American Chemical Society.

Graphene Nano-ribbons

When graphene is patterned into long strips with small widths, the electrons become spatially confined and this splits the two-dimensional energy dispersion into one-dimensional modes to open a bandgap, E_g in the material[66]. It was subsequently shown that by electron beam lithography and a subsequent etching step, a nano-ribbon of width 20 nm with an induced band gap of about 30 meV could be fabricated[67]. The band gap in the nano-ribbon is tunable, is controlled by the width of the nanoribbon and type of the edge-states and nano-ribbons with widths <10 nm and $E_g \approx 0.35$ eV have been realized[68–70].

The size of the bandgap is approximated by the equation

$$E_g = \frac{\alpha}{W - W*} \tag{1.10}$$

where α takes on a value between 0.2 and 1.5 eV nm, W is the width of the nano-ribbon and W* is a fitting parameter[69,71].

The high dependence of the bandgap on the edge states and relative inability to control the edge states stalled progress on the use of graphene in field effect transistors (FET). However, Chen et al. have recently shown that nano-ribbons with arm-chair configuration edge states could be produced by a bottom up process, reigniting the interest in use of graphene in FETs[72]. Still, the inherently small band gaps and low electron mobilities will likely limit the use of graphene to power applications[73].

Graphene with Attached Atoms

The other class of graphene modifications involves the attachment of atoms or functional groups to the carbon basal plane. Of these, fluorographene, graphene and GO are well-established modified graphene materials[74]. The substitution or addition of atoms and or functional groups to graphene, alters the physical and electronic properties of the material. This generally causes a reduction in the physical strength and electron mobility and opens a band gap in the material. Halogenated graphenes have the general chemical formula $C_aH_bX_c, (a \geq b+c)$ where X represents the halide. From first-principle calculations, a band gap of between 0.1 and 7.5 eV can be realized, but not all stoichiometric combinations are expected to be stable at room temperature[75]. Of the halide attached graphenes, fluorinated graphene has received the most attention and has been produced in an inert environment and found to be stable at room temperature. Besides this, chlorinated and brominated graphenes have also been realized experimentally.[76–81]. Finally, oxygen functional groups have also been attached to the graphene basal plane to give GO. The first reported method of producing GO goes as far back as 1860 by Brodie and was reported on again by Staudenmaier in 1898[82,83]. More recently, Hummer and Offeman described a method of oxidising graphite by the use of strong oxidizing agents and this method, with modifications, has been the mainstay technique for the production of GO[84,85]. Due to the significance of GO in this work, a review of the material is performed in the following section.

1.2 Graphene Oxide

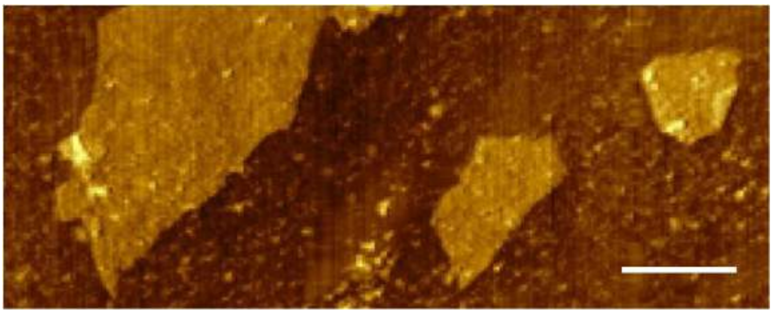

Figure 1.6: Atomic force microscope image of single layered GO with typical thickness of 1 nm and a typical lateral size of about 0.5 μm. The scale bar inset is 400 nm in length.

GO is an alternative to single layer CVD grown graphene if a water dispersible material is desired. By itself, graphene is a non-polar material and has low dispersibility in most solvents[86,87]. By adding covalently bound oxygen functional groups hydrogen bonds can be formed between water and the flake, giving a large E_2^{GO-Sol} value, Equation (1.6), a negative $\Delta\, H_{mix}$ value, Equation (1.9), and allows GO to be suspended readily in the aqueous medium[88].

A typical GO sheet with a measured thickness of 1 nm is shown in Fig. 1.6. The lateral size of the flake is highly dependent on both the grade of graphite powder and the production process used to manufacture GO. However, as a general rule, larger lateral sizes are preferred.

While GO and the analogous graphite oxide have been known to chemistry for a long time, there remains many unanswered questions regarding the material. In fact, just this year Yeh *et al.* uncovered the fortunate inclusion of a contaminant during the production process of GO that helps explain the stability of GO in water[89]. When a GO flake is hydrated, the carboxylic groups lose a hydrogen atom and this causes an accumulation of negative charges on the flake which should, in theory, tear the flake apart[90]. However, these negative charges are neutralized and the layer is prevented from disintegrating by the presence of cationic metal contaminants introduced during production[89].

There remains many unanswered questions regarding the chemical and electronic make-up of GO and the purpose of this section is to provide a backdrop of the knowledge available and to highlight areas of interest that the thesis will cover.

1.2.1 Production and Properties of GO

The process of GO production begins with graphite powder which is reacted with sulphuric acid, potassium persulphate and phosphorous pentoxide. The graphite powder is kept in this mixture for a few hours before washing and further oxidation with potassium permanganate. Quenching the mixture at this step produces a bright yellow suspension of GO and GO flakes can be filtered from this suspension typically by the use of an anodized aluminium oxide filter disk.

It is in this filtration step where the cation that stabilizes the GO flake is inadvertently introduced. After filtration, the filtrate is typically redispersed in water to give a suspension with the the characteristic brownish-black colour of a GO suspension[84,85].

The method of GO production can be classified into one of three major techniques, namely the Hummers, Brodies and Staudenmaier's methods[82–85]. It is important to note that the different methods of GO production give different types of GO that have unique physical properties[91]. While GO is a generic term used to describe graphene flakes with attached oxygen functional groups that possess a tunable electronic band gap, these GO materials may not be chemically or electronically identical.

Exposing graphite powder to harsh oxidizing conditions causes oxidation in a three-step process. The first step involves the intercalation of oxidising agents between the graphene sheets, followed by a multi-step reaction that gives graphite oxide[92]. Finally, the graphite oxide becomes GO when it is exposed to water and the intercalating molecules react with the water molecules[93]. However, these steps lead to the formation of a carbon rich by product known as oxidative debris (OD) which needs to be removed by a base wash or by hydrazine[94,95]. However, if hydrazine is used, it has the effect of removing OD and reducing GO at the same time[94]. Additionally, it is now known that OD is responsible for electroactivity in GO[96].

Besides allowing the material to be deposited by spray deposition onto virtually any surface of arbitrary shape, one of the biggest advantages to the water solubility of GO, is that it uses a non-toxic solvent. Although graphene is slightly soluble in NMP, NMP is toxic industrial chemical and hence not a desirable medium for making graphene sheet suspensions[97,98].

Initially insulating, conductivity can be restored to GO after reduction which involves the removal of oxide functional groups. The removal of the functional groups return the carbon atoms to a state of sp^2 hybridization and π bonds, which are responsible for electrical conductivity, are restored[9]. However, even in the best case scenarios, reduced GO has the twin drawbacks of higher sheet resistance and lower carrier mobility than even highly grained mono-layer graphene sheets[99,100]. This is mainly attributed to defect formation in the graphene basal plane during the oxidation and subsequent reduction steps, as well as, an inability to remove all oxygen groups from the flakes during reduction. This ten disrupts the conducting π-electron network and causes the lower conductivities and mobilities observed[101]. As might be expected, there is relationship between the density of oxygen functional groups on the graphene basal plane in GO to the optical band gap exhibited by the material[102–104]. Starting at 3.5 eV, the optical band-gap of graphene can be tuned to values as low as 1.0eV when the material is exposed to hydrazine for up to 108 hours[104]. However, the inability to remove all the oxygen atoms from the basal plane and to repair the defects introduced due to carbon vacancies or grain formation remains one of the greatest challenges in the use of GO as a starting material for graphene based devices[105].

1.2.2 Methods of Reduction

One way forward is to improve the methods of GO reduction to increase oxygen functional group removal. However a good reduction technique has to do more than merely remove oxygen functional groups. As described earlier, the oxidation step is harsh and has the possibility of introducing vacancies in the flake and even cause grain boundaries. Ideally, the reduction step will restore carbon atoms to vacancy sites as well as to rearrange the carbon atoms in the basal plane to remove grain boundaries, thereby improving the overall electron mobility across the reduced GO flake.

Methods to achieve this can be broadly classified into thermal or chemical means and may be employed simultaneously to improve reduction results. As will be detailed later, chemical means can help shorten the time and temperatures required to remove the oxygen functional groups and may event rearrange atoms to remove grain boundaries.

1.2.2.1 Thermal Reduction

Direct heat treatment of the GO film, releases oxygen functional groups and restores conductivity to the flake. As the reduction temperature is increased from 823 to 1373 K, the sheet resistance of a 10 nm thick sample falls from to 19.8 to 1.8 k$\Omega/\square$, while the transmittance increases from 60 to 75 %[106].
However, the temperature is not the only concern in thermally reducing GO. Both the reduction atmosphere and substrate play important roles in determining the properties of the reduced GO that is produced. Hydrogen gas diluted in argon is typically used as a reducing gas in thermal reduction experiments, however the presence of hydrogen is not a prerequisite for GO reduction[107]. In fact, GO can be thermally reduced in a nitrogen or argon environment or even in a vacuum to yield transparent conducting films with sheet resistances on the order of $10^2 - 10^3$ $\Omega/\square$ and optical transmittances of ~80 % at 550 nm[107,108].
The sheet resistance values of these films can be further reduced by the introduction of a carbonaceous sources such as alcohol vapours or methane during the thermal reduction process[107,109]. These carbonaceous sources aid in improving the conducting properties of these films by healing vacancies which then improves electron mobility and increases film conductivity. With these improvements, the time taken for reduction can be shortened by up to six times and the sheet resistance values for films with ~95 % transmittance improved from 500 to 10 k$\Omega/\square$[107,109].

1.2.2.2 Chemical Reduction

Besides the methods of using a reducing-gas and high temperatures mentioned in the previous section, the chemically bound oxygen functional groups can also be effectively removed by the use of strong reducing agents such as hydrazine, metals and their halides, sulphur and ascorbic acid (AA)[30,110–115]. The methods to produce reduced GO are varied and the temperature range used to accomplish the reduction is highly dependent on the chemical reducing agent used. Importantly, the films produced by reduced GO from these methods also have varying transmittance and sheet resistance values.
Hydrazine is one of the most effective chemicals used in the reduction of GO and has been shown to reduce the optical bandgap in GO[104]. This depends on the

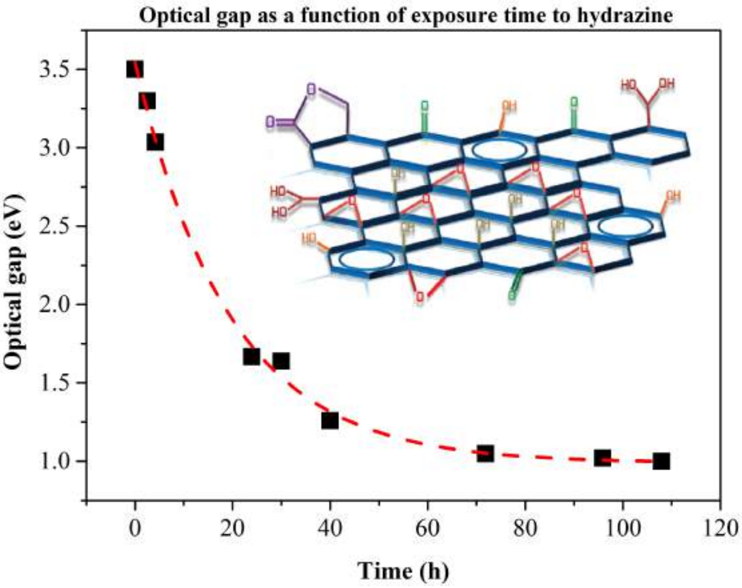

Figure 1.7: Change in the optical gap in graphene as the exposure time to hydrazine vapour is increased. The gap reduces from 3.5 eV in untreated GO to 1.0 eV after exposure to hydrazine for 108 hours.
Adapted with permission from refernce [104]. Copyright 2012 American Chemical Society.

time of exposure of GO to hydrazine and increasing exposure time meant more oxygen groups were removed from the GO flake. This causes the closing of the optical band gap as shown in Fig. 1.7. After more than 100 hours of exposure to hydrazine, the optical bandgap is reduced from 3.5 to ~1.0 eV.

In another example, using indium(I) chloride as the reducing agent has the effect of selectively removing epoxides while regenerating the network of sp^2 hybridized carbon atoms in GO[113]. With the restoration of the network, a 10× increase in the conductivity of the film was observed, as compared to a film that was reduced using hydrazine only. Despite only removing epoxides, the conductivity was improved significantly be repairing the C–C network in the flakes.

These examples show that restoring conductivity to GO involves two major steps:

i. The efficient removal of oxygen functional groups from the basal plane
ii. Restoring the quality of the basal plane for maximal electron mobility

While attractive, the second example opens up the possibility of metal contamination in the reduced film. Additionally, in what might be the largest draw backs faced when using metals in the reduction process, a large amount of metallic compound was required to reduce a small amount of GO that is reduced. To put things in numbers, metallic reducing agents are typically required to be present in concentrations 2-20 times higher than the concentration of GO present[112,113]. The volume of waste produced, as well as the cost of metallic chemicals required are likely to stop these methods from being adopted in large scale operations.

Besides hydrazine and metallic halides, AA has also been touted as an effective and environmentally friendly chemical alternative that can reduce GO[114,115]. The process typically requires mixing GO with AA and allowing the chemical reaction to progress at 353 K over a period of 12 to 48 hours. After the reaction is complete, reduced GO papers with high conductivities and lower optical transmissions can be made. The authors of these early works showed that the reduction capabilities of AA rivalled that of hydrazine and gave films with sheet resistances as low as 4.5 Ω/□ in 300 μm thick samples[115].

It was proposed that AA reacted specifically with epoxy and hydroxyl groups on the GO flake in a two step process that removes the functional group and restores a π-bond on the reduced GO flake; a proposed schematic of this process is shown in Fig. 1.8. It was also shown that adding a base to the mixture of AA and

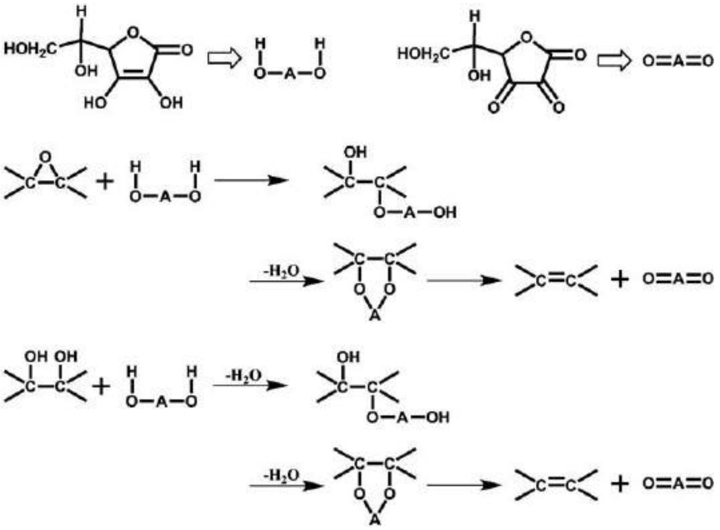

Figure 1.8: Schematic of GO reduction by AA as proposed by Gao *et al.* The AA selectively targets either epoxides (top) or hydroxyls on adjacent carbon atoms, reducing GO by the removal of a water molecule. The oxidized AA is then released from the GO flake and this restores the π-bond between the adjacent carbon atoms. Reprinted with permission from reference [114]. Copyright 2010 American Chemical Society.

GO would shorten the time taken for reduction to just 15 minutes and further decrease the sheet resistance of the reduced GO paper as well[116]. It was also reported that the rate of reaction could be further enhanced by subjecting the mixture to ultrasound treatment as it had the effect of lowering the activation energy of the reduction reaction[117].

In closing, it is interesting to note that none of the reports mentioned above attempted to use the mixture of AA reduced GO to fabricate TCEs. In fact, the research direction for this mixture thus far has mainly been focused on the improvements in conductivity and applications reported thus far were limited to the formation of hydrogels, conductive wires and as a modification applied to the glassy carbon electrode[118–120].

1.2.3 Challenges in Understanding GO

Besides the method of production, there are many other factors that may contribute to the differences that researchers have observed in GO. In the years since the wide-scale study of GO, we have come to learn several interesting and unexpected facts about the material. Researchers used to think that aqueous GO was a stable. However, it recently became clear that aqueous GO was a dynamic material. While the suspension remains stable, the chemical structure of the GO flake undergoes changes over time, when aqueous or dried[121–124]. We next learnt that there is a second material known as OD that is produced as a by-product of the oxidation process and then found out that it was the accidental introduction of aluminium ions that stabilized the GO sheet in water and prevented it from disintegrating[89,94,95].

While these important and often disrupting findings help in deepening the body of knowledge available on GO, they also help to shed light on the difficulties faced by earlier researchers.

For example, it has always been a challenge to build a satisfactory working model to describe GO despite the great effort that had been expended. As recently as 2010, a review article made the comment that the structure of GO is difficult to ascertain “and even to this day no unambiguous model exists”[125]. As with any theoretical model, there is a need for continuous and iterative updates when new facts become available until a satisfactory model is built. However, there remains no doubt that the intermediate models developed thus far are essential towards progress in the field and that establishing an unambiguous model for GO would do for the GO community what the discovery of deoxyribonucleic acid (DNA) did for the study of biology.

1.2.3.1 Models of GO

The Lerf-Klinowski (LK) model began as a model to describe graphite oxides, in which only epoxides and hydroxides were incorporated onto the graphitic material[126]. In the same year, the authors revisited their model and added carboxylic acids to the model, as shown in Fig. 1.9 and this model is currently the most widely used model to describe GO[127]. A recent update to this model known as the Ajayan (AJ) model adds ketones and lactols as functional groups in GO[128]. These models assume a random distribution of oxygen groups on the basal plane and no order is expected, while the Dékány model supposes that a periodic structure occurring within each flake[129].

The community is well on its way towards finalizing a theoretical model that is capable of incorporating all available knowledge about GO and it is likely that a robust theoretical model to describe GO will be arrived at soon. However, there are still gaps in the characterization information that need to be filled.

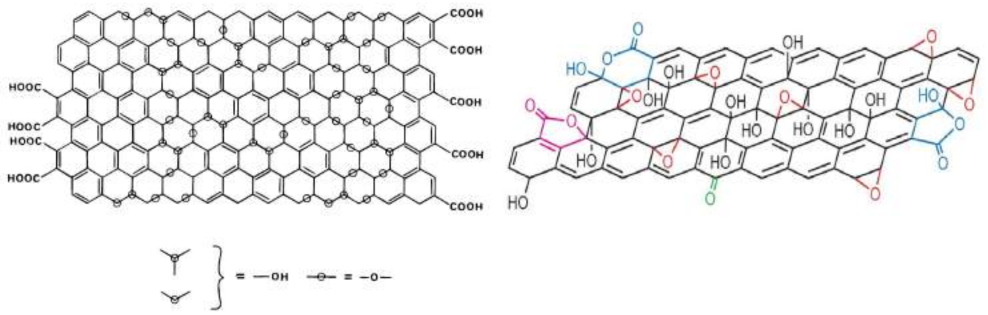

Figure 1.9: Models of GO. Left shows the Lerf-Klinowski model and the Ajayan model is shown on the right.

Reprinted with permission from reference [127]. Copyright 1998 American Chemical Society.

Reprinted by permission from Macmillan Publishers Ltd: Reference [128], copyright 2009.

1.2.3.2 Different Types of GO

A major difficulty in identifying the nature of GO, is the fact that there are three main techniques of producing it, namely the Hummers, Brodies and Staudenmaier's methods[82–84]. The methods have been modified for greater oxidation of the individual flakes and one report has even shown that GO produced by the Hummer's and Brodie's techniques have different physical characteristics[91].

According to the report, one would be able to tell if the GO material was made by the Hummer's or Brodie's method by comparing the relative ratios of the carbonyl bound and the hydroxyl bound C $1s_{1/2}$ electrons in the XPS spectra, from the position of the X-ray diffraction peak or even from the thermo-gravimetric analysis (TGA) graphs as GO produced by the Brodie's method has a higher onset temperature of 554 K while the onset temperature in GO produced by the Hummer's method is 486 K.

It would be ideal if one model of GO was sufficient to account for all these differences, but many open ends still exist in this topic. The ability to identify the exact type and relative concentrations of each oxygen group present in GO would be useful towards developing this canonical model.

1.2.3.3 Presence of Oxidative Debris

In the 60 years since the first study made on the structure of graphite oxide by Beckett & Croft in 1952, researchers have been trying to explain the amorphous nature of GO[130]. The presence of OD was first observed by Fan *et al.* in 2008, and characterized by Rourke *et al.*three years later, may help explain away some of these challenges[94,131].

Fig. 1.10 is a representation of OD, which is a carbon rich by-product that naturally forms during the production of GO and is responsible for the electroactivity inherent in GO[94,96]. It is the reason for the steep increase in the rate of mass loss at temperatures greater than 473 K during TGA analysis of GO, is likely the material that causes the exfoliation effect observed by You *et al.* and likely contributes to the difficulties that arise during GO characterization[91].

What becomes clear then is that identifying the exact oxygen groups present in OD-free GO is an important step in improving the understanding and modelling of GO. This understanding can also help in focusing effort towards developing

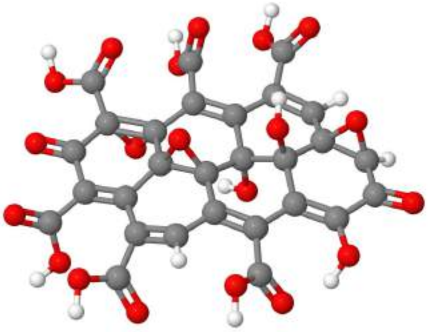

Figure 1.10: Proposed model of OD in the article by Rourke et al.[94]
Adapted from reference [94]. Copyright © 2011 John Wiley and Sons

better reduction techniques tailored specifically for the removal of the oxygen groups present on the flake.

Although the consensus is that it is extremely unlikely that ‘new’ by-products will be found in GO in the future, this finding gives a strong reason to revisit the widely accepted models of GO that have been proposed prior to 2011 and to reflect on mechanisms and processes that have been proposed in the past.

How would this material fit into these models and are there interactions that may have been erroneously ascribed to GO when it should have been ascribed to OD? The implications of these findings may weave together the disparate tapestry of ideas that are used to describe GO and bring the community closer to the completion of the canonical model.

1.2.3.4 Limitations in Data from XPS

A major challenge faced by the community in GO characterization by XPS lies in the deconvolution of the spectra of these GO materials. Typically, the identity of a peak is determined if, within certain tolerances, it matches the binding energies from other organic molecules. This normally allows the identification of the type of functional group present in a material. However, there are times when it is not possible to discern this from the spectra and a peak is sometimes widened to improve the fit.

For example, the O $1s_{1/2}$ electrons in oxygen functional groups such as hydroxyls and epoxies, which form a single bond to carbon atoms, typically have lower binding energies than the same atoms from oxygen atoms in carbonyl groups,

groups that form double bonds with carbon atoms. If the peaks of individual functional groups cannot be discerned from the spectra, a wider peak can be used to account for all O $1s_{1/2}$ electrons from functional groups that are singly or doubly bonded to carbon atoms[132].

This method of spectra deconvolution has led the charge in XPS characterization of GO, however there are still difficulties present in the process of peak deconvolution that are limiting the accuracy of these results. While there are many detailed XPS characterization studies on GO, the vast majority of these studies use only the C $1s_{1/2}$ spectra to identify changes in the GO[30,91,96,123,133,134]. The method can identify the relative ratios of sp^2 and sp^3 hybridized carbon atoms and confirm if the sample present is a GO derivative or amorphous carbon, but has a few limitations that can only be overcome by a characterization study of the O $1s_{1/2}$ spectra.

One limitation encountered is related to the relative sensitivity factors of the C $1s_{1/2}$ and the O $1s_{1/2}$ electrons. O $1s_{1/2}$ electrons have a relative sensitivity ratio that is 2.93 times greater than C $1s_{1/2}$ electrons, and under the same characterization conditions will give more accurate information about the functional groups present than the C $1s_{1/2}$ spectrum[135].

The next limitation is related to the relative composition of peaks in the O and C $1s_{1/2}$ spectra. In GO samples with a high carbon to oxygen (C/O) ratio, the large sp^2 peak present in the C $1s_{1/2}$ spectra, contributed by the un-oxidized carbon atoms can mask the signal from functionalized carbon atoms, thereby reducing the accuracy of any characterization results; on the other hand, it should be obvious that the O $1s_{1/2}$ spectra is immune to this problem.

At the start of the PhD in 2011, it was discussed that an improved set of characterization peaks for the O $1s_{1/2}$ spectra would be very useful in furthering the understanding on GO. Surprisingly, the problem was not solved in the following years and in an article that was published in 2014, Susi *et al.* commented on the O $1s_{1/2}$ spectra of GO, saying that "the line-shape variations of graphene have not been extensively examined in experimental reports" and more work is still required on the XPS characterization of the O $1s_{1/2}$ electrons in GO[136].

1.2.3.5 Metastability of GO

Adding another layer of complexity to this difficult topic is the recent discussion about the liquid phase and dry metastability of GO, best summarized as a change in the material over time. In its simplest form, GO metastability can be thought of as an ageing process due to the migration of oxygen functional groups on the GO flake that then results in changes in the physical characteristics of the GO film or suspension[121–124]. This effect is visualized in Fig. 1.11, where the suspensions, which were originally the same colour, gradually darkened after being kept at 353 K for up to 72 hours.

When GO produced by the Hummer's method is suspended in water, the translation of the functional groups on the GO flake is driven by the temperature to reduce the total energy of the flake and results in the formation of oxygen rich domains[122]. The speed of formation of these oxygen rich domains can be controlled by the external temperature of the suspension and can be used to tune some aspects of the GO material[122].

Using this technique, the conductivity of the film is improved by up to four orders of magnitude. However, with sheet resistances in the order of 100 kΩ/□, the material is not conductive enough to be used in TCE applications. Further reduction techniques will need to be applied to the resulting GO material, and this will have implications on the effect an efficacy of established reduction techniques.

While it is unanimously agreed that optical absorption is red shifted as a result of metastability, there is contention if the C/O ratio is maintained[121,122]. The formation of vinylogous carboxylic acids and generation of hydronium ions as described by Dimiev *et al.*, will decrease the C/O ratio, however if GO is as stable as Kumar *et al.* say it is, we would not expect the C/O ratio to change[121,122].

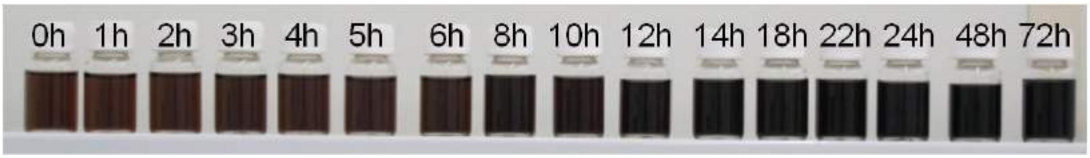

Figure 1.11: Experiment conducted to show the change in colour of the GO suspension over time when it was annealed at 353 K. All bottles came from the same parent suspension and were the same colour prior to annealing; the suspensions gradually darkened as an effect of liquid phase metastability.

Adding a base to an aqueous suspension of GO results in the evolution of CO_2 and at the same time, base washing GO is a known method to remove OD from as-deposited GO. What then is the relationship between the evolution of CO_2 and OD and do the aluminium ions that stabilize the GO sheets in the aqueous suspension play a role in this reaction[89,95,121]? Answering these questions will aid in building the canonical GO model.

Still, GO is not metastable in its aqueous suspension only; even after it has been deposited as a film, GO produced by the Hummer's method can continue to change. The hydrogen atoms between the GO sheets reduce epoxides to hydroxyls and hydroxyls to water molecules as the material approaches an equilibrium state over the course of 30 days[123]. Even as a dried powder, a reduction in the concentration of epoxide groups present in GO was observable over a period of 30 weeks[124].

These findings go to show that GO as a material is constantly changing and may continue to change well beyond the established scope of these studies. Understanding these changes and being able to predict them will be important milestones to enable the usage of GO in future material systems.

1.3 Uses of Graphene & Graphene Derivatives

According to an IDTechEx report in 2012, the development of graphene technologies have come to the point where technological uses are poised to exit the trough of disillusionment and to enter a phase of enlightenment[137,138]. This represents the maturing of the use of graphene in a particular technology sector and that there are real benefits to using graphene in these areas.

With nearly 8000 patents published between 2004 & 2012 in topics ranging from additives to active layers, innovation in the field is intense there appears to be many potential uses for graphene[3]. This observation is supported by surveying journal articles that use graphene as a subject of scientific research and as a active or passive material in a device or system.

By searching through the journal databases, of the 36,742 graphene or GO articles published between 2004 and 2013, 11,394, or just over 31 %, of the articles used graphene or GO as an additive, catalyst, device, sensor or transistor. In the remainder of this section, some of the uses of graphene or GO are listed and the state of the art of graphene and/or GO based technology for each use is discussed.

1.3.1 Transparent Conducting Electrodes (TCE)

With its high absorbance value of 2.3 % per layer or nearly 7 % nm^{-1} of material and low intrinsic carrier density of ~10^{10}cm^{-2} it is surprising that graphene should even be considered as a candidate TCE material[18,19,139]. However, graphene and GO are highly flexible and this advantage opens up new technological possibilities, making them attractive electrode materials in some use cases.

Before moving further into this discussion, it should be apparent that the values of both sheet resistance and transmittance are thickness dependent and that thicker films a given material are less transparent and will have lower sheet resistances than thinner films of the same material. It would thus be beneficial to use a thickness independent figure of merit (FOM) to describe the quality of a free-standing film as a TCE. The FOM value would give the relationship between these physical variables allowing material systems with varying thickness, sheet resistance and transmittance values to be compared.

The sheet resistance of the film is related to the thickness by[105]

$$R_{sh} = (\sigma_{dc}\, t)^{-1} \tag{1.11}$$

Additionally, the transmittance of a film is related to its thickness according to the equation[140]

$$T = \left(1 + \frac{Z_0}{2}\sigma_{op}\, t\right)^{-2} \tag{1.12}$$

where $Z_0(377\Omega)$ is the impedance of free space and t is the thickness of the film. Combining these equations by substitution of t, the FOM ($\frac{\sigma_{dc}}{\sigma_{op}}$) is found to be[105]

$$\frac{\sigma_{dc}}{\sigma_{op}} = \left[\left(\frac{1}{\sqrt{T}} - 1\right)\frac{2\, R_{sh}}{Z_0}\right]^{-1} \tag{1.13}$$

In this form, the larger the σ_{dc}/σ_{op} values signify that the film has low sheet resistance and high transmittance values.

The FOM relates the optical conductivity to the direct current conductivity of the film and as a point of reference, ITO with a sheet resistance of 10 Ω/□ and transmittance of 90 % has $\sigma_{dc}/\sigma_{op} = 349$. Comparatively, the calculated FOM for highly doped graphene is about 330 abd this is comparable to the performance characteristics of ITO[105].

Wang *et al.* showed a linear relationship between the reduction in transmission and the number of layers of graphene added to the stacked film. By stacking four layers of MLG and doping the stack with gold chloride, they fabricated a TCE with a low sheet resistance of 80 Ω/□ and transmittance of 90 % to give a film with FOM of 44[141]. However, because the gold chloride dopant atoms were not chemically bonded to the graphene sheets, the doping effect was not stable over time and the sheet resistance had a tendency to diffuse away[142]. This caused a gradual increase in the sheet resistance of the film and a loss in the quality of the film as a TCE.

On top of this, stacking monolayer graphene is never perfect and the process introduces voids and gaps between the layers. As a result of this, interlayer spacings are typically larger than the 3.35 Å typically found for graphite[16]. While this affects the transmittance value of the film marginally, the sheet resistance is significantly impacted and is typically much higher than that of ideal MLG[141,143].

Ferroelectric materials can also be used to increase the carrier densities in graphene and in 2012, Khrapach *et al.* intercalated few-layer graphene with iron chloride, Fig. 1.12, and showed in the small scale that sheet resistances of 8.8 $\Omega/\square$ and a transmittance of 84 % could be achieved[144]. In the samples, the hole mobilities were shown to be as high as 3650 cm^2(V s)-1 and hole carrier densities of up to 8.9 $\times 10^{14}$ cm^{-2} were possible[144]. While attractive, this method is not scalable for large area devices unless large area graphene was used. Ni *et al.* showed that this this could be done with chemical vapour deposited graphene and with a non-volatile ferroelectric material. This new structure had a carrier density of up to 3×10^{13} cm^{-2}, improved the sheet resistance of the monolayer to 120 $\Omega/\square$ while retaining a high transmittance of 95 %[145].

Metals can also be incorporated into the graphene material to improve its electrical conductivity. There are a variety of methods to incorporate the metallic atoms

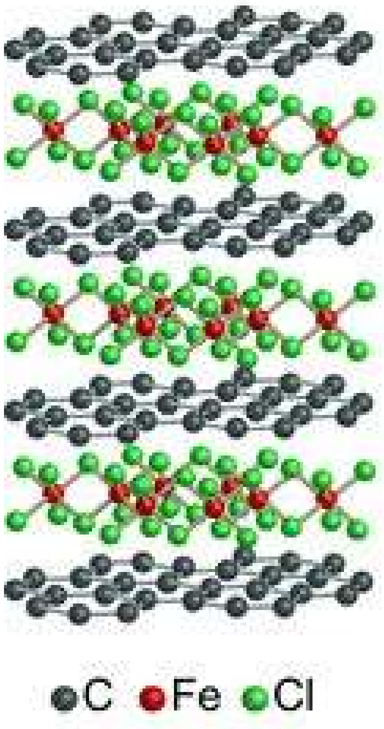

Figure 1.12: Schematic of the iron-chloride ferro-electrically doped few layer graphene called Graphexeter.

Reprinted with permission from reference [144]. Copyright © 2012, John Wiley and Sons.

onto graphene, such as nanowires or nanoparticles which have proven themselves to be exceptionally effective in lowering the sheet resistance of the films.

By electrochemical lithiation, lithium was intercalated into few layer graphene and showed optical transmission of 91.7 % with an associated sheet resistance of 3.0 $\Omega/\square$[146]. Using silver nanowires and graphene, a film with sheet resistance of 30 $\Omega/\square$ and a transmittance of 86.3 %, close to the performance characteristics of ITO, was fabricated[146].

It is also possible to use GO in the place of graphene in some of the above mentioned examples. For example, GO can be spin-coated onto silver nanowires and reduced by exposure to plasma or iodine to give films with 92.0 % transmittance and sheet resistance as low as 17.3 $\Omega/\square$[147,148]. These films exhibited greater temperature and and humidity stability than comparable silver nanowire only TCEs and the improvement is attributed to the protection afforded by the reduced GO layer that limits the interaction of the air with the silver nanowires.

1.3.2 Chemical Sensing

As early as 2007, Schedin *et al.* showed that due to the low intrinsic noise in micrometer sized graphene sheets, the event of a single molecule adsorbtion could be detected as a step-wise change in the resistance of the device[149]. Although graphene had demonstrated sensitivity to the presence of an analyte and the high surface area to volume ratio made it attractive as a sensing platform, it soon became clear that, graphene did not have the selectivity required to be an effective chemiresistive gas sensor.

The typical graphene based sensor setup is shown in Fig. 1.13 and it becomes apparent that all modifications must be made directly on the graphene sheet. A few methods have been developed to overcome the lack of selectivity in these sensors, but with the exception of one technique, selectivity towards gas sensing invariably came with an associated cost of reduced sensitivity. It was shown that despite the lack of selectivity on the part of the graphene film, the presence of certain molecules on the film left a fingerprint that could be detected from the low frequency noise spectra[150]. Though not shown, this would theoretically allow the film to retain its single molecular sensitivity and provides a method that may potentially identify the molecule present.

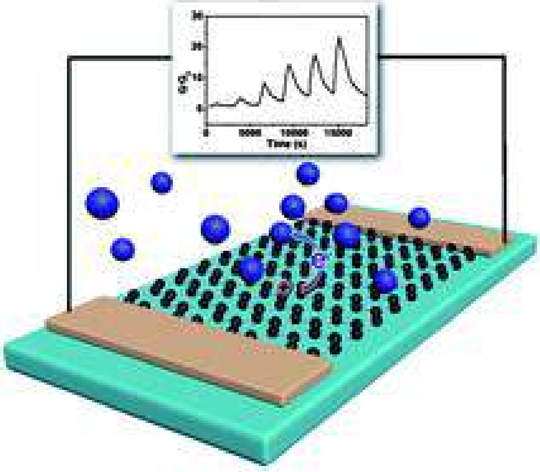

Figure 1.13: Depiction of the setup of a typical graphene base sensor and associated response due to the introduction of a an analyte.
Reproduced from reference [151] with permission of the Royal Society of Chemistry.

Other methods of improving the selectivity of the graphene film involve functionalization of the graphene or the addition of selective sensing particles by decorating the layer with nanoparticles or metals and their oxides[151]. In these situations, the functionalizing material is always in intimate contact with the graphene material and in some cases is even chemisorbed onto the graphene film. Using gold nanoparticles, ammonia gas can be sensed at concentrations of 58 parts per million and with optimization, a system that uses palladium and reduced GO exhibited sensitivity to nitrogen monoxide at concentrations as low as 2 parts per billion[152,153].

Besides gas sensing, graphene has also been used for detection of cancer biomarkers and to sequence DNA[154,155]. While the principle used in biomarker sensing is similar to that used by the gas sensor, in which a sensing molecule is dispersed onto the graphene layer, the graphene DNA sequencer makes use of a pore on the graphene sheet. As the DNA molecule passes through the pore on the graphene sheet, the base-pair that passes through the pore interacts with the edge carbon atoms and the transconductance of the sheet is changed. Depending on the base-pair in the pore, the transconductance changes and this can be used as a reading[155].

1.3.3 Field Effect Transistors

One of the earliest uses of the graphene in a device was a FET shown by Lemme *et al.*when they used a graphene nano-ribbon as the channel in a top-gated field effect device as shown in Fig. 1.14[156]. They showed that by changing the applied field, the source-drain current could be modulated and also established that even with the top gate present, graphene retained electron and hole mobilities of 530 and 710 cm^2/Vs respectively, which is much higher than the electron mobility of 490 cm^2/Vs and hole mobility of 95 cm^2/Vs in silicon.

The next major step came when graphene was used in a FET for high frequency electronics[157]. At 50 GHz, the intrinsic cut-off frequency achieved for this FET was double that of a comparable silicon based metal-oxide semiconductor field effect transistor[157]. Following this, an on-off ratio of ~100 and ~2000 was achieved in a graphene FET at room temperature and 20 K respectively[158].

Further improvements were made by changing the geometry of the device and using hexagonal boron nitride. These changes gave a device with a temperature independent on-of ratio that could go as high as 10,000[159]. However, this came at a cost of low device current, on the order of picoamps, and limited the potential uses of such a device setup[159]. However, by using graphene as the source and drain contacts, Roy *et al.* fabricated a device with high on-off ratio of 1,000,000 using tungsten selenide and molybdenum sulphide as the channel material[160].

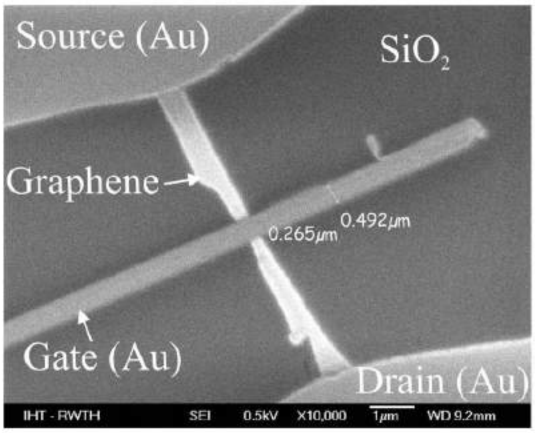

Figure 1.14: Scanning electron microscope image of a graphene transistor made from a graphene nanoriboon.

This series of developmental steps shows the importance of the high carrier mobilities in graphene and the limitations that graphene has. Without the ability to induce a sufficiently large band gap, the on-off ratios in a device with a graphene channel will always be too small for reliable use.

1.3.4 Energy Storage

The specific surface area of monolayer graphene and GO can be estimated at about 2600 m^2/g, a value that far exceeds the specific surface area of graphite powder, 0.6 m^2/g and carbon black ~20 m^2/g[161,162]. If the large specific surface area of graphene can be utilized efficiently, this would increase the specific energy density of secondary batteries this has become a strong driver in the quest to use graphenic materials in energy storage devices.

In one of the first reports on the use of graphene in secondary batteries, Yoo *et al.* showed a device that had a specific capacity 784 mAh/g when the graphene electrodes were used with other carbon based molecules[163]. However, the devices had low cycle durability and lost more than 10 % of its capacitance within 22 charge/discharge cycles at a charging density of 0.05 A/g.

Since then, cycle durabilities have increased significantly and by using nitrogen-doped graphene, Qiu *et al.* fabricated devices suitable for high power usage which can retain up to 80 % of its initial device specific capacity of 480 mAh/g for at least 700 cycles[164]. There is also strong interest in utilizing the high specific power of graphene based batteries and recent work has shown that graphene enhanced Ni-Fe batteries with an effective specific capacity of 115 mAh/g and have cycle durabilities of over 1000 cycles, even when cycled at a rate of about 24 C[165].

Graphene has also been used in supercapacitors which can deliver very high power and cycle durability but at a cost of low energy densities. Initial work with the material gave a device with a specific capacitance of 117 F/g and an energy density of 31.9 Wh/kg when used with an aqueous sulphuric acid electrolyte[166]. By using nitrogen doped graphene, the specific capacitance reached a new high of 170.1 F/g at an energy density of 72.37 Wh/kg[167]. The use of graphene in supercapacitor energy storage for devices as diverse as speakers and electric trams may mark a new starting point of these stored energy devices[168,169].

1.3.5 Material Enhancement

Graphene can be used to enchance the mechanical strength of materials and Khan *et al.* have shown that the incorporation of carbon nanotubes and graphene in polyethylene terephthalate fibres at loading concentrations as low as 2 wt% leads to a 2 to 4 time increase in the strength of the material[170].

Rather surprisingly, this strengthening effect is also observed in GO. Despite the oxygen functional groups and vacancies in GO, the material can still add mechanical strength to a polymeric system. By adding 1 wt% of GO to gelatin, Panzavolta *et al.* showed that the Young's modulus of the gelatin was increased by more than 50 % and the fracture stress by more than 60 %[171].

GO can be used as more than just an additive; graphene fibres (GF) have also been prepared from GO. Using a variety methods GF of different tensile strengths have been developed and one of the biggest advantages that using GF has over other more established materials such as carbon nanotubes and carbon fibres is the lowered cost of production associated with GFs[172]. However, the technology is still in its infancy and its mechanical and electrical properties are poorer than the state of the art carbon nanofibres[172].

There are clear benefits to the use of graphene and GO as an additive in material systems and there is growing industrial use of these materials to improve the mechanical performance of a product. With ever improving production techniques, it is believed that the material will soon find use in electronic devices as well.

1.4 Scope of Work

Graphene is extremely well understood by the scientific community as it has been studied extensively in the decade since its official discovery. The significant challenges that remain are mainly engineering in nature that makes use of the established body of knowledge about graphene to incorporate the material into or develop it into new and existing technologies. GO on the other hand has continually thrown up unexpected surprises. From the discovery of oxidative debris in 2011 to the understanding of its metastable nature in 2013, there continues to be a need to improve the fundamental understanding of GO[94,121].

One of the goals that was established at the start of the Ph.D. was to contribute towards building a canonical model of GO and even now, as described by Eigler & Hirsch, GO remains a "polydisperse material, whose exact structure is very difficult to precisely define"[173]. However, as discovered later in Chapter 4,building such a canonical model may not be possible due to the inherently amorphous nature of GO.

While the XPS studies of GO were many, it was noted that almost all the work was focused on the C $1s_{1/2}$ spectra in graphene and GO and there was a distinct lack of information on the O $1s_{1/2}$ spectra. In the followed years, this did not change significantly, and the lack of experimental reports was also noted by Susi *et al.* in 2014[136].

Additionally, there continues to be a need to develop the understanding of the reduction process in GO in the different atmospheric conditions that may be encountered during production. When incorporating GO into electronic devices, differences in the gaseous environment and temperature profiles may affect the quality of the reduced GO and this will need to be understood as well.

This scope of the work in this thesis will cover the following:

i. Experimental characterization of the O $1s_{1/2}$ electrons in GO under different environmental and chemical conditions
ii. Evaluation of models of graphene from the type and quantity of oxygen functional groups found
iii. Study GO metastability from the perspective of the O $1s_{1/2}$ spectra
iv. Harmonize the recently discovered aspects of GO with the above findings

Having developed this understanding of GO, the material is used in:

i. Transparent conducting electrodes and
ii. Gas sensing devices

The goal of the first application is to produce a film with the highest possible transmittance and lowest possible associated sheet resistance by means of an industrially scalable process. Here, an industrially scalable process means that the deposition technique must be scalable to cover large areas, that the entire process does not require excessively high operating temperatures and that the use of expensive and/or environmentally dangerous chemicals is avoided. After this has been established and the GO only TCEs have been reliably and reproducibly made, the TCEs are to be enhanced by the introduction of secondary materials that will lower the sheet resistance of the TCE with minimal effect on the transmittances of the resulting films.

For the second application, reduced GO will be used in conjunction with a sensing polymer and the combination is tested for its effectiveness as a gas sensor in a novel device architecture. The design of the device is such that the strengths of each material complements the shortcoming of the other. In this case, GO is conferred analyte selectivity by the sensing polymer which typically has very low conductance values, while the current passing through the device at low voltage is increased by the presence of reduced GO. The operating principle of this device architecture will then be studied and from this understanding further improvements to the design proposed.

References

[1] JD Fitz Gerald, GM Pennock, and GH Taylor. **Domain-structure in MP (mesophase pitch)-based fibres**. *Carbon*, **29**:139–164, 1991, DOI:10.1016/0008-6223(91)90065-Q. 1

[2] Ronald A. Greinke and Richard I. Bretz. **Low surface acid intercalated graphite and method**, Dec 1994. US Patent 5,376,450. 1

[3] Patent Information Team. **Graphene - The worldwide patent landscape in 2013**. Technical report, Intellectual Property Office, The Intellectual Property Office, Concept Hourse, Cardiff Road, Newport, NP10 BQQ, March 2013. 1, 2, 27

[4] Thomas W. Ebbeson. **Carbon Nanotubes**. *Annu. Rev. Mater. Sci.*, **24**:235–264, 1994, DOI:10.1146/annurev.ms.24.080194.001315. 1

[5] X. Zhao, Ohkohchi M., M. Wang, S. Iijima, T. Ichihashi, and Y. Ando. **Preparation of high-grade carbon nanotubes by hydrogen arc discharge**. *Carbon*, **35**:775–781, 1997, DOI:10.1016/S0008-6223(97)00033-X. 1

[6] Claire Berger, Zhimin Song, Tianbo Li, Xuebin Li, Asmerom Y. Ogbazghi, Rui Feng, Zhenting Dai, Marchenkov Alexei N., Edward H. Conrad, Phillip N. First, and Walt A. de Heer. **Ultrathin Epitaxial Graphite: 2D Electron Gas Properties and a Route toward Graphene-based Nanoelectronics**. *J. Phys. Chem. B.*, **108**(52):19912–19916, 2004, DOI:10.1021/jp040650f. 1

[7] K. S. Novosolev, A. K. Geim, S. V. Morozov, D. Jiang, Y. Zhang, S. V. Dubonos, I. V. Grigorieva, and A. A. Firsov. **Electric Field Effect in Atomically Thin Carbon Films**. *Science*, **306**:666–669, 2004, DOI:10.1126/science.1102896. 2

[8] K. S. Novosolev, D. Jiang, F. Schedin, T. J. Booth, V. V. Khotkevich, S. V Morozov, and A. K. Geim. **Two-dimensional atomic crystals**. *Proc. Natl. Acad. Sci.*, **102**(30):10451–10453, 2005, DOI:10.1073/pnas.0502848102. 2

[9] K. S. Novosolev, A. K. Geim, S. V. Morozov, D. Jiang, M. I. Katsnelson, I. V. Grigorieva, S. V. Dubonos, and A. A. Firsov. **Two-dimensional gas of massless Dirac fermions in graphene**. *Nature*, **438**:197–200, 2005, DOI:10.1038/nature04233. 2, 16

[10] Nobel Media AB 2014. **The Nobel Prize in Physics 2010**. www.nobelprize.org/nobel_prizes/physics/laureates/2010/ [Last checked Oct 2014]. 2

[11] Yuanbo Zhang, Yan-Wen Tan, Horst L. Stormer, and Philip Kim. **Experimental observation of the quantum Hall effect and Berry's phase in graphene**. *Nature*, **438**:201–204, 2005, DOI:10.1038/nature04235. 2

[12] A. K. Geim and K. S. Novoselov. **The rise of graphene**. *Nat. Mater.*, **6**(3):183–191, 2007, DOI:10.1038/nmat1849. 3

[13] Mark Peplow. **Graphene: The quest for supercarbon**. *Nature*, **503**(7476):327–329, 2013, DOI:10.1038/503327a. 3

[14] J.N.B. Rodrigues, N.M.R. Peres, and J.M.B. Lopes dos Santos. **Scattering by linear defects in graphene: A continuum approach**. *Phys. Rev. B*, **86**:214206, 2012, DOI:10.1103/PhysRevB.86.214206. 4

[15] Michael M. Scherer, Stefan Uebelacker, Daniel D. Scherer, and Carsten Honerkamp. **Interacting electrons on trilayer honeycomb lattices**. *Phys. Rev. B*, **86**:155415, 2012, DOI:10.1103/PhysRevB.86.155415. 4

[16] D. D. L. Chung. **Graphite**. *J. Mater. Sci.*, **37**:1475–1489, 2002, DOI:10.1023/A:10149153077378. 4, 28

[17] E. Rollings, G.-H. Gweon, S.Y. Zhou, B.S. Mun, J.L. McChesney, B.S. Hussain, A.V. Fedorov, First P.N., W. A. de Heer, and

A. Lanzara. **Synthesis and characterization of atomically thin graphite films on a silicon carbide substrate**. *J. Phys. Chem. Solids*, **67**:2172–2177, 2006, `DOI:10.1016/j.jpcs.2006.05.010`. 5

[18] R.R. Nair, P. Blake, A.N. Grigorenko, K.S. Novoselov, T.J. Booth, T. Stauber, N.M.R. Peres, and A.K. Geim. **Science**. *Fine structure constant defines visual transparency of graphene*, **320**:1308, 2008, `DOI:10.1126/science.1156965`. 27

[19] K. F. Mak, M. Y. Sfeir, Y. Wu, C. H. Lui, J. A. Misewich, and T. F. Heinz. **Measurement of the optical conductivity of graphene**. *Phys. Rev. Lett.*, **101**(19):196405, 2008, `DOI:10.1103/PhysRevLett.101.196405`. 27

[20] K.S. Novoselov, A.K. Geim, S.V. Morozov, D. Jiang, M.I. Katsnelson, I.V. Grigorieva, S.V. Dubonos, and A.A. Firsov. **Two-dimensional gas of massless Dirac fermions in graphene**. *Nature*, **438**:197–200, 2005, `DOI:10.1038/nature04233`. 4

[21] S. Roddaro, P. Pingue, V. Piazza, V. Pellegrini, and F. Beltram. **The Optical Visibility of Graphene: Interference Colors of Ultrathin Graphite on SiO_2**. *Nano Lett.*, **7**:2707–2710, 2007, `DOI:10.1021/nl0711581`. 4

[22] P.R. Wallace. **The Band Theory of Graphite**. *Phys. Rev.*, **71**:622, 1947, `DOI:10.1103/PhysRev.71.622`. 5

[23] Michael S. Fuhrer, Chun Ning Lau, and Allan H. MacDonald. **Graphene: Materially Better Carbon**. *MRS Bull.*, **35**:289–295, 2010, `DOI:10.1557/mrs2010.551`. 5

[24] S. V. Morozov, K. S. Novoselov, M. I. Katsnelson, F. Schedin, D. C. Elias, J. A. Jaszczak, and A. K Geim. **Giant Intrinsic Carrier Mobilities in Graphene and Its Bilayer**. *Phys. Rev. Lett.*, **100**:016602, 2008, `DOI:10.1103/PhysRevLett.100.016602`. 5

[25] Jian-Hao Chen, Chaun Jang, Shudong Xiao, Masa Ishigami, and Michael Fuhrer. **Intrinsic and extrinsic performance limits of graphene devices on SiO_2**. *Nat. Nanotechnol.*, **3**:206–209, 2008, `DOI:10.1038/nnano.2008.58`. 5

[26] Pinshane Y. Huang, Carlos S. Ruiz-Vargas, Arend M. van der Zande, William S. Whitney, Mark P. Levendorf, Joshua W. Kevek, Shivank Garg, Jonathan S. Alden, Caleb J. Hustedt, Ye Zhu, Jiwoong Park, Paul L. McEuen, and David A. Muller. **Grains and grain boundaries in single-layer graphene atomic patchwork quilts**. *Nature*, **469**:389–392, 2011, `DOI:10.1038/nature09718`. 5

[27] Stuart T. Jackson and Ralph G. Nuzzo. **Determining hybridization differences for amorphous carbon from the XPS C1s envelope**. *Appl. Surf. Sci.*, **90**:195–203, 1995, `DOI:10.1016/0169-4332(95)00079-8`. 5

[28] Javier Diaz, Guido Paolicelli, Salvador Ferrer, and Fabio Comin. **Separation of the sp^3 and sp^2 components in the C1s photoemission spectra of amorphous carbon films**. *Phys. Rev. B*, **54**:8064–8069, 1996, `DOI:10.1103/PhysRevB.54.8064`. 5

[29] Steven J. Schmieg and David N. Belton. **Highly Oriented Pyrolytic Graphite by XPS**. *Surf. Sci. Spectra*, **1**:333, 1992, `DOI:10.1116/1.1247662`. 5

[30] Cecilia Mattevi, Goki Eda, Stefano Agnoli, Steve Miller, K. Andre Mkhoyan, Ozgur Celik, Daniel Mastrogiovanni, Gaetano Granozzi, Eric Garfunkel, and Manish Chhowalla. **Evolution of Electrical, Chemical and Structural Properties of Transparent and Conducting Chemically Derived Graphene Thin Films**. *Adv. Funct. Mater.*, **19**:2577–83, 2009, `DOI:10.1002/adfm.200900166`. 5, 17, 24

[31] Charles Martin, E.T. Arakawa, T.A. Callcott, and J.C. Ashley. **Low energy electron attenuation length studies in thin amorphous carbon films**. *J. Electron Spectrosc. Relat. Phenom.*, **35**:307–317, 1985, `DOI:10.1016/0368-2048(85)80064-5`. 5

[32] Charles Martin, E.T. Arakawa, T.A. Callcott, and R.J. Warmack. **Attenuation**

lengths of low-energy electrons in free-standing carbon films. *J. Electron Spectrosc. Relat. Phenom.*, **42**:171–175, 1987, `DOI:10.1016/0368-2048(87)85017-X`. 5

[33] ISO 18115: 2001. **Surface Chemical Analysis - Vocabulary**. *International Organization for Standardization, Geneva*, 2001. 5

[34] A. Jablonski and J. Zemek. **Overlayer thickness determination by XPS using the multiline approach**. *Surf. Interface Anal.*, **41**:193–204, 2009, `DOI:10.1002/sia.3005`. 6

[35] M.P. Seah and S.J. Spencer. **Ultrathin SiO_2 on Si: I Quantifying and removing carbonaceous contamination**. *J. Vac. Sci. Technol. A*, **21**:345–352, 2003, `DOI:10.1116/1.1535173`. 6

[36] M.P. Seah and S.J. Spencer. **Ultrathin SiO_2 on Si: II Issues in quantification of the oxide thickness**. *Surf. Interface Anal.*, **33**:640–652, 2002, `DOI:10.1002/sia.1433`.

[37] M.P. Seah and R. White. **Ultrathin SiO_2 on Si: III mapping the layer thickness efficiently by XPS**. *Surf. Interface Anal.*, **33**:960–963, 2002, `DOI:10.1002/sia.1478`.

[38] M.P. Seah and S.J. Spencer. **Ultrathin SiO_2 on Si: IV Intensity measurements in XPS and deduced thickness linearity**. *Surf. Interface Anal.*, **33**:515–524, 2003, `DOI:10.1002/sia.1565`.

[39] M.P. Seah, S.J. Spencer, F. Bensebaa, I. Vickridge, H. Danzebrink, M. Krumney, T. Gross, W. Osterle, E. Wendler, B. Rheinländer, Y. Azuma, I. Kojima, N. Suzuki, Suzuki M., S. Tanuma, D.W. Moon, H.J. Lee, Hyun Mo Cho, H.Y. Chen, A.T.S. Wee, T. Osipowicz, J.S. Pan, W.A. JOrdaan, R. Hauert, U. Klotz, C. van der Marel, M. Verheijen, Y. Tamminga, C. Jeynes, P. Bailey, S. Biswas, U. Falke, N.V. Nguyen, D. Chandler-Horowitz, J.R. Ehrstein, D. Muller, and J.A. Dura. **Critical review of the current status of thickness measurements for ultrathin SiO_2 on Si Part V: Results of a CCQM pilot study**. *Surf. Interface Anal.*, **36**:1269–1303, 2004, `DOI:10.1002/sia.1909`.

[40] M.P. Seah. **Ultrathin SiO_2 on Si: VI Evaluation of uncertainties in thickness measurement using XPS**. *Surf. Interface Anal.*, **37**:300–309, 2005, `DOI:10.1002/sia.2020`.

[41] M.P. Seah and S.J. Spencer. **Ultrathin SiO_2 on Si: VII Angular accuracy in XPS and an accurate attenuation length**. *Surf. Interface Anal.*, **37**:731–736, 2005, `DOI:10.1002/sia.2070`. 6

[42] P.J. Cumpson and M.P. Seah. **Elastic scattering corrections in AES and XPS. II. Estimating attenuation lengths and conditions required for their valid use in overlayer/substrate experiments**. *Surf. Interface Anal.*, **25**:430–446, 1997, `DOI:10.1002/(SICI)1096-9918(199706)25:6<430::AID-SIA254>3.0.CO;2-7`. 6

[43] Stephanie Reich and Christian Thomsen. **Raman spectroscopy of graphite**. *Philos. Trans. Royal Soc. Lond. A*, **362**:2271–2288, 2004, `DOI:10.1098/rsta.2004.1454`. 7

[44] D. L. Mafra, J. Kong, K. Sato, R. Saito, M. S. Dresselhaus, and P. T. Araujo. **Using the G' Rama Cross-Section to Understand the Phonon Dynamics in Bilayer Graphene Systems**. *Nano Lett.*, **12**:2883–2887, 2012, `DOI:10.1021/nl300477n`.

[45] A. Das, S. Pisana, B. Chakraborty, S. Pisanec, S.K. Saha, U.V. Waghmare, K.S. Novoselov, H.R. Krishnamurthy, A.K. Geim, A.C. Ferrari, and A.K. Sood. **Monitoring dopants by Raman scattering in an electrochemically top-gated graphene transistor**. *Nat. Nanotechnol.*, **3**:210–215, 2008, `DOI:10.1038/nnano.2008.67`.

[46] Andrea C. Ferrari and Denis M. Basko. **Raman spectroscopy as a versatile tool for studying the properties of graphene**. *Nat. Nanotechnol.*, **8**:235–246, 2013, `DOI:10.1038/nnano.2013.46`. 7

[47] A.C. Ferrari, J.C. Meyer, V. Scardaci, C. Casiraghi, M. Lazzeri, F. Mauri, S. Piscanec, D. Jian, K.S. Novoselov, S. Roth,

and A.K. Geim. **Raman Spectrum of Graphene and Graphene Layers**. *Phys. Rev. Lett.*, **97**:187401, 2006, `DOI:10.1103/PhysRevLet.97.187401`. 7, 8

[48] Toshiyuki Kobayashi, Masashi Bando, Nozomi Kimura, Keisuke Simizu, Kadono Koji, Nobuhiko Umezu, Kazuhiko Miyahara, Shinji Hayazaki, Sae Nagai, Yukiko Mizuguchi, Yosuke Murakami, and Daisuke Hobara. **Production of a 100-m-long high-quality graphene transparent conductive film by roll-to-roll chemical vapor deposition and transfer process**. *Appl. Phys. Letts.*, **102**:023112, 2013, `DOI:10.1063/1.4776707`. 7

[49] Alfonso Reina, Xiaoting Jia, John Ho, Daniel Nezich, Hyungbin Son, Vladimir Bulovic, Mildred S. Dresselhaus, and Jing Kong. **Large area, few-layer graphene films on arbitrary substrates by chemical vapor deposition**. *Nano Lett.*, **9**:30–35, 2009, `DOI:10.1021/nl801827v`. 9

[50] Keun Soo Kim, Yue Zhao, Houk Jang, Sang Yoon Lee, Jong Min Kim, Kwang S. Kim, Jong-Hyun Ahn, Philip Kim, Jae-Young Choi, and Bung Hee Hong. **Large-scale pattern growth of graphene films for stretchable transparent electrodes**. *Nature*, **457**:706–710, 2009, `DOI:10.1038/nature07719`.

[51] Zongping Chen, Wencai Ren, Libo Gao, Bilu Liu, Songfeng Pei, and Hui-Ming Cheng. **Three-dimensional flexible and conductive interconnected graphene networks grown by chemical vapour deposition**. *Nat. Mater.*, **10**:424–428, 2011, `DOI:10.1038/nmat3001`. 9

[52] Yenny Hernandez, Valeria Nicolosi, Mustafa Lotya, Fiona M. Blighe, Zhenyu Sun, Sukanta De, I. T. McGovern, Brendan Holland, Michele Byrne, Yurii K. Gun'Ko, John J. Boland, Peter Niraj, Georg Duesberg, Satheesh Krishnamurthy, Robbie Goodhue, John Hutchison, Vittorio Scardaci, Andrea C. Ferrari, and Jonathan N. Coleman. **High-yield production of graphene by liquid-phase exfoliation of graphite**. *Nat. Nanotechnol.*, **3**:563–568, 2008, `DOI:10.1038/nnano.2008.215`. 9

[53] Umar Khan, Mustafa O'Neill, Arlene Lotya, Sukanta De, and Jonathan N. Coleman. **High-concentration solvent exfoliation of graphene**. *Small*, **6**:864–871, 2010, `DOI:10.1002/sml.200902066`.

[54] Umar Khan, Harshit Porwal, Arlene O'Neill, Khalid Nawaz, Peter May, and Jonathan N. Coleman. **Solvent-exfoliated graphene at extremely high concentration**. *Langmuir*, **27**:9077–9082, 2011, `DOI:10.1021/la201797h`. 9

[55] L. Guardia, M.J. Fernández-Merino, J.I. Paredes, P. Solís-Fernández, S. Villar-Rodil, A. Martínez-Alonso, and J.M.D. Tascón. **High-throughput production of pristine graphene in an aqueous dispersion assisted by non-ionic surfactants**. *Carbon*, **49**:1653 – 1662, 2011, `DOI:10.1016/j.carbon.2010.12.049`. 9

[56] Mustafa Lotya, Paul J. King, Umar Khan, Sukanta De, and Jonathan N. Coleman. **High-concentration surfactant stabilized graphene dispersions**. *ACS Nano*, **4**:3155–3162, 2010, `DOI:10.1021/nn1005304`. 9

[57] Liying Jiao, Xinran Wang, Georgi Diankov, Hailiang Wang, and Hongjie Dai. **Facile synthesis of high-quality graphene nanoribbons**. *Nat. Nanotechnol.*, **5**:321–325, 2010, `DOI:10.1038/nnano.2010.54`. 11

[58] Verónica Barone, Oded Hod, and Gustavo E. Scuseria. **Electronic Structure and Stability of Semiconducting Graphene Nanoribbons**. *Nano Lett.*, **6**:2748–2754, 2006, `DOI:10.1021/nl0617033`.

[59] Melinda Y. Han, Barbaros Özyilmaz, Yuanbo Zhang, and Philip Kim. **Energy Band-Gap Engineering of Graphene Nanoribbons**. *Phys. Rev. Lett.*, **98**:206805, 2007, `DOI:10.1103/PhysRevLett.98.206805`. 11

[60] D. C. Elias, R. R. Nair, T. M. G. Mohiuddin, S. V. Morozov, P. Blake, M. P. Halsall, A. C. Ferrari, D. W. Boukhvalov, M. I. Katsnelson, A. K. Geim, and K. S. Novoselov. **Control of Graphene's Properties by Reversible Hydrogenation: Evidence for Graphane**. *Science*, **323**:610–613, 2009, `DOI:10.1126/science.1167130`. 11

[61] L. Firlej, B. Kuchta, C. Wexler, and P. Pfeifer. **Boron substituted graphene: energy landscape for hydrogen adsorption**. *Adsorption*, **15**:312–317, 2009, `DOI:10.1007/s10450-009-9182-9`. 11

[62] Ruitao Lü, Qing Li, Andrs R. Botello-Mndez, Takuya Hayashi, Bei Wang, Ayse Berkdemir, Qingzhen Hao, Ana Laura Elas, Rodolfo Cruz-Silva, Humberto R. Gutirrez, Yoong Ahm Kim, Hiroyuki Muramatsu, Jun Zhu, Morinobu Endo, Humberto Terrones, Jean-Christophe Charlier, Minghu Pan, and Mauricio Terrones. **Nitrogen-doped graphene: beyond single substitution and enhanced molecular sensing**. *Sci. Rep.*, **2**:586, 2012, `DOI:10.1038/srep00586`.

[63] Frédéric Joucken, Yann Tison, Jérôme Lagoute, Jacques Dumont, Damien Cabosart, Bing Zheng, Vincent Repain, Cyril Chacon, Yann Girard, Andrés Rafael Botello-Méndez, Sylvie Rousset, Robert Sporken, Jean-Christophe Charlier, and Luc Henrard. **Localized state and charge transfer in nitrogen-doped graphene**. *Phys. Rev. B*, **85**:161408, 2012, `DOI:10.1103/PhysRevB.85.161408`.

[64] Petr Lazar, Radek Zboril, Martin Pumera, and Michal Otyepka. **Chemical nature of boron and nitrogen dopant atoms in graphene strongly influences its electronic properties**. *Phys. Chem. Chem. Phys.*, **16**:14231–14235, 2014, `DOI:10.1039/C4CP01638F`. 11

[65] Dacheng Wei, Yunqi Liu, Yu Wang, Hongliang Zhang, Liping Huang, and Gui Yu. **Synthesis of N-Doped Graphene by Chemical Vapor Deposition and its Electrical Properties**. *Nano Lett.*, **9**:1752–1758, 2009, `DOI:10.1021/nl803279t`. 12

[66] B. Obradovic, R. Kotlyar, F. Heinz, P. Matagne, T. Rakshit, M.D. Giles, A. Stettler, and D.E. Nikonov. **Analysis of graphene nanoribbons as a channel material for field-effect transistor**. *Appl. Phys. Letts.*, **88**:142102, 2006, `DOI:10.1063/1.2191420`. 12

[67] Zhihong Chen, Yu-Ming Lin, Michael J. Rooks, and Phaedon Avouris. **Graphene nano-ribbon electronics**. *Phys. E*, **40**:228–232, 2007, `DOI:10.1016/j.physe.2007.06.020`. 12

[68] Xiaolin Li, Xinran Wang, Li Zhang, Sangwon Lee, and Hongjie Dai. **Chemically Derived, Ultrasmooth Graphene Nanoribbon Semiconductors**. *Science*, **319**:1229–1232, 2008, `DOI:10.1126/science.1150878`. 12

[69] K. Nakada, M. Fujita, G. Dresselhaus, and M. S. Dresselhaus. **Edge state in graphene ribbons: nanometer size effect and edge shape dependence**. *Phys. Rev. B*, **54**:017954, 1996, `DOI:10.1103/PhysRevB.54.17954`. 12

[70] Young-Woo Son, Marvin L. Cohen, and Steven G. Louie. **Energy gaps in graphene nanoribbons**. *Phys. Rev. Lett.*, **97**:216803, 2006, `DOI:10.1103/PhysRevLett.97.216803`. 12

[71] Melinda Y. Han, Barbaros Özylimaz, Yuangbo Zhang, and Phillip Kim. **Energy Band-Gap Engineering of Graphene Nanoribbons**. *Phys. Rev. Lett.*, **2007**:206805, 98, `DOI:10.1103/PhysRevLett.98.206805`. 12

[72] Yen-Chia Chen Chen, Ting Cao, Chen Chen, Zahra Pedramrazi, Danny Haberer, Dimas G. de Oteyza, Felix R. Fischer, Steven G. Louie, and Michael F. Crommie. **Molecular bandgap engineering of bottom-up synthesized graphene nanoribbon heterojunctions**. *Nat. Nanotechnol.*, **10**:TBA, 2015, `DOI:10.1038/nnano.2014.307`. 12

[73] Frank Schwierz. **Graphene transistors**. *Nat. Nanotechnol.*, **5**:487–496, 2010, `DOI:10.1038/nnano.2010.89`. 12

[74] Frantiřek Karlický, Kasibhatta Kumara, Ramanatha Datta, Michal Otyepka, and Radek Zbořil. **Halogenated Graphenes: Rapidly Growing Family of Graphene Derivatives**. *ACS Nano*, **7**:6434–6464, 2013, `DOI:10.1021/nn4024027`. 13

[75] F. Karlicky, R. Zboril, and M. Otyepka. **Band Gaps and Structural Properties of Graphene Halides and Their Derivates: A Hybrid Functional Study with Localized Orbital Basis Sets**. *J. Chem. Phys.*, **137**:034709, 2012, `DOI:10.1063/1.4736998`. 13

[76] Rahul R. Nair, Wencai Ren, Rashid Jalil, Ibtsam Riaz, Vasyl G. Kravets, Liam Britnell, Peter Blake, Fredrik Schedin, Alexander S. Mayorov, Shengjun Yuan, Mikhail I. Katsnelson, Hui-Ming Cheng, Wlodek Strupinski, Lyubov G. Bulusheva, Alexander V. Okotrub, Alexander N. Grigorenko, Kostya S. Novosolev, and Andre K. Geim. **Fluorographene: A two-dimensional counterpart of teflon**. *Small*, **6**:2877–2884, 2010, `DOI:10.1002/smll.201001555`. 13

[77] R. Zboril, F. Karlicky, A. B. Bourlinos, T. A. Steriotis, A. K. Stubos, V. Georgakilas, K. Safarova, D. Jancik, C. Trapalis, and M. Otyepka. **Graphene Fluoride: A Stable Stoichiometric Graphene Derivative and Its Chemical Conversion to Graphene**. *Small*, **6**:2885–2891, 2010, `DOI:10.1002/smll.201001401`.

[78] J. T. Robinson, J. S. Burgess, C. E. Junkermeier, S. C. Badescu, T. L. Reinecke, F. K. Perkins, M. K. Zalalutdniov, J. W. Baldwin, J. C. Culbertson, and P. E. and Sheehan. **Properties of Fluorinated Graphene Films**. *Nano Lett.*, **10**:3001–3005, 2010, `DOI:10.1021/nl101437p`.

[79] B. Li, L. Zhou, D. Wu, H. L. Peng, K. Yan, Y. Zhou, and Z. F. Liu. **Photochemical Chlorination of Graphene**. *ACS Nano*, **5**:5957–5961, 2011, `DOI:10.1021/nn201731t`.

[80] J. Zheng, Liu Hong-Tao, Wu Bin, Di Chong-An, Guo Yun-Long, Wu Ti, Yu Gui, Y.-Q. Liu, and D.-B Zhu. **Production of Graphite Chloride and Bromide Using Microwave Sparks**. *Sci. Rep.*, **2**:662, 2012, `DOI:10.1038/srep00662`.

[81] K. Gopalakrishnan, K. S. Subrahmanyam, P. Kumar, A. Govindaraj, and C. N. R. Rao. **Reversible Chemical Storage of Halogens in Few-Layer Graphene**. *RSC Adv.*, **2**:1605–1608, 2012, `DOI:10.1039/C1RA00403D`. 13

[82] L. Staudenmaier. **Verfahren zur Darstellung der Graphits'aure**. *Ber. Dtsch. Chem. Ges.*, **31**:1481–1487, 1898, `DOI:10.1002/cber.18990320208`. 13, 15, 22

[83] BC Brodie. **Sur le poids atomique du graphite**. *Ann. Chim. Phys.*, **59**:466–472, 1860. 13

[84] W. S. Hummers and R. E. Offeman. **Preparation of Graphitic Oxide**. *J. Am. Chem. Soc.*, **80**:1339–1339, 1958, `DOI:10.1021/ja01539a017`. 13, 15, 22

[85] T. Chen, Baoqing Zeng, J L Liu, J H Dong, X Q Liu, Z Wu, X Z Yang, and Z M Li. **High throughput exfoliation of graphene oxide from expanded graphite with assistance of strong oxidant in modified Hummers method**. *J Phys.: Conf. Ser.*, **188**:012051, 2009, `DOI:10.1088/1742-6596/188/1/012051`. 13, 15

[86] Lixin Xu, John-Wesley McGraw, Fan Gao, Mark Grundy, Zhibin Ye, Zhiyong Gu, and Jeffrey L. Shepherd. **Production of high-concentration graphene dispersions in low-boiling point organic solvents by liquid-phase noncovalent exfoliation of graphite with a hyperbranched polyethylene and formation of graphene/ethylene copolymer composites**. *J. Phys. Chem. C*, **117**:10730–10742, 2013, `DOI:10.1021/jp4008009`. 14

[87] Min Yi, Zhigang Shen, Xiaojing Zhang, and Shulin Ma. **Achieving concentrated graphene dispersions in water/acetone mixtures by the strategy of tailoring Hansen solubility parameters**. *J. Phys. D: Appl. Phys.*, **46**:025301, 2013, `DOI:10.1088/0022-3727/46/2/025301`. 14

[88] Shiren Wang, Yue Zhang, Noueddine Abidi, and Luis Cabrales. **Wettability and surface free energy of graphene films**. *Langmuir*, **25**(18):11078–11081, 2009, DOI:10.1021/la901402f. 14

[89] Che-Ning Yeh, Kalyan Raidongia, Jiaojing Shao, Quan-Hong Yang, and Jiaxing Huang. **On the origin of the stability of graphene oxide membranes in water**. *Nat. Chem.*, **7**:166–170, 2015, DOI:10.1038/nchem.2145. 14, 20, 26

[90] Laura J. Cote, Jaemyung Kim, Zhen Zhang, Cheng Sun, and Jiaxing Huang. **Tunable assembly of graphene oxide surfactant sheets: wrinkles, overlaps and impacts on thin film properties**. *Soft Matter*, **6**:6096–6101, 2010, DOI:10.1039/C0SM00667J. 14

[91] Shujie You, Serhiy M. Luzan, Tamas Szabo, and Alexandr V. Talyzin. **Effect of synthesis method on solvation and exfoliation of graphite oxide**. *Carbon*, **52**:171–180, 2013, DOI:10.1016/j.carbon.2012.09.018. 15, 22, 24

[92] Ayrat M. Dimiev and James M. Tour. **Mechanism of Graphene Oxide Formation**. *ACS Nano*, **8**:3060–3068, 2014, DOI:10.1021/nn500606a. 15

[93] M. Tour, James and Ayrat M. Dimiev. **Mechanism of graphene oxide formation**. *ACS Nano*, **8**:3060–3068, 2014, DOI:10.1021/nn500606a. 15

[94] Jonathan P. Rourke, Priyanka A. Pandey, Joseph J. Moore, Matthew Bates, Ian A. Kinloch, Robert J. Young, and Neil R. Wilson. **The Real Graphene Oxide Revealed: Stripping the Oxidative Debris from the Graphene-like Sheets**. *Angew. Chem. Int. Ed.*, **50**:3173–3177, 2011, DOI:10.1002/anie.201007520. 15, 20, 22, 23, 35

[95] Helen R. Thomas, Stephen P. Day, William E. Woodruff, Cristina Vallés, Robert J. Young, Ian A. Kinloch, Gavin W. Morley, John V. Hanna, Neil R. Wilson, and Jonathan P. Rourke. **Deoxygenation of Graphene Oxide: Reduction or Cleaning?** *Chem. Mater.*, **25**:3580–3588, 2013, DOI:10.1021/cm401922e. 15, 20, 26

[96] Alessandra Bonanni, Adriano Ambrosi, Chun Kiang Chua, and Martin Pumera. **Oxidation Debris in Graphene Oxide Is Responsible for Its Inherent Electroactivity**. *ACS Nano*, **8**:4197–4204, 2014, DOI:10.1021/nn404255q. 15, 22, 24

[97] K.P. Lee, N.C. Chromey, R. Culik, J.R. Barnes, and P.W. Schneider. **Toxicity of N-methyl-2-pyrrolidone (NMP): Teratogenic, subchronic and two-year inhalation studies**. *Fundam. Appl. Toxicol.*, **9**:222–235, 1987, DOI:10.1016/0272-0590(87)90045-5. 15

[98] Torka S. Poet, Chris R. Kirman, Michael Bader, Michael L. van Thriel, Christoph nad Gargas, and Paul M. Hinderliter. **Quantitative risk analysis for N-methyl pyrrolidone using physiologically based pharmacokinetic and benchmark dose modelling**. *Toxicol. Sci.*, **113**:468–482, 2010, DOI:10.1093/toxsci/kfp264. 15

[99] Toshiyuki Kobayashi, Nozomi Kimura, Junbin Chi, Shintaro Hirata, and Daisuke Hobara. **Channel-Length-Dependent Field-Effect Mobility and Carrier Concentration of Reduced Graphene Oxide Thin-Film Transistors**. *Small*, **6**:1210–1215, 2010, DOI:10.1002/smll.200902407. 16

[100] A. W. Tsen, L. Brown, M. P. Levendorf, F. Ghahari, P. Y. Huang, R. W. Havener, C. S. Ruiz-Vargas, D. A. Muller, P. Kim, and J. Park. **Tailoring electrical transport across grain boundaries in polycrystalline graphene**. *Science*, **336**(6085):1143–1146, 2012, DOI:10.1126/science.1218948. 16

[101] Boya Dai, Lei Fu, Lei Liao, Nan Liu, Kai Yan, Yongsheng Chen, and Zhongfan Liu. **High-Quality Single-Layer Graphene via Reparative Reduction of Graphene Oxide**. *Nano Res.*, **4**:434–439, 2011, DOI:10.1007/s12274-011-0099-8. 16

[102] Y. Shen, P. Zhou, Q.Q. Sun, J. Li, L.Y. Chen, D.W. Zhang, and X.B. Wang. **Optical investigation of reduced graphene oxide by spectroscopic ellipsometry and the band-gap tuning**. *Appl. Phys. Letts.*, **99**:141911, 2011, `DOI:10.1063/1.3646908`. 16

[103] Haiming Huang, Zhibing Li, Juncong She, and Weiliang Wang. **Oxygen density dependent band gap of reduced graphene oxide**. *J. Appl. Phys.*, **111**:054317, 2012, `DOI:10.1063/1.3694665`.

[104] Akshay Mathkar, Dylan Tozier, Paris Cox, Peijie Ong, Charudatta Galande, Kaushik Balakrishnan, Arava Leela Mohana Reddy, and Pulickel M. Ajayan. **Controlled, Stepwise Reduction and Band Gap Manipulation of Graphene Oxide**. *J. Phys. Chem. Lett.*, **3**(8):986–991, 2012, `DOI:10.1021/jz300096t`. 16, 17, 18

[105] Sukanta De and Jonathan N. Coleman. **Are there fundamental limitations on the sheet resistance and transmittance of thin graphene films?** *ACS Nano*, **4**:2713–2720, 2010, `DOI:10.1021/nn100343f`. 16, 28

[106] Xuan Wang, Linjie Zhi, and Klaus Mllen. **Transparent, Conductive Graphene Electrodes for Dye-Sensitized Solar Cells**. *Nano Lett.*, **8**:323–327, 2008, `DOI:10.1021/nl072838r`. 17

[107] Boya Dai, Lei Fu, Lei Liao, Nan Liu, Kai Yan, Yongsheng Chen, and Zhongfan Liu. **High-quality single-layer graphene via reparative reduction of graphene oxide**. *Nano Res.*, **4**:434–439, 2011, `DOI:10.1007/s12274-011-0099-8`. 17

[108] Héctor A. Becerril, Jie Mao, Zunfeng Liu, Randall M. Stoltenberg, Zhenan Bao, and Yongsheng Chen. **Evaluation of Solution-Processed Reduced Graphene Oxide Films as Transparent Conductors**. *ACS Nano*, **2**:463–470, 2008, `DOI:10.1021/nn700375n`. 17

[109] Ching-Yuan Su, Yanping Xu, Wenjing Zhang, Jianwen Zhao, Aiping Liu, Xiaohong Tang, Chuen-Horng Tsai, Yizhong Huang, and Lain-Jong Li. **Highly Efficient Restoration of Graphitic Structure in Graphene Oxide Using Alcohol Vapors**. *ACS Nano*, **4**:5285–5292, 2010, `DOI:10.1021/nn101691m`. 17

[110] Dongxing Yang, Aruna Velamakanni, Ulay Bozoklu, Sungjin Park, Meryl Stoller, Richard D. Piner, Sasha Stankovich, Inhwa Jung, Daniel A. Field, Carl A. Ventrice Jr., and Rodney S. Ruoff. **Chemical analysis of graphene oxide films after heat and chemical treatments by x-ray photoelectron and micro-raman spectroscopy**. *Carbon*, **47**:145–152, 2009, `DOI:10.1016/j.carbon.2008.09.045`. 17

[111] Hongbin Feng, Rui Cheng, Xin Zhao, Xiangfeng Duan, and Jinghong Li. **A low-temperature method to produce highly reduced graphene oxide**. *Nat. Commun.*, **4**:1539, 2013, `DOI:10.1038/ncomms2555`.

[112] Xiaoguang Mei and Jianyong Ouyang. **Ultrasonication-assisted ultrafast reduction of graphene oxide by zinc powder at room temperature**. *Carbon*, **49**:5389 – 5397, 2011, `DOI:10.1016/j.carbon.2011.08.019`. 19

[113] Chun Kiang Chua and Martin Pumera. **Regeneration of a Conjugated sp^2 Graphene System through Selective Defunctionalization of Epoxides by Using a Proven Synthetic Chemistry Mechanism**. *Chem. - Eur. J.*, **20**:1871–1877, 2014, `DOI:10.1002/chem.201304131`. 18, 19

[114] Jian Gao, Fang Liu, Yiliu Liu, Ning Ma, Zhiqiang Wang, and Xi Zhang. **Environment-Friendly Method To Produce Graphene That Employs Vitamin C and Amino Acid**. *Chem. Mater.*, **22**:2213–2218, 2010, `DOI:10.1021/cm902635j`. 19

[115] Jiali Zhang, Haijun Yang, Guangxia Shen, Ping Cheng, Jingyan Zhang, and Shouwu Guo. **Reduction of graphene oxide vial-ascorbic acid**. *Chem. Commun.*, **46**:1112–1114, 2010, `DOI:10.1039/B917705A`. 17, 19

[116] M. J. Fernández-Merino, L. Guardia, J. I. Paredes, S. Villar-Rodil, P. Soliís-Fernández, A. Martínez-Alonso, and

J. M. D. Tascón. **Vitamin C Is an Ideal Substitute for Hydrazine in the Reduction of Graphene Oxide Suspensions**. *J. Phys. Chem. C*, **114**:6426–6432, 2010, DOI:10.1021/jp100603h. 20

[117] Abulikemu Abulizi, Kenji Okitsu, and Jun-Jie Zhu. **Ultrasound assisted reduction of graphene oxide to graphene in l-ascorbic acid aqueous solutions: Kinetics and effects of various factors on the rate of graphene formation**. *Ultrason. Sonochemistry*, **21**:1174–1181, 2014, DOI:10.1016/j.ultsonch.2013.10.019. 20

[118] Zhuyin Sui, Xuetong Zhang, Yu Lei, and Yunjun Luo. **Easy and green synthesis of reduced graphite oxide-based hydrogels**. *Carbon*, **49**:4314–4321, 2011, DOI:10.1016/j.carbon.2011.06.006. 20

[119] Jun Chen, Roderick L. Shepherd, Joselito M. Razal, Xiao Huang, Weimin Zhang, Jie Zhao, Andrew T. Harris, Shu Wang, Andrew I. Minett, and Hua Zhang. **Scalable Solid-Template Reduction for Designed Reduced Graphene Oxide Architectures**. *ACS Appl. Mater. Interfaces*, **5**:7676–7681, 2013, DOI:10.1021/am402084y.

[120] Hui Xiong and Baokang Jin. **The electrochemical behavior of AA and DA on graphene oxide modified electrodes containing various content of oxygen functional groups**. *J. Electroanal. Chem.*, **661**:77–83, 2011, DOI:10.1016/j.jelechem.2011.06.034. 20

[121] Ayrat M. Dimiev, Lawrence B. Alemany, and James. M. Tour. **Graphene oxide. Origin of acidity, its instability in water and a new dynamic structural model**. *ACS Nano*, **7**:576–588, 2013, DOI:10.1021/nn3047378. 20, 25, 26, 35

[122] Priyank V. Kumar, Neelkanth M. Bardhan, Sefaattin Tongay, Jinqiao Wu, Angela M. Belcher, and Jeffrey C. Grossman. **Scalable enhancement of graphene oxide properties by thermally driven phase transformation**. *Nat. Chem.*, **6**:151–158, 2014, DOI:10.1038/nchem.1820. 25

[123] S. Kim, S. Zhou, Y. Hu, M. Acik, Y. J. Chabal, C. Berger, W. de Heer, A. Bongiorno, and E. Riedo. **Room-temperature metastability of multilayer graphene oxide films**. *Nat. Mater.*, **11**(6):544–549, 2012, DOI:10.1038/nmat3316. 24, 26

[124] Chun Kiang Chua and Martin Pumera. **Light and Atmosphere Affect the Quasi-equilibrium States of Graphite Oxide and Graphene Oxide Powders**. *Small*, **11**:1266–1272, 2015, DOI:10.1002/smll.201400154. 20, 25, 26

[125] D. R. Dreyer, S. Park, C. W. Bielawski, and R. S. Ruoff. **The chemistry of graphene oxide**. *Chem. Soc. Rev.*, **39**(1):228–240, 2010, DOI:10.1039/b917103g. 20

[126] Heyong He, Jacek Klinowski, Michael Forster, and Anton Lerf. **A new structural model for graphite oxide**. *Chem. Phys. Lett.*, **287**:53–56, 1998, DOI:10.1016/S0009-2614(98)00144-4. 21

[127] Anton Lerf, Heyong He, Michael Forster, and Jacek Klinowski. **Structure of Graphite Oxide Revisited**. *J. Phys. Chem. B*, **102**:4477–4482, 1998, DOI:10.1021/jp9731821. 21

[128] Wei Gao, Lawrence B. Alemany, Lijie Ci, and Pulickel M. Ajayan. **New insights into the structure and reduction of graphite oxide**. *Nat. Chem.*, **1**:403–408, 2009, DOI:10.1038/nchem.281. 21

[129] Tamas Szabo, Otto Berkesi, Peter Forgo, Katalin Josepovits, Yiannis Sanakis, Dimitris Petridis, and Imre Dekany. **Evolution of Surface Functional Groups in a Series of Progressively Oxidized Graphite Oxides**. *Chem. Mater.*, **18**:2740–2749, 2006, DOI:10.1021/cm060258+. 21

[130] RJ Beckett and RC Croft. **The Structure of Graphite Oxide**. *J. Phys. Chem.*, **56**:929–941, 1952, DOI:10.1021/j150500a001. 22

[131] Xiaobin Fan, Wenchao Peng, Yang Li, Xianyu Li, Shulan Wang, Guoliang

ZHANG, AND FENGBAO ZHANG. **Deoxygenation of Exfoliated Graphite Oxide under Alkaline Conditions: A Green Route to Graphene Preparation**. *Adv. Mater.*, **20**:4490–4493, 2008, `DOI:10.1002/adma.200801306`. 22

[132] O. AKHAVAN. **The effect of heat treatment on formation of graphene thin films from graphene oxide nanosheets**. *Carbon*, **48**(2):509–519, 2010, `DOI:10.1016/j.carbon.2009.09.069`. 24

[133] D. S. SUTAR, GULBAGH SINGH, AND V. DIVAKAR BOTCHA. **Electronic structure of graphene oxide and reduced graphene oxide monolayers**. *Appl. Phys. Letts.*, **101**:103103, 2012, `DOI:10.1063/1.4749841`. 24

[134] THOMAS N. BLANTON AND DEBASIS MAJUMDAR. **Characterization of X-ray irradiated graphene oxide coatings using X-ray diffraction, X-ray photoelectron spectroscopy, and atomic force microscopy**. *Powder Diffr.*, **28**:68–71, 2013, `DOI:10.1017/S0885715613000109`. 24

[135] J. H SCOFIELD. **HARTREE-SLATER SUBSHELL PHOTOIONIZATION CROSS-SECTION AT 1254 AND 1487 eV**. *J. Electron Spectrosc. Relat. Phenom.*, **8**:129–137, 1976, `DOI:10.1016/0368-2048(76)80015-1`. 24

[136] T. SUSI, M. KAUKONEN, P. HAVU, M. P. LJUNGBERG, P. AYALA, AND E. I. KAUPPINEN. **Core level binding energies of functionalized and defective graphene**. *Beilstein J. Nanotechnol.*, **5**:121–132, 2014, `DOI:10.3762/bjnano.5.12`. 24, 35

[137] KHASHA GHAFFARZADEH AND CATHLEEN THIELE. **Graphene Markets, Technologies and Opportunities 2013-2018**. Technical report, IDTechEx, Downing Park, Station Road, Swaffham Bulbeck, Cambridge CB25 0NW, United Kingdom, 2012. 27

[138] GARTNER INC. **Gartner Hype Cycle**. `http://www.gartner.com/technology/research/methodologies/hype-cycle.jsp` [Last checked Oct 2014]. 27

[139] JUNBO WU, MUKUL AGRAWAL, HECTOR A. BECERRIL, ZHENAN BAO, ZUNFENG LIU, YONGSHENG CHEN, AND PETER PEUMANS. **Organic Light-emitting diodes on solution-processed graphene transparent electrodes**. *ACS Nano*, **4**:43–48, 2010, `DOI:10.1021/nn900728d`. 27

[140] M. DRESSEL AND G. GRUNER. **Electrodynamics of Solids: Optical Properties of Electrons in Matter**. Cambridge University Press, Cambridge, U.K., 2002. 28

[141] YU WANG, SHI WUN TONG, XIANG FAN XU, ÖZYLIMAZ, AND KIAN PING LOH. **Interface engineering of layer-by-layer stacked graphene anodes for high-performance organic solar cells**. *Adv. Mater.*, **23**:1514–1518, 2011, `DOI:10.1002/adma.201003673`. 28

[142] LOH KIAN PING. **Personal communications**. Unpublished, 2013. Discussion on the gold chloride doped multilayered graphene. 28

[143] L.M. MALARD, M.A. PIMENTA, G. DRESSELHAUS, AND M.S. DRESSELHAUS. **Raman spectroscopy in graphene**. *Phys. Rep.*, **473**:51–87, 2009, `DOI:10.1016/physrep.2009.02.003`. 28

[144] IVAN KHRAPACH, FREDDIE WITHERS, THOMAS H. BOINTON, DMITRY K. POLYUSHKIN, WILLIAM L. BARNES, SAVERIO RUSSO, AND MONICA F. CRACIUN. **Novel Highly Conductive and Transparent Graphene-Based Conductors**. *Adv. Mater.*, **24**:28442849, 2012, `DOI:10.1002/adma.201200489`. 29

[145] GUANG-XIN NI, YI ZHENG, SUKANG BAE, CHIN YAW TAN, ORHAN KAHYA, JING WU, BYUNG HEE HONG, KUI YAO, AND BARBAROS ÖZYILMAZ. **GrapheneFerroelectric Hybrid Structure for Flexible Transparent Electrodes**. *ACS Nano*, **6**:3935–3942, 2012, `DOI:10.1021/nn3010137`. 29

[146] WENZHONG BAO, JIAYU WAN, XIAOGANG HAN, XINGHAN CAI, HONGLI ZHU, DOHUN KIM, DAKANG MA, YUNLU XU, JEREMY N. MUNDAY, H. DENNIS DREW, MICHAEL S. FUHRER, AND LIANGBING HU. **Approaching the limits of transparency and conductivity in**

graphitic materials through lithium intercalation. *Nat. Commun.*, **5**:4224, 2014, `DOI:10.1038/ncomms5224`. 30

[147] Yumi Ahn, Youngjun Jeong, and Youngu Lee. **Improved Thermal Oxidation Stability of Solution-Processable Silver Nanowire Transparent Electrode by Reduced Graphene Oxide**. *ACS Appl. Mater. Interfaces*, **4**:6410–6414, 2012, `DOI:10.1021/am301913w`. 30

[148] In Kyu Moon, Jae Il Kim, Hanleem Lee, Kangheon Hur, Woon Chun Kim, and Hyoyoung Lee. **Graphene Oxide Nanosheets as an Adhesive Over-Coating Layer for Flexible Transparent Conductive Electrodes**. *Sci. Rep.*, **3**:1112, 2013, `DOI:10.1038/srep01112`. 30

[149] F. Schedin, A. K. Geim, S. V. Morozov, E. W. Hill, P. Blake, M. I. Katsnelson, and K. S. Novoselov. **Detection of individual gas molecules adsorbed on graphene**. *Nat. Mater.*, **6**:652–655, 2007, `DOI:10.1038/nmat1967`. 30

[150] Sergey Rumyantsev, Guanxiong Liu, Michael S. Shur, Radislav A. Potyrailo, and Alexander A. Balandin. **Selective Gas Sensing with a Single Pristine Graphene Transistor**. *Nano Lett.*, **12**:2294–2298, 2012, `DOI:10.1021/nl3001293`. 30

[151] Wenjing Yuan and Gaoquan Shi. **Graphene-based gas sensors**. *J. Mater. Chem. A*, **1**:10078–10091, 2013, `DOI:10.1039/c3ta11774j`. 31

[152] Madhav Gautam and Ahalapitiya H. Jayatissa. **Ammonia gas sensing behavior of graphene surface decorated with gold nanoparticles**. *Solid State Electron*, **78**:159 – 165, 2012, `DOI:10.1016/j.sse.2012.05.059`. 31

[153] Weiwei Li, Xiumei Geng, Yufen Guo, Jizan Rong, Youpin Gong, Liqiong Wu, Xuemin Zhang, Peng Li, Jianbao Xu, Guosheng Cheng, Mengtao Sun, and Liwei Liu. **Reduced Graphene Oxide Electrically Contacted Graphene Sensor for Highly Sensitive Nitric Oxide Detection**. *ACS Nano*, **5**:6955–6961, 2011, `DOI:10.1021/nn201433r`. 31

[154] Z. Tehrani, G. Burwell, M. A. Mohd Azmi, A. Castaing, R. Rickman, J. Almarashi, P. Dunstan, A. Miran Beigi, S. H. Doak, and O. J. Guy. **Generic epitaxial graphene biosensors for ultrasensitive detection of cancer risk biomarker**. *2D Mater.*, **1**:025004, 2014, `DOI:10.1088/2053-1583/1/2/025004`. 31

[155] S. Garaj, W. Hubbard, A. Reina, J. Kong, D. Branton, and J. A. Golovchenko. **Graphene as a subnanometre trans-electrode membrane**. *Nature*, **467**:190–193, 2010, `DOI:10.1038/nature09379`. 31

[156] Max C. Lemme, T.J. Echtermeyer, M. Baus, and H. Kurz. **A Graphene Field-Effect Device**. *IEEE Electron Device Lett.*, **28**:282–284, 2007, `DOI:10.1109/LED.2007.891668`. 32

[157] Yu-Ming Lin, K. Jenkins, D. Farmer, Alberto Valdes-Garcia, P. Avouris, Chun-Yung Sung, Hsin-Ying Chiu, and B. Ek. **Development of graphene FETs for high frequency electronics**. In *Electron Devices Meeting (IEDM), 2009 IEEE International*, pages 1–4, Dec 2009. 32

[158] Fengnian Xia, Damon B. Farmer, Yu-ming Lin, and Phaedon Avouris. **Graphene Field-Effect Transistors with High On/Off Current Ratio and Large Transport Band Gap at Room Temperature**. *Nano Lett.*, **10**:715–718, 2010, `DOI:10.1021/nl9039636`. 32

[159] L. Britnell, R. V. Gorbachev, R. Jalil, B. D. Belle, F. Schedin, A. Mishchenko, T. Georgiou, M. I. Katsnelson, L. Eaves, S. V. Morozov, N. M. R. Peres, J. Leist, A. K. Geim, K. S. Novoselov, and L. A. Ponomarenko. **Field-Effect Tunnelling Transistor Based on Vertical Graphene Heterostructures**. *Science*, **335**:947–950, 2012, `DOI:10.1126/science.1218461`. 32

[160] Tania Roy, Mahmut Tosun, Jeong Seuk Kang, Angada B. Sachid, Sujay B. Desai, Mark Hettick, Chenming C. Hu, and Ali Javey. **Field-Effect Transistors Built from**

All Two-Dimensional Material Components. *ACS Nano*, **8**:6259–6264, 2014, `DOI:10.1021/nn501723y`. 32

[161] O.N. Shornikova, E.V. Kogan, N.E. Sorokina, and V.V. Avdeev. **The specific surface area and porous structure of graphite materials**. *Russian J. Phys. Chem. A*, **83**:1022–1025, 2009, `DOI:10.1134/S0036024409060260`. 33

[162] Jaspard H. Atkins. **Porosity and surface area of carbon black**. *Carbon*, **3**:299 – 303, 1965, `DOI:10.1016/0008-6223(65)90064-3`. 33

[163] EunJoo Yoo, Jedeok Kim, Eiji Hosono, Hao-shen Zhou, Tetsuichi Kudo, and Itaru Honma. **Large Reversible Li Storage of Graphene Nanosheet Families for Use in Rechargeable Lithium Ion Batteries**. *Nano Lett.*, **8**:2277–2282, 2008, `DOI:10.1021/nl800957b`. 33

[164] Yongcai Qiu, Wanfei Li, Wen Zhao, Guizhu Li, Yuan Hou, Meinan Liu, Lisha Zhou, Fangmin Ye, Hongfei Li, Zhanhua Wei, Shihe Yang, Wenhui Duan, Yifan Ye, Jinghua Guo, and Yuegang Zhang. **High-Rate, Ultralong Cycle-Life Lithium/Sulfur Batteries Enabled by Nitrogen-Doped Graphene**. *Nano Lett.*, **14**:4821–4827, 2014, `DOI:10.1021/nl5020475`. 33

[165] Hailiang Wang, Yongye Liang, Ming Gong, Yanguang Li, Wesley Chang, Tyler Mefford, Jigang Zhou, Jian Wang, Tom Regier, Fei Wei, and Hongjie Dai. **An ultrafast nickeliron battery from strongly coupled inorganic nanoparticle/nanocarbon hybrid materials**. *Nat. Commun.*, **3**:917, 2012, `DOI:10.1038/ncomms1921`. 33

[166] S R C Vivekchand, Chandra Sekhar Rout, K S Subrahmanyam, A Govindaraj, and C N R Rao. **Graphene-based electrochemical supercapacitors**. *J. Chem. Sci.*, **120**:9–13, 2008, `DOI:10.1007/s12039-008-0002-7`. 33

[167] P. Tamilarasan and S. Ramaprabhu. **Nitrogen-Doped Graphene for Ionic Liquid Based Supercapacitors**. *J. Nanosci. Nanotechnol.*, **15**:1154–1161, 2015, `DOI:10.1166/jnn.2015.8890`. 33

[168] Blueshift. **Hydrogen: Next-Generation Supercapacitor-Powered Portable Speaker**. `http://www.crowdsupply.com/blueshift/hydrogen` [Last checked Jan 2015]. 33

[169] Railway Gazette. **Supercapacitors to be tested on Paris STEEM tram**. `http://www.railwaygazette.com/news/single-view/view/supercapacitors-to-be-tested-on-paris-steem-tram.html` [Last checked Jan 2015]. 33

[170] Umar Khan, Karen Young, Arlene O'Neill, and Jonathan N. Coleman. **High strength composite fibres from polyester filled with nanotubes and graphene**. *J. Mater. Chem.*, **22**:12907–12914, 2012, `DOI:10.1039/C2JM31946B`. 34

[171] Silvia Panzavolta, Barbara Bracci, Chiara Gualandi, Maria Letizia Focarete, Emanuele Treossi, Konstantinos Kouroupis-Agalou, Katia Rubini, Federico Bosia, Lucas Brely, Nicola M. Pugno, Vincenzo Palermo, and Adriana Bigi. **Structural reinforcement and failure analysis in composite nanofibers of graphene oxide and gelatin**. *Carbon*, **78**:566 – 577, 2014, `DOI:10.1016/j.carbon.2014.07.040`. 34

[172] Huhu Cheng, Chuangang Hu, Yang Zhao, and Liangti Qu. **Graphene fiber: a new material platform for unique applications**. *NPG Asia Mater.*, **6**:e113, 2014, `DOI:10.1038/am.2014.48`. 34

[173] Sigfried Eigler and Andreas Hirsch. **Chemistry with graphene and graphene oxide-challenges for synthetic chemists**. *Angew. Chem. Int. Ed.*, **53**(30):7720–7738, 2014, `DOI:10.1002/anie.201402780`. 35

2

Equipment Used and Device Fabrication

2.1 X-ray Photoelectron Spectrometry (XPS)

XPS in surface analysis provides information on the binding energy of core electrons in a sample. Through careful characterization, analysis and good interpretation of the data detailed electronic information about the sample can be obtained. Two types of characterizations can be made, a low-resolution and a high-resolution spectrum. Analysis of the the low-resolution spectrum can give information about the identity and relative abundance of the elements present. On the other hand, an analysis of the high-resolution spectrum can give detailed information on the type and relative quantities of chemical bonds that have formed between the elements present in the sample.

XPS is a surface sensitive technique that probes the electronic information of atoms at the bulk-vacuum boundary. However in recent times, the distinction between bulk and surface has decreased in relevance. If the film thicknesses are comparable to the electron information depth of approximately 10 nm, a XPS characterization can be a bulk characterization[1–3]. This increases the usefulness of XPS characterizations as, unlike before, it is now possible to probe the electronic structure of the entire working device through a single XPS characterization.

In this section, some fundamentals of XPS characterization will be explained and details on the photoemission process, the information depth and the XPS apparatus are included.

2.1.1 Photoemission Theory

XPS characterization involves the use of X-ray photons to excite electrons in core orbitals and the subsequent collection and analysis of these photo-excited electrons. Briefly, the binding energy, E$_b$, of core electrons in orbitals such as the 1s, 2s and 2p orbitals depend on their interaction with (i) the nucleus, (ii) screening effects by other electrons and (iii) the spin-orbit coupling[4]. Besides these interactions that occur within the atom, the binding energy values is also dependent on the local bonding configuration and depends on the identity of neighboring atoms, as well as the type of bonds that are formed with these atoms.

In a typical XPS characterization, a beam of high energy photons is shone onto a sample where one of three events occur:

i. The photon passes through without interacting with the sample
ii. The photon is scattered
iii. The photon is absorbed and an electron is liberated

The photo-excitation and emission process as described in the third event is a three step event that involves[5]:

1. Photon absorption and electron excitation
2. Transport of the excited electron through the material towards the surface
3. Escape of the excited electron through the sample surface and into the vacuum

When an electron is excited and liberated from the sample, it is emitted with kinetic energy, E$_k$,

$$E_k = h\nu - E_b - \phi \tag{2.1a}$$

and rearranging for E$_B$,

$$E_b = h\nu - E_k - \phi \tag{2.1b}$$

where hν is the photon energy and ϕ is the work function of the sample[6].

The benefit of identifying electrons by their binding energy is that it removes the photon dependence of the observation. A schematic of the photoemission and electron detection events at the source and detector, respectively, is shown in Fig. 2.1 along with a representation of some orbital energies.
The shift in the binding energy of the atom under study then depends on the number of bonds formed with and the electro-negativities of the neighbouring atoms[7]. When electrons are withdrawn from the valence orbitals, there is a tendency for the binding energy to decrease, while the opposite is true when electrons are donated into the valence orbitals. These changes are detectable as a binding energy shift in the high resolution XPS spectra and by analysis of the area of these peaks, the relative concentrations of the different chemical bonds can be compared.

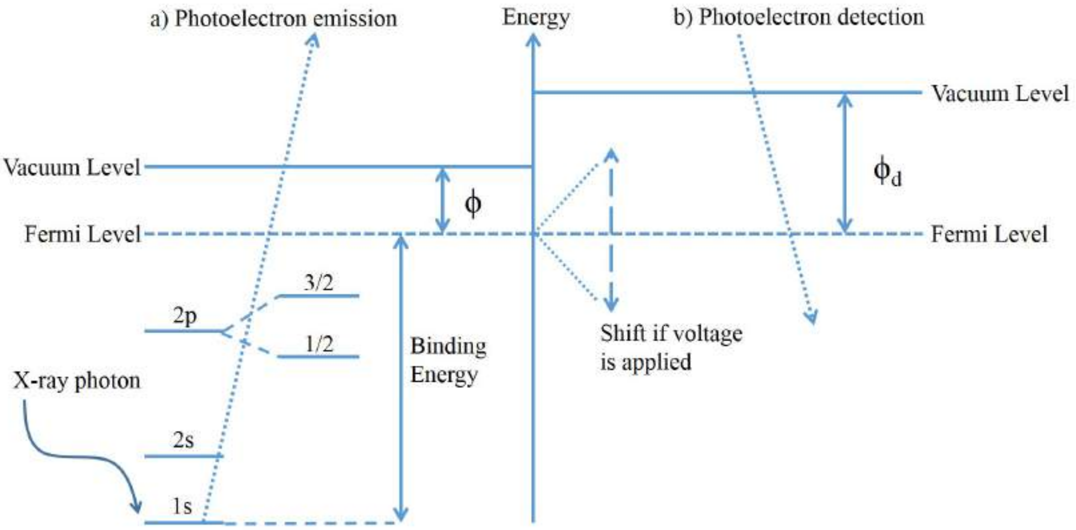

Figure 2.1: Schematic of the photoelectron (a) emission and (b) detection events at the sample and detector respectively. In this example, the incoming x-ray excites an electron in the 1s orbital and the excited electron is emitted from the sample and subsequently detected. Here, ϕ_D is the work function of the detector and the energy levels are not drawn to scale.

2.1.2 Information Depth

The information depth is the depth beneath the surface from which 95 - 99% of detected electrons in a XPS characterization experiment originate[3]. This value is related to the electron attenuation length, λ, and using an exponential depth distribution function, the information depth extends to 3 or 5 λ beneath the surface of the sample.

λ is a function of electron kinetic energy and as the kinetic energy increases from 0.5 to 1000 eV, the attenuation length decreases from ~1000 monolayers to a minimum of 2 monolayers at about 30 eV before gradually increasing again at higher kinetic energies[8,9]. The graph of this behavior is shown in Fig. 2.2 and for the kinetic energies of interest in this thesis (800 - 1200 eV), the expected electron attenuation length is ~10 monolayers.

Assuming detection at normal incidence, a typical XPS characterization is expected to yield information from the the first 30 to 50 monolayers of the sample. In an isotropic sample, an excited electron is emitted with equal probability in all directions and the information depth can be decreased by tilting the sample off normal incidence. This is because, for the same depth from the surface, an

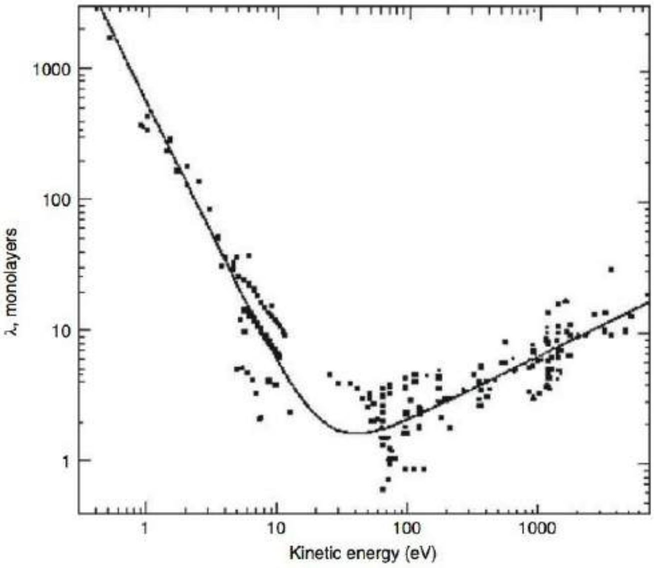

Figure 2.2: Dependence of the electron attenuation length, λ, in monolayers, on the kinetic energy of the electron.

Reprinted with permission from reference [10]. Copyright © 2004 John Wiley and Sons.

electron traveling perpendicularly with respect to the surface will pass through less material, and hence encounter fewer scattering events. Consequently, an off-normal incidence characterization will have the effect of capturing the electronic information of the atoms closer to the boundary layer of the sample than a characterization made at normal incidence.

2.1.3 XPS of Oxygen Atoms

Oxygen is a highly reactive element and has a strong affinity with atoms of other elements and is a central element in the characterization work of this thesis. However, despite the extensive XPS studies made on O 1s$_{1/2}$ electrons in other carbonaceous compounds, experimental studies of these electrons in GO are currently still lacking.

The binding energies of the O 1s$_{1.2}$ electrons in various functional groups were summarised by Beamson and Briggs in 1992 and a summary of these binding energies is shown in Fig. 2.3[11]. In most cases, the binding energy of the O 1s$_{1/2}$ electrons are influenced by the type of functional groups that the oxygen atoms are in, as evidenced by the wide spread of average binding energy values across the chart, while the class of organic compound, *i.e.* aliphatic or aromatic, is of secondary influence. Finally, in most cases, the uncertainty bars are narrower than the spread of binding energy values, indicating that the compound with which the functional group is attached to is of tertiary importance in influencing the binding energy of the O $1s_{1/2}$ electrons.

As shown in Fig. 2.3, there is a ~4 eV spread in the binding energies of the electrons and with a typical full width half maximum (FWHM) of 1.0 eV, it would be theoretically possible to differentiate up to 7 different oxygen functional groups, if they had distinct binding energies within the energy range. As discussed in Section 1.2.3.1, currently hypothesized GO models have no more than 5 oxygen functional groups, namely hydroxyls, epoxides, carbonyls, carboxyls and lactols, on the carbon basal plane[12]. Based on Fig. 2.3, the expected binding energies of the O 1s$_{1/2}$ electrons in these functional groups are summarized in Table 2.1.

It should be clarified that because GO is not a classical hydrocarbon, the actual binding energies from a characterization experiment may differ from the data shown in Table 2.1, however this is a starting point for the analysis. This data

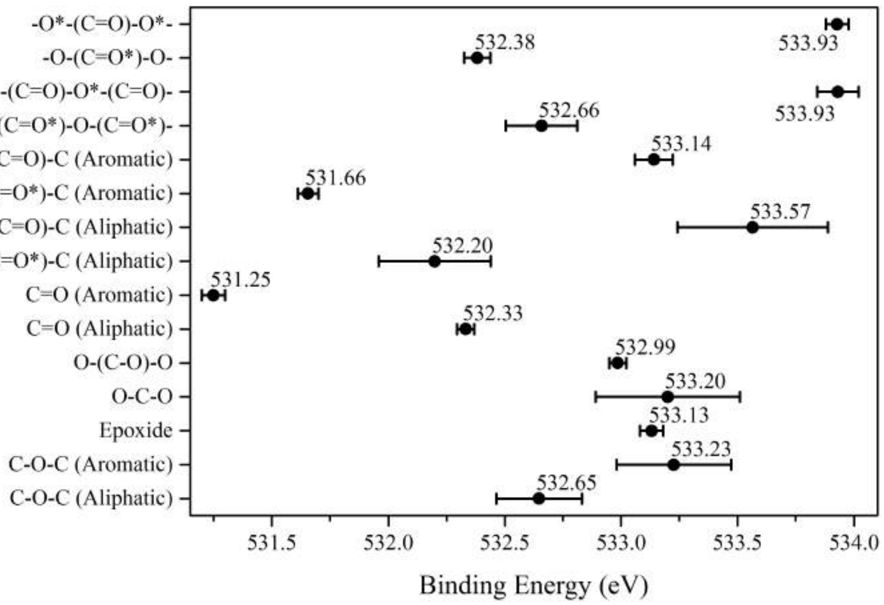

Figure 2.3: Summary of O $1s_{1/2}$ electron binding energies by Beamson and Briggs. The spread in the average values of the B.E. and the smaller spread of the error bars indicates clearly that the binding energies of these electrons depend primarily on the functional group that the oxygen atom had formed. The compound that the functional group is attached to is of secondary importance in determining the B.E. of the electron. Plot from data in Appendix 3.1 & 3.2 of reference [11].

Table 2.1: Tabulation of the binding energies of O $1s_{1/2}$ electrons (as was shown in Fig. 2.3) from the relevant functional groups that are expected to be present in GO. For the carboxyl groups, the * denotes the oxygen atom represented.

Functional Group		**Binding Energy / eV**
Hydroxide	–OH	532.7
Epoxide	C-O-C	533.1
Carbonyl	>C=O	532.3
Carboxyl	–(CO*)OH –(CO)O*H	532.2 533.7

also shows that there is good reason to expect that individual peaks can be resolved from the O $1s_{1/2}$ spectra for each of the functional groups[13–15].

From a survey of the reported results, it is known that the binding energies of the O $1s_{1/2}$ electrons in functional groups that form double bonds with the carbon atoms in the graphene basal plane have higher binding energies than the same electrons in functional groups that only form single bonds with the carbon atoms. That is to say, the electrons in the O $1s_{1/2}$ orbital of the -OH in hydroxyls and carboxyls and of the C-O-C in epoxides have lower binding energies than electrons in the same orbital of the C=O group in carbonyls and carboxyls[12,15].

The theoretical study of Susi *et al.* has replicated this observation, however it also showed that the binding energies of these O $1s_{1/2}$ electrons will change if a vacancy is present in the graphene basal plane near the functional group[16]. In this case, the appearance of the vacancy causes a restructuring on the graphene sheet that affects the electronic structure of the material and a detailed XPS study on the O $1s_{1/2}$ spectra is done in Chapter 3 to address these claims experimentally.

2.1.4 XPS Equipment

X-ray Source

The X-ray source is the SPECS XR50M operated at 200 W in the non-focused mode, giving a spot size of 3.5×1 mm^2 on the sample. To generate the x-ray photons, electrons from a cathode source strike an aluminium target material after accelerating through a 15 kV electric field. The accelerated electrons knock out Al $1s_{1/2}$ core electrons, leaving behind a hole. Subsequently, an electron from the Al $2p_{1/2}$ or Al $2p_{3/2}$ orbital recombines with the hole in the Al $1s_{1/2}$ orbital, and X-rays with an energy of 1486.7 eV and a corresponding line width of 0.4 eV are emitted. This transition gives the $K\alpha_{1,2}$ x-ray photon and is about 100 times as intense as the Bremsstrahlung background[17].

X-ray Monochromator

The presence of Bremsstrahlung radiation causes a reduction in the signal to noise ratio and this can limit the sensitivity of the characterization, especially if a quantitative characterization is desired. This can be avoided by the use of a monochromator which reduces the intensity of the unwanted background wavelengths and has the added advantage of protecting the sample from damage induced by these photons. On top of this, the use of a monochromator can improve energy resolution by reducing the X-ray line-width and this allows the separation of peaks with closer binding energies.

The monochromator used was a SPECS Focus 500 Ellipsoidal Crystal Monochromator. The monochromator was adjusted such that the X-ray photons were incident upon the $(10\bar{1}0)$ surface of the quartz mirror in the monochromator at an angle of 23.149 °. Only incident photons with an energy of 1486.7 eV were Bragg diffracted and this served to reduce the line-width of the incident photons from 0.4 eV, at the source, to 0.25 eV, after the monochromator[18].

Analyser

The analyser consists of three main parts, namely the electrostatic lens assembly, the hemispherical analyser and the 7-channel detector. Depending on the equipment settings, only electrons entering the electrostatic lens with a predetermined amount of kinetic energy will successfully arrive at the detector and contribute to the count rate on the spectrum[19].

The operation of the analyser begins at the electrostatic lens assembly and ends at the detector and electrons are retarded by the application of an electric field along this path. In the constant analyser energy (CAE) mode, which was used for all the characterizations in this thesis, electrons having the required kinetic energy were selected by varying the electric field in the electrostatic lens while the hemispherical plates in the analyser were held at fixed potential difference. Upon entering the hemispherical analyser, only electrons that had the specified pass energy would arrive at the detector. Electrons that had too little or too much energy would respectively either fail to make it into the analyser or veer off path and away from the detector[19].

In these characterizations, the CAE mode was chosen because:

i. the kinetic energies of the electrons were high, typically >150eV and
ii. the energy range was large as carbon and oxygen peaks occurred at ~285 and ~530 eV respectively

In the CAE mode, a constant analyser resolution was maintained across this energy range, which was essential for accurate quantitative analysis across such large energy ranges.

The alternative constant retard ratio (CRR) mode was not chosen as it was more suitable for Auger spectra which typically have lower kinetic energies. Briefly, the CRR mode changes the potentials in both the electrostatic lens and hemispherical analyser while maintaining a constant ratio between these potentials.

While this technique gives better energy resolution when detecting electrons with low kinetic energy and protects the detection system from the high intensity background radiation, it also causes the analyser resolution to vary with energy. This energy dependent resolution was not desirable in during the analysis and explains why the CRR mode was not used.

Analysis Software

The recorded spectra were analysed using the XPSPEAK Version 4.1 software. The software uses a χ^2 minimization routine to optimize parameters such as the binding energy value, FWHM, area, and line-shape of the peaks in the fitting[20]. The steps in a typical fitting routine were as follows:

1. The expected number of peaks were manually added onto the spectra with approximated peak parameters.
2. The software optimized the fit by adjusting the parameters in ±0.1 steps in each iteration cycle.
3. The software continued the optimisation routine for a specified number of iteration cycles.
4. More iteration cycles were conducted until the χ^2 value for each spectra was less than unity.
5. In special cases, the optimisation was done across multiple spectra at the same time.

   In these optimizations, parameters could be linked across multiple spectra, thereby ensuring that the value for the parameter chosen is optimum for the entire set of experiments. This implementation is especially useful in characterizations that involve in-situ measurements of a single sample under variable conditions such as sample temperature or gaseous pressure.

2.2 Deposition Techniques

Two deposition techniques were used to fabricate thin films, namely ultrasonic spray deposition and physical vapour deposition (PVD). In this section, the operational principles of and particular details for the use of these devices are shown. Deposition parameters were characterized for the machines so that there could be control over the thickness of the active materials used in the completed devices.

2.2.1 Ultrasonic Spray Coater

Films of GO and AgNW were made by use of the Accumist ultrasonic spray coater from Sonotek and an image of the setup is shown in Fig. 2.4. In this machine, the solution is fed towards the spray nozzle which is kept vibrating at an ultrasonic frequency. The liquids that come in contact with the atomizing surface in the nozzle form a mist of small liquid droplets that are transported out of the nozzle by a carrying gas of compressed air. The mixture of air and atomized solution leave the nozzle and, aided by gravity, arrive on the target substrate. The solvent in the solution evaporates and leaves behind the solute, which then forms the thin film. A schematic of the nozzle detailing the locations of the inlet valves is shown in Fig. 2.5.

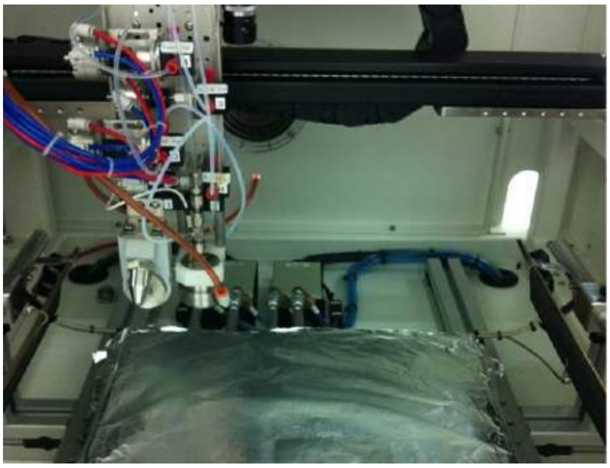

Figure 2.4: Image of the ultrasonic spray coater that was used to deposit silver nanowires and graphene oxide. The setup consists of the spray assembly shown in the top left corner of the image, mounted onto an automated frame with a heated platform that the sample was placed onto during deposition.

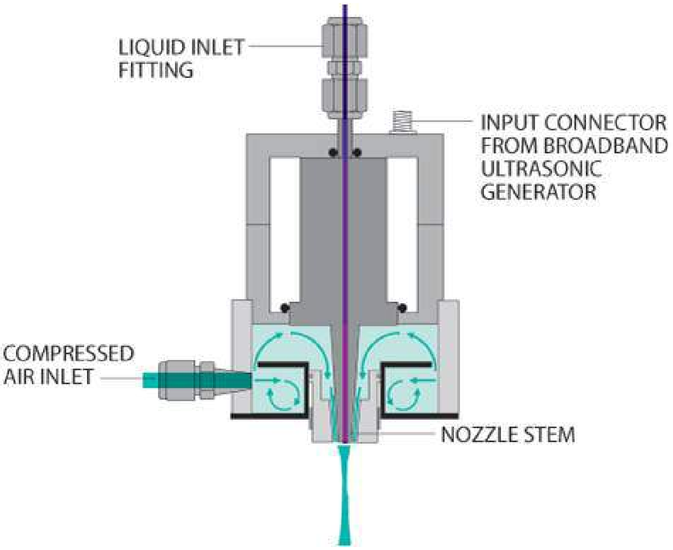

Figure 2.5: Schematic of the ultrasonic spray nozzle detailing the various parts of the assembly. The solution was infused from the top and agitated by the ultrasonic generator to form small liquid droplets which were transported to the substrate by a stream of compressed air.

The liquid spray can be shaped by the geometric properties of the spray nozzle and in this set-up, a conical surface was used to maximize the spread of the infused solution. The conical surface was driven to vibrate at 120 kHz and this was expected to give a median water droplet diameter of 18 μm. This meant that all water based solvents would have similar performance characteristics and give similarly sized droplets during the deposition[21].

The type of solvent used as well as the size, shape and concentration of the solute in the solution play important roles in determining the properties of film that results from this deposition technique. While the size, shape and to some extent the solvent used cannot be modified for a give experiment, the concentration of the solute in the concentration is easily controlled through dilution. However, diluting the solution will require higher infuse rates or more passes to achieve the same sample thickness and these adjustments are not without their own problems. The various parameters that affect the deposition and an explanation on how the deposition is affected by each parameter is summarised in the following box.

An overlapping set of parallel lines was chosen as the method of deposition and this is shown in Fig. 2.6, along with other possible nozzle paths. The path

Parameters affecting films made by ultrasonic spray deposition

i. Rate of solution infusion
   Faster infusion rates allow more solute particles to be deposited in the same amount of time, giving a thicker film.
ii. Nozzle move speed
   For the same solution infusion rates, slower nozzle movement speeds increase the quantity of solution deposited and gives a thicker film, but increases the time taken for the deposition.
iii. Platform temperature
   This affects the quality of the films formed as low substrate temperatures may lead to longer drying times and the occurrence of unexpected drying effects that may result in higher surface roughness[22].
iv. Path taken by the nozzle
   The nozzle path is manually programmed and this means that the separation between successive deposition lines as well as the waiting time between each line can be varied.
v. Number of passes that the nozzle makes
   The time taken for sample deposition is lengthened when more passes used, but this allows lower solution infuse rates to be used.

is chosen so as to maximise coating uniformity across the target substrate and while a S-shaped path would complete the deposition in a shorter period of time, it would also cause higher deposition concentrations along the shorter ends of the spray path.

The overlapping parallel lines mimicked, to some extent, a multi-nozzle system as shown in Fig. 2.6(d). The spray path was set up such that after the first set of spray lines had been deposited, the successive set of spray lines were deposited between the initial spray lines. With the exception of the left and right fringes of the sample, the deposition is designed to increase the uniformity across the entire target surface as shown in Fig. 2.6(c). A caveat for this technique is that successive spray lines must be spaced at a distance close to half the width of the spray cone, otherwise the overlaps from successive lines will not match to give the uniform deposition.

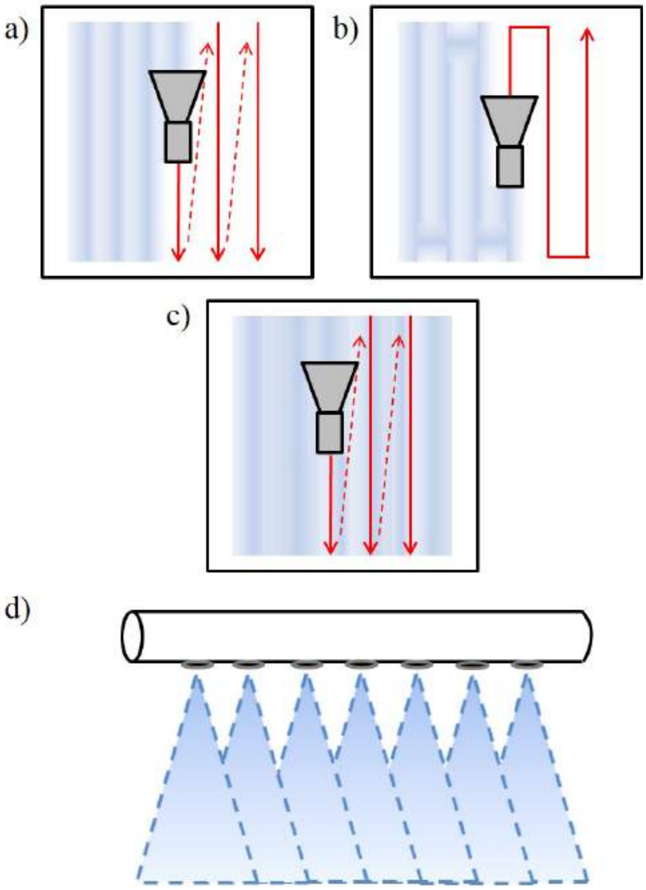

Figure 2.6: Schematics of possible nozzle paths during deposition. a) Series of parallel deposition lines, b) S-shaped deposition pattern, c) increased uniformity of deposition when a second set of parallel deposition lines is made with a horizontal offset and d) an example of a multi-nozzle system that can be used for quick large area deposition.

The machine was also designed to allow two solutions to be infused into the nozzle at the same time. This was especially useful as it could prevent early reaction between the solutions used. In the early experiments, GO & AA were mixed just before deposition and while this worked in samples with low AA concentrations, at high AA concentrations, the reaction was rapid and very often led to the formation of reduced GO before deposition. The reduced GO formed particulates and clumps and this prevented the mixture from passing out of the nozzle and onto the target substrate. By making use of the dual-feed system,

AA and GO could be held separately in different reservoirs and mixed just before deposition on the substrate. This ensured a uniform mixture of AA and GO on the substrate, prevented the formation of clumps and allowed a high degree of control over the mixing ratio of GO and AA.
A scratch test was performed on the samples and profiles taken using an atomic force microscope, see page 74. The characterisation results of the spray deposition are shown in Table 2.2, where the number of passes and infuse rate of a suspension of 5 mg/ml GO are varied to give GO films of different thicknesses. As shall be shown later in Chapter 4, the variation in film thickness is not a reflection of the actual amount of GO deposited. The transmittances and sheet resistances of films fabricated by spray coating were well controlled by the number of passes and infuse rate.

Table 2.2: Tabulation of GO film thicknesses in nanometers as the infuse rate and number of passes were increased. Data shows a general increase in film thickness with increasing flow rate and number of passes used, but low film uniformity affected the consistency of the results.

Infuse rate μl min^{-1}	1	2	3	4	**Number of Passes**
25	19	16	19	16	**Thickness of film /nm**
50	15	13	37	32	
75	31	19	34	39	
100	23	16	36	40	

2.2.2 Physical Vapour Deposition

PVD involves the heating of a source material at a high temperature and in high vacuum. The source sublimates or evaporates and the gaseous source material travels upwards towards the target substrate, which is suspended directly above the source. Upon contact with the cooler target substrate, the material cools and forms a film on the substrate. Designs can be made on the target substrate by placing a mask in the path between the material source and the target substrate. However, care must be taken to minimize the gap between the mask and target substrate. Failure to do so would result in fringing effects, resulting in thickness non-uniformity or electrical shorts. Additionally, the target substrate is typically kept rotating during evaporation so as to ensure an even deposition of the source material on the substrate.

In this work, two machines were used for PVD, a LESKER Tool and a MBRAUN evaporator. While the basic mode of operation is similar in both machines, the control mechanism was different in each device. In the LESKER tool, the source was maintained at a specified temperature during the deposition cycle, while the power passing through the metallic crucible that contained the source was kept constant in the MBRAUN evaporator. This meant that the former device was better suited for the deposition of temperature sensitive organic materials, while the latter was better suited for the fast deposition of metallic materials which were not temperature sensitive.

Fig. 2.7, shows a computer-aided design drawing of the inter-digitated metallic electrodes used in the gas sensor device that was fabricated by PVD. The dimensions of the fingers and the electrodes are specified in millimetres and the design is laser cut from a thin sheet of metal to form the mask.

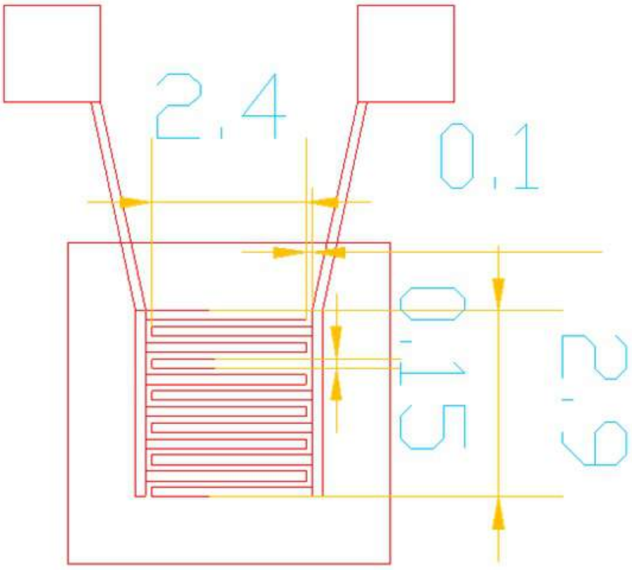

Figure 2.7: Computer aided design drawing of the inter-digitated finger electrodes used in the fabrication of gas sensor devices with a device area of about 7.5 mm^2. The dimensions shown are in millimetres.

2.2.3 Spin Coating

Spin coating was also used as a technique for film deposition and initial TCE films of GO were made with spin coating as it was expected to produce thin uniform layers of material. However, no spin parameters were found that would allow the reliable fabrication of a film with uniform surface coverage over the surface of a 50×50 mm large glass substrate.

Still, the method was successfully used to produce thin films of organic materials that were later used in the gas sensors. These molecules were dissolved in denser and more viscous solvents and the resulting solution adhered well to the silicon substrates. The film thickness was controlled by the:

1. **Solution concentration:** Ceteris paribus, films formed from dilute solutions were thinner than films from more concentrated solution.
2. **Spin rate:** Ceteris paribus, higher spin rates give thinner films than lower spin rates.
3. **Spin time:** Ceteris paribus, longer spin times give thinner and more uniform layers than shorter spin times so long as the spin time does not exceed film drying time.

After spin deposition using a CEE® 200 spin coater, the film thickness would be characterised by a scratch test using the atomic force microscope. The relationship between the spin speed, solution concentration and resulting film thickness for nickel phthalocyanine in tetrahydrofuran is shown in Table 2.3.

Table 2.3: Characterization of film thicknesses, in nanometers, of nickel phthalocyanine in tetrahydrofuran deposited by spin coating for a spin time of one minute and acceleration rate of 400 rpm/s.

Spin Speed / rpm	10	11	13	15	20	25	**Concentration / mg ml^{-1}**
500	–	53	–	88	99	–	**Thickness of film / nm**
800	16	40	68	72	74	169	
1000	9	36	53	53	74	190	

2.3 Device Fabrication Processes

TCEs were fabricated by testing different methods of GO deposition onto glass substrates, with each method having its own strengths and weaknesses. It was not possible to spin coat GO solution onto glass, as the resulting films would be too thin and the surface coverage too poor to be useful in TCEs. Dip coating was also tested but had similar problems. Ultrasonic spray coating was chosen as the deposition process was reliably repeatable and good control could be acheived over the deposition quantity.

On the other hand, gas sensors were fabricated to minimise changes to existing procedures so that the improvements or problems brought to the system by the introduction of GO could be identified and compared. In this section, the steps used in the fabrication of all devices are recorded in detail.

2.3.1 Substrate Cleaning

Prior to deposition of any films, substrates were thoroughly cleaned by use of solvents and ultrasonication. All substrates were cleaned in the following manner:

1. Rinse with de-ionised water.
2. Ultrasonication for 15 minutes in Extran® diluted in water at a concentration of 2 %
3. Washing in de-ionised water, 3 cycles
4. Ultrasonication for 15 minutes in acetone
5. Heating in isopropanol at 353 K for 30 minutes

The effect of each step on the cleanliness of a glass substrate is shown in Fig. 2.8. As shown, the particulates are effectively removed by the cleaning process and this is important as the presence of these particles may inadvertently affect the final devices. These effects could come in the form of variations in the transmittance or the sheet resistances of the deposited films. Furthermore, the presence of these particulates introduces a new dimension of uncertainty and much effort was expended to avoid issues that could arise from these particulates.

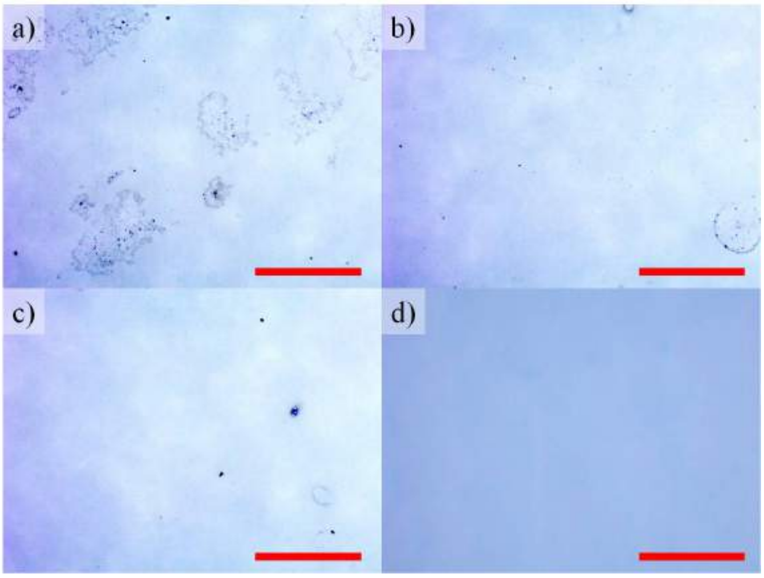

Figure 2.8: Optical images showing the cleanliness of the glass substrate a) before cleaning, b) after ultrasonication in dilute Extran®, c) after ultrasonication in acetone and d) after heating in isopropanol for 30 minutes. The scale bar in the images is 250 μm.

2.3.2 Transparent Conducting Electrodes

While only spray coating was used to deposit GO, there were still a variety of processes used in the manufacture of TCEs. The variety in these methods ranged from pre-annealing the GO suspension before deposition to post deposition annealing of the film. Additionally, different temperatures were also used in the reduction step. Further clarification for specific samples can be found in Chapter 4 and the following steps outline the general process flow and parameters used for the deposition of GO and AgNW onto glass or silicon substrates.

Deposition Steps

1. Substrates were warmed on a heated platform to 383 K for several minutes prior to deposition
2. GO with a concentration of 5mg/ml was deposited at a infused rate of 50 μl/min and 2 passes were made
3. If AA was used, it was infused at a rate of 150 μl/min at a concentration of 1.66 mg/ml

4. Samples were thermally annealed in a oven at 353 K for up to 72 hours in a sealed beaker
    - If water water vapor was required, an excess of water was added to the beaker before sealing; the water would evaporate during the heating process to provide a high water vapor environment
5. Thermal reduction was typically done at 573 K and in a nitrogen glove box for 15 hours
    - In some experiments, the thermal reduction step was done in air for varying lengths of time

AgNW were deposited using 4 passes for each deposition and a high infuse rate of 500 μl/min because the suspension had to be diluted to prevent it from clogging at the nozzle. With the exception of these parameters, the deposition process of AgNW was very similar to that used for GO deposition.

2.3.3 Gas Sensor

The fabrication of a basic gas sensor began with the deposition of the inter-digitated electrodes, shown in Fig. 2.7, by PVD. The inter-digitated fingers came in two thicknesses, 20 and 60 nm and had a nickel layer that was 20 nm thick under the large square shaped contact pads. This was done to improve the adhesion of gold to the silicon substrate.

The sensing materials were subsequently deposited onto the electrodes by spin coating, spray coating and/or PVD depending on the material to be deposited. A schematic of a bilayer gas sensor is shown in Fig. 2.9 where the bottom layer of GO was deposited by spray coating while the top layer of phthalocyanine was deposited by PVD or spin coating. Similarly, monolayer gas sensors were made by deposition of phthalocyanines or GO onto the metallic electrodes according to the methods and parameters summarized in Table 2.4

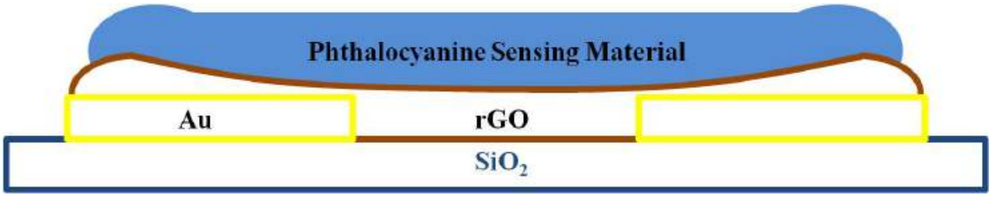

Figure 2.9: Schematic showing the general design of the bilayer gas sensor. The phthalocyanine only gas sensor is similar but only has a monolayer of material on the electrodes instead of two.

Table 2.4: Various deposition parameters and the thickness of the film used in the gas sensor. In spray coating, the parameters are the infuse rate and number of passes. In PVD, the parameters are pressure and deposition rate and where relevant, deposition temperature. In spin-coating, the parameters are solution concentration, spin rate and spin time.

Material	Method	Parameters	Thickness
Graphene Oxide	Spray Coating	$25 - 50\ \mu$l min^{-1} 1 – 4 passes	5 – 40 nm
Zinc Phthalocyanine	PVD	643 K $<1 \times 10^{-6}$ mbar 0.1 – 1 Å/s	1 – 65 nm
Nickel Phthalocyanine dissolved in Tetrahydrofuran	Spin Coating	10 mg ml^{-1} 1000 rpm 60 s	40 nm
Nickel or Gold	PVD	$<1 \times 10^{-6}$ mbar 1 Å/s	20/60 nm

2.4 Characterization Setups

The characterization setups consisted of a mix of commercially available devices and application specific jigs along with the appropriate software that was either commercially designed and shipped with the device or programmed in-house using LabVIEW. This allowed for a high degree of flexibility in the design of experiments and in each case a standard measurement procedure was finally decided upon after appropriate testing had been done.

2.4.1 Optoelectronic Properties

To characterize TCEs, both the optical and electrical transmittance of the films had to be taken. As the deposited films were soft and easily scratched, optical transmittance characterizations were done before electrical transmittance characterizations. Here, details on the machines used in the characterization setup and procedures followed are recorded.

Optical Transmittance

Figure 2.10: Perkin Elmer LAMBDA 950 UV/Vis/NIR Spectrophotometer

Optical transmittance characterizations were made using a Perkin Elmer LAMBDA 950 UV/Vis/NIR Spectrophotometer, from 300 to 1500 nm in 1 nm steps. Taking reference from an uninterrupted beam of light, the intensity of a particular wavelength in a beam of white light passing through the sample is compared against the intensity of the same wavelength in the reference beam. The difference in intensity between the beams is then converted into a percentage transmittance value, %T, and the process repeated across the entire wavelength range.

After taking into account reflection and interference, a transmittance value of the hypothetically free-standing film can be calculated. Using this value, the absorbance value, A, can be derived using the following equation:

$$A(\lambda) = 2 - log_{10}\left(\%T(\lambda)\right) = 2 - log_{10}\left(e^{-\alpha(\lambda)l}\right) \tag{2.2}$$

where $\alpha(\lambda)$ is the wavelength dependent attenuation coefficient and l is the thickness of the film.

As a point of practicality, rather than using the entire spectrum, the value at 550 nm is taken as the nominal transmittance or absorbance value of the film and used as a reference point for comparing the transmissivity of different TCEs. It is this nominal transmittance value that is also used in the calculation of the FOM shown in Equation (1.13).

The purpose of characterizing the transmittance across the range of wavelengths is to allow the measurement of the optical gap in the material by the method of a Tauc plot[23,24]. This is done by plotting $\left(\frac{hc\alpha}{\lambda}\right)^r$ against photon energy, $\left(\frac{hc}{\lambda}\right)$ and extrapolating the tangent at the point of inflection on the graph towards the x-axis. The value of the optical band gap is the x-coordinate of the intersection between this extended line and the x-axis and an example is shown in Fig. 2.11. $\left(\frac{hc\alpha}{\lambda}\right)^r$ and $\left(\frac{hc}{\lambda}\right)$ are related according to:

$$\left(\frac{hc}{\lambda}\alpha(\lambda)\right)^r = B\left(\frac{hc}{\lambda} - E_g\right) \tag{2.3}$$

where c is the speed of light ($3.0 \times 10^8\,ms^{-1}$), B is a proportionality constant, r is a value that represents the type of transition that occurs in the material and E_g is the calculated optical bandgap. The allowed values of r and the corresponding transition that it represents are as follows:

- r = 2 – direct allowed transitions
- r = 2/3 – direct forbidden transitions
- r = 1/2 – indirect allowed transitions
- r = 1/3 – indirect forbidden transitions

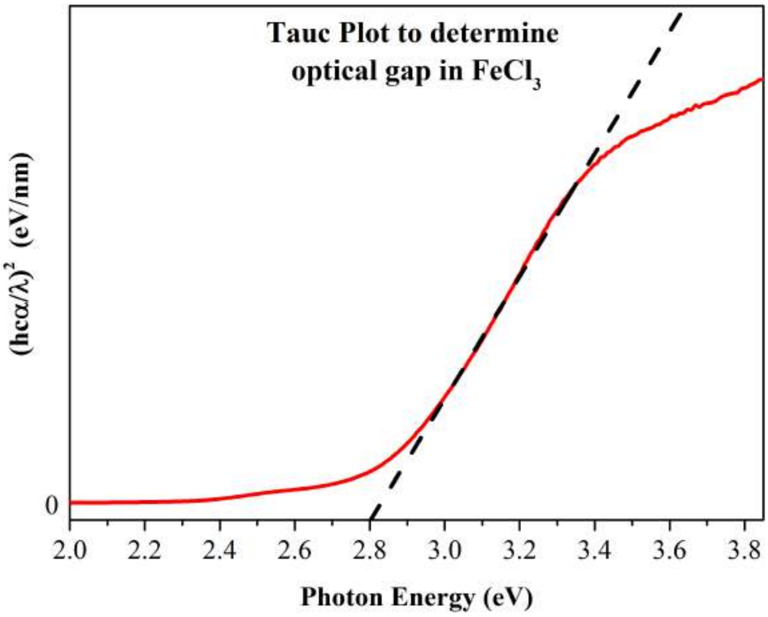

Figure 2.11: Determination of optical gap in Ferric (III) Chloride by the method of a Tauc plot. The optical transition is a direct allowed transition and here, r = 2. The tangent at the point of inflection is extended to the x-axis and the optical bandgap found to be 2.8 eV.

Sheet Resistance

The sheet resistance of the film was measured by use of a specially designed jig that lowered two 1.2 cm × 0.6 cm large rectangular gold plated copper contact plates onto the deposited TCE, Fig. 2.12(d). The contacts were set at a fixed distance of 1.2 cm apart and all sheet resistance measurements were made across this 1.2 cm × 1.2 cm square. While conformability throughout the overlap region would be improved by the use of evaporated gold contact pads, the use of a jig wouldshorten the time taken to make electrical characterizations of the deposited TCEs. A large volume of samples were made and while it would have improved accuracy, it was also impractical to evaporate gold electrodes onto every sample. As can be seen later, in Chapter 4, this concern has a minor impact on characterization results as low sheet resistance values were readily captured using this jig.

As shown in Fig. 2.12(a) & (b), the sample is held by the black lower bracket and the contact pads are fixed onto a platform that is held perpendicularly above the substrate. Confined by the four corner supports, the contact pads was only

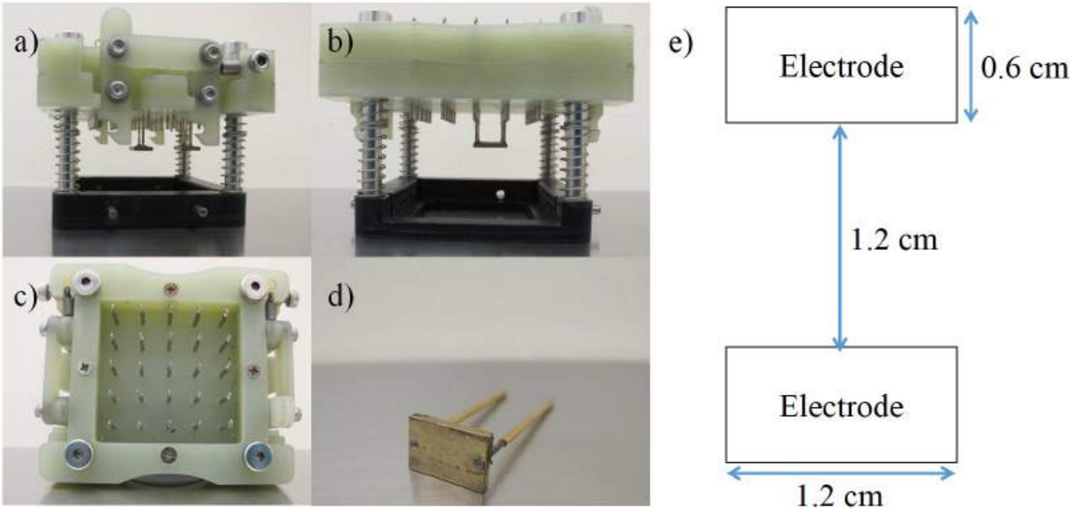

Figure 2.12: a) Side, b) front, and c) top profile of the sheet resistance jig and d) the gold coated contact pad used in the setup. e) Schematic of electrode placement and measurement area.

allowed to move in the direction normal to the plane of the substrate and this helped to minimize the likelihood of scratching the sample when bringing the pads into electrical contact with the deposited TCE. The resistance was then measured across the contact pads using the two-point probe method and the corresponding sheet resistance value calculated by dividing this resistance value by 1.44 cm^2, the area between the contact pads. Subsequently, this would be used to find the FOM of the TCE.

2.4.2 Gas Station Set-up

Fig. 2.13 shows the general operating principle of the gas sensor testing setup. Gas volumes are controlled by the mass flow controllers and are pre-mixed before they are introduced into the gas chamber and removed by the exhaust; Fig. 2.14 shows the gas control board, complete with piping and mass flow controllers.

The gas mixture was kept flowing constantly to ensure that the component concentrations were kept at the pre-set level. The electrical conductivity of the fabricated gas-sensor device was constantly measured by use of a Keithley 2636B, the values recorded in real-time and these processes were coordinated by software that was coded in LabVIEW.

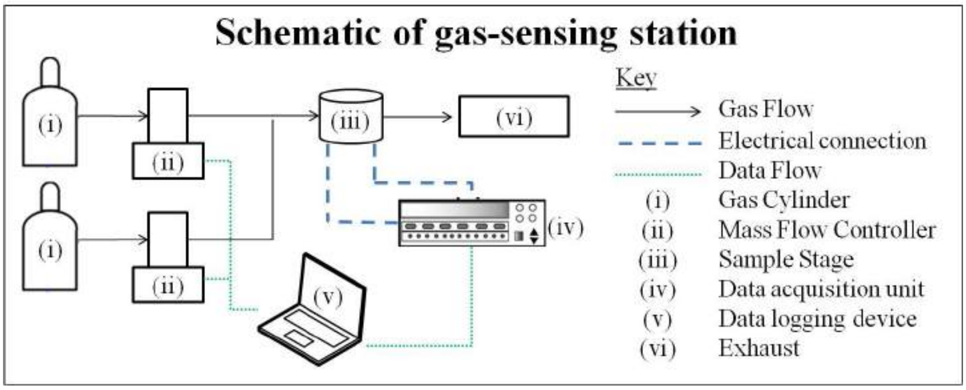

Figure 2.13: Schematic showing the various parts of the gas station setup. The data acquisition unit (DAU) used was a Keithley 2636B. The DAU and the mass flow controllers were controlled by software written using LabVIEW.

Figure 2.14: Photo of the setup showing parts (ii) and (iii) of Fig. 2.13, that controls the concentration and rate of gas flowing towards the sensor that is mounted in the measurement setup up shown in Fig. 2.15.
Photograph courtesy of Robert Bosch SEA.

In a typical experiment, the completed devices were first mounted onto the sample holder as shown in Fig. 2.15. Electrical contact was then made by lowering the contacts onto the pre-fabricated metallic squares. The chamber could subsequently be sealed to prevent environmental factors such as exhaled breath and ambient light from interfering with the characterization before the devices were tested for sensitivity to nitrogen dioxide.

Figure 2.15: Image of the mounting element that the gas sensor is inserted into for characterization measurements.
Photograph courtesy of Robert Bosch SEA.

2.4.3 Imaging Techniques

A bench top optical microscope, the Zeiss Axio Scope A1 in Bright Field mode, was employed for optical imaging of the samples. However, where higher resolutions were required, the following characterization machines were employed.

Atomic Force Microscopy
A Veeco di Dimension D3100V table top atomic force microscope (AFM), mounted on an air table, was used to characterize film thicknesses and to identify physical properties about the films. The microscope was operated in a sound proof dark box, in the tapping mode, using a standard silicon-nitride tip. Images were

typically taken at 512 sample points per line in trace-retrace mode at a needle translation speed of no more than 10 μm/s.

The thickness of a film was established by application of a scratch test. In a scratch test, the film is first scratched by an apparatus such as the cleaned blunt end of a pair of tweezers. The groove made by the scratch is then characterized by AFM and after appropriate data correction, a profile of the groove is extracted from the image. This profile is fit to an appropriate step function and the height of the film extracted from this fitting; Fig. 2.16 shows an example of this.

Scanning Electron Microscopy

A JEOL JSM-6700F scanning electron microscope was used to resolve features on the samples that were on the order of a hundred nanometres. The thin film samples were typically fabricated on insulating substrates and the sample was then mounted onto the sample holder. Where required, an electrical connection was made between the sample film and the film to reduce the effect of electron loss charging on the sample. The sample and sample holder were then introduced into the machine and the apparatus evacuated to a pressure of less than 2×10^{-6} mbar prior to characterization. In this case, the accelerating field was set at either 5 or 10 kV.

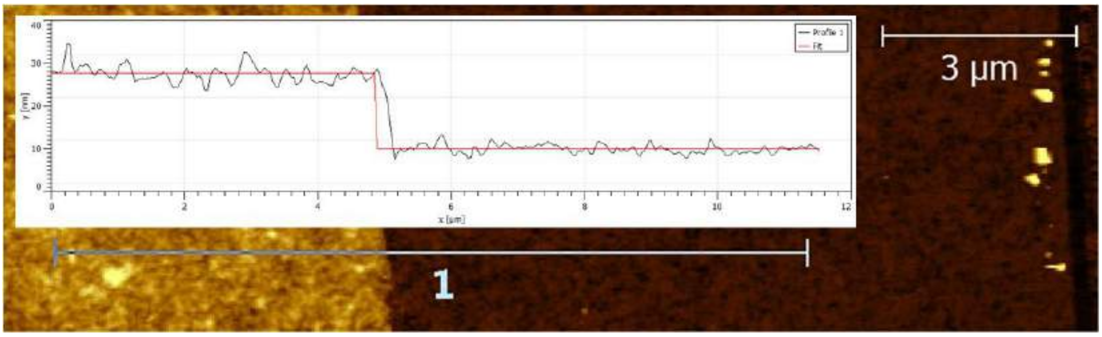

Figure 2.16: AFM characterization of a scratch test. The graph of the profile with the fitted curve is shown inset and the film here is 16 nm thick.

2.4.4 Thermogravimetric Analysis

Thermograms of the materials were made using a TA Instruments Q500 thermogravimetric analyser shown in Fig. 2.17. In a typical characterization measurement, about 4mg of the dried sample was placed into a cleaned crucible. The crucible and sample were then heated in a nitrogen environment and beginning at room temperature, the temperature of the sample and crucible raised at a rate of 5K/min up to a maximum temperature of 673 K. The mass of the sample was tracked as the temperature increased and changes in the total mass signalled that physical or chemical reactions had occurred in the sample.

These thermograms were subsequently analysed to give information such as initial moisture content, mass loss onset temperatures and thermal stability. This information was then employed in conjunction with other characterization techniques to give a complete picture of the effect of temperature on the samples. However, it should be noted that the gaseous atmosphere has an effect on many samples and one-to-one correspondence between the findings in TGA and other methods require that the same gaseous environment be replicated in every experiment.

Figure 2.17: TA Instruments Q500 Thermogravimetric Analyser

References

[1] Charles Martin, E.T. Arakawa, T.A. Callcott, and J.C. Ashley. **Low energy electron attenuation length studies in thin amorphous carbon films**. *J. Electron Spectrosc. Relat. Phenom.*, **35**:307–317, 1985, `DOI:10.1016/0368-2048(85)80064-5`. 49

[2] Charles Martin, E.T. Arakawa, T.A. Callcott, and R.J. Warmack. **Attenuation lengths of low-energy electrons in freestanding carbon films**. *J. Electron Spectrosc. Relat. Phenom.*, **42**:171–175, 1987, `DOI:10.1016/0368-2048(87)85017-X`.

[3] ISO 18115: 2001. **Surface Chemical Analysis - Vocabulary**. *International Organization for Standardization, Geneva*, 2001. 49, 52

[4] Christopher J. Foot. **Atomic Physics**. Oxford University Press, 2012. Chapter 2. 50

[5] C. N. Berglund and W. E. Spicer. **Photoemission studies of copper and silver: theory**. *Phys. Rev.*, **8**:A1030 – A1044, 1976, `DOI:10.1103/PhysRev.136.A1030`. 50

[6] Albert Einstein. **Über einen die Erzeugung und Verwandlung des Lichtes betreffenden heuristischen Gesichtspunkt**. *Ann. Phys.*, **17**:132–148, 1905, `DOI:10.1002/andp.19053220607`. 50

[7] K. Siegbahn, C. Nordling, A. Fahlman, R. Nordberg, K. Hamrin, J. Hedman, G. Johansson, T. Bergmark, S.-E. Karlsson, I. Lindgren, and B. Lindberg. **ESCA. Atomic, Molecular and Solid State Structure by Means of Electron Spectroscopy**. Uppsala, 1967. Chapter 5. 51

[8] C.J. Powell. **Attenuation lengths of low-energy electrons in solids**. *Surf. Sci.*, **44**:29–46, 1974, `DOI:10.1016/0039-6028(74)90091-0`. 52

[9] D. Briggs and M.P. Seah. **Practical Surface Analysis by Auger and X-ray Photoelectron Spectroscopy**. John Wiley & Sons, 2nd edition, 1990. 52

[10] M.P. Seah and W.A. Dench. **Quantitative electron spectroscopy of surfaces: A standard data base for electron inelastic mean free paths in solids.** *Surf. Interface Anal.*, **1**:2–11, 1979, `DOI:10.1002/sia.740010103`. 52

[11] G. Beamson and D. Briggs. **High Resolution XPS of Organic Polymers - The Scienta ESCA300 Database**. Wiley Interscience, 1992. Appendices 3.1 and 3.2. xiii, 53, 54

[12] Wei Gao, Lawrence B. Alemany, Lijie Ci, and Pulickel M. Ajayan. **New insights into the structure and reduction of graphite oxide**. *Nat. Chem.*, **1**:403–408, 2009, `DOI:10.1038/nchem.281`. 53, 55

[13] O Akhavan. **The effect of heat treatment on formation of graphene thin films from graphene oxide nanosheets**. *Carbon*, **48**(2):509–519, 2010, `DOI:10.1016/j.carbon.2009.09.069`. 55

[14] Cecilia Mattevi, Goki Eda, Stefano Agnoli, Steve Miller, K. Andre Mkhoyan, Ozgur Celik, Daniel Mastrogiovanni, Gaetano Granozzi, Eric Garfunkel, and Manish Chhowalla. **Evolution of Electrical, Chemical and Structural Propeties of Transparent and Conducting Chemically Derived Graphene Thin Films**. *Adv. Funct. Mater.*, **19**:2577–83, 2009, `DOI:10.1002/adfm.20090166`.

[15] Abhijit Ganguly, Surbhi Sharma, Pagona Papakonstantinou, and Jeremy Hamilton. **Probing the Thermal Deoxygenation of Graphene Oxide Using High-Resolution In Situ X-ray-Based Spectroscopies**. *J. Phys. Chem. C*, **115**(34):17009–17018, 2011, `DOI:10.1021/jp203741y`. 55

[16] T. Susi, M. Kaukonen, P. Havu, M.P. Ljungberg, P. Ayala, and E.I. Kauppinen. **Core level binding energies of functionalized and defective graphene**. *Beilstein J. Nanotechnol.*, **5**:121–132, 2014, `DOI:10.3762/bjnano.5.12`. 55

[17] SPECS GmbH, Voltastraße, 5, 13355 Berlin, Germany. *SPECS: XR50 M User Manual, Version 1.5*, Dec 2009. 55

[18] SPECS GmbH, Voltastraße, 5, 13355 Berlin, Germany. *SPECS: Focus 500 User Manual, Version 1.6*, May 2009. 56

[19] Omicron Nanotechnology, Limburger Straße 75, D-65232 Taunusstein. *OMICRON: EA 125 Energy Analyser: User Guide, Version 2.3*, July 2005. 56

[20] Raymund W.M. Kwok. **XPS Peak, Version 4.1**, 1999 [Last checked Feb 2015]. Software available at `http://www.uksaf.org/xpspeak41.zip`. 57

[21] Sono-Tek Corporation, LICO Electronics GmbH, A-2320 kledering, Klederinger Str. 31. *Ultrasonic Spray Nozzle Systems*, 2015. 59

[22] Seung Yol Jeong, Sung Hun Kim, Joong Tark Han, Hee Jin Jeong, Sunhye Yang, and Geon-Woong Lee. **High-Performance Transparent Conductive Films Using Rheologically Derived Reduced Graphene Oxide**. *ACS Nano*, pages 870–878, 2011, `DOI:10.1021/nn102017f`. 60

[23] J. Tauc. **Optical Properties and Electronic Structure of Amorphous Ge and Si**. *Mater. Res. Bull.*, **15**:37–46, 1968, `DOI:10.1016/0025-5408(68)90023-8`. 70

[24] J. Tauc, R. Grigorovici, and A. Vancu. **Optical Properties and Electronic Structure of Amorphous Germanium**. *Phys. Status Solidi*, **15**:627–637, 1966, `DOI:10.1002/pssb.19660150224`. 70

3

XPS Study on GO Chemistry

Experimental studies on the O $1s_{1/2}$ spectra in GO are currently lacking and as reduction methods improve and the carbon to oxygen ratios in the chemically reduced samples increases, there is a need to address this gap in knowledge[1]. Here, XPS characterization of GO by the C $1s_{1/2}$ and O $1s_{1/2}$ spectra was compared and advantages in the use of the O $1s_{1/2}$ spectra identified. The individual peaks of each oxygen functional group in the spectra were identified and verified by means of chemical and theoretical analysis. Making use of the newly identified peaks, a sample of low-oxygen content GO was characterized; this characterization served to underscore the importance of understanding the O $1s_{1/2}$ spectra in GO.

Armed with information on the oxygen functional groups, a discussion on liquid phase metastability and its effect on GO was made. By comparing the O $1s_{1/2}$ spectra before and after the effects of metastability had set in, changes in the physical and electronic properties of GO were correlated with changes in the chemistry of the material and the contributions of these findings to the theoretical modelling of GO were also discussed.

Finally, the chemical reaction between $FeCl_3$ and GO was explored and the contributions of $FeCl_3$ to the reduction of GO characterized. While the intercalation of ferroelectric materials resulted in exceptional transparency and electrical conductivity in FLG, mixing $FeCl_3$ with GO gave a less than spectacular effect[2,3]. These effects were studied by looking at the multiplet peaks in the Fe $2p_{3/2}$ spectra and other effects on the O $1s_{1/2}$ spectra.

3.1 The O $1s_{1/2}$ Spectra in GO

3.1.1 Limitations of the C $1s_{1/2}$ Spectra

The C $1s_{1/2}$ spectra in GO is well studied, as it can give information regarding both the carbon basal plane and oxygen functional groups on GO at the same time, with many studies assigning similar functionalities to the different peaks identified as summarized in Table 3.1. While the references used in Table 3.1 are not an exhaustive list, only the first four reported on the O $1s_{1/2}$ spectra as well and these values are shown in Table 3.2. This disparity in research effort is striking and was addressed experimentally by the author in reference [4].

The differences between an analysis of the C $1s_{1/2}$ spectrum and the O $1s_{1/2}$ spectrum are as follows:

1. The photo-ionization cross section of the electrons in the O $1s_{1/2}$ orbital is 2.93 times greater than that of the electrons in the C $1s_{1/2}$ orbital[5]
   This means that at the same atomic concentration, the O $1s_{1/2}$ spectrum will be more intense than the carbon spectrum
2. While the C=C & C–C bonded carbon atoms yields information about the π-electron fraction, this is a large contribution to the C $1s_{1/2}$ spectrum[6]
   This will mask changes in the relative contributions of the remaining functional groups during analysis
3. The oxygen functional groups are more chemically reactive than carbon atoms in the basal plane of GO
   As such, more chemical and bonding information can be derived from an analysis of the O $1s_{1/2}$ spectra than from an analysis of the C $1s_{1/2}$ spectra
4. As opposed to an analysis of the C $1s_{1/2}$ spectrum, an analysis of the O $1s_{1/2}$ spectrum is a direct method of looking at chemical changes in GO
   Changes in the binding energy of C $1s_{1/2}$ electrons depend on the coupling strength between itself and the oxygen functional group, while the O $1s_{1/2}$ spectrum probes the functional groups directly

In all samples, charging was accounted for by correcting the C $1s_{1/2}$ peak to a B.E. value of 284.7 eV.

Section 3.1 is based on the publication *"Identification of functional groups and determination of carboxyl formation temperature in graphene oxide using the XPS O 1s spectrum"*[4].

Table 3.1: Binding energy values of the C $1s_{1/2}$ electrons in carbon atoms bonded to different oxygen functional groups. All values are in eV.

No.	C $1s_{1/2}$						Ref.
	C=C/ C–C	C–OH	C–O–C	C=O	COOH	$\pi \rightarrow \pi^*$	
1	284.6	286.1		287.5	289.2	290.6	[7]
2	285.0	286.9 – 287.1		288.8		–	[8]
3	285.0	286.5		287.5	289.0	–	[9]
4	284.5	285.9	286.6	287.5	288.9	–	[10]
5	284.5	286.7		288.7		–	[11]
6	284.7	286.7		288.3		–	[12]
7	–	–	–	288.5		291	[13]
8	284.9	286.7		288.5		–	[14]
9	284.7	286.9		287.9		–	[15]
10	284.8	285.6	286.9	287.9	289.4	–	[16]

Table 3.2: Binding energy values of the O $1s_{1/2}$ electrons in oxygen atoms either singly or doubly bound to graphene oxide or in water. In number 4, phenol is an –OH bound to an aromatic carbon while the C atom in C–OH is an aliphatic carbon. All values are in eV.

No.	C $1s_{1/2}$	O $1s_{1/2}$				Ref.
	C=C/ C–C	C=O	C–O–C /C–OH	Phenol	H_2O	
1	284.6	531.2	533.0	–	–	[7]
2	285.0	531.4	532.9	–	–	[8]
3	285.0	530.7	532.5	–	533.1	[9]
4	284.5	531.1	532.0	533.4	534.7	[10]

The advantages of studying GO using the O $1s_{1/2}$ spectra is clearly shown by the two XPS spectra in Fig. 3.1. In this characterization, GO was mixed with 0.10M of NaOH at a volume ratio of 3:1 and the mixture was dispersed onto a cleaned glass substrate. The original sample was then cut in two and these smaller samples were subsequently subject to heat treatment at 573 K for either one or 15 hours in a nitrogen filled glove box before XPS characterization.

No obvious changes in the composition of GO can be seen in the C $1s_{1/2}$ spectra besides the 15 % increase in area of the peak that occurred at 291.4 eV, which is commonly attributed to the $\pi \rightarrow \pi^*$ transition[10,17,18]. This transition is a plasmon peak that occurs in graphene and it points to there being more π-bonds forming between the carbon atoms as a result of the longer heating time. The peak representing C=C & C–C bonded carbon atoms in the C $1s_{1/2}$ spectra contributed to over 60 % of the area in the spectra and this had the effect of drowning out information contributed by the other peaks.

Put in quantitative terms, the carbon atoms bound to an oxygen functional group constituted 40 % of the area in this C $1s_{1/2}$ spectrum and a 10 % change in the contribution from any of the functional groups translated into a 4 % change in the area of the peak. This 10 % change would have been reflected as a 10 % change

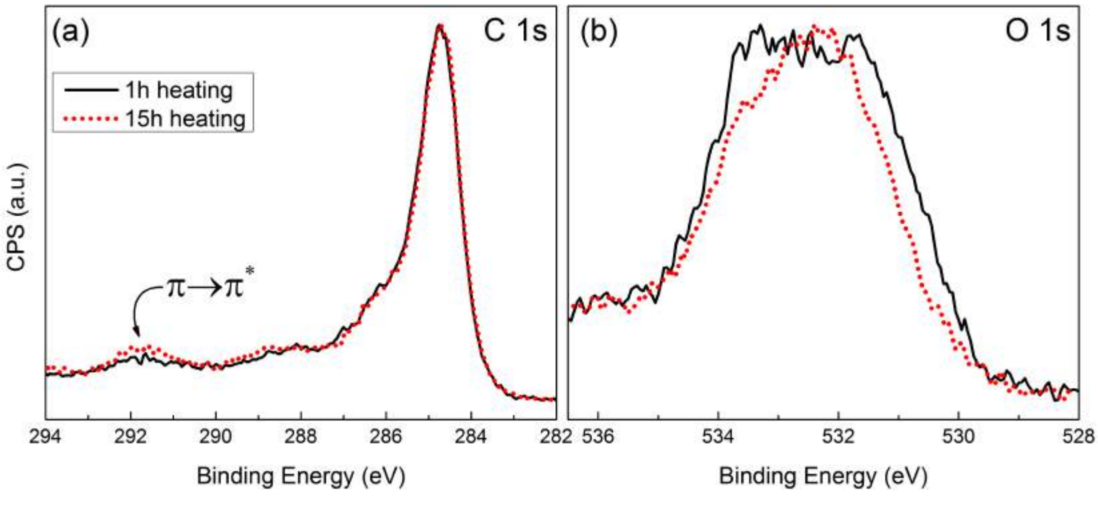

Figure 3.1: XPS spectra of the a) C $1s_{1/2}$ and b) O $1s_{1/2}$ electrons in GO mixed with NaOH after heating in a nitrogen environment at 573 K for one hour (black solid line) or 15 hours (red dotted line). While the change in the overall shape of the spectra is not clear from the C $1s_{1/2}$ data, the O $1s_{1/2}$ spectra clearly show that a chemical reaction had occurred in the mixture.

in the area of the O $1s_{1/2}$ spectra and, in this case, using the C $1s_{1/2}$ spectrum effectively reduces the signal strength by 2.5×. Furthermore, this scaling factor is expected to grow larger as the GO material is further reduced.

At higher carbon to oxygen ratios, the C=C & C–C contribution to the area of the spectrum can increase to over 90 % and in these cases, a further 10 % change in the concentration of a oxygen functional group is still a 10 % change in the O $1s_{1/2}$ spectrum, but in terms of carbon atoms bound to an oxygen functional group, this is a 1 % change in the total area of the C $1s_{1/2}$ spectrum[10,13]. Effectively, the high area C=C & C–C peak causes a reduction in the sensitivity of the characterization to changes in the composition of oxygen functional groups in GO and an associated decrease in confidence of the quantitative analysis results.

Looking at the O $1s_{1/2}$ spectra of the same samples and with reference to the binding energies shown in Table 3.2, two points become apparent:

i. There is a change in the composition of the oxygen functional groups on GO as a result of the extended heating time
ii. Contrary to the reports, two peaks are insufficient to represent all the functional groups present in GO

The first point serves to reiterate the limitations imposed by an analysis that relies solely on the C $1s_{1/2}$ spectra and the second point shows the gap in knowledge that needs to be bridged. Clearly, there are benefits to studying the O $1s_{1/2}$ spectra when trying to determine the composition of functional groups in GO.

Using the O $1s_{1/2}$ spectra, even without peak fitting, it is possible to deduce that either the FWHM of the peaks had been reduced or that the concentration of at least two functional groups in GO had been reduced. Here, because every electron excitation and subsequent detection event that contributed to the spectra had its origin from an oxygen functional group residing on the basal plane of the GO material, there was no high area peak contribution to drown out the information signal that the functional groups were providing.

Coming to the next point, more than two peaks were required to fit the O $1s_{1/2}$ spectrum. If only two peaks were used to fit the spectrum, as suggested by Mattevi *et al.* & You *et al.*, no good fit could be achieved[7,8].

The samples differed only in the amount of time that they were heated in a nitrogen environment and all other conditions, such as the substrate used, the deposition conditions and the characterization conditions were kept exactly the same. Additionally the FWHM in an XPS characterization is only affected by conditions such as the lifetime of the core hole, natural FWHM of the exciting photons, the instrument settings and surface charging and these were kept the same for both samples. As such, the FWHM of the peaks in both the samples was also expected to be the similar if not the same.

A better explanation would require the use of three or more peaks and the resulting O $1s_{1/2}$ spectrum fit by changing the areas of these peaks. Besides the observational inferences, this suggestion is further supported by the two reports in Table 3.1 which listed distinct binding energies values for C $1s_{1/2}$ electrons in carbon atoms chemically bound to four different oxygen functional groups[10,16]. While findings on the C $1s_{1/2}$ spectra are not directly transferable to the O $1s_{1/2}$ spectra, there is sufficient evidence thus far to conclude that at least three peaks should be used to fit the O $1s_{1/2}$ spectra of GO.

This result clearly demonstrates the limitations inherent in an analysis of the C $1s_{1/2}$ spectrum of GO and the current deficiency of information regarding the O $1s_{1/2}$ spectra of the same. While the C $1s_{1/2}$ spectrum is still an important characterization result as it gives holistic information about the GO material, this analysis is not as sensitive to changes in the composition of the oxygen functional groups as an O $1s_{1/2}$ analysis. Only an analysis of the O $1s_{1/2}$ spectrum can give this information and it is unfortunate that XPS characterization of this spectrum is still lacking. This gap in characterization knowledge will become especially important if the use of GO requires control over the type of functional groups present or when the carbon to oxygen ratio becomes exceptionally high.

This problem can be approached by first understanding the areas where understanding is lacking. Besides the difference in reported binding energy values for O $1s_{1/2}$ electrons in different functional groups, by comparing the reports in Table 3.2 it is also found that:

1. **The combined C–OH & C–O–C peak does not adequately describe the GO system**

   Only one peak is used to represent the O $1s_{1/2}$ electron from these functional groups and as a result, either the binding energy of this peak is seen to either shift significantly or the FWHM vary dramatically during reduction[9,10].

2. **Different photon energies were used to excite the samples**
   While most of the reports in Table 3.2 used an excitation photon with an energy of 1486.7 eV, Mattevi *et al.* used a 1253.6 eV photon to excite the sample and this introduces some uncertainty when comparing results[7–10].
3. **A correct binding energy value for oxygen in water is needed**
   The peak representing electrons from trapped water molecules in GO only occurs in two of the reports and Ganguly *et al.* showed that the water molecules had escaped at temperatures below 473 K while Akhavan reported its presence in the sample at temperatures as high as 773 K[9,10]. It would be very helpful for characterizations if this discrepancy could be resolved.

3.1.2 Influence of Oxidative Debris (OD)

The presence of foreign materials in samples is frustrates XPS characterizations and despite being a heavily studied material new foreign materials continue to be found in aqueous GO. The most recent addition was made by Yeh *et al.* who found that trace quantities of aluminium from the filtration process remained in the GO solution and this served to stabilize the GO sheets in an aqueous suspension[19]. Before this, in 2011, Rourke *et al.* made known the presence of OD in aqueous GO and isolated the material from normal GO sheets[20]. Since then, OD has been found to be responsible for electroactivity, fluorescence and chemical activity in GO, while impeding catalytic activity[11,21–23]. However, the effect that OD has on XPS characterization had not been explored sufficiently.

OD is a carbon-rich material known to contain carboxyl, hydroxyl and epoxide groups and it decomposes from the as-deposited sample when the temperature of the sample is raised above 473 K[20]. While the functional groups in OD are expected to be the same functional groups that occur on GO, it is not known if the O $1s_{1/2}$ electrons from these functional groups in OD have the same binding energies and this creates difficulties during the assignment of functional groups to peaks during analysis of the XPS spectra. Crucially, the C $1s_{1/2}$ spectra shown in the reports revealed that besides its lower decomposition temperature, OD was expected to be chemically similar to GO and this information has to be consider when making any analysis of the XPS spectra[20,24].

As such, the difficulties in harmonizing the understanding of O $1s_{1/2}$ binding energies that were summarized at the end of Section 3.1 may be influenced by the presence of OD and this means that OD should be removed prior to any characterization work. To check for the presence of OD in the GO samples used, a sample of aqueous GO was dried and the dried film subject to TGA. The thermogram of this sample is shown in Fig. 3.2 and like the GO sample of Rourke *et al.*, the rate of mass loss is greatest at ~473 K, corresponding to the decomposition of OD. Additionally, it was noted that in both this sample and that of Rourke *et al.*, the decomposition temperature of OD occurred within the temperature range of exfoliation as described by You *et al.* This would mean that it is decomposition of OD and not the functional groups, as previously thought, that is responsible for exfoliation in GO. Finally, You *et al.* observed a 50 % loss in mass in the sample after it had been heated to 673 K and this was similar to the 51.7 % mass loss at 673 K in this sample[8].

Since OD is a by product of the oxidation process that turns graphite into GO, the type of OD produced would depend on the method of oxidation. It was shown that the decomposition temperature of OD in GO made by the Hummer's method differed from that of OD in GO produced by Brodie's method[25]. In fact,

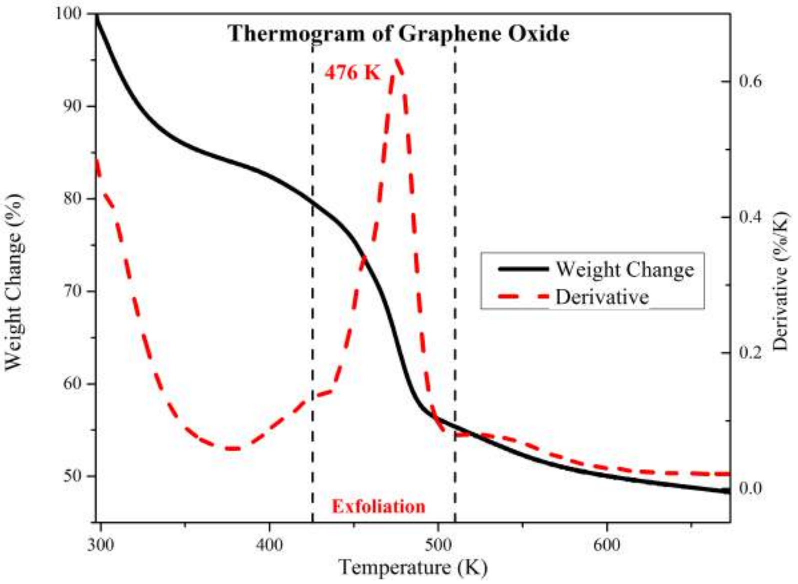

Figure 3.2: Thermogram of GO heated from room temperature to 673 K showing that the rate of mass loss is the greatest at 476 K. The temperature range for exfoliation as described by You *et al.*is highlighted between the dotted lines.

OD in GO made by the Brodie's method has a higher decomposition temperature than OD in GO made by the Hummer's method[25]. This is in line with the higher exfoliation temperature of OD in GO made by the Brodie's method and this shows once again, that the exfoliation effect in GO is very likely due to the decomposition of OD[8]. With this confirmed, an experiment was designed to exclude the effects of OD on the O $1s_{1/2}$ spectra while attempting to identify the binding energy values for these electrons from the various functional groups present in GO.

3.1.3 Identification of Oxygen Functional Groups

A reference XPS characterization of GO was first made with the GO material on a conductive metallic substrate and the spectrum is shown in Fig. 3.3. The spectrum showed the characteristic two hump feature of the C $1s_{1/2}$ spectrum of as deposited GO with a peak to peak separation of about 2.0 eV. Considerations made when performing this characterization were:

1. The effect of surface charging
   GO is an insulator and a thin sample deposited onto a conductive substrate could allow distortion of the spectra due to surface charging to be avoided.
2. Influence of substrate on sample
   Since a thin sample was used, the resulting spectra could reflect substrate induced effect
3. Occurrence of oxygen on conductive substrate
   Natural oxidation will occur on the surface of the metals and electrons from these oxygen atoms may turn up in the O $1s_{1/2}$ spectra, especially since a thin GO sample was used

Additionally, the possibility of secondary chemical shift due to the oxygenation, or lack thereof, of neighbouring carbon atoms was also considered[26]. However, it was unclear if these oxygen atoms, which were attached to a next-next neighbour carbon atom, would have an observable influence on these binding energies.

While the exact binding energy values from this sample would not be useful, this spectrum could be used to confirm the qualitative effects that occur on GO in the next experiment.

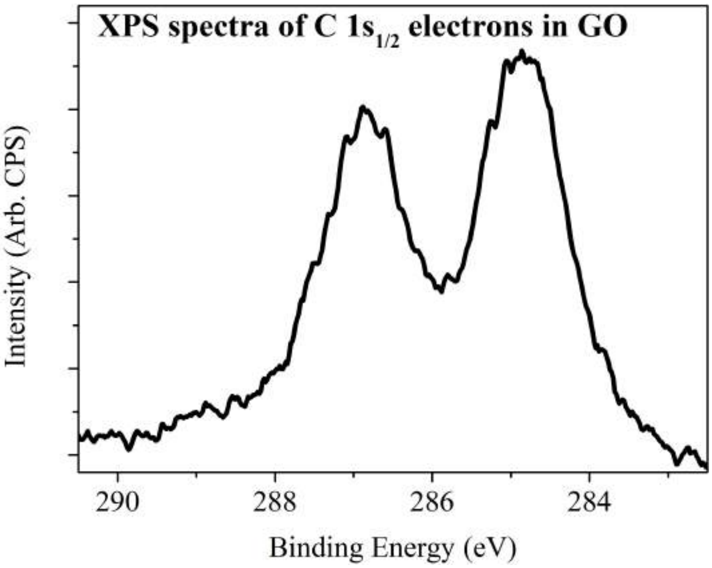

Figure 3.3: XPS spectra of the C $1s_{1/2}$ electrons in a sample of GO on a conductive substrate, showing the characteristic double hump feature of GO.

Following this, an in-situ XPS characterization experiment was performed on another thin sample of as deposited GO. The sample was ~20 nm thick, and subjected to heating at multiple temperature steps between 473 and 573 K. The deposited film was first introduced into the XPS chamber held at an ultra high vacuum, $<8\times10^{-9}$ Torr, and the experimental steps involved in each characterization measurement were as follows:

i. The temperature of the sample holder ensemble was raised to 473 K.
ii. This temperature was held constant for 15 minutes to allow OD removal and chemical reactions to occur before the heat source was disconnected.
iii. XPS characterization data for the C $1s_{1/2}$ and O $1s_{1/2}$ spectra were acquired.
iv. The heat source was reconnected and the temperature of the ensemble increased to the next specified temperature.
v. The sample holder ensemble was held at the new constant temperature for a total of 15 minutes.
vi. The process is repeated, beginning from step (iii) for the following temperatures: 493, 513, 543, 561 and 573 K.

The XPS spectra from this experiment are shown in Fig. 3.4, where the spectra are arranged such that the highest heating temperature corresponds with the topmost, orange coloured spectrum and the lowest heating temperature is the bottommost black coloured spectrum. The C $1s_{1/2}$ spectra was used both as a method of verification for the findings in the O $1s_{1/2}$ spectra and as a reference spectra to correct for any charging effects that might occur in the samples. Here the electrons in sp^2 hybridized carbon atoms in a C=C or C–C bond were corrected to a binding energy of 284.7 eV.

The C $1s_{1/2}$ spectra were first analysed by the method of peak fitting using peaks at 284.7, 285.6, 286.3, 288.2 and 288.8 eV, corresponding to the C=C/C–C, C-OH, C–O–C, C=O and COOH groups respectively; fitting details are shown in Table 3.3 on page 92. It was assumed that the FWHMs would be similar for all the peaks in the same spectra and as shown, the FWHM of most peaks varied by no more than ±0.1 eV. Unsurprisingly, after correcting for the C=C/C–C binding energy, the binding energy values shown here were close to those reported by Ganguly *et al.* and Akhavan; see reference numbers 3 & 4 in Table 3.1[9,10].

With the increase in temperature from 473 to 573 K, the peaks were broadened and a slight shift in the main peak feature towards lower binding energies was observable in the C $1s_{1/2}$ spectra. This indicated a reduction in the number of carbon-oxygen bonds and an increase in the number of C=C & C–C bonds in the sample. Additionally, the difference between the C $1s_{1/2}$ spectrum in Fig. 3.3 and the highly similar C $1s_{1/2}$ spectra between 473 and 543 K in Fig. 3.4, confirms that most of the OD had been removed in the first heating step.

The C-O-C and C-OH peaks are discussed in this section while the C=O and CO*OH peaks are discussed in the following one, along with GO metastability.

3.1.3.1 By Analysis of the O $1s_{1/2}$ Spectra

With these confirmations, it could be confidently concluded that the O $1s_{1/2}$ spectra in Fig. 3.4(b) was a reflection of only the oxygen atoms in GO and that any changes in the spectra could be directly attributed to changes in the GO material. From the series of C $1s_{1/2}$ spectra, it was observed that increasing the temperature of the system resulted in a reduction in area of peaks from electrons with higher binding energies. These peaks corresponded to carbon atoms bound to oxygen atoms and while it could be concluded that there was a decrease in concentration of these bonds, the actual changes are more clearly observable in the O $1s_{1/2}$ spectra. Furthermore, from the O $1s_{1/2}$ spectra, it was observed that

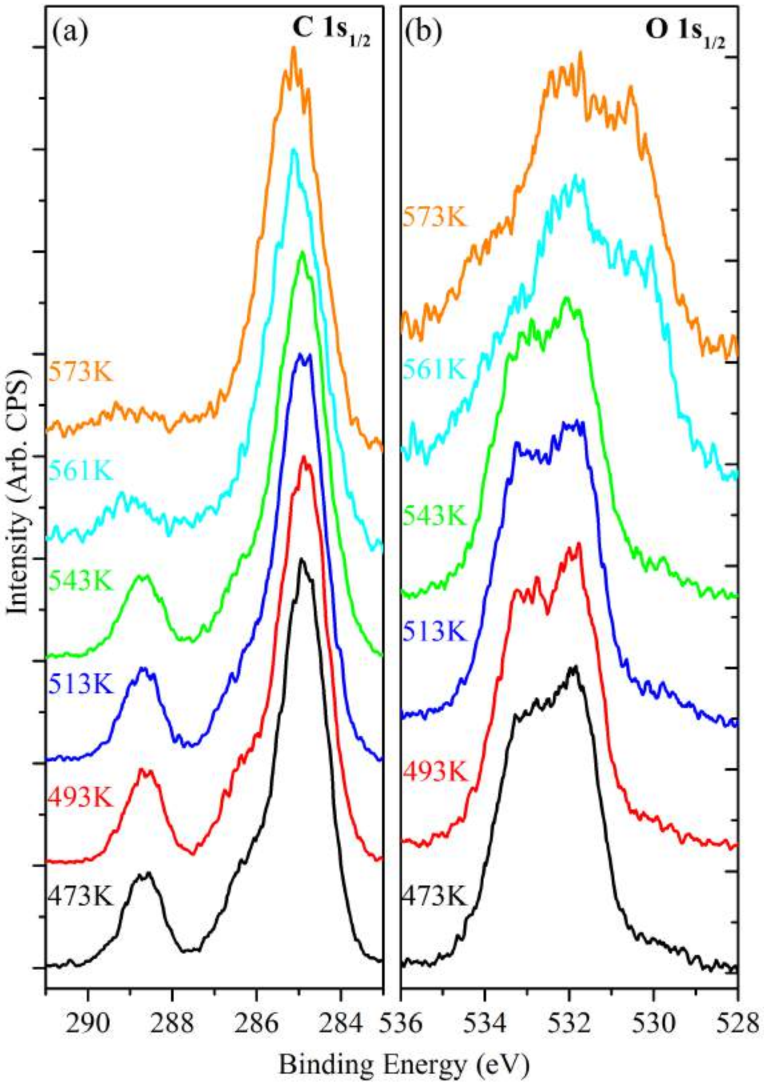

Figure 3.4: XPS spectra of the (a) C $1s_{1/2}$ and (b) O $1s_{1/2}$ electrons in GO that was heated in a vacuum at various temperatures. Spectra are corrected according to the C $1s_{1/2}$ electrons in sp^2 hybridized carbon atoms in either a C=C or C–C bond and have a binding energy values of 284.7 eV. While the reduction in area of peaks representing oxygen bound carbon atom is observable in the C $1s_{1/2}$ spectra, the details of these changes are clearer in the O $1s_{1/2}$ spectra.

the changes to the peak shape were not obvious without peak analysis between 473 and 543 K. However, this changed between 544 and 560 K and a majority of the O $1s_{1/2}$ electrons with higher binding energies were removed, leaving behind a large proportion of oxygen groups with lower O $1s_{1/2}$ electron binding energies. The peaks were assigned to functional groups according to the Lerf-Klinowski and Ajayan models in which up to five oxygen containing functional groups were expected[13,27]. These are the hydroxyl, epoxy, carbonyl, carboxyl and lactol functional groups and if each of the oxygen atoms in this list had a unique O $1s_{1/2}$ electron binding energy value up to seven peaks were expected; as carboxyls and lactols have two oxygen atoms each. However, a visual inspection of the O $1s_{1/2}$ spectra in Fig. 3.4 suggests that four peaks were sufficient to give a good fit.
Considering first the 473 K spectrum, at least three peaks would be required to fit this spectrum, one low area peak at the low binding energy region and two high area peaks to make up the main peak. Tracing these peaks vertically upwards on the page, towards higher heating temperatures, the appearance of a fourth peak at the low binding energy region, between the main peak and the first low area peak becomes evident. The emergence of this peak becomes clear in the fitted spectra shown in Fig. 3.5 and the the fitting details of these spectra and all intermediate spectra are show in in Table 3.3.

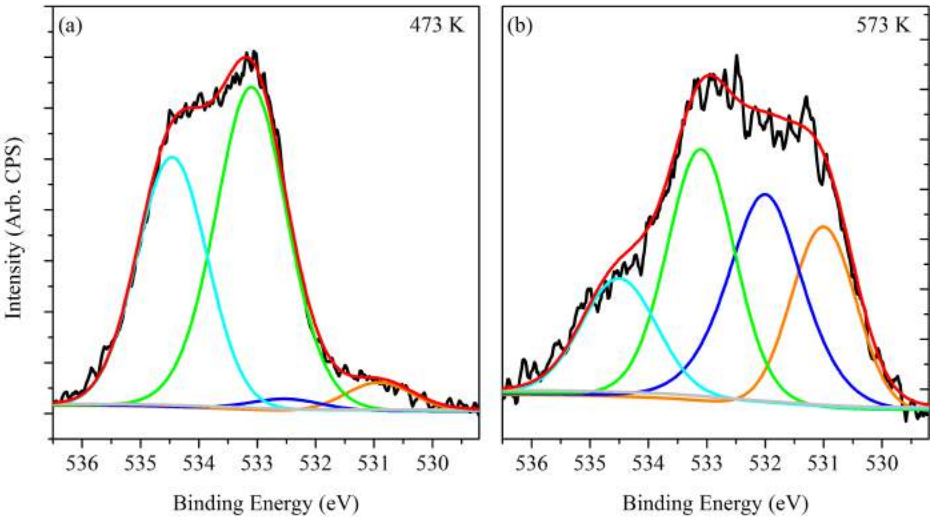

Figure 3.5: XPS spectra of GO heated at (a) 473 and (b) 573 K with peak fitting; fitting details are shown in Table 3.3. The two low binding energy peaks are not prominent in the 473 K spectrum but emerge in the 573 K spectrum.

Table 3.3: Fitting details of the C $1s_{1/2}$ and O $1s_{1/2}$ spectra in Fig. 3.4 and 3.5. The O in (CO)OH is the oxygen with a double bond to the carbon atom and all the spectra fit such that $\chi^2 < 1$.

		C $1s_{1/2}$			**O $1s_{1/2}$**		
Temp. / K	**Functional Group**	**B.E. / eV**	**FWHM**	**%Area**	**B.E. / eV**	**FWHM**	**%Area**
473	C=O	288.2	1.2	7.1	530.9	1.4	4.4
	(CO)OH	288.9	1.2	8.8	532.4	1.4	1.8
	C–OH	285.6	1.2	10.5	533.1	1.4	53.9
	C–O–C	286.3	1.2	11.4	534.5	1.4	39.9
	C=C/C–C	284.7	1.2	62.3			
493	C=O	288.2	1.1	6.8	531.0	1.3	3.3
	(CO)OH	288.9	1.1	7.1	532.3	1.4	4.3
	C–OH	285.5	1.1	12.6	533.1	1.4	49.9
	C–O–C	286.4	1.2	10.6	534.4	1.4	42.5
	C=C/C–C	284.7	1.2	62.9			
513	C=O	288.3	1.1	6.9	531.0	1.4	5.4
	(CO)OH	288.7	1.1	7.2	532.3	1.5	0.1
	C–OH	285.7	1.3	8.6	533.1	1.4	47.9
	C–O–C	286.3	1.2	9.8	534.5	1.5	46.6
	C=C/C–C	284.7	1.2	67.6			
543	C=O	288.2	1.2	8.1	530.8	1.3	4.6
	(CO)OH	288.9	1.2	6.4	532.3	1.4	8.5
	C–OH	285.7	1.4	5.7	533.1	1.5	48.8
	C–O–C	286.2	1.2	9.9	534.4	1.4	38.0
	C=C/C–C	284.7	1.3	69.8			
561	C=O	288.2	1.5	3.6	530.9	1.4	27.0
	(CO)OH	288.8	1.4	5.5	532.3	1.5	31.3
	C–OH	285.7	1.4	5.6	533.1	1.5	24.6
	C–O–C	286.3	1.5	6.5	534.5	1.5	17.1
	C=C/C–C	284.7	1.5	78.9			
573	C=O	288.1	1.5	2.2	531.0	1.3	23.0
	(CO)OH	288.9	1.5	5.2	532.3	1.5	30.7
	C–OH	285.6	1.4	7.2	533.1	1.4	31.1
	C–O–C	286.3	1.5	5.1	534.4	1.5	15.1
	C=C/C–C	284.7	1.5	80.3			
Expected Value ±0.1	C=O	288.2	–	–	530.9	–	–
	(CO)OH	288.8	–	–	532.3	–	–
	C–OH	285.6	–	–	533.1	–	–
	C–O–C	286.3	–	–	534.4	–	–
	C=C/C–C	284.7	–	–			

Comparing the change in %Area of the functional groups in the C $1s_{1/2}$ and O $1s_{1/2}$ spectra, a correlation between the relative changes in areas is observed. From the C $1s_{1/2}$ spectra, carbon atoms singly-bound to oxygen atoms were initially present in higher concentrations and this fell to concentration levels that were similar to those of the carbon atoms doubly-bound to oxygen atoms. A similar observation can be made from the O $1s_{1/2}$ where the much higher concentration of oxygen atoms singly bound to carbon fell to concentration levels that were comparable to that of oxygen atoms doubly-bound to carbon. However, as mentioned earlier, the high area C=C & C–C peak present in the C $1s_{1/2}$ spectra makes the quantitative analysis of the oxygen functional groups present less reliable than a quantitative analysis of the same groups from the O $1s_{1/2}$ spectra.

The assignment of functional groups to O $1s_{1/2}$ peaks are similar to those by Ganguly *et al.* and Akhavan, with peaks having lower binding energies being assigned to carboxyl and carbonyl groups and peaks having higher binding energies assigned to epoxy and hydroxyl groups[9,10]. However, they differ in that each broader peak was separated into two peaks with smaller FWHMs.

This assignment is supported by the report by Susi *et al.*who showed that these broad peaks could be separated into two narrower peaks. Accordingly, the peaks with binding energies of 530.9, 532.3, 533.1 and 534.4 eV were assigned to the O $1s_{1/2}$ electrons from carbonyl, carboxyl, hydroxyl and epoxy groups respectively. The influence of oxygenation on neighbouring carbons, mentioned on page 87 was not observable in these characterization.

In their theoretical calculations, Susi *et al.* have shown that O $1s_{1/2}$ electrons in[1]:

i. the C=O group always have the lowest binding energy
ii. the C=O group in carbonyls and carboxyls have different binding energies
iii. the OH group in carboxyls and hydroxyls have similar binding energies
iv. the epoxide and hydroxyl groups have the same binding energy in pristine graphene and have different binding energies in non-pristine graphene,
v. the epoxide peak has the highest binding energy if separable from the hydroxyl peak
vi. the epoxide peak has a binding energy that is 1.99 eV higher in non-pristine graphene than in pristine graphene

Additionally, Hossain *et al.* have assigned a binding energy of 531.9 eV for electrons originating from the O $1s_{1/2}$ orbital in an oxygen atom bound to pristine graphene in an epoxy and used a C $1s_{1/2}$ binding energy of 284.5 eV for electrons originating from sp^2 hybridised carbon atoms[28]. Using this value, correcting for the difference in C $1s_{1/2}$ binding energy values used* and the increase in binding energy due to the non-pristine nature of GO, the expected binding energy value of the O $1s_{1/2}$ peak from C–O–C in GO was 534.1 eV; this was within 0.3 eV of the value shown in Table 3.3.

Furthermore, Hossain *et al.* also reported the presence of two low intensity peaks at 530.8 and 533.4 eV, values very similar to those shown in Table 3.3. This is important as it is very likely that these electrons originated from the O $1s_{1/2}$ orbitals of oxygen atoms in functional groups situated on the edge of the graphene flake. Carbon atoms at edge sites are equivalent to carbon atoms next to vacancy sites and the similarities between the binding energies found by Hossain *et al.* and those found here are hardly surprising.

From the experimental conditions described in their report, it can be deduced that the low intensity spectral lines represented functional groups that contained only oxygen, namely epoxides and carbonyls. Following the convention that O $1s_{1/2}$ electrons in oxygen atoms that form double bonds with carbon atoms have lower binding energies than the same electrons in oxygen atoms that form single bonds with carbon atoms, carbonyls should be assigned to the peak at 530.9 eV and epoxides should be assigned to the peak at 534.4 eV. This echoed the findings of this report and provides yet more proof that the peaks were assigned correctly.

While no information is available about the O $1s_{1/2}$ electrons in the lactol groups of GO, it is dimensionally similar to a carboxyl group and the O $1s_{1/2}$ electrons originating from this group were assumed to have similar binding energies as those from carboxyl groups[13]. As such, the contribution from lactols to the O $1s_{1/2}$ spectra is expected to overlap with the contributions to the spectra by the carboxyl groups for the purpose of this discussion.

In this section it was shown that a minimum of four peaks were required to fit the O $1s_{1/2}$ spectra of GO and these peaks were uniquely assigned to functional groups in GO. In the following sections, the these assignments will be thoroughly analysed by means of mathematical analysis and experimental methods.

---

* The binding energy of the C $1s_{1/2}$ electrons in sp^2 hybridised carbon atoms in C=C and C–C bonds is set to 284.7 eV in this thesis.

3.1.3.2 By Quantitative Analysis

The analysis begins with a theoretical model GO based upon the Lerf-Klinowski model[27]. This model is a defect free, square flake of graphene, with sides of length 300 nm and a C–C bond length similar to that of graphite at 1.42 Å[29]. The graphene flake will have armchair edge sites along two sides and zig-zag edge sites perpendicular to these armchair edge sites and this sample has an estimated 1.05×10^4 edge sites and 6.87×10^6 basal plane sites. Accordingly, the GO flake is built with epoxides and hydroxyls on the basal plane and on the edge of this flake, while in addition to these two functional groups, carbonyls and carboxyls are allowed on the edge of the flake as well.

From this calculation, it is estimated that 0.15 % of all available reactive sites are edge states with each site having an equal possibility of being a:

i. sp^2 hybridized carbon in a graphene-like ring,
ii. sp^3 hybridized carbon in an epoxide or hydroxyl or
iii. sp^2 hybridized carbon in a carbonyl or carboxyl.

Taking the average, it is estimated that 33 % of all edge sites are sp^2 hybridized carbon in a carbonyl or carboxyl. The hydroxyls, epoxies and carbonyls contribute one oxygen atom per functional group, but the epoxy group is unique as it takes up two binding sites per bound oxygen atom. Also, while the carboxyl group contributes two oxygen atoms per functional group, it also opens the hexagonal carbon ring, creating a bonding site for a carbonyl in the process. Since the average was taken in this theoretical model, it is also assumed, for simplicity, that these effects of carboxyls and epoxy groups on the number of binding sites on the edge of the flake cancel each other out.

Typically, unreduced GO has a C/O ratio of 2.0, meaning that there is one oxygen atom to every two carbon atoms in the flake and with 0.05 % of the binding sites reserved for carbonyls and carboxyls, the calculation allowed no more than 0.10 % of the oxygen atoms to be bound to the flake as carbonyls and carboxyls; this calculated concentration is far lower than any carboxyl and carbonyl concentrations reported[7,10]. As such, the prediction shows that there should initially be an appreciable concentration of carboxyls and carbonyls in GO on the graphene basal plane. A large concentration of vacancies on the basal plane will need to be created to accommodate this and, in turn, this ensures that hydroxyls and epoxies will occur near a vacancy site on the basal plane. This means that the binding energies of electrons from the O $1s_{1/2}$ orbitals of these functional groups will be separable as calculated by Susi *et al.*[1]

The change in C/O ratio with respect to temperature was calculated by taking the ratio of the areas of the spectra in Fig. 3.6 after scaling them according to the appropriate sensitivity factors[5]. The sample at 473 K had a C/O ratio of 3.35 and the carbonyl and carboxyl groups on the edge of the sheets were calculated to represent up to 0.15 % of the oxygen atoms present. However, this is still insufficient to account for the ~6 % presence of carbonyls and carboxyls shown in the O $1s_{1/2}$ peak fitting data of Table 3.3. This meant that the higher proportion of carbonyls and carboxyls could only be accounted for by considering (i) irregular flake shapes and (ii) the presence of vacancies on the basal plane.

Firstly, due to the fact that flakes are of arbitrary shapes and sizes, the surface to edge ratio in real GO can exceed 0.15 %. As shown in Fig. 3.7, a smaller square flakes of side 100 nm can have up to 0.46 % of sites as edge sites and this, coupled with an arbitrary concave edge shapes, can increase the number of edge sites available for carbonyl and carboxyl groups slightly. Secondly and more significantly, the creation of vacancies in the basal plane can increase the number of sites available for carbonyls and carboxyls. For each vacancy created, up to 3 carbonyl bonds can be accommodated on the the basal plane and a minimum of 2 % of vacancies would be required in the basal plane to accommodate all the carbonyls and carboxyls.

Next, changes to the composition of the functional groups with increased heating temperature was characterized. These values were previously listed in Table 3.3 and with a starting value of 6.2 % at the a heating temperature of 473 K, the composition of carbonyls and carboxyls present in GO rose gradually to 13.1 % of the O $1s_{1/2}$ spectrum at 543 K. At 561 K, this composition percentage increased dramatically to 49.2 % and a maximum carbonyl and carboxyl composition of 53.7 % was reached at the heating temperature of 573 K. This increase suggested that, besides hydroxyl and epoxide loss, carbonyls and carboxyls were being created in GO during thermal annealing.

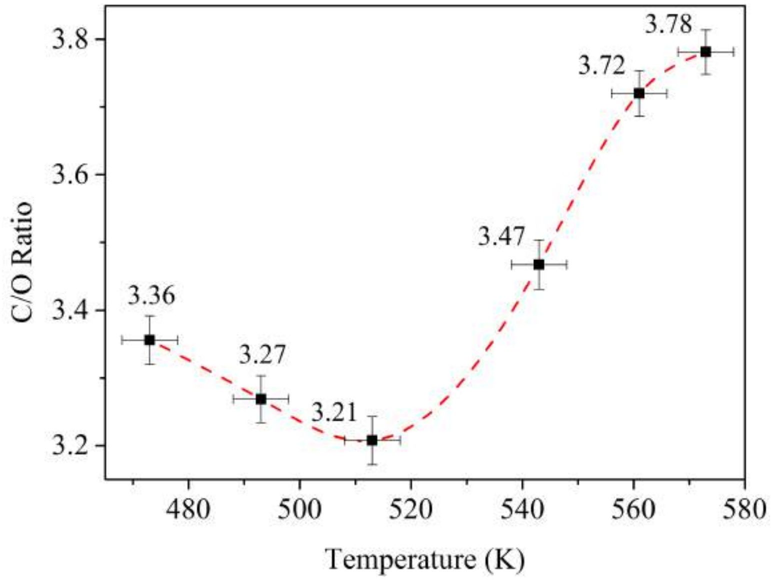

Figure 3.6: Change in C/O ratio of the samples as the temperature increases as calculated from the spectra in Fig. 3.4. The C/O ratio drops initially due to remnant OD removal, however, this stops at about 513 K and oxygen functional group removal dominates.

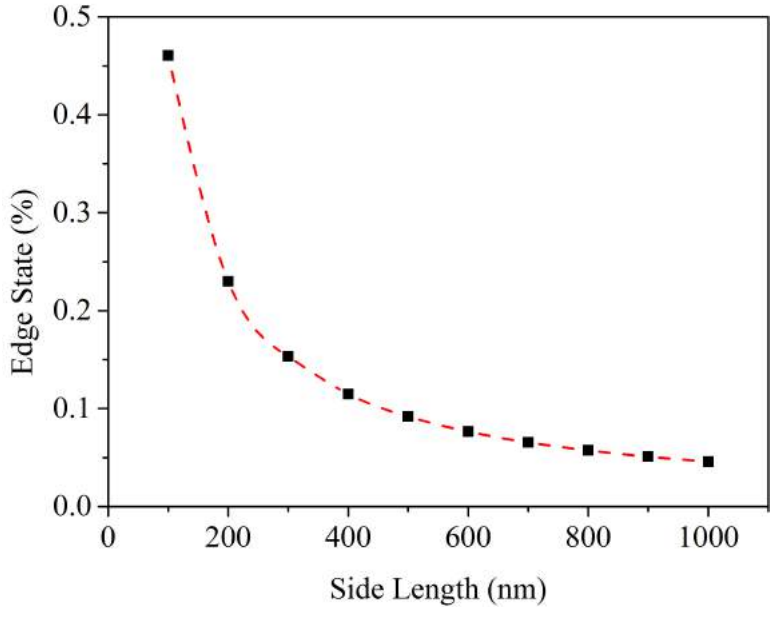

Figure 3.7: Calculated percentage of edge states on square graphene sheets with sides of length 100 to 1000 nm.

This observed increase was confirmed by factoring in the calculated change in the C/O ratio between 510 and 573 K, shown in Fig. 3.6. Within this temperature range the C/O ratio increased from 3.21 to 3.78, an 18 % increase, but in the same time, the proportion of carbonyls and carboxyls in the GO material increased by 831 %. This percentage increase was calculated after taking into account the effect of oxygen functional group loss on the actual number of oxygen atoms present in the sample and is calculated as follows.

Assuming that the number of carbon atoms under study remained constant during the analysis, the increase in the C/O ratio must come from a reduction in the concentration of oxygen functional groups. Using an arbitrary number of 10,000 carbon atoms under analysis, at a temperature of 510 K, the C/O ratio is 3.21 and there are 3115 oxygen atoms in the same area of analysis. Of these, 5.5 % or 171 of the atoms are in a carbonyl or carboxyl bond. As the C/O ratio increased to 3.78 at 573 K, the number of oxygen atoms under study was decreased to 2646, with 53.7 % of these atoms, or 1421 oxygen atoms, bound to carbon as a carbonyl or carboxyl. This then gives the calculated 831 % increase in the carbonyl and carboxyl concentration in the sample.

In this case, because the percentage increase in carbonyl and carboxyl formation far exceeded the increase of the C/O ratio, the increase in composition of carbonyls and carboxyls cannot be solely attributed to hydroxyl and epoxy group removal. It must then be concluded that beginning at a heating temperature of 543 K, the conversion of functional groups on the GO flake to carbonyls and carboxyls was observed.

Before moving further into the analysis, the accuracy of the changes in the C/O ratio were first confirmed by a calculation of the uncertainty of each measurement[30,31]. In these calculations, systematic errors inherent in the determination of C $1s_{1/2}$ and O $1s_{1/2}$ peak intensities were ignored as this would only affect the absolute value of the C/O ratio and any relative error would only carry forward in the calculations[32].

Random errors, on the other hand, would vary from measurement to measurement and affect the accuracy of the characterization. Random errors include the effects of stray magnetic fields, probability of miscounting at high count-rates, also known as electron collection inefficiency as well as the fact that the count rate is a Poisson distribution. While the effect of stray magnetic fields is easily managed by good construction and design of the setup, random errors due to electron collection inefficiency and random errors due to the distribution cannot be avoided[32].

The uncertainty due to these random fluctuations (σ_{RF}) was calculated as the square root of the square sum of electron collection inefficiency and counting errors[32]:

$$\sigma_{RF} = \sqrt{\sigma_{CE}^2 + \sigma_{RE}^2} \tag{3.1}$$

with σ_{CE} & σ_{RE} defined as follows.

The equation of electron collection inefficiency (σ_{CE}) is:

$$\sigma_{CE} = 1 - \frac{N}{N_0} = N\tau/D, \tag{3.2}$$

where D is the number of channels in the detector (7 channels), τ is the pulse width of the electron detection event (< 200 ns), N_0 is the true count rate and N is the measured count-rate (~15 kcps).

Counting errors (σ_{RE}) are calculated by:

$$\frac{1}{\sigma_{RE}} = \frac{1}{\chi_C^2}\left[\frac{I_C}{\sigma_{I_C}}\right]^2 + \frac{1}{\chi_O^2}\left[\frac{I_O}{\sigma_{I_O}}\right]^2 \tag{3.3}$$

where the subscripts C and O represent carbon and oxygen respectively. Representing these element with 'i', the remaining symbols are χ_i, the fractional composition of the element in the sample – calculated from the C/O ratio, I_i, the area of the spectrum and σ_{I_i}, the standard deviation of the peak areas of each element, calculated by use of Monte Carlo simulation implemented in CasaXPS[33].

Typical values for σ_{CE} & σ_{RE} were 0.05 % & 0.73 % respectively and this gave a σ_{RF} of 0.74 %. Between 473 and 510 K, the C/O ratio fell by 4.5 % and up to a heating temperature of 573 K, the C/O ratio rose by 12.5 %; these changes were much larger than the uncertainty attributed to random fluctuations and this confirmed the validity of the observed changes in the C/O ratio.

3.1.3.3 By Chemical Reactions

Thermogravimetric Analysis

To better understand these changes, the C/O ratio was compared against the TGA thermogram of GO which is shown in Fig. 3.8. The GO material in this batch had a typical C/O ratio of 1.8 and as seen in Fig. 3.6, this increased to 3.36 at 473 K. Subsequently, the C/O ratio decreased to a minimum of 3.2 at 513 K before reaching a maximum of 3.8 at the final measurement temperature of 573 K. As seen in the thermogram, the temperatures of 425, 510 and 545 K mark the starting temperatures of three regions of interest on the differential curve and these temperatures correspond to a change in chemical activity in the sample.

As marked in Fig. 3.8, the exfoliation region from 425 to 510 K overlaps with the region of falling C/O ratio in Fig. 3.6, while carboxyl formation occurred after 543 K, correlating with a change in the mass loss regime on the thermogram. Despite the differences in samples and characterization techniques, the observed similarities in temperature region helps to validate the importance of these observations.

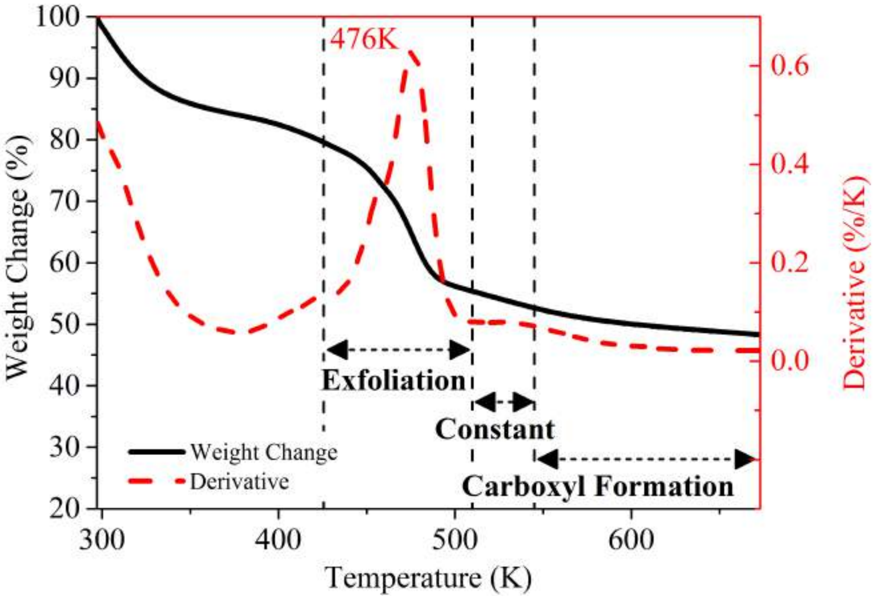

Figure 3.8: Thermogram of GO with the differential peak occurring at 476 k. The exfoliation region labelled as You *et al.* have described in their report, while the carboxylation region is assigned based on the analysis in Chapter 3.1.3.2.

Verification of O $1s_{1/2}$ peaks

Since it was already known from Table 3.2 that O $1s_{1/2}$ electrons in C–O bonds had higher binding energies, $\geq$532.0 eV, than in C=O bonds, $\leq$532.0 eV, identification of each functional group could be achieved by selectively removing one of the two peaks present within each envelope. In this section, one of the C–O bonds will be selectively removed to prove the presence of that functional group in GO while the C=O bonds will be separated by a different technique discussed later in Chapter 3.2.3.

A list of chemicals with the expected reactions between itself and GO is shown in Table 3.4 and in most cases, the chemicals were mixed with GO prior to deposition. The samples would subsequently be heated for varying lengths of time at either 483 or 573 K before characterization by XPS. In the case of 3-aminopropyltriethoxysilane (APTES), which came as a liquid, GO samples were thermally annealed before immersion in a bath of APTES that was maintained at 353 K for 2h.

In the first experiment, NaOH was added to GO to a concentration of 0.10M and two samples were made from this mixture. The first sample was heated at 483 K and the second sample at 573 K in a nitrogen environment for one hour. The samples were then characterized by XPS and the resulting O $1s_{1/2}$ spectra shown in Fig. 3.9. As expected, there is a reduction in the area of the peak with the highest binding energy in the sample heated at 483 K and the complete removal of this peak in the sample heated at 573 K, signalling that the C–O–C ring had opened and there was a reduction in the quantity of these bonds in the sample.

Table 3.4: Chemicals and the expected reactions with functional groups on GO.

Chemical	Expected Reaction	Ref.
NaOH	C–O–C ring opening to give either ionic oxygen or C–OH	[34,35]
APTES	Removal of oxygen from C–O–C	[36]
NaCl	Unknown, but likely similar to NH_4Cl	–
NH_4Cl	Unknown, but likely similar to NaCl	–

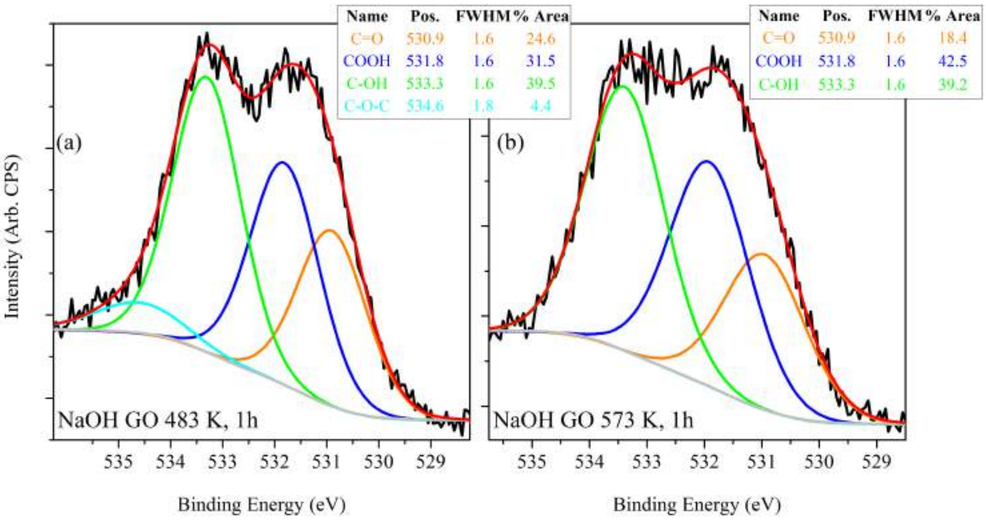

Figure 3.9: O $1s_{1/2}$ spectra of GO mixed with NaOH at a concentration of 0.10M and heated for one hour in a nitrogen environment at either (a) 483 or (b) 573 K. The C/O ratios of these samples were 4.41 and 4.95 respectively.

The experiment was repeated at higher NaOH concentrations and with longer heating times. In this experiment, NaOH was mixed into the GO solution at concentrations of either 0.10 or 0.20 M and the samples were heated in a nitrogen environment for 15 hours at either 483 or 573 K. The XPS characterization of the O $1s_{1/2}$ electrons from these samples are shown in Fig. 3.10.

Comparing the spectra in Fig. 3.9 & 3.10, in all cases, doubling the concentration of NaOH in the solution and increasing the heating time from one to 15 hours had no effect on the C–O–C functional group removal in GO when heated at 483 K. It is possible that NaOH acts as a catalyst to remove epoxide bonds or that at 0.10 M of NaOH, the reactant is already in excess and doubling this concentration had no effect on the sample[35]. Additionally, comparing Fig. 3.9(a), Fig. 3.10(a) & (c) increasing the heating time had no effect on the removal of C–O–C and the area of this peak remained between 2.6 and 4.4 % of the total area of the spectra. Interestingly, in all samples that were heated to 573 K in the presence of NaOH (Fig. 3.9(b), Fig. 3.10(b) & (d)), the C–O–C peak was removed completely, leaving behind only the hydroxyl groups. This identification was further confirmed by the following chemical reactions.

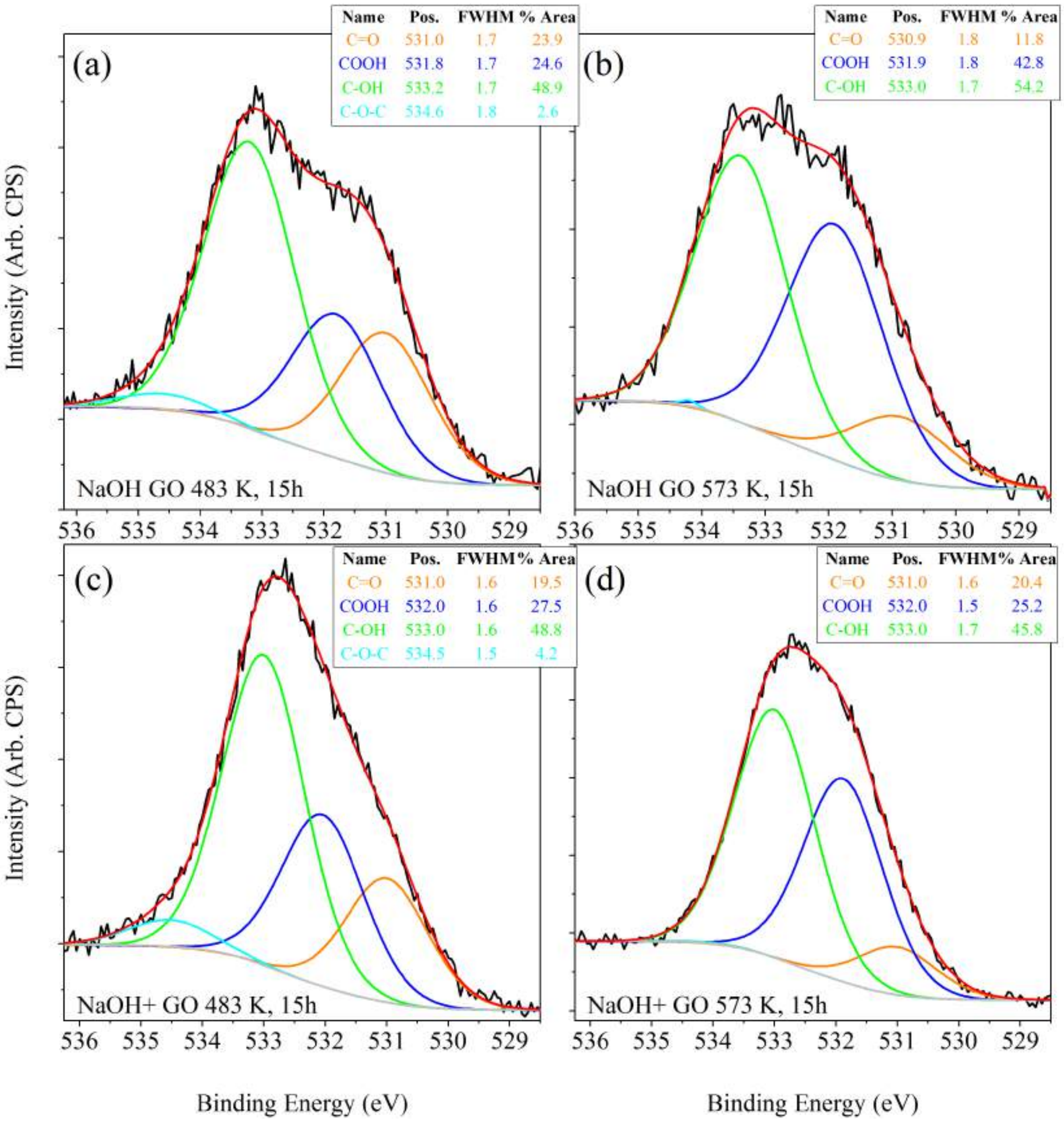

Figure 3.10: O $1s_{1/2}$ spectra of GO mixed with NaOH at 0.10 M (NaOH GO) and heated at (a) 483 or (b) 573 K for 15 h, with C/O ratios of 4.48 and 4.96 respectively. (c) and (d) are subject to the same heat treatments, but have 0.20 M of NaOH (NaOH+ GO) mixed into the solution and have C/O ratios of 4.45 and 4.64 respectively. As shown, the temperature plays an important role in the removal of C–O–C, while the heating time and NaOH concentration appears to have no significant impact.

Yang *et al.* introduced GO to APTES at 353 K and this resulted in the opening of the epoxy ring along with the subsequent removal of the oxygen atom[36]. In this experiment, GO samples were first heated at 483 or 573 K to remove OD and thermally reduce the sample. These heated samples were then immersed in a bath of APTES maintained at 353 K on a hotplate for two hours and after removal from the APTES bath, they were characterized by XPS. Fig. 3.11 shows the O $1s_{1/2}$ spectra of these characterizations and as expected the peak at 534.4 eV is removed, while a new peak due to the oxygen atoms in APTES appeared at 535.8 eV. Remarkably, the O $1s_{1/2}$ spectra from the two samples appear very similar despite the different initial heating temperatures. Besides showing that the C–O–C functional group is selectively removed from GO, it is also showed that the APTES–GO reaction is complex and favours the formation of C–OH bonds in the material.

In the final set of experiments of this section, GO was mixed with NaCl and NH_4Cl at a concentration of 0.10 M before heating at 573 K for 15 hours in a nitrogen environment. While the effects of these chemicals on GO are not known prior to these characterizations, some inferences can be made. NaCl was chosen

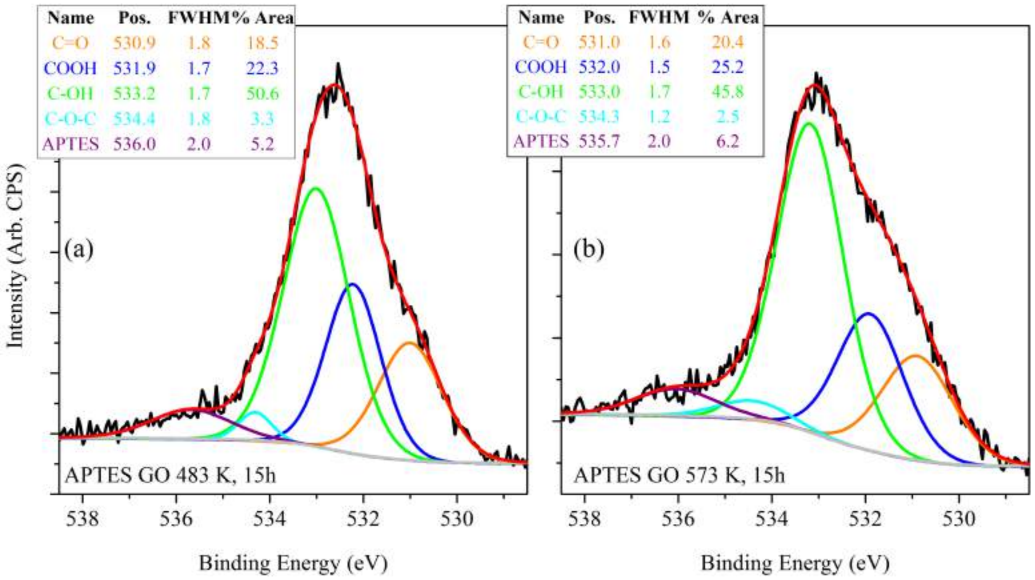

Figure 3.11: O $1s_{1/2}$ spectra of GO immersed in an APTES bath for two hours at 353 K after heating at (a) 483 and (b) 573 K, C/O ratios of 3.47 and 4.04 respectively. Interestingly, the spectra looked remarkably similar despite the different reaction conditions.

for comparability against the NaOH samples, and the NH_4Cl sample was chosen to compare the effect of the cation on the reaction.

Chen *et al.* described NaOH as a catalyst in removing hydroxyls from GO and showed that NaOH removed the hydogen atom from the hydroxyl while Na^+ and H_2O worked together to extract the oxygen atom[35]. In changing the anion from OH to Cl, no differences are to be expected as the NaOH catalyst would automatically be generated after the first epoxides were removed and changing the cation would in theory prevent the reaction from occurring at all. Rather surprisingly, the O $1s_{1/2}$ spectra in Fig. 3.12 tell a different story.

Beginning with Fig. 3.12(a), the epoxides were removed as expected. However, the spectra also show that, at 67 %, the proportion of hydroxyls in this sample was far greater than the <49 % of hydroxyls seen in similar samples heated with NaOH, as seen in Fig. 3.10 (b) & (d). Substituting NaCl with NH_4Cl gives a similar result, with a near total removal of the C–O–C peak from the spectrum in Fig. 3.12(b). The higher concentration of hydroxyls in this sample came primarily from a reduction in the area of COOH functional group peaks and at this point, the data suggests that the presence of the chloride ions favour the formation of hydroxyls over carboxyls.

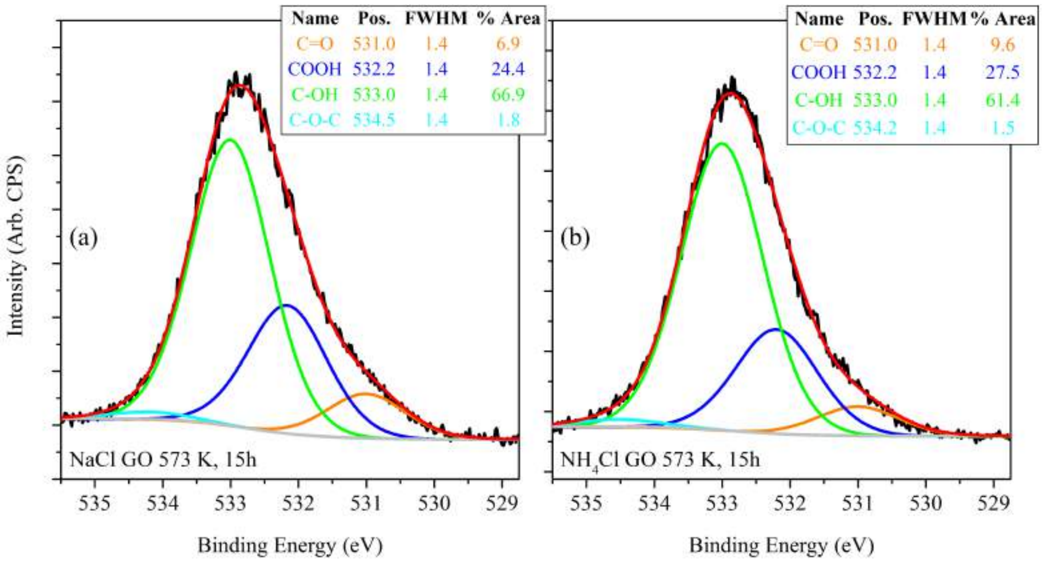

Figure 3.12: O $1s_{1/2}$ spectra of GO mixed with (a) NaCl and (b) NH_4Cl after heating at 573 K for 15 h in a nitrogen environment, C/O ratios of 2.35 and 2.38 respectively.

Although this experiment does not shed light on the chemical processes, it does prove that the area of the peak with the highest binding energy is reduced and in some cases removed from the O $1s_{1/2}$ spectrum. Based on this observation, along with other theoretical results, it was possible to identify that the epoxy functional group contributed electrons to this peak.

3.1.3.4 Concluding Remarks on O $1s_{1/2}$ Assignments

In many reports the XPS spectra of thermally reduced GO were shown with temperature increments in the order of hundreds of Kelvin. Due to the large range of heating temperatures, a multitude of effects such as OD removal and vacancy healing occur and this makes the analysis of the XPS spectra challenging. Here, the presence of OD affects the accuracy of the analysis while vacancy healing changes the binding energy of O $1s_{1/2}$ electrons. As a result of this, the binding energies of O $1s_{1/2}$ electrons in each of the different functional groups have yet to be identified.

While it has always been clear that O $1s_{1/2}$ electrons from oxygen atoms in C–O bonds have higher binding energies than the same electrons in C=O bonds, individual peaks for each functional group within these larger umbrella groups were lacking. By first heating the sample to 473 K to remove OD and increasing the temperature gradually to 573 K, four distinct peaks with binding energies of 530.9±0.1, 532.3±0.1, 533.1±0.2 and 534.4±0.2 eV were identified; the C $1s_{1/2}$ electron binding energy in C=C & C–C bonds for these samples was referenced at 284.7 eV. In these characterizations, the influence of secondary chemical shifts due to the oxygenation of neighbouring carbon atoms was not observed. Through chemical reactions with NaOH, 3-aminopropyltriethoxysilane, NaCl and NH_4Cl, the peak representing the epoxide functional groups at 534.4 eV was removed, leaving only the peak representing the hydroxide functional groups at 533.1 eV.

A TGA characterization was performed and the resulting thermogram compared against changes observed in the C/O ratio of the sample. The analysis revealed that the exfoliation of GO was caused by the decomposition of OD and that the removal of OD resulted in a decrease in the C/O ratio. To verify this finding, the experiment was repeated three months after the initial results and the graph of the C/O ratio of this experiment is shown in Fig. 3.13.

The upward trend of the C/O ratio was retained and variations between Figures 3.6 & 3.13 are explained as follows. The concentration of OD in each sample of GO can vary and having less OD in this sample resulted in an insignificant decrease in the C/O ratio between the temperatures of 460 & 520 K. Additionally, the lower C/O ratios were caused by liquid phase metastability which causes the formation of difficult to remove carboxyls in GO[4,37].

By comparison with theoretical predictions, and as will be verified later, the 530.9 and 532.3 eV peaks were assigned to carbonyls and carboxyls respectively. By tracking the proportion of these peaks in the O $1s_{1/2}$ spectra and comparing the changes in these values against changes in the C/O ratio, the formation of carboxyls on the GO sheet between the temperatures of 543 and 561 K was observed. The change in contribution would have been too subtle to pick up if only the C $1s_{1/2}$ spectra were used and this highlighted the importance of the often overlooked O $1s_{1/2}$ spectra in the quantitative analysis of GO.

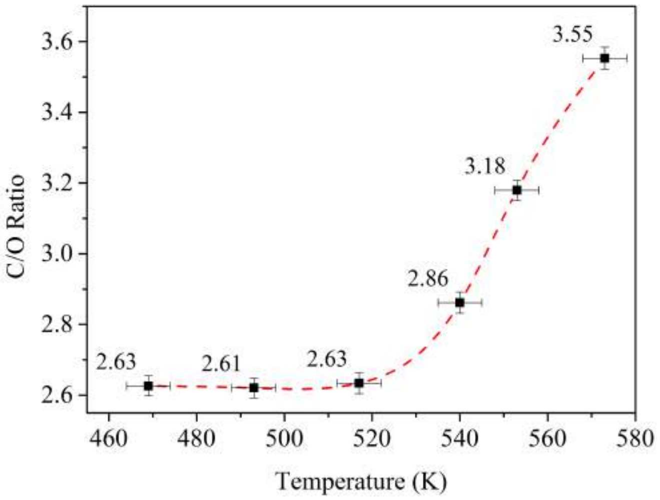

Figure 3.13: C/O ratio of a repeat in-situ heating experiment conducted three months after the first characterization in Fig. 3.6. The lower C/O ratios are due to liquid phase metastability that results in the formation of difficult to remove carboxyls.

3.2 Metastability of Aqueous GO

Having the ability to identify the peaks from the O $1s_{1/2}$ spectra, allows greater insight into the effect of metastability in GO to be determined[37–39]. As shown in Fig. 3.14, the longer a dilute suspension of GO was kept at 353 K, the darker the colour of the suspension became. Here, the GO suspension was kept in air-tight bottles and a temperature of 353 K was chosen to accelerate the effects of liquid phase metastability on the suspension[37]. Heating was done in the dark and this ensured that any changes in the colour of the suspension could attributed solely to the effect of heat on GO. Here, the effect of metastability on the composition of oxygen functional groups is studied and used to verify the identities of the carboxyl and carbonyl peaks in the O $1s_{1/2}$ XPS spectra.

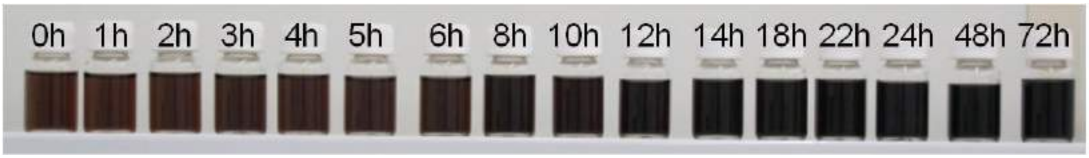

Figure 3.14: Temperature enhanced liquid phase metastability of GO causes the observed colour change in the GO suspension. The samples came from the same parent suspension and any changes are due to the effect of heat.

3.2.1 Computation of Functional Group Energies

Functional Group Bond Energy

As mentioned earlier in Chapter 1.2.3.5, the cause of metastability in GO has been attributed to the motion of functional groups across the graphene basal plane. This would only be possible if the C–O bond in the various functional groups were sufficiently weak and to test this, the bond strengths of the functional groups on the graphene basal plane were calculated using the Vienna Ab-initio Simulation Package (VASP)[40–43]. VASP simulations use periodic boundary conditions and the structures used in these calculations consisted of a single functional group on a graphene sheet with side lengths of three unit cells and the wave functions of the electrons in the atoms were approximated using ultra-soft psuedopotentials[44,45].

Structures were first drawn by manually positioning atoms in three-dimensional space before they were optimized and the the energy of these systems, E_i, recorded. The convention used here assigned the value of 0 to represent the entire system and the values 1 to represent the graphene sheet and 2 to represent the functional group. In this way, the bond energy between the graphene sheet and the functional group, E_b, was calculated by subtracting the energy of the components from the energy of the system:

$$E_b = E_0 - \sum_{i=1}^{2} E_i \tag{3.4}$$

The difference between the zero point energy (ZPE) of the system and its components, d(ZPE), was calculated in a similar fashion:

$$d(\mathrm{ZPE}) = \mathrm{ZPE}_0 - \sum_{i=1}^{2} \mathrm{ZPE}_i \tag{3.5}$$

and the ZPE corrected binding energy , E_b^{ZPE}, found to be:

$$E_b^{\mathrm{ZPE}} = E_b + d(\mathrm{ZPE}) \tag{3.6}$$

In this calculation, only hydroxides and epoxides were considered as the translation of carbonyls and carboxyls across the graphene sheet would require the concurrent translation of a broken bond or vacancy respectively. To simplify this first-level theoretical analysis, the functional groups were assumed to be non-mobile and no calculations were performed for these functional groups.

To calculate the binding energy of the functional groups on the graphene sheet, three different binding sites had to be considered as well. These are the bridge (B), hexagonal (H) and top (T) sites and the functional groups were sited on these three locations before energy minimization and ZPE calculations were performed. These sites are shown in the schematic of Fig. 3.15(a).

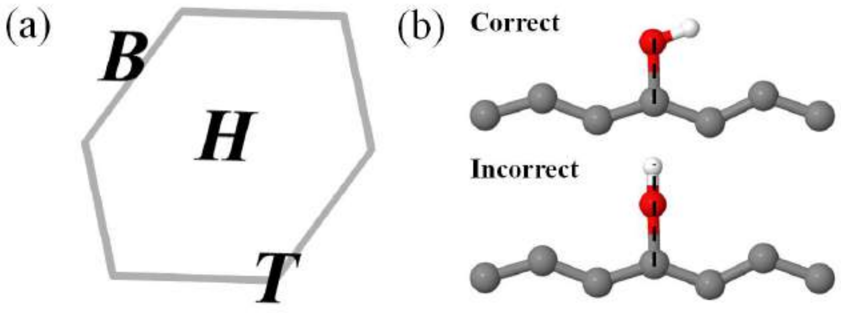

Figure 3.15: (a) Schematic showing the bridge (B), hexagonal (H) and top (T) sites on the graphene sheet where the epoxides and hydroxides could attach themselves. (b) The hydrogen in the hydroxide group must be positioned off center with respect to the perpendicular from the graphene basal plane passing through the oxygen atom, dotted line.

It was found that the energy of the system with a hydroxide group attached was minimized only when the hydrogen atom in the hydroxide group was positioned away from the line made by a perpendicular from the graphene sheet passing through the oxygen atom. When the hydrogen atom was placed along this line, the system was unstable and the energy minimized structure required the removal of the hydrogen atom from the system.

Table 3.5 summarizes the energies of the various systems described and the calculated E_b and E_b^{ZPE} values. From this table, it could be deduced that hydroxides preferred the T-site and epoxides preferred the B-site when bound to the graphene basal plane. For the epoxides, the B-site was, by far, the most stable binding site and, neglecting intermediate states, 0.71 eV would be needed to move the oxygen atom from this site to a T-site. Translation of the hydroxide across the graphene basal plane came at a lower energetic cost, with a mere 0.15 eV increase in the energy of the system when the functional group travelled from a T-site to a B-site. These calculations also showed that, while it might have been possible for both the hydroxide and epoxide to traverse a H-site during translation, the high energetic cost involved meant that this motion would not be preferred. Instead, the carbon-carbon bonds and the carbon atoms in the basal plane could be thought of as 'railway tracks' and the functional groups would travel like 'railway cars' along these 'railway tracks' if sufficient energy was provided.

Table 3.5: Calculation of system and component energies made using VASP and the evaluation of binding energies between the functional groups and the graphene basal plane. All values are in eV and the preferred site for each functional group is highlighted by the red box.

Monolayer Graphene

E_1	-166.06
ZPE_1	6.03

Components

	Hydroxide (–OH)	*Epoxide (–O–)*
E_2	-7.59	-1.60
ZPE_2	0.46	–

Systems

	Graphene with –OH			*Graphene with –O–*		
Site	B	H	T	B	H	T
E_0	-174.20	-174.03	-174.50	-170.07	-168.29	-169.21
ZPE_0	6.66	6.57	6.81	6.26	6.14	6.10

Binding Energy on Graphene

	Hydroxide (–OH)			*Epoxide (–O–)*		
Site	B	H	T	B	H	T
E_b	-0.55	-0.38	-0.85	-2.42	-0.63	-1.55
E_b^{ZPE}	-0.38	-0.30	-0.53	-2.19	-0.53	-1.48

Molecular dynamic simulation showing an epoxide translation

Using models from the bond energy calculations, molecular dynamical (MD) simulations were performed and an epoxide was observed to 'walk' from one B-site to a neighbouring B-site. This suggested that, in an ideal graphene sheet, there was enough energy in the combined buckling of the sheet buckling and vibration of the epoxide oxygen atom to cause the atom to translate across the surface of the graphene sheet. A series of images showing the translation of this epoxide is shown in Fig. 3.16.

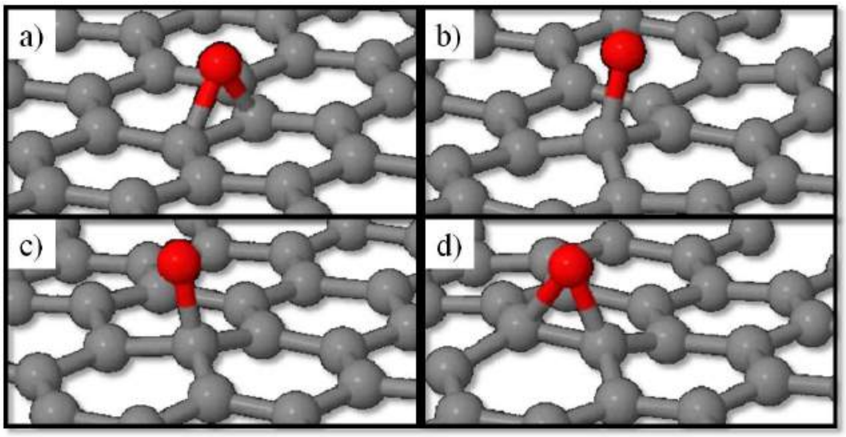

Figure 3.16: Series of images from a MD simulation showing the epoxide functional group 'walking' across the graphene basal plane.

System energy reduction due to functional groups coalescing

As a final test in this series of computational experiments, the energy of two hypothetical GO systems were computed and compared. For simplicity, only epoxides and hydroxides were used and these functional groups were either randomly dispersed across the graphene basal plane or grouped together in a dense configuration as shown in Fig. 3.17.

After optimizing these systems, it was found that despite having the same number of atoms and functional groups, the system with functional groups dispersed across the entire graphene sheet had a higher energy than the system with functional groups collected together. Despite the fact that both the collection and dispersion of these functional groups was done in a random manner, the total energy was still observed to have been reduced by 2.31 eV. It would therefore be reasonable to expect that other more optimized configurations could exist in

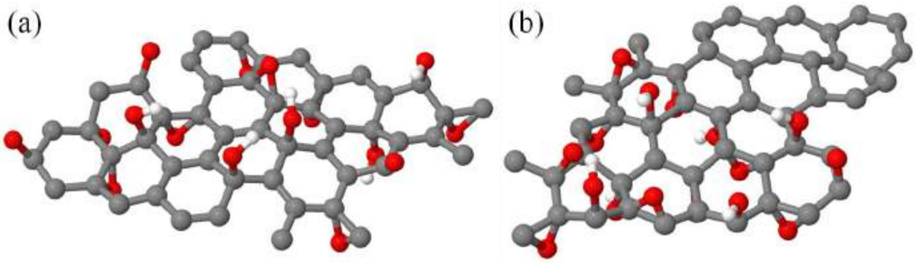

Figure 3.17: Images of the structures that were used in the comparison. In (a), the functional groups are randomly dispersed across the basal plane and when grouped together as shown in (b) the energy of the system was reduced by 2.31 eV.

nature. The GO sheet with the functional groups collected together was more energetically stable than the GO sheet with functional groups dispersed across the entire sheet and this reduction in energy could provide an energy gradient to promote the coalescence of these oxygen functional groups and be the driver of liquid and solid phase metastability.

Summary of computation results

The hydroxide and epoxide bond energies with the graphene basal plane were calculated and it was deduced that the translation of these functional groups across the graphene sheet would likely be constrained along particular paths. These paths tracked the bonds between and locations of the carbon atoms in the sheet and, due to the amount of energy required, the likelihood of either a hydroxide or an epoxide passing through the H-site was low.

Following this, through a MD simulation, the translation of an epoxide from one B-site to an adjacent B-site was observed. This happened when the graphene sheet buckled, temporarily allowing one of two epoxide bonds to break. From this state and with the acquired momentum, the oxygen traversed a T-site before finally landing on an adjacent B-site.

Calculations showed that the energy of a system with oxygen functional groups dispersed across the entire graphene basal plane was higher than that of a system with the oxygen functional groups coalesced together. This was consistent with experimental observation and, as was shown in the simulation, that this drove the transport of functional groups across the graphene basal plane, causing both liquid and solid phase metastability[46].

3.2.2 Metastability Induced Changes in Oxygen Composition

A fresh sample of GO (fresh-GO) was heated in a nitrogen only environment at 573 K for 15 hours and the sample was characterized by XPS. A large volume, >20 ml, of GO solution was then kept in an air tight darkened bottle for one year at room temperature. The aged solution was then used to make another GO sample (aged-GO) which was also subject to the same heat treatment and characterization. The O $1s_{1/2}$ spectra of these characterizations are shown in Fig. 3.18 and the aged-GO sample shows a significant reduction in the proportional contribution of the C–OH peak.

Rather surprisingly, the reduction in proportional contribution of the C–OH peak is not due to a reduction in the concentration of that functional group on GO but instead is due to an increase in the concentration of the other functional

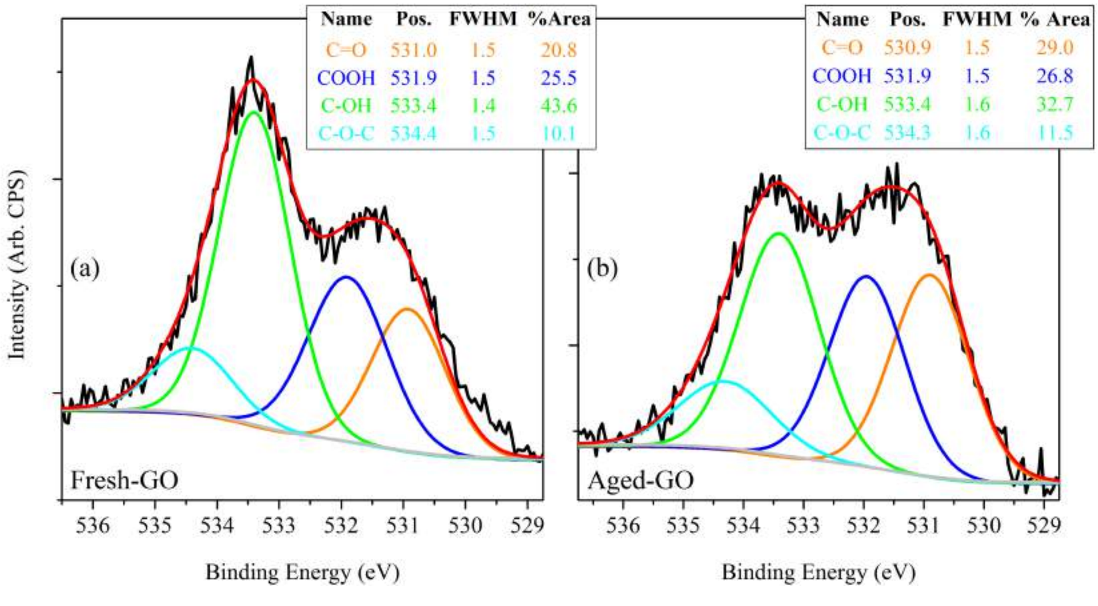

Figure 3.18: O $1s_{1/2}$ spectra of (a) fresh- and (b) aged-GO after heating in nitrogen environment at 573 K for 15 hours. Comparing the spectra of fresh-GO with the in-situ reduced sample in Fig. 3.5(b) shows that the presence of a nitrogen environment changes the composition of functional groups after heating. Contributions to the C-OH peak come from both hydroxyls and carboxyls.

Section 3.2.2 is based on the publication *"Identification of functional groups and determination of carboxyl formation temperature in graphene oxide using the XPS O 1s spectrum"*[4].

Table 3.6: Breakdown of the actual number of oxygen functional groups in the fresh- and aged-GO samples per 1000 carbon atoms.

	Fresh GO		**Aged GO**	
C/O ratio	6.10		4.70	
Number of Oxygen Atoms	164		213	
Functional Group	Percentage / %	Number of Atoms	Percentage / %	Number of Atoms
C=O	*20.8*	34	*29.0*	62
COOH	*25.5*	42	*26.8*	57
C–OH	*43.6*	72	*32.7*	70
C–O–C	*10.1*	16	*11.5*	24

groups, as shown in Table 3.6. In these samples, the C/O ratio of the fresh- and aged-GO samples were 6.10 and 4.70 respectively and overall, the C/O ratio in these samples was higher than the C/O ratio of the samples heated in a vacuum. Calculating the number of oxygen functional groups per 1000 carbon atoms in the sample in absolute terms showed that the number of C–OH bonds had not changed in either the fresh or aged sample. Instead, liquid phase metastability had resulted in the formation of more C=O and COOH functional groups per 1000 carbon atoms after heating at 573 K.

To further understand this difference, the UV-vis absorption spectra of the fresh- and aged-GO were compared. Samples of the same thickness were deposited by ultrasonic spray deposition onto quartz substrates and the UV-vis spectra obtained from this characterization shown in Fig. 3.19. The point of maximum absorption occurred at 230 nm and the intensity of this absorption was the same in both samples. Following this, at longer wavelengths, a broadband increase in absorption was observed as well as the widening of the shoulder occurring at 300 nm. Saxena *et al.* concluded that the characteristic peak at 230 nm was due to a $\pi \rightarrow \pi^*$ transition and that the shoulder at 300 nm was caused by a n$\rightarrow \pi^*$ transition, commonly associated with the presence of peroxide bonds[47].

Knowing that the sample thicknesses were the same, the similarity in absorbance of the peak at 230 nm showed that the number of sp^2 hybridized carbon atoms in the samples had remained unchanged. Following this, the increase in absorption at 300 nm was evidence that the oxygen atoms had clustered together, forming

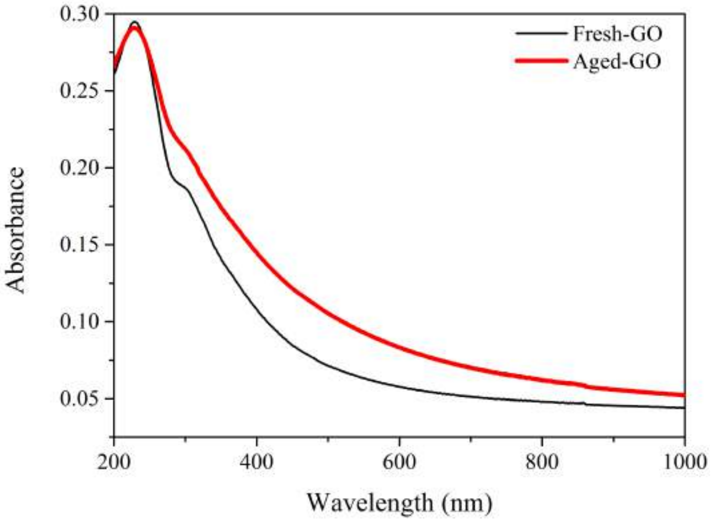

Figure 3.19: UV-vis spectra of fresh- (thin black line) and aged-GO (thick red line) thin films deposited by ultrasonic spray, with the aged sample showing a broadband increase in absorption. The characteristic peak at 230 nm and the shoulder at 300 nm are due to the $\pi \rightarrow \pi^*$ transition and peroxide absorption.

regions of high oxygen concentration on the GO flake and this was in line with the expectations of liquid phase metastability[37]. Additionally, the clustering of oxygen atoms also allowed for the overlap of domains of un-functionalized carbon atoms to give graphitic domains which were responsible for the broadband increase in absorption observed[37].

Further evidence for the clustering of the oxygen functional groups on the GO flake can be obtained by use of Tauc plot[48,49]. The theory and calculation details were discussed in Chapter 2.4.1 and Mathkar *et al.* have shown that the optical bandgap on GO is directly related to the concentration of oxygen functional groups on the flake[50]. The Tauc plot of the fresh- and aged-GO samples are shown in Fig. 3.20 and, at 2.24 eV, the optical bandgap of fresh-GO is shown to be larger than the optical bandgap of aged-GO at 1.41 eV. As mentioned earlier, the shoulder at 4.1 eV (λ = 230 nm) is due to peroxide absorption and is ignored for the determination of the optical bandgap. The higher C/O ratio and optical bandgap of fresh-GO means that though lower in concentration, the oxygen functional groups were well dispersed across the graphene sheet and the lower C/O ratio and optical bandgap of aged-GO indicated that there were regions on the sample that had a very low concentrations of oxygen functional groups.

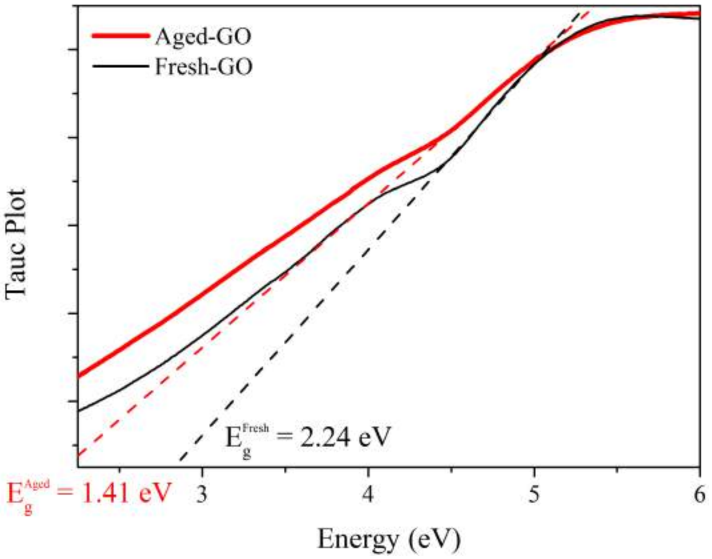

Figure 3.20: Tauc plot of fresh- (thin black line) and aged-GO (thick red line) in an indirect allowed transition. The calculated optical bandgap of the samples are 2.24 and 1.41 eV respectively.

Additionally, Zhou and Bongiorno have shown, using nudged elastic band density field theory calculations, that the energy of a system is reduced by between 0.1 to 0.8 eV when two oxygen functional groups are placed in close proximity of one another[51]. This means that the formation of oxygen rich domains on the GO material is energetically favourable and provides a strong motivation for the clustering effect to occur.

Having shown that the oxygen functional groups in aged-GO are positioned closer together than in fresh-GO, any differences in the composition of these groups on GO after heating at 573 K must be due to the increased proximity. In their work, Zhou and Bongiorno had also shown that (i) when hydroxyls are placed in close proximity the formation of an epoxide with the release of a water molecule is exothermic and has a lower activation energy of 0.5 eV and (ii) when two epoxides were placed in close proximity, the formation of carbonyls was exothermic with an activation energy of 0.8 eV[51]. This explained the observations listed in Table 3.6 where there was an increase in the number of epoxide, carbonyl and carboxyl groups in the aged-GO sample.

3.2.3 Determination of Carbonyl and Carboxyl Peaks

To differentiate the carbonyl peak from the carboxyl peak in the O $1s_{1/2}$ XPS spectrum, the mechanics of formation of these functional groups in GO must be discussed. Ignoring edge states, the formation of carbonyls from two epoxides involves the breaking of C–C bond on the basal plane while the formation of a carboxyl creates a vacancy on the basal plane, as shown in Fig. 3.21.

In Chapter 3.1.3.1, it was shown that after removing OD, a majority of oxygen functional groups were bound to the GO flake as either hydroxyls or epoxides with a small but measurable quantity of carbonyls and carboxyls on the plane. Since (i) an epoxide is formed from two hydroxyls, (ii) two carbonyls from two epoxides and (iii) a carboxyl from a carbonyl and a hydroxyl, the closer positioning of the functional groups in aged-GO, as compared to fresh-GO, meant that there was a higher likelihood that carbonyls and carboxyls would form. As shown in Table 3.6, while the number of hydroxyl groups in the aged sample was similar in both the fresh- and aged-GO samples, the number of carboxyls had increased and this meant that electrons contributing to the C-OH peak must have come from carboxyl groups.

Figure 3.21: Schematic of (a) two adjacent epoxides that result in the formation of (b) two carbonyls and (c) the creation of a vacancy on the basal plane due to the formation of a carboxyl group (carboxyl is shown projected into the plane). The carbon plane extends beyond what is drawn here and the carbon atoms are represented in grey, the oxygen atoms in red and the hydrogen atoms in white.

Section 3.2.3 is based on the publication *"Identification of functional groups and determination of carboxyl formation temperature in graphene oxide using the XPS O 1s spectrum"*[4].

Understanding that the formation of a carboxyl group requires hydroxyls, it becomes obvious that this is also a self limiting reaction. Without referring to Table 3.6, it should be clear that the formation of more carboxyls in the aged-GO sample leads to there being fewer free hydroxyl functional groups present in the sample. This also means that there are now fewer hydroxyls to react with the newly formed carbonyls to form carboxyls and, as shown in Fig. 3.21, the formation of a carboxyl group incurs the creation of a vacancy and two dangling bonds that are easily terminated with carbonyls, while the formation of two carbonyls can occur when two epoxides meet on the same pair of carbon atoms[51]. As such, when compared against the fresh-GO sample, the rate of carbonyl formation is expected to exceed the rate of carboxyl formation in the aged-GO samples.

Per 1000 carbon atoms, the 62 carbonyls in the aged-GO sample was found to be nearly double the 34 carbonyls in the fresh-GO sample, see Table 3.6. At the same time, the 57 carboxyls in the aged-GO sample was 36 % greater than the 42 carboxyls groups in the fresh GO sample. This shows a greater increase in the number of carbonyls than carboxyls in the aged-sample after heating and is in line with the above theory.

3.2.4 Effect of Metastability on TGA

Metastability on GO manifests itself as a clustering of the oxygen functional groups on the graphene basal plane, and as shown in Fig. 3.22, the peak differential temperature and region of constant mass loss are increased by about 5 K as well. While the overall shape of the thermogram is similar to that of fresh-GO in Fig. 3.2, the increased temperature of the peak of the differential curve and region of constant mass loss show that, just like GO, OD is subject to the effects of metastability as well.

As was shown in Table 3.6, the main effects of metastability on GO are a decrease in the C/O ratio and a more than proportional increase in the number of C=O bonds in the aged-GO material. As the the bonds between oxygen and carbon atoms are converted from weaker single bonds to stronger double bonds, the activation temperatures for chemical processes occurring in GO are expected to increase as well as evidenced by the higher onset temperature shown in Fig. 3.22.

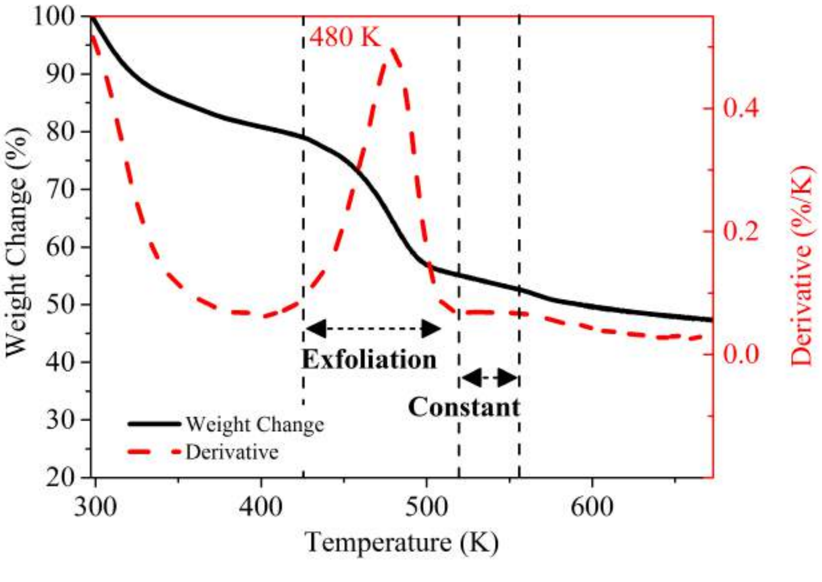

Figure 3.22: TGA thermogram of aged-GO has a similar shape to that of fresh-go in Fig. 3.8. The peak of the differential curve occurred at 480 K and the region of constant rate of mass loss was between 517 and 560 K. These temperatures were about 5 K higher than those in the fresh-GO sample.

3.3 Low Oxygen Content GO

The assignment of the the O $1s_{1/2}$ peaks was tested on a specially prepared sample of edged-functionalized graphene oxide (EFGO) from Garmor, Inc[52]. The company claims that oxygen functional groups in EFGO were present only on the edge of the graphene sheet and the pristine hexagonal lattice maintained on the basal plane of the flake. A sample of this material was subject to XPS characterization and the C and O $1s_{1/2}$ spectra are shown in Fig. 3.23.

The C/O ratio of this sample was found to be 6.7 and despite the unique method of production, the C $1s_{1/2}$ electron binding energy of this sample was found to be similar to that of GO made by the Hummer's method shown in Table 3.1. The peak fitting results are summarized in Table 3.7 and the binding energy of O $1s_{1/2}$ electrons was found to match the values found for GO produced by the Hummer's method listed in Table 3.3. From the peak fitting results of the C $1s_{1/2}$ spectrum, it appeared that the C–OH and C–O–C bonds were present in higher

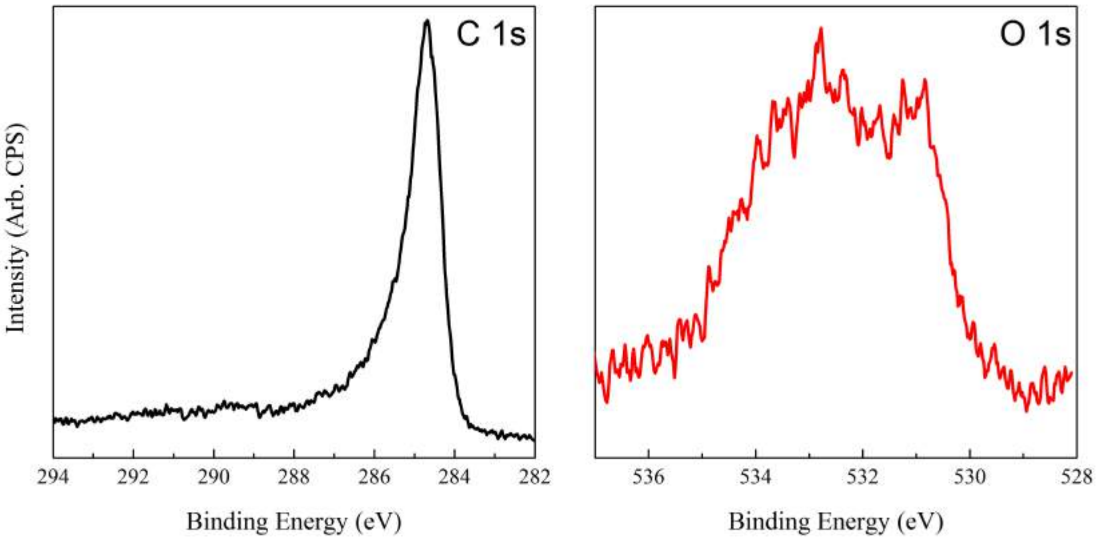

Figure 3.23: XPS characterization spectra of the C and O $1s_{1/2}$ electrons in EFGO. As expected, the low oxidation level results in a C $1s_{1/2}$ spectrum consisting mainly of electrons from sp^2 hybridized carbons, with some low area peaks representing the oxygen bound carbon atoms occurring at the edge of the sample. While it would be difficult to find the contributions of the functional groups by peak fitting of the C $1s_{1/2}$ spectrum, this was much easier when the O $1s_{1/2}$ spectrum is used.

Table 3.7: Fitting details of EFGO with a C/O ratio of 6.7. The C $1s_{1/2}$ spectrum is dominated by a high area peak at 284.7 eV, making the deconvolution of the spectrum difficult. As compared to the C $1s_{1/2}$ spectrum, the O $1s_{1/2}$ spectrum can be fit to a higher with greater confidence, with more accurate quantitative results.

	C $1s_{1/2}$			**O $1s_{1/2}$**		
Functional Group	**B.E. / eV**	**FWHM**	**%Area**	**B.E. / eV**	**FWHM**	**%Area**
C=O	287.7	1.0	12.2	530.9	1.3	31.9
(CO)OH				532.2	1.3	24.2
C–OH	286.4	1.0	2.3	533.2	1.3	27.3
C–O–C				534.3	1.3	16.6
C=C/C–C	284.7	0.9	85.5			

concentration than the C=O and COOH bonds. However, the accuracy of this observation is limited by the high area peak representing electrons from C=C and C–C in sp^2 hybridized carbon atoms, making it difficult to find accurate fitting values for these peaks.

On the other hand, using the O $1s_{1/2}$ spectrum allowed the composition of oxygen functional groups in the material to be decided with greater confidence. As shown in Table 3.7, the functional groups appeared in roughly the same proportion in the material, unlike GO produced by the Hummer's method in which a majority of the functional groups in as-prepared GO are in the form of epoxies and hydroxyls. Besides this, the data was also used to verify the assignment of the C=O and COOH peaks. As the contribution to the C–OH peak comes from both the hydroxyl and carboxyl groups, this meant that the area of the COOH peak in the sample can be, at most, equal to that of the C–OH peak and can never be greater. The contribution to spectral area of the 530.9 eV peak is 4.6 %higher than the contribution to the spectral area of the C–OH electrons at 533.2 eV. This rules out the assignment of the COOH group to the peak with a binding energy of 530.9 eV and confirms the assignment to a carbonyl group.

3.4 $FeCl_3$ in GO

In an attempt to adapt the stellar TCE properties of graphene intercalated with $FeCl_3$ onto a GO, a sample was made by mixing $FeCl_3$ with GO at mixing concentrations of 0 to 15 %[2]. While the resulting films had less than spectacular TCE properties, the cause of these poor results were explained by studying the XPS spectra of these samples.

The introduction of $FeCl_3$ meant that new peaks would be introduced to the O $1s_{1/2}$ spectrum and this introduced new challenges into the deconvolution of the spectrum. Due to the oxidation state independence of the binding energy of the O $1s_{1/2}$ electrons, the Fe $2p_{3/2}$ spectrum would be required in this analysis. As such, the use of Fe multiplet theory is fundamental to this study and this theory will first be covered[53]. Subsequently, the theory will be used to analyse the experimental findings and conclusions drawn to explain the lack-lustre TCE properties of GO mixed with $FeCl_3$.

3.4.1 XPS of GO mixed with $FeCl_3$

In 2012, Khrapach *et al.* showed that intercalating FLG with $FeCl_3$ allowed the fabrication of a small TCE that had a sheet resistance of 8.8 $\Omega/\square$ and a transmittance of 84 %, giving a $\sigma_{\mathrm{dc}}/\sigma_{\mathrm{op}}$ value of 235[2]. In this experiment, varying quantities of $FeCl_3$ was mixed with GO and the resulting mixture spray-coated onto a glass substrate. The samples were then heated at either 473 or 573K in a nitrogen environment and the resulting TCEs characterized for transmittance and sheet resistance. These measurement values and the corresponding calculated $\sigma_{\mathrm{dc}}/\sigma_{\mathrm{op}}$ values are tabulated in Table 3.8.

As $FeCl_3$ decomposes at ~523 K, the difference in performance of the TCEs in these two scenarios is expected to be due to the effect of $FeCl_3$ decomposition[54–56]. The close proximity between the decomposing $FeCl_3$ and the oxygen atoms in GO would allow the possibility of a chemical reaction to occur and this would be observable in the O $1s_{1/2}$ spectra as shown in Fig. 3.24.

Table 3.8: Characterization details of GO mixed with $FeCl_3$. The σ_{dc}/σ_{op} values fall with increasing $FeCl_3$ concentration when heated at 473 K and the trend was reversed when the samples were heated at 573 K. % T – Transmittance at 550 nm, R_{sh} – sheet resistance.

	Doping / vol%	**% T / %**	**R_{sh} / kΩ $\square^{-1}$**	**$\sigma_{dc}/\sigma_{op}\times10^{-3}$**
As Deposited	0.0	95.5	–	–
	5.0	87.2	–	–
	10.0	83.6	–	–
	15.0	77.8	–	–
473 K, 15 h	0.0	77.7	322	4.36
	5.0	67.3	446	1.93
	10.0	63.6	862	0.863
	15.0	60.4	1170	0.563
573 K, 15 h	0.0	76.7	163	8.14
	5.0	55.6	49.6	11.2
	10.0	49.1	34.4	12.8
	15.0	39.2	23.2	13.6

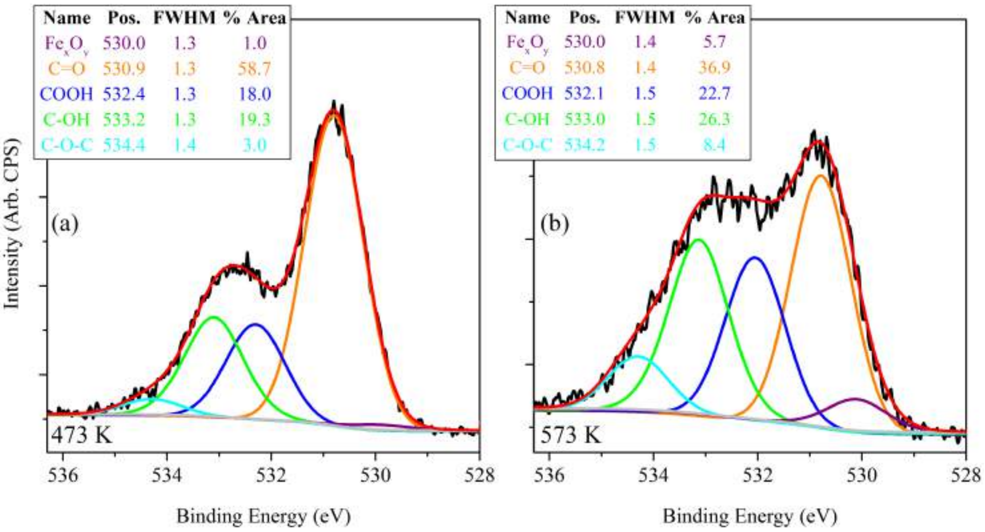

Figure 3.24: As the heating temperature is increased from (a) 473 to (b) 573 K, the area of the C=O peak decreases and the area of the Fe_xO_y peak increases.

From the O $1s_{1/2}$ spectra it was possible to deduce that the presence of $FeCl_3$ increases the likelihood of carbonyl and carboxyl formation, with a majority of the hydroxide functional groups present bound in a carboxylic group. As the heating temperature and $FeCl_3$ concentration were increased, carbonyl release was favoured and this may be responsible for the significant decrease in sheet resistance of the samples. However, the binding energy of the O $1s_{1/2}$ electrons in oxygen atoms bound to metallic cations were not useful in determining the oxidation state of the cation that the oxygen atom was bound to. This statement will be explained in a later section, but on the positive side, the same Fe_xO_y peak can be used to verify the accuracy of the assigned peak binding energy values.

3.4.1.1 Binding Energy of Metallic O $1s_{1/2}$ Electrons

In a series of articles, T. Yamashita & P. Hayes had a discussion with E. Paparazzo on whether the binding energy of the O $1s_{1/2}$ electrons were affected by the oxidation state of the metal that the oxygen atom was bound to[57–59]. Yamashita & Hayes claimed that the oxidation state of the O $1s_{1/2}$ electrons were unaffected by the oxidation state of the metal and showed this with oxides of iron[57,60]. However, Paparazzo had shown earlier that for a given first row transition metal oxide, the O $1s_{1/2}$ binding energy increased with decreasing oxidation number of the cation and reported a linear binding energy shift of up to 0.5 eV from Fe_2O_3 to $Fe_{1-x}O$[61,62].

However, it should be noted that a binding energy of 529.3 eV for the O $1s_{1/2}$ electrons in Fe_2O_3 is unusually low and this shift could instead be caused by the formation of metal bound hydroxides as shown by McIntyre & Zetaruk[61–63]. In their work they showed that the binding energies of the O $1s_{1/2}$ electrons in FeOOH formed two distinct peaks at 530.0 ±0.2 and 531.1 ±0.2 eV with the former peak being assigned to electrons from the oxygen atom and the latter peak assigned to electrodes from the oxygen in the hydroxide group.

To verify this, data on the binding energy of O $1s_{1/2}$ electrons was collated from XPS experiments that involved transition metals from the first row of the periodic table. This data is displayed in Table 3.9 and is arranged according to the oxidation number of the transition metal and corrected to a C $1s_{1/2}$ electron binding energy of 284.7 eV.

Table 3.9: O $1s_{1/2}$ electron binding energies from oxygen atoms chemically bound to transition metals (Me) as Me_xO_y or $Me_x(OH)_y$. The Me are from the fourth row of the periodic table and are at various oxidation states. All values were corrected to a C $1s_{1/2}$ binding energy of 284.7 eV.

Element	Binding Energy / eV			Ref.
	Oxidation State			
	1+	2+	3+	
$^{52}_{24}$Cr			530.1 ±0.2 (OH = +1.7)	[64]
$^{55}_{25}$Mn		530.0	530.0 (OH = +1.2)	[64]
$^{56}_{26}$Fe		530.0	530.0 ±0.3 (OH = +1.4)	[61–64]
$^{59}_{27}$Co		530.1 ±0.2 (OH = +1.3)		[64]
$^{59}_{28}$Ni		529.4 ±0.1 (OH = +1.6)		[64]
$^{64}_{29}$Cu	530.2			[65]
	530.2	529.7 (OH = +1.0)		[66]
		530.3		[67]
Zn$^{65}_{30}$		529.8		[66]

With the exception of nickel which has a low binding energy, it was observed that, regardless of oxidation state, the binding energy of electrons in the O $1s_{1/2}$ orbital of oxygen atoms chemically bound to transition metals is 530.0 ±0.2 eV and that the binding energy of a similar electron in a hydroxide chemically bound to the same transition metal is at least 1.0 eV higher. While this meant that it would be impossible to identify the oxidation number of the transition metal from the O $1s_{1/2}$ spectra, it became exceptionally useful when correcting the spectra for charging effects. The binding energy of electrons from the O $1s_{1/2}$ orbitals could be used as a reference point and the binding energy values of the oxygen functional groups in GO could be verified independently.

By taking reference from the O $1s_{1/2}$ peak from Fe_xO_y the binding energy values of the same electrons from the different functional groups on GO could be confirmed. Using the table in Fig. 3.24(b), the binding energies of the O $1s_{1/2}$ electrons in carbonyls, carboxyls, hydroxyls and epoxides on GO are 530.8, 532.1, 533.0 and

534.2 eV respectively and are within ±0.2 eV values found for GO in Table 3.3 and EFGO in Table 3.7. This result confirmed the accuracy of the assigned binding energy values of the various peaks.

3.4.1.2 Multiplet Theory

The multiplet structure in a XPS spectra originates from an interaction between the partially filled core shell after photoionization and the presence of an unpaired electron in the outer shell. This interaction affects the kinetic energy of the photoemitted electron and results in the formation of a multi-peak envelope in the observed spectrum. Gupta & Sen calculated the multiplet spectra from this interaction for free ion states, accounting for electrostatic and spin-orbit interactions on the Hartree-Fock model and the resulting spectra is shown in Fig. 3.25. By performing a peak fitting on the graphs, the binding energy and relative areas of these multiplet peaks would be identified[53].

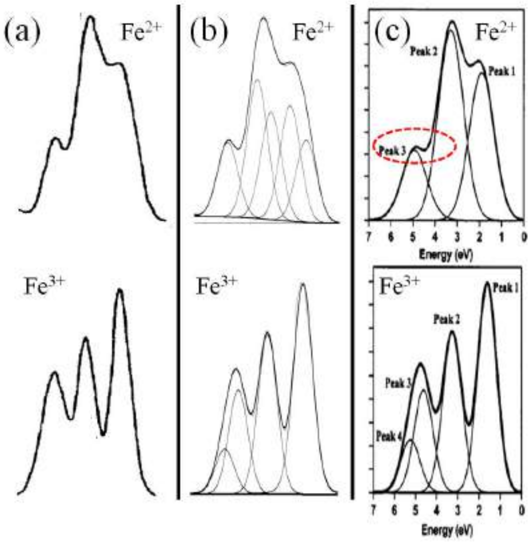

Figure 3.25: (a) Original graphs of multiplet peaks by Gupta & Sen, (b) the fitting of these multiplet peaks to find the relative contributions and binding energies of the individual components in the envelope and (c) similar fitting made by Grosvenor *et al.* with the observed difference in the Fe^{2+} spectrum circled in red. The graphs are drawn to the same scale and five peaks are required to achieve an adequate fit.

Reprinted with permission from reference [53]. Copyright 1975 by the American Physical Society.

Reprinted with permission from reference [68]. Copyright © 2004 John Wileyand Sons.

The data from the original article was extracted first by digitizing the original data and the resulting envelope was characterized by peak fitting using peaks that had the same FWHM. The relative areal contributions and binding energies of the various peaks from this peak fitting for the Fe^{2+} and Fe^{3+} multiplet envelopes are shown in Table 3.10. Notably, despite having been calculated for free ions, these multiplet peaks have been successfully used to analyse oxidized transition metals at various oxidation levels[63,64,68].

The breakdown of the individual peak components were listed in the work by Grosvenor *et al.* and a check revealed a noticeable discrepancy between the original calculated data and their multiplet envelope[68]. The multiplet envelope for the Fe^{2+} ion is shown and the difference highlighted in Fig. 3.25(c)[64,68]. Instead of three peaks, using five peaks are required to give a good fit to this envelope.

This distinction is important because while only three peaks are rightfully expected from a basic coupling schemes, the inclusion of a spin-orbit component may have caused a splitting of the levels[69]. As such, it would be more accurate to approach peak fitting from this perspective and, rather than force a fit with three peaks, five peaks should be used to fit the Fe^{2+} spectrum. Doing this ensured that the widths of the peaks in both the Fe^{2+} and Fe^{3+} were the same and this is in line with the basic principles of Gupta & Sen[53]. As a final point, although

Table 3.10: Summary of the peak areas and binding energies (B.E.) in the multiplet envelopes of the Fe^{2+} and Fe^{3+} ions, followed by the values from Grosvenor *et al.* Here, B.E. values are referenced to the first peak in the Fe^{2+} envelope, while Grosvenor *et al.* referenced the first peak of each envelope at 0 eV. The %Area values in each envelope sum to 100 % and the peaks have a FWHM of 1.05 eV.

		Peak	1	2	3	4	5
This work	**Fe^{2+}**	B.E. / eV	0	+0.7	+1.5	+2.0	+3.3
		%Area	19.3	21.4	19.3	25.0	15.0
	Fe^{3+}	B.E. / eV	+0.1	+1.7	+3.1	+3.7	
		%Area	40.6	30.4	21.0	8.00	
Grosvenor	**Fe^{2+}**	B.E. / eV	0	+1.4	+3.0		
		%Area	36.1	46.4	17.5		
	Fe^{3+}	B.E. / eV	0	+1.6	+2.9	+3.5	
		%Area	39.9	30.4	19.6	10.1	

the distinction between three and five peaks in multiplet envelope is of theoretical significance, random errors in a typical characterization may be larger than the difference described here and the use of the experimental data compiled by Grosvenor *et al.* was sufficiently accurate.

3.4.2 Chemistry of $FeCl_3$ and GO

An aqueous suspension of GO was mixed with 15 vol% of $FeCl_3$ and the resulting mixture deposited onto a glass substrate. Upon standing the mixture, a light green tint was observed at the top of the mixture, while the bulk of the mixture remained dark brown and orange. Just like it was in the GO experiment, the temperature of the sample was raised incrementally and the sample was characterized by XPS after each temperature increment. The resulting Fe $2p_{3/2}$ spectra are shown in Fig. 3.26 and the main peak is observed to shift slightly towards lower binding energies as the heating temperature was increased.

The contributions of the various iron containing compounds were subsequently identified by application of the multiplet peak envelopes that were recorded by Grosvenor *et al.*[68] An example of a good fit using the correct set of multiplet peaks and a poor fit using an incorrect set of multiplet peaks is shown in Fig. 3.27. In this example, the sample consisted of almost equal concentrations of $FeCl_2$ and $FeCl_3$ and is in line with the observation from Fig. 3.24 that there is negligible contribution from the Fe_xO_y peak to the spectrum at 473 K.

The presence of Fe^{2+} ions in the mixture explained why a green tinge was observed when standing the mixture and this meant that $FeCl_3$ had hydrolyzed under these conditions. The reactions between these reactants complicated understanding of the system, but by studying the products of this reaction some insight could be developed.

In this example, a pre-peak and a surface peak were used and this practice was consistently used throughout the fitting process[68]. The surface peak is a spectral feature the arises due to electron energy loss to the surface of the sample, while the pre-peak is a peak that appear just before the first Fe multiplet peak in the spectrum[68]. Following through for all the Fe $2p_{3/2}$ spectra, the relative contributions of the various ferric compounds in the sample were tracked and are listed in Table 3.11.

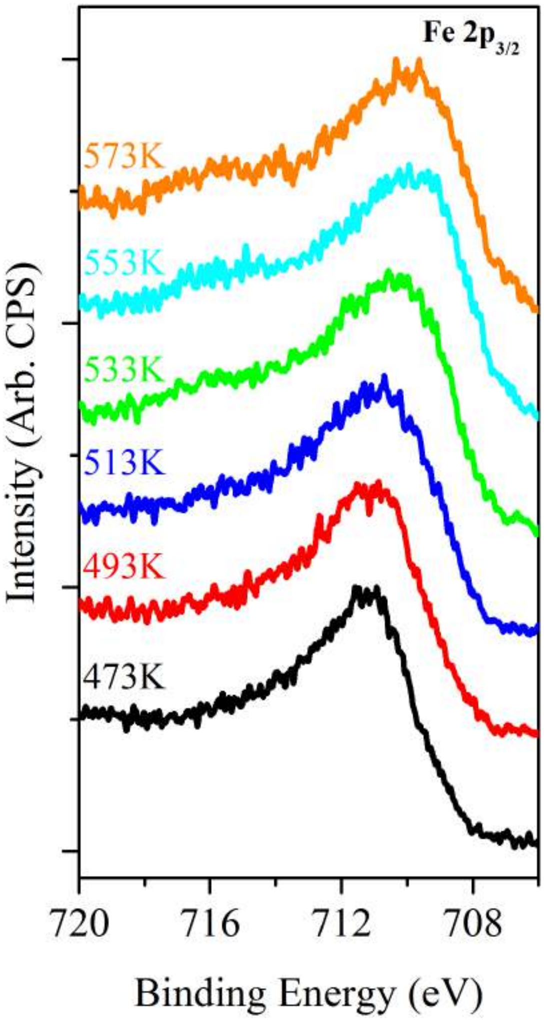

Figure 3.26: Series of Fe 2p$_{3/2}$ spectra from a mixture of $FeCl_3$ and GO as the heating temperature was increased from 473 to 573 K. The low binding energy edge of the spectra was observed to shift towards lower binding energies as the temperature was increased.

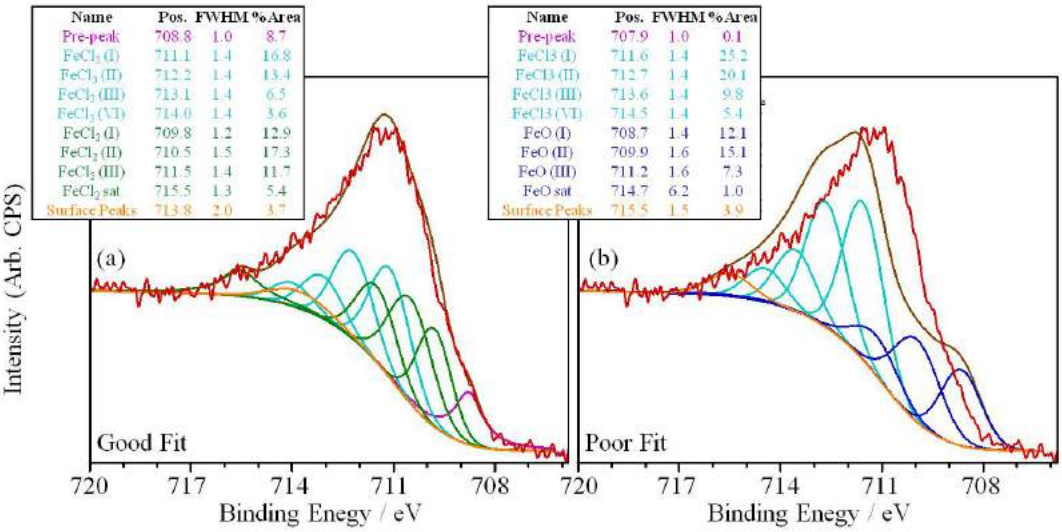

Name	Pos.	FWHM	%Area
Pre-peak	708.8	1.0	8.7
FeCl$_3$ (I)	711.1	1.4	16.8
FeCl$_3$ (II)	712.2	1.4	13.4
FeCl$_3$ (III)	713.1	1.4	6.5
FeCl$_3$ (VI)	714.0	1.4	3.6
FeCl$_2$ (I)	709.8	1.2	12.9
FeCl$_2$ (II)	710.5	1.5	17.3
FeCl$_2$ (III)	711.5	1.4	11.7
FeCl$_2$ sat	715.5	1.3	5.4
Surface Peaks	713.8	2.0	3.7

Name	Pos.	FWHM	%Area
Pre-peak	707.9	1.0	0.1
FeCl3 (I)	711.6	1.4	25.2
FeCl3 (II)	712.7	1.4	20.1
FeCl3 (III)	713.6	1.4	9.8
FeCl3 (VI)	714.5	1.4	5.4
FeO (I)	708.7	1.4	12.1
FeO (II)	709.9	1.6	15.1
FeO (III)	711.2	1.6	7.3
FeO sat	714.7	6.2	1.0
Surface Peaks	715.5	1.5	3.9

Figure 3.27: Fitting of Fe 2p$_{3/2}$ spectra from GO mixed with FeCl$_3$ heated at 473 K. (a) Fit made using FeCl$_2$ and FeCl$_3$ fits the spectrum well, while (b) which is fit using FeCl$_3$ and FeO is shown to be a poor fit.

Table 3.11: Relative contributions of FeCl$_3$ FeCl$_2$ and FeO in the sample as the temperature increased from 473 to 573 K and a graph of these values.

Temperature / K	**Relative contribution / %**			
	FeCl$_3$	FeCl$_2$	FeO	
473	49.0	51.0	0.0	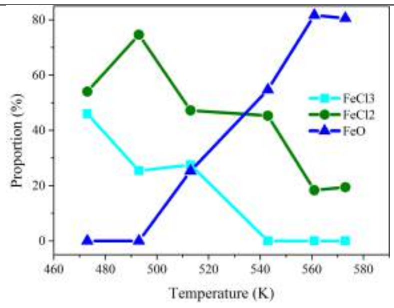
493	25.4	74.6	0.0	
513	27.5	47.2	25.3	
533	0.0	45.3	54.7	
553	0.0	18.3	81.7	
573	0.0	19.4	80.6	

The multiplet envelopes were distinct and only the combination of iron compounds used in this table could be used to fit the Fe $2p_{3/2}$ spectra. No other combination of multiplet envelopes, at any relative concentrations, would be able to fit the spectra as well. For the samples with Fe_xO_y in the O $1s_{1/2}$ spectra the use of multiplet envelopes made it was possible to confirm that it was FeO and not Fe_2O_3, Fe_3O_4 or FeOOH that was present in the sample.

At a temperature of 473 K, the oxidation state of the Fe ion was reduced from 3+ in $FeCl_3$ to 2+ in $FeCl_2$. This had the effect of increasing the carbonyl concentration in GO, as was shown in Fig. 3.24, and comparing this against the O $1s_{1/2}$ spectrum of GO at the same temperature (Fig. 3.5) the increase in carbonyl concentration can be understood as follows:

i. Fe^{3+} in $FeCl_3$ is reduced to Fe^{2+} in $FeCl_2$ and a chlorine anion is released
ii. GO is oxidised when a hydroxyl functional group loses its hydrogen and the remaining oxygen atom forms an epoxide in the flake
iii. The increased formation of epoxides results in an increased concentration of carbonyls in GO
iv. The carbonyls do not become carboxyls because there are no hydroxyl groups remaining, as evidenced by the equal %Area of the peaks representing carboxyls and hydroxyls in Fig. 3.24(a)
v. The redox reaction was subsequently balanced by the formation of HCl which can escape from the sample at elevated temperatures

As the temperature was raised, the $FeCl_2$ and $FeCl_3$ molecules decomposed and the Fe cation would be attracted to the electron rich oxygen atoms in the carbonyl groups on GO. The atoms are chemically bound to form FeO and this remains on the sample, while the remaining chloride ions can react to form chlorine gas. Here, the GO is reduced by the removal of the oxygen atom, while the chlorine atoms are oxidised when the gaseous chlorine is formed.

The equation for these reactions are represented as:

$$\text{GO–(C–OH)} + \text{FeCl}_3 \rightarrow \text{GO–(C=O)} + \text{FeCl}_2 + \text{HCl} \tag{3.7a}$$

$$\text{GO–(C=O)} + \text{FeCl}_2 \overset{\Delta}{\rightarrow} \text{rGO} + \text{FeO} + \text{Cl}_2 \tag{3.7b}$$

The presence of $FeCl_3$ in the sample facilitated the formation and subsequent removal of the carbonyl groups in GO and gave rise to the improved sheet resistance values shown in Table 3.8. However, due to the presence of FeO in the resulting film, the transmittance values of these films were far too low for practical use in TCEs. Considerable effort was spent into finding methods of FeO removal from the reduced GO sample, however no satisfactory method was found. In the following chapter, the use of GO in TCEs will be explored.

References

[1] T. Susi, M. Kaukonen, P. Havu, M. P. Ljungberg, P. Ayala, and E. I. Kauppinen. **Core level binding energies of functionalized and defective graphene**. *Beilstein J. Nanotechnol.*, **5**:121–132, 2014, `DOI:10.3762/bjnano.5.12`. 79, 93, 96

[2] Ivan Khrapach, Freddie Withers, Thomas H. Bointon, Dmitry K. Polyushkin, William L. Barnes, Saverio Russo, and Monica F. Craciun. **Novel Highly Conductive and Transparent Graphene-Based Conductors**. *Adv. Mater.*, **24**:1521–4095, 2012, `DOI:10.1002/adma.201200489`. 79, 123

[3] Guang-Xin Ni, Yi Zheng, Sukang Bae, Chin Yaw Tan, Orhan Kahya, Jing Wu, Byung Hee Hong, Kui Yao, and Barbaros Özyilmaz. **Graphene Ferroelectric Hybrid Structure for Flexible Transparent Electrodes**. *ACS Nano*, **6**:3935–3942, 2012, `DOI:10.1021/nn3010137`. 79

[4] Yue Chau Garen Kwan, Ging Meng Ng, and Cheng Hon Alfred Huan. **Identification of functional groups and determination of carboxyl formation temperature in graphene oxide using the XPS O 1s spectrum**. *Thin Solid Films*, **590**:40–48, 2015, `DOI:10.1016/j.tsf.2015.07.051`. 80, 107, 114, 118

[5] J. H Scofield. **HARTREE-SLATER SUBSHELL PHOTOIONIZATION CROSS-SECTION AT 1254 AND 1487 eV**. *J Electron Spectrosc. Relat. Phenom.*, **8**:129–137, 1976, `DOI:10.1016/0368-2048(76)80015-1`. 80, 96

[6] Shuai Wang, Perq-Jon Chia, Lay-Lay Chua, Li-Hong Zhao, Rui-Qi Png, Sankaran Sivaramakrishnan, Mi Zhou, Roland G.-S. Goh, Richard H. Friend, Andrew T.-S. Wee, and Peter K.-H. Ho. **Band-like Transport in Surface-Functionalized Highly Solution-Processable Graphene Nanosheets**. *Adv. Mater.*, **20**:3440–3446, 2008, `DOI:10.1002/adma.200800279`. 80

[7] Cecilia Mattevi, Goki Eda, Stefano Agnoli, Steve Miller, K. Andre Mkhoyan, Ozgur Celik, Daniel Mastrogiovanni, Gaetano Granozzi, Eric Garfunkel, and Manish Chhowalla. **Evolution of Electrical, Chemical and Structural Propeties of Transparent and Conducting Chemically Derived Graphene Thin Films**. *Adv. Funct. Mater.*, **19**:2577–83, 2009, `DOI:10.1002/adfm.200900166`. 81, 83, 85, 95

[8] Shujie You, Serhiy M. Luzan, Tamas Szabo, and Alexandr V. Talyzin. **Effect of synthesis method on solvation and exfoliation of graphite oxide**. *Carbon*, **52**:171–180, 2013, `DOI:10.1016/j.carbon.2012.09.018`. 81, 83, 86, 87

[9] O Akhavan. **The effect of heat treatment on formation of graphene thin films from graphene oxide nanosheets**. *Carbon*, **48**(2):509–519, 2010, `DOI:10.1016/j.carbon.2009.09.069`. 81, 84, 85, 89, 93

[10] Abhijit Ganguly, Surbhi Sharma, Pagona Papakonstantinou, and Jeremy Hamilton. **Probing the Thermal Deoxygenation of Graphene Oxide Using High-Resolution In Situ X-ray-Based Spectroscopies**. *J. Phys. Chem. C*, **115**(34):17009–17018, 2011, `DOI:10.1021/jp203741y`. 81, 82, 83, 84, 85, 89, 93, 95

[11] Alessandra Bonanni, Adriano Ambrosi, Chun Kiang Chua, and Martin Pumera. **Oxidation Debris in Graphene Oxide Is Responsible for Its Inherent Electroactivity**. *ACS Nano*, **8**:4197–4204, 2014, `DOI:10.1021/nn404255q`. 81, 85

[12] S. Kim, S. Zhou, Y. Hu, M. Acik, Y. J. Chabal, C. Berger, W. de Heer, A. Bongiorno, and E. Riedo. **Room-temperature metastability of multilayer graphene oxide films**. *Nat. Mater.*, **11**(6):544–549, 2012, `DOI:10.1038/nmat3316`. 81

[13] Wei Gao, Lawrence B. Alemany, Lijie Ci, and Pulickel M. Ajayan. **New insights into the structure and reduction of graphite oxide**. *Nat. Chem.*, **1**:403–408, 2009, `DOI:10.1038/nchem.281`. 81, 83, 91, 94

[14] Lin Ziyin, Yao Yagang, Li Zhuo, Liu Yan, Li Zhou, and Wong Ching-Ping. **Solvent-Assisted Thermal Reduction of Graphene Oxide**. *J. Phys. Chem. C*, **114**:14819–14825, 2010, `DOI:10.1021/jp1049843`. 81

[15] Chen Wufeng and Yan Lifeng. **Preparation of graphene by a low-temperature thermal reduction at atmosphere pressure**. *Nanoscale*, **2**:559–563, 2010, `DOI:10.1039/b9nr00191c`. 81

[16] Xiaochong Zhao, Hong Lin, Junfeng Li, Li Xin, Chenyang Liu, and Jianbao Li. **Low-cost preparation of a conductive and catalytic graphene film from chemical reduction with AlI3**. *Carbon*, **50**:3497 – 3502, 2012, `DOI:10.1016/j.carbon.2012.03.017`. 81, 84

[17] Kashyap Dave, Kyung Hee Park, and Marshal Dhayal. **Two-step process for programmable removal of oxygen functionalities of graphene oxide: functional, structural and electrical characteristics**. *RSC Adv.*, **5**:95657–95665, 2015, `DOI:10.1039/C5RA18880F`. 82

[18] Yan-Xin Liu, Zhong-Jie Du, Yan Li, Chen Zhang, Cong-Ju Li, Xiao-Ping Yang, and Hang-Quan Li. **Surface covalent encapsulation of multiwalled carbon nanotubes with poly(acryloyl chloride) grafted poly(ethylene glycol)**. *J. Polym. Sci. Part A: Polym. Chem.*, **44**:6880–6887, 2006, `DOI:10.1002/pola.21748`. 82

[19] Che-Ning Yeh, Kalyan Raidongia, Jiaojing Shao, Quan-Hong Yang, and Jiaxing Huang. **On the origin of the stability of graphene oxide membranes in water**. *Nat. Chem.*, **TBA**:TBA, 2015, `DOI:10.1038/nchem.2145`. 85

[20] Jonathan P. Rourke, Priyanka A. Pandey, Joseph J. Moore, Matthew Bates, Ian A. Kinloch, Robert J. Young, and Neil R. Wilson. **The Real Graphene Oxide Revealed: Stripping the Oxidative Debris from the Graphene-like Sheets**. *Angew. Chem. Int. Ed.*, **50**:3173–3177, 2011, `DOI:10.1002/anie.201007520`. 85

[21] Helen R. Thomas, Cristina Valles, Robert J. Young, Ian A. Kinloch, Neil R. Wilson, and Jonathan P. Rourke. **Identifying the fluorescence of graphene oxide**. *J. Mater. Chem. C*, **1**:338–342, 2013, `DOI:10.1039/C2TC00234E`. 85

[22] Xiaomeng Li, Xiaoyang Yang, Li Jia, Xiao Ma, and Liande Zhu. **Carbonaceous debris that resided in graphene oxide/reduced graphene oxide profoundly affect their electrochemical behaviors**. *Electrochem. Commun.*, **23**:94 – 97, 2012, `DOI:10.1016/j.elecom.2012.07.016`.

[23] Chenliang Su, Muge Acik, Kazuyuki Takai, Jiong Lu, Si-jia Hao, Yi Zheng, Pingping Wu, Qiaoliang Bao, Toshiaki Enoki, Yves J. Chabal, and Kian Ping Loh. **Probing the catalytic activity of porous graphene oxide and the origin of this behaviour**. *Nat. Commun.*, **3**:1298, 2012, `DOI:10.1038/ncomms2315`. 85

[24] Xiaobin Fan, Wenchao Peng, Yang Li, Xianyu Li, Shulan Wang, Guoliang Zhang, and Fengbao Zhang. **Deoxygenation of Exfoliated Graphite Oxide under Alkaline Conditions: A Green Route to Graphene Preparation**. *Adv. Mater.*, **20**:4490–4493, 2008, `DOI:10.1002/adma.200801306`. 85

[25] Helen R. Thomas, Stephen P. Day, William E. Woodruff, Cristina Vallés, Robert J. Young, Ian A. Kinloch, Gavin W. Morley, John V. Hanna, Neil R. Wilson, and Jonathan P. Rourke. **Deoxygenation of Graphene Oxide: Reduction or Cleaning?** *Chem. Mater.*, **25**:3580–3588, 2013, `DOI:10.1021/cm401922e`. 86, 87

[26] G. Beamson and D. Briggs. **High Resolution XPS of Organic Polymers - The Scienta ESCA300 Database**. Wiley Interscience, 1992. Appendices 3.1 and 3.2. 87

[27] Anton Lerf, Heyong He, Michael Forster, and Jacek Klinowski. **Structure of Graphite Oxide Revisited**. *J. Phys. Chem. B*, **102**:4477–4482, 1998, `DOI:10.1021/jp9731821`. 91, 95

[28] M. Z. Hossain, J. E. Johns, K. H. Bevan, H. J. Karmel, Y. T. Liang, S. Yoshimoto, K. Mukai, T. Koitaya, J. Yoshinobu, M. Kawai, A. M. Lear, L. L. Kesmodel, S. L.

TAIT, AND M. C. HERSAM. **Chemically homogeneous and thermally reversible oxidation of epitaxial graphene**. *Nat. Chem.*, **4**(4):305–309, 2012, `DOI:10.1038/nchem.1269`. 94

[29] D. D. L. CHUNG. **Graphite**. *J. Mater. Sci.*, **37**:1475–1489, 2002, `DOI:10.1023/A:10149153077378`. 95

[30] M.P. SEAH AND M. TOSA. **Linearity in Electron Counting and Detection Systems**. *Surf. Interface Anal.*, **18**:240–246, 1992, `DOI:10.1002/sia.740180309`. 98

[31] P.J. CUMPSON AND M.P. SEAH. **Random uncertainties in AES and XPS: II: Quantification using either relative or absolute measurements**. *Surf. Interface Anal.*, **18**:361–367, 1992, `DOI:10.1002/sia.740180509`. 98

[32] M.P. SEAH. **AES and XPS measurements: Reducing the Uncertainty and Improving the Accuracy**. *Appl. Surf. Sci.*, **70-71**:1–8, 1993, `DOI:10.1016/0169-4332(93)90388-R`. 98, 99

[33] N. FAIRLEY. **©Casa software Ltd.**, 2005. `http://www.casaxps.com`. 99

[34] SIGFRIED EIGLER, STEFAN GRIMM, FERDINAND HOF, AND ANDREAS HIRSCH. **Graphene oxide: a stable carbon framework for functionalization**. *J. Mater. Chem. A*, **1**:11559–11562, 2013, `DOI:10.1039/C3TA12975F`. 101

[35] CHU CHEN, WEIXIN KONG, HAI-MING DUAN, AND JUN ZHANG. **Theoretical simulation of reduction mechanism of graphene oxide in sodium hydroxide solution**. *Phys. Chem. Chem. Phys.*, **16**:12858–12864, 2014, `DOI:10.1039/C4CP01031K`. 101, 102, 105

[36] HUAFENG YANG, FENGHUA LI, CHANGSHENG SHAN, DONGXUE HAN, QIXIAN ZHANG, LI NIU, AND ARI IVASKA. **Covalent functionalization of chemically converted graphene sheets via silane and its reinforcement**. *J. Mater. Chem.*, **19**:4632–4638, 2009, `DOI:10.1039/B901421G`. 101, 104

[37] PRIYANK V. KUMAR, NEELKANTH M. BARDHAN, SEFAATTIN TONGAY, JINQIAO WU, ANGELA M. BELCHER, AND JEFFREY C. GROSSMAN. **Scalable enhancement of graphene oxide properties by thermally driven phase transformation**. *Nat. Chem.*, **6**:151–158, 2014, `DOI:10.1038/nchem.1820`. 107, 108, 116

[38] AYRAT M. DIMIEV, LAWRENCE B. ALEMANY, AND JAMES. M. TOUR. **Graphene oxide. Origin of acidity, its instability in water and a new dynamic structural model**. *ACS Nano*, **7**:576–588, 2013, `DOI:10.1021/nn3047378`.

[39] CHUN KIANG CHUA AND MARTIN PUMERA. **Light and Atmosphere Affect the Quasi-equilibrium States of Graphite Oxide and Graphene Oxide Powders**. *Small*, **11**:1266–1272, 2015, `DOI:10.1002/smll.201400154`. 108

[40] G. KRESSE AND J. HAFNER. **Ab initio molecular dynamics for liquid metals**. *Phys. Rev. B*, **47**:558, 1993, `DOI:10.1103/PhysRevB.47.558`. 108

[41] G. KRESSE AND J. HAFNER. **Ab initio molecular-dynamics simulation of the liquid-metal-amorphous-semiconductor transition in germanium**. *Phys. Rev. B*, **49**:14251, 1994, `DOI:10.1103/PhysRevB.49.14251`.

[42] G. KRESSE AND J. FURTHMLLER. **Efficiency of ab-initio total energy calculations for metals and semiconductors using a plane-wave basis set**. *Comput. Mat. Sci.*, **6**:15, 1996, `DOI:10.1016/0927-0256(96)00008-0`.

[43] G. KRESSE AND J. FURTHMLLER. **Efficient iterative schemes for ab initio total-energy calculations using a plane-wave basis set**. *Phys. Rev. B*, **54**:11169, 1996, `DOI:10.1103/PhysRevB.54.11169`. 108

[44] D. VANDERBILT. **Soft self-consistent pseudopotentials in a generalized eigenvalue formalism**. *Phys. Rev. B*, **41**:7892, 1990, `DOI:10.1103/PhysRevB.41.7892`. 108

[45] G. KRESSE AND J. HAFNER. **Norm-conserving and ultrasoft pseudopotentials for first-row and transition-elements**. *J. Phys.: Condens. Matter*, **6**:8245, 1994, `DOI:10.1088/0953-8984/6/40/015`. 108

[46] Lay-Lay Chua, Shuai Wang, Perq-Jon Chia, Lan Chen, Li-Hong Zhao, Wei Chen, Andrew T.-S. Wee, and Peter K.-H. Ho. **Deoxidation of graphene oxide nanosheets to extended graphenites by unzipping elimination**. *J. Chem. Phys.*, **129**:114702, 2008, `DOI:10.1063/1.2975330`. 113

[47] Sumit Saxena, Trevor A. Tyson, Shobha Shukla, Ezana Negusse, Haiyan Chen, and Jianming Bai. **Investigation of structural and electronic properties of graphene oxide**. *Appl. Phys. Lett.*, **99**:013104, 2011, `DOI:10.1063/1.3607305`. 115

[48] J. Tauc. **Optical Properties and Electronic Structure of Amorphous Ge and Si**. *Mater. Res. Bull.*, **15**:37–46, 1968, `DOI:10.1016/0025-5408(68)90023-8`. 116

[49] J. Tauc, R. Grigorovici, and A. Vancu. **Optical Properties and Electronic Structure of Amorphous Germanium**. *Phys. Status Solidi*, **15**:627–637, 1966, `DOI:10.1002/pssb.19660150224`. 116

[50] Akshay Mathkar, Dylan Tozier, Paris Cox, Peijie Ong, Charudatta Galande, Kaushik Balakrishnan, Arava Leela Mohana Reddy, and Pulickel M. Ajayan. **Controlled, Stepwise Reduction and Band Gap Manipulation of Graphene Oxide**. *J. Phys. Chem. Lett.*, **3**(8):986–991, 2012, `DOI:10.1021/jz300096t`. 116

[51] Si Zhou and Angelo Bongiorno. **Origin of the chemical and kinetic stability of graphene oxide**. *Sci. Rep.*, **3**:2484, 2013, `DOI:10.1038/srep02484`. 117, 119

[52] Garmor Tech. **Garmor**, 6317 McCoy Road, Suite 100, Orlando, Florida 32822, U.S.A. [Last checked Mar 2015]. `http://www.garmortech.com`. 121

[53] R.P. Gupta and S.K. Sen. **Calculation of multiplet structure of core p-vacancy levels. II**. *Phys. Rev. B*, **12**:15–19, 1975, `DOI:10.1103/PhysRevB.12.15`. 123, 127, 128

[54] K. Nagai, H. Kurata, S. Isoda, and T. Kobayashi. **Thermal behavior of stage-2 $FeCl_3$ graphite intercalation compound studied by analytical electron microscopy**. *J. Phys. Chem. Solids*, **53**:883–888, 1992, `DOI:10.1016/0022-3697(92)90114-S`. 123

[55] A.S. Skoropanov, T.A. Kizina, G.I. Samal, A.A. Vecher, Yu.N. Novikov, and M.E. Vol'pin. **Thermal analysis of graphite intercalation compounds with $FeCl_3$**. *Synth. Met.*, **9**:355–360, 1984, `DOI:10.1016/0379-6779(84)90002-X`.

[56] D. Herein, T. Braun, and R. Schlögl. **On the nature of the so-called iron-graphite**. *Carbon*, **35**:17–29, 1997, `DOI:10.1016/S0008-6223(96)00078-4`. 123

[57] Toru Yamashita and Peter Hayes. **Effect of curve fitting parameters on quantitative analysis of $Fe_{0.94}O$ and Fe_2O_3 using XPS**. *J. Electron Spectrosc. Relat. Phenom.*, **152**:6–11, 2006, `DOI:10.1016/j.elspec.2006.02.002`. 125

[58] Ernesto Paparazzo. **On the quantitative XPS analysis of Fe_2O_3 and $Fe_{1-x}O$ oxides**. *J. Electron Spectrosc. Relat. Phenom.*, **154**:38–40, 2006, `DOI:10.1016/j.elspec.2006.10.005`.

[59] Toru Yamashita and Peter Hayes. **Reply to Paparazzo**. *J. Electron Spectrosc. Relat. Phenom.*, **154**:41–42, 2006, `DOI:10.1016/j.elspec.2006.09.004`. 125

[60] Toru Yamashita and Peter Hayes. **Analysis of XPS spectra of Fe^{2+} and Fe^{3+} ions in oxide materials**. *Appl. Surf. Sci.*, **254**:2441–2449, 2008, `DOI:10.1016/j.apsusc.2007.09.063`. 125

[61] Ernesto Paparazzo. **XPS Analysis of Iron Aluminum Oxide Systems**. *Appl. Surf. Sci.*, **25**:1–12, 1986, `DOI:10.1016/0169-4332(86)90021-8`. 125, 126

[62] Ernesto Paparazzo. **XPS and auger spectroscopy studies on mixtures of the oxides SiO_2, Al_2O_3, Fe_2O_3, Cr_2O_3,**. *J. Electron Spectrosc. Relat. Phenom.*, **43**:97–112, 1987, `DOI:10.1016/0368-2048(87)80022-1`. 125

[63] N.S. McIntyre and D.G. Zetaruk. **X-ray photoelectron spectroscopic studies of iron oxides**. *Anal. Chem.*, **49**:1521–1529, 1977, `DOI:10.1021/ac50019a016`. 125, 128

[64] Mark C. Biesinger, Brad P. Payne, Andrew P. Grosvenor, Leo W.M. Lau, Andrea R. Gerson, and Roger St.C. Smart. **Resolving surface chemical states in XPS analysis of first row transition metals, oxides and hydroxides: Cr, Mn, Fe, Co and Ni**. *Appl. Surf. Sci.*, **257**:2717–2730, 2011, `DOI:10.1016/j.apsusc.2010.10.051`. 126, 128

[65] Aimé Mosser and Michelangelo Romeo. **Natural and synthetic copper phyllosilicates studied by XPS**. *Clay Clay Miner.*, **40**:593–95, 1992, `DOI:10.1346/CCMN.1992.0400514`. 126

[66] Mark C. Biesinger, Leo W.M. Lau, Andrea R. Gerson, and Roger St.C. Smart. **Resolving surface chemical states in XPS analysis of first row transition metals, oxides and hydroxides: Sc, Ti, V, Cu and Zn**. *Appl. Surf. Sci.*, **257**:887–898, 2010, `DOI:10.1016/j.apsusc.2010.07.086`. 126

[67] Jian-Xiong Li and An-Hua Liu. **Reduction of Copper Oxide Induced by 172nm Vacuum Ultraviolet Radiation at Ambient Temperature**. *J. Electron. Mater.*, **40**:2105–2110, 2011, `DOI:10.1007/s11664-011-1714-x`. 126

[68] A. P. Grosvenor, B. A. Kobe, M.C. Biesinger, and N.S. McIntyre. **Investigation of multiplet splitting of Fe 2p XPS spectra and bonding in iron compounds**. *Surf. Interface Anal.*, **36**:1564–1574, 2004, `DOI:10.1002/sia.1984`. 127, 128, 129

[69] Frank de Groot and Akio Kotani. **Core Level Spectroscopy of Solids**. CRC Press, 2008. Chap. 4. 128

4

Graphene Oxide Transparent Conducting Electrodes

Ultrasonic spray deposition was chosen as the method to fabricate a transparent conducting electrode (TCE) using GO. It allowed the reliable and repeatable fabrication of films while a high degree of control over various deposition parameters could be maintained. These parameters included concentration of the suspension, temperature of the substrate during deposition, the size and material that the substrate is made of.

This chapter begins with a theoretical study of the optimal thickness of a GO TCE based on the figure of merit (FOM), followed by a series of experiments that incrementally improve the FOM of the GO based TCE. The challenges were approached systematically with the various stages of development as follows:

Phase 1 – Spray deposition parameters

- Develop a baseline for the performance of a GO only TCE
- Establish ideal deposition parameters that give a good TCE

Phase 2 – Improving the reduction of GO

- Reduce sheet resistance by increasing the degree of reduction of GO
- Build on previous knowledge to optimise film thickness

Phase 3 – Addition of conductive network

- Find ideal method of using nanowires in the TCE
- Testing of network stability

4.1 Calculating Optimal Film Thickness

In Section 1.3.1, the sheet resistance and transmittance values of graphene were related to the thickness of the film by Equation (1.11) and (1.12) respectively. The equations were then combined to give a FOM for the TCE by calculating the $\sigma_{\mathrm{dc}}/\sigma_{\mathrm{op}}$ value of the film:

$$\frac{\sigma_{dc}}{\sigma_{op}} = \left[\left(\frac{1}{\sqrt{T}} - 1\right)\frac{2\,R_{sh}}{Z_0}\right]^{-1} \tag{4.1}$$

The number of GO layers present in the sample had to be a discrete integer number of monolayers and since these monolayers have a fixed thickness per monolayer and parametrizable sheet resistance and absorbance values, the FOM can be converted into an equation that is a function of the number of layers of GO present. Using N to represent the number of layers in the sample, the equations for the sheet resistance, $R_{sh}(N)$, and the transmittance, T (N), are

$$R_{sh}(N) = \frac{1}{e\mu n_i N} = \frac{2820}{N}\,\Omega/\square\; = \frac{R_0}{N}\,\Omega/\square \tag{4.2a}$$

$$T(N) = (1-\pi\alpha)^N = (1-\pi\frac{e^2}{\hbar c})^N = (97.7)^N\,\% = T_0^N\% \tag{4.2b}$$

where e = 1.602×10^{-19} C is the elementary charge, μ = (~10^5 cm^2/Vs) is the carrier mobility, $n_i \approx 2.22 \times 10^{10}\mathrm{cm}^{-2}$ is the approximate intrinsic carrier concentration in graphene, N is the number of layers, $\alpha \approx \frac{1}{137}$ is the fine structure constant and c = 3×10^8 m/s is the speed of light[1–4]. The value 2820 in the numerator of Equation (4.2a) is an estimate and depends on n_i which is in turn depends on the doping concentration of the layer.

For visual clarity, the symbols T_0 and R_0 were used to represent the transmittance and sheet resistance values of a monolayer of the graphene material, and the FOM equation becomes

$$\frac{\sigma_{dc}}{\sigma_{op}}(N) \;=\; \left[\left(\frac{1}{\sqrt{T_0^N}} - 1\right)\frac{2\,\frac{R_0}{N}}{Z_0}\right]^{-1} \tag{4.3}$$

Taking the differential of Equation (4.3) with respect to N,

$$\begin{aligned}\frac{d\,\frac{\sigma_{dc}}{\sigma_{op}}}{d\,N} &= \frac{d}{d\,N}\frac{Z_0}{2\,R_0}\left[\frac{N\,T_0^{\frac{N}{2}}}{1-T_0^{\frac{N}{2}}}\right] \\ &= \frac{Z_0}{2\,R_0}\left[\frac{T_0^{\frac{N}{2}}\left(1+N\ln(T_0)-T_0^{\frac{N}{2}}\right)}{(1-T_0^{\frac{N}{2}})^2}\right]\end{aligned} \tag{4.4}$$

Since Z_0 is a constant and R_0 and T_0 were constants for the system, it would be interesting to consider the effects of varying N for various T_0 values. Requiring N $\in \mathbb{Z}$, N $\geq$ 1 and 0 $\leq$ T_0 $\leq$ 1, only the determinant term, $\left(1+N\ln(T_0)-T_0^{\frac{N}{2}}\right)$, was of concern in this derivative; all other terms in the equation had a positive value. However, the determinant does not factorize neatly and it was instructive to graph it as a function of N for different values of T_0 as shown in Fig. 4.1.

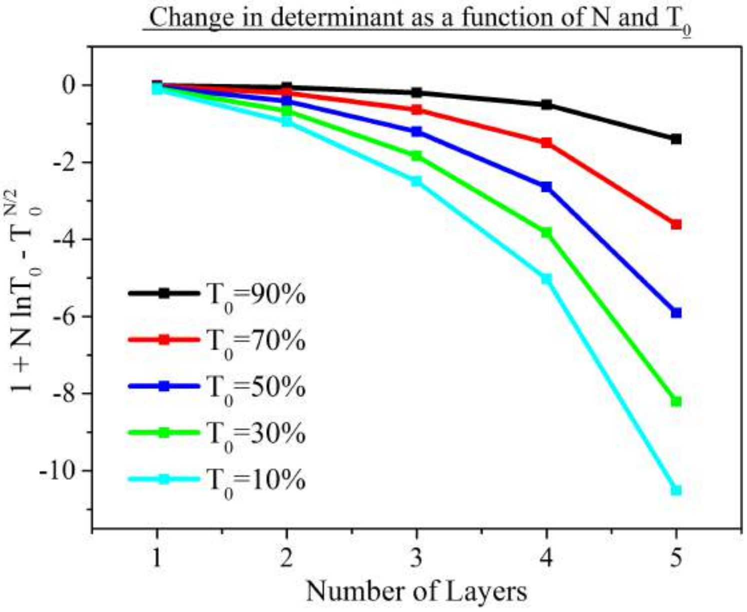

Figure 4.1: Graph showing how the determinant in Equation (4.4) changes for 1 $\leq$ N $\leq$ 5 and T_0 = 10, 30, 50, 70 & 90%. For all values of N, the number of layers, and T_0, the transmittance of a monolayer, the determinant is negative; this means that the derivative of $\frac{\sigma_{dc}}{\sigma_{op}}$ with respect to N is always negative and that the highest FOM value obtainable for any system is from a monolayer.

The determinant was negative for all allowed values of N and T_0 and this meant that the derivative in Equation (4.4) was also negative for all allowed values of N and T_0. In making a TCE, adding a layer over the absolute minimum number of layers required had the effect of reducing the TCE properties of the film.

This meant that the design principle behind fabricating a TCE using a layered material was to use the minimum number of sheets necessary to achieve the mechanical or conductive properties required of the film. The sheet resistance would then be reduced by increasing the carrier concentration of each sheet of the layered material.

While this theoretical background demands that TCEs be fabricated from the thinnest layers possible, other parameters exist to guide the fabrication process as well. Uniform surface coverage is required for good TCE fabrication and the random deposition pattern emitted from the nozzle during spray deposition may make it difficult to achieve a uniform deposition within one pass. Additionally, the arrangement of the GO flakes may change depending on how the layers are deposited and this may also have an effect on the resulting deposition and interactions that may occur due to the volume of suspension infused or the rate of nozzle motion may not have individually identifiable effects.

In the following section, these interactions were explored experimentally in order to characterize the effect of spray deposition parameters on the FOM of the resulting TCE.

4.2 Phase 1 – Spray Deposition Parameters

In the early stages of the Ph.D. work, films were fabricated with the goal of characterizing chemical information from the sample and control of the deposition was not considered. This changed when it came to the use of GO in the fabrication of TCEs. As GO is a highly transparent material, even more transparent than graphene, and ultra thin samples were required, it was near impossible to observe any colour changes on the transparent glass panel after deposition which would have indicated successful film fabrication. Typically, it was only after thermal reduction that the films would become visible on the glass panel.

The trick used to confirm that GO had been deposited onto the glass panel was to observe the subtle change in the colour of the edge of the panel after deposition. While the absorbance by a few layers of GO present would be insufficient to noticeably change the colour of light passing perpendicularly through the glass panel and GO layers, the light that is emitted from the edge of the glass panel arrives at the panel edge through a less direct route and in the process, the colour of the emitted light is changed.

After passing through the deposited GO film, the light beam enters the glass panel where, at the appropriate incidence angle, the light beam could undergo multiple internal reflections. The beam of light continues to propagate down the length of the glass panel and each time it was reflected of the top of the glass panel, as shown in Fig. 4.2, it would interact with the GO film. Interaction of the light ray with GO resulted in the reduction of the intensity of some wavelengths while achieving a good reflection of other wavelengths. At the end of these reflections,

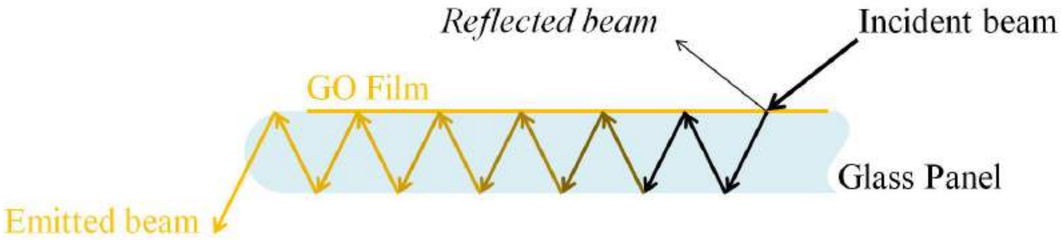

Figure 4.2: Schematic of a series of internal reflections occurring within the glass panel that imparts a brownish hue onto the light that is emitted from the edge of the glass panel when a layer of GO is deposited.

the light beam would have interacted with the GO film a sufficient number of times such that certain wavelengths were 'selected'.

The colour of light emitted from the edge of a normal glass panel was bluish-green and when a thin, nearly transparent layer of GO deposition was deposited onto the glass panel, the colour of the light emitted from the edge turned slightly brown. This observation gave confidence that a layer of GO had indeed been deposited onto the glass panel.

4.2.1 Optimization of parameters

Having developed confidence in the deposition technique, the deposition of a thin layer of GO was optimized by designing an experiment that would deposit a constant volume of GO suspension onto the glass panel, while varying the deposition parameters used to deliver the suspension. As the final volume of GO suspension used in the TCE may also influence the quality of the final film, this characterization was made starting with an arbitrary volume of GO.

Three parameters could be varied in the deposition process and they were the:

(i) suspension infuse rate,
(ii) number of passes per deposition cycle and
(iii) speed of nozzle motion.

These parameters were related according to the following equation:

$$\frac{\text{Infuse rate } \times \text{ Number of passes}}{\text{Nozzle move speed}} = \text{Constant volume} \tag{4.5}$$

A total of 16 different combinations of deposition parameters were used and these are summarized in Table 4.1. The infuse rate was varied between 0.025 and 0.100 ml min^{-1}, for between one and four deposition passes and the nozzle head move speed adjusted according to Equation (4.5). The width of the spray cone was approximately 20 mm and the volume of solution deposited onto each sample was estimated at 4.0 nl mm^{-2}. The concentration of the GO suspension here was 5.0 mg ml^{-1} and the GO suspension was deposited onto the glass panel with a coverage of about 1×10^{-8} g mm^{-2}. As a point of comparison, a monolayer of graphene weights 3.8×10^{-10} g mm^{-2} and dividing the mass of of GO deposited by this value gives an estimated deposition of 20 monolayer of GO in the film.[5].

Table 4.1: Tabulated values of the required spray head move rate for a given suspension infuse rate and number of deposition passes used in this experiment.

Infuse rate / μg ml^{-1}	1	2	3	4	**Number of Passes**
25.0	10.4	20.8	31.2	41.6	**Nozzle move speed / mm s^{-1}**
50.0	20.8	41.6	62.5	83.3	
75.0	31.2	62.5	93.7	125	
100	41.6	83.3	125	167	

GO was deposited onto cleaned glass panels according to the parameters in Table 4.1 with two samples being made for each set of deposition parameters. After deposition, the samples were thermally reduced by heating at 573 K for 15 hours. Following this, the samples were characterized for sheet resistance using the jig, for transmittance using the spectrophotometer and for thickness by atomic force microscopy. These average of these characterization values, along with the calculated $\sigma_{\mathrm{dc}}/\sigma_{\mathrm{op}}$ value are tabulated in Table 4.2.

While the experiment was planed such that the same volume of material would be deposited on every sample, the data in Table 4.2 showed that the depositions were not as similar as would have been expected. This was likely caused by dynamic interactions that happened between GO and the glass panel during spraying; adhesion between the glass panel and GO may be different just before GO arrived at the glass panel, when the glass panel was wet by the suspension and when a fresh suspension of GO was deposited onto an existing layer of GO on the glass panel that had already dried. Changing the volume deposited each time affected the wetness of the glass panel which would then affect the deposition.

A contour map of the $\sigma_{\mathrm{dc}}/\sigma_{\mathrm{op}}$ values proved to be instructive in this analysis. As seen in Fig. 4.3, the quality of the deposition, as defined by the $\sigma_{\mathrm{dc}}/\sigma_{\mathrm{op}}$ value, changed depending on the deposition parameters. In this case, the best TCE was fabricated by infusing the 5 mg/ml GO suspension at a rate of 50.0 μl/min over two passes. On average, these samples had a sheet resistance of 106 k$\Omega/\square$, a transmittance of 72.9 % and a corresponding $\sigma_{\mathrm{dc}}/\sigma_{\mathrm{op}}$ value of 10.4×10^{-3}.

Table 4.2: Sheet resistance, transmittance at a wavelength of 550 nm, thickness and σ_{dc}/σ_{op} values for the 16 deposition parameters used in the characterization experiment.

	Sheet Resistance / kΩ $\square^{-1}$				**Transmittance / %**				
Passes	1	2	3	4	1	2	3	4	**Passes**
25.0	206	301	204	170	69.8	74.5	74.5	59.8	
50.0	161	106	158	144	72.9	72.9	74.5	59.2	
75.0	108	131	156	122	67.3	71.1	73.1	63.4	
100	153	158	231	169	67.6	70.1	73.1	65.9	
Infuse Rate / μl min^{-1}	**Thickness / nm**				**σ_{dc}/σ_{op} / $\times 10^{-3}$**				
25.0	19.1	16.3	16.1	16.2	4.63	3.95	5.82	3.78	
50.0	14.7	12.7	37.3	31.6	6.82	10.4	7.54	4.37	
75.0	31.2	18.5	33.7	39.0	8.01	7.71	7.10	6.02	
100	22.5	15.7	36.1	40.1	5.71	6.15	4.81	4.82	

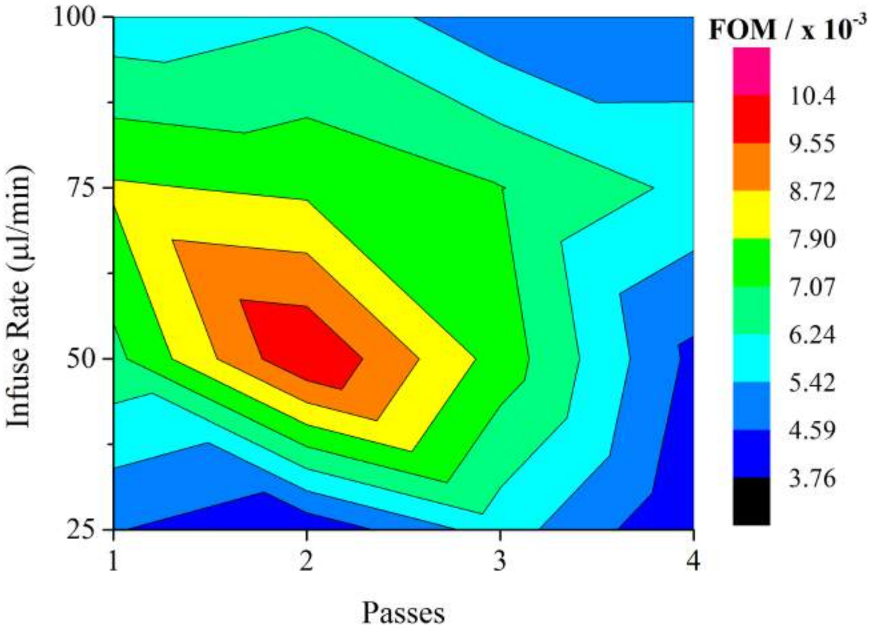

Figure 4.3: Contour map of the σ_{dc}/σ_{op} values from Table 4.2. The best samples were produced using 2 passes and a infuse rate of 0.050 ml/min giving a FOM of 10.4×10^{-3}.

As evident from the characterization results, these thermally reduced GO only films were neither sufficiently transparent nor were they sufficiently conductive for use as a TCE and much work would be required to bring it within range of the typical 85 % transmissivity and 15 Ω/□ of ITO. The modification strategy involved:

1. Improving the level of GO reduction
   This would increase the conductivity of the film and reduce its sheet resistance, but would reduce the transmittance of the film at the same time.
2. Making the GO film thinner
   This would improve the transmittance of the TCE and this is important as the transmittance of the same amount of GO would decrease further as the level of reduction was increased.

4.2.2 Repeatability of depositions

The reliability of the deposition was checked by fabricating three samples using the best parameters identified in the previous section and comparing their FOM values. The characterization values of these samples are tabulated in Table 4.3 and the transmittance with respect to wavelength graphed in Fig. 4.4.

As shown, the average $\sigma_{\mathrm{dc}}/\sigma_{\mathrm{op}}$ value of these samples was 9.8 × 10^{-3} and this was close to the FOM value of the optimized samples shown in Table 4.2. This meant that as long as the deposition parameters were replicated exactly, it would be possible to fabricate films of GO with very similar optoelectronic properties.

Table 4.3: Sheet resistance, transmittance and FOM value of 3 samples fabricated using the same deposition parameters. The samples showed some variations in transmittance and sheet resistance values but the range of variance was small.

Sample	**Transmittance @ 550nm / %**	**Sheet Resistance / kΩ □$^{-1}$**	$\sigma_{\mathrm{dc}}/\sigma_{\mathrm{op}}$ **/ ×10^{-3}**
1	73.5	110	10.3
2	74.9	120	10.1
3	72.1	118	9.0
Average	73.5±1.4	116±6	9.8±0.8

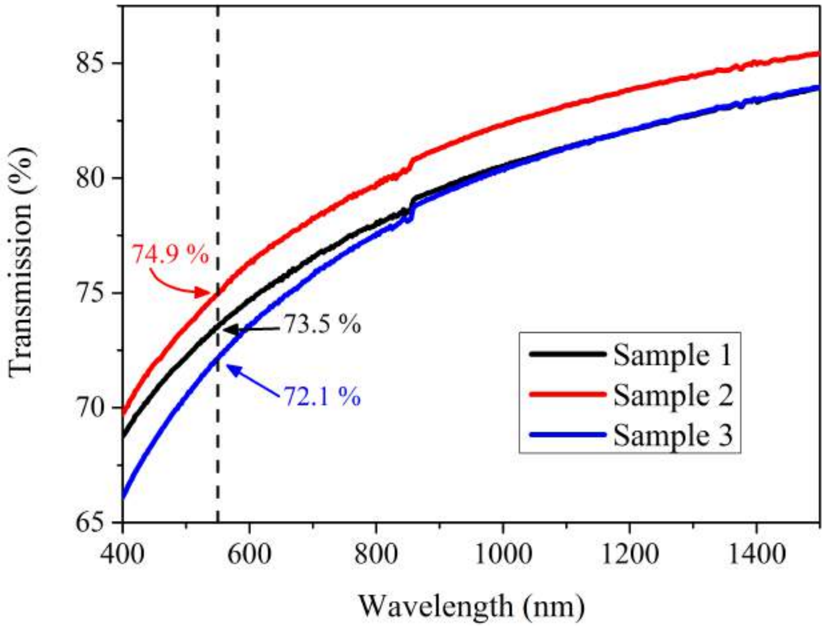

Figure 4.4: Transmittance graph of the three samples fabricated to test the reliability of depositions made by the ultrasonic spray coater. The transmittance of the samples at 550 nm are shown to be quite close, with an average value of 73.5±1.4 %.

While this preliminary check confirmed that the same deposition parameters would regularly give films with similar transmittance and sheet resistance properties, the reliability of this deposition technique will be further confirmed in the remainder of this chapter.

In the next section, experiments shown were designed to systematically analyse changes to the optoelectronic properties of the film when particular modifications were made to the fabrication steps. In many of the following experiments, a reference sample was made using a standard set of deposition parameters. These reference samples were compared to ensure no errors were introduced during the deposition process and across the experiments, these standard samples showed very little variation in their $\sigma_{\text{dc}}/\sigma_{\text{op}}$ values. In one experiment, eight samples were fabricated using the same deposition parameters and showed little variance in the sheet resistance and transmittance values, giving further proof that the deposition technique was reliable.

4.3 Phase 2 – Improving GO Reduction with Ascorbic Acid

As explained previously, the two point strategy of improving the GO TCE involved increasing the degree of reduction of the film and reducing the thickness of the film. These points will be addressed in the section, beginning with a method to improve the degree of reduction. While thermal reduction at a high temperature of 1373 K was shown to be very effective in removing the oxygen functional groups on GO, this exceptionally high operating temperature may become a problem when attempting to integrate reduced GO with another material that is not as thermally robust[6]. Alternatively, hydrazine is an excellent reagent that is capable of reducing GO to give reduced GO with a high C/O ratio. However, there exist real concerns regarding the use of this chemical at the industrial scale[7,8].

Hydrazine is a possibly-carcinogenic, combustible liquid that affects the reproductive systems in animals and is very toxic to aquatic organisms[9]. Where possible, it would be preferable that the large scale industrial application of this chemical be avoided. This hypothetical problem could become reality if GO were to be used to fabricate TCEs as large volumes of hydrazine would be required to reduce GO. The exhaust gases from this process, which will likely contain hydrazine, needs to be cleaned before discharge and it is desirable to avoid this chain of events.

In 2010, Gao *et al.* and Zhang *et al.* showed that AA was a useful reducing agent which had reduction capabilities rivalling those of hydrazine when used with GO[10,11]. On top of this, AA did not possess any of the environmentally harmful properties that hydrazine did and made it an ideal reagent for use in large volumes. Additionally, AA reduction of GO occurred at low temperatures and this meant that high operating temperatures could be avoided during film fabrication.

In the following section, the theoretical reaction between GO and AA is explained and after that, the experimental results from incorporating AA into a GO thin film are shown. There were many methods of incorporating AA into the GO matrix and the series of experiments that led to the fabrication of the best GO-AA TCE are tracked and explained here.

4.3.1 Theory of Reaction

In their report, Gao *et al.* gave a possible mechanism of GO reduction by the action of AA and the process is outlined in the schematic shown in Fig. 4.5[10]. They suggested that it was the hydroxyl groups on the furan of AA that reacted with the epoxy or hydroxyl group on GO by first forming bonds with GO and subsequently detaching itself from the carbon basal plane. In the process, GO would be de-oxygenated, a water molecule formed and a conductive π bond would be restored to the basal plane. In fact, they showed that reducing GO with AA resulted in a material that had a conductivity of 7700 S/m which was higher than the conductivity of 4160 S/m that the sample reduced using hydrazine had.

Although Gao *et al.* showed that GO reduced with AA had conductivities exceeding that of GO reduced by hydrazine, the sample produced by Zhang *et al.* had a conductivity of only 800 S/m[11]. The conductivity of GO reduce by hydrazine was ~4000 S/m and this means that besides using AA as a reduction agent, the process in which AA is introduced to GO and even the method of deposition have significant effects on the optoelectronic properties of the TCE.

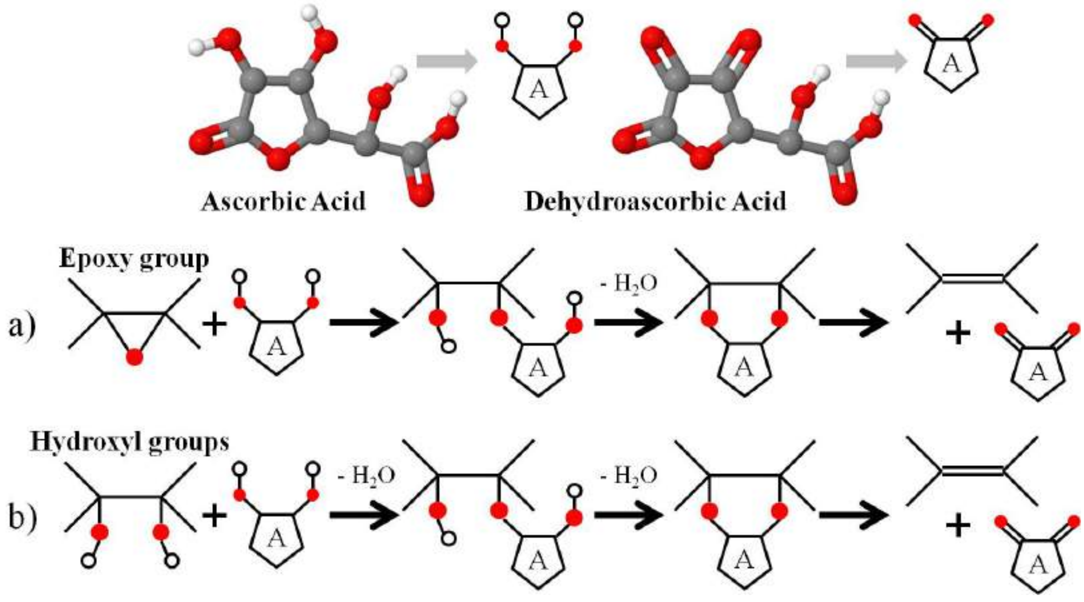

Figure 4.5: Schematic of the reduction reaction of AA on GO that removes (a) an epoxide and (b) a hydroxyl functional group from the basal plane. Grey, red and white spheres represent carbon, oxygen and hydrogen atoms respectively.

Adapted with permission from reference [10]. Copyright 2010 American Chemical Society.

As a final point, it was also shown that while being more environmentally friendly than hydrazine, AA had the same efficacy in the reduction of GO[12]. This was a compelling reason to employ AA in the chemical reduction of GO that would be deposited by ultrasonic spray coating for the fabrication of TCEs. Besides mixing GO with AA, there were also various pre- and post-deposition processes that could be employed to improve the reduction of GO and increase the FOM of the fabricated TCE. The task at hand was to optimize a strategy, through the manipulation of these deposition parameters, that would allow the fabrication of a TCE with a high $\sigma_{\mathrm{dc}}/\sigma_{\mathrm{op}}$ value.

4.3.2 Experiment Results

4.3.2.1 TGA Analysis of GO-AA Mixture

In this characterization, AA was a powder and used as-is, while AA was stirred into GO at mass ratio of 10:1 and the mixture quickly dried by dropping the mixture onto a glass panel kept at at 323 K. The GO-AA mixture formed a film on the glass panel and this film was scraped off the panel for use in the characterization. About 4 mg of each sample was used and these thermograms are shown in Figs. 4.6 & 4.7.

Thermogravimetric analysis of GO was conducted and the graph in Fig. 3.8 records a mass loss of 43.2 % at a temperature of 483 K. At a similar temperature, AA lost 38.3 % of its original mass, see Fig. 4.6, and using these values, the GO-AA mixture had an expected mass loss of 38.3 % at 500 K*.

However, the mass loss observed in the sample at 500 K was 28.3 % and this was less than three-quarters of the expected value. The disparity between the expected mass loss and the actual mass loss was likely due to the chemical interaction between GO and AA while the mixture was still an aqueous suspension. This results suggested that the chemical reaction between GO and AA happened quickly at room temperature and this had ramifications on the deposition method. Further to this, the effect of AA on OD had yet to be determined and this may have consequences on the conversion of OD into gaseous components as well.

On a positive note, this observation supported the hypothesized reactions between GO and AA that was shown in Fig. 4.5. Water and dehydroascorbic acid were the

---

* $\frac{1}{11} \times 43.2\% + \frac{10}{11} \times 37.8\% = 38.3\%$

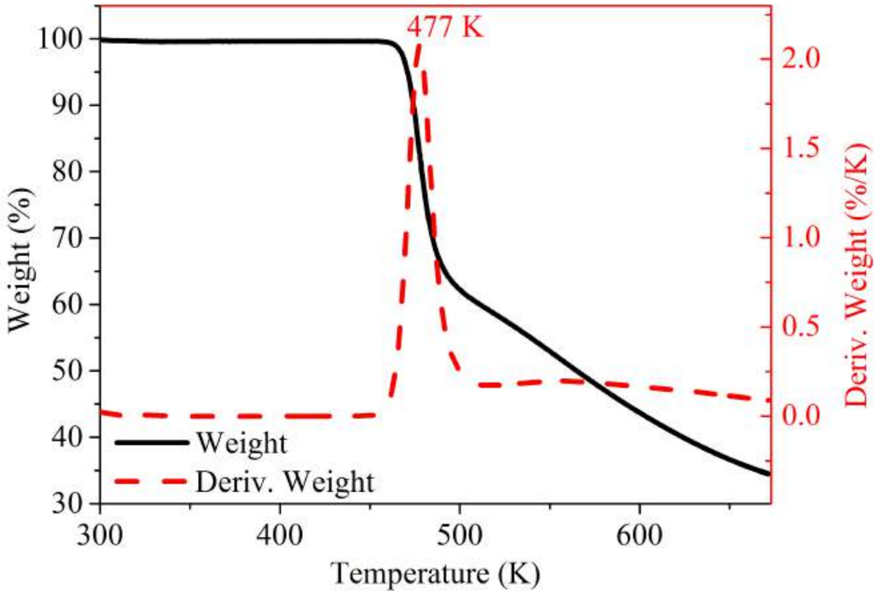

Figure 4.6: Thermogram of ascorbic acid that was heated from room temperature to 673 K at a rate of 5 K/min.

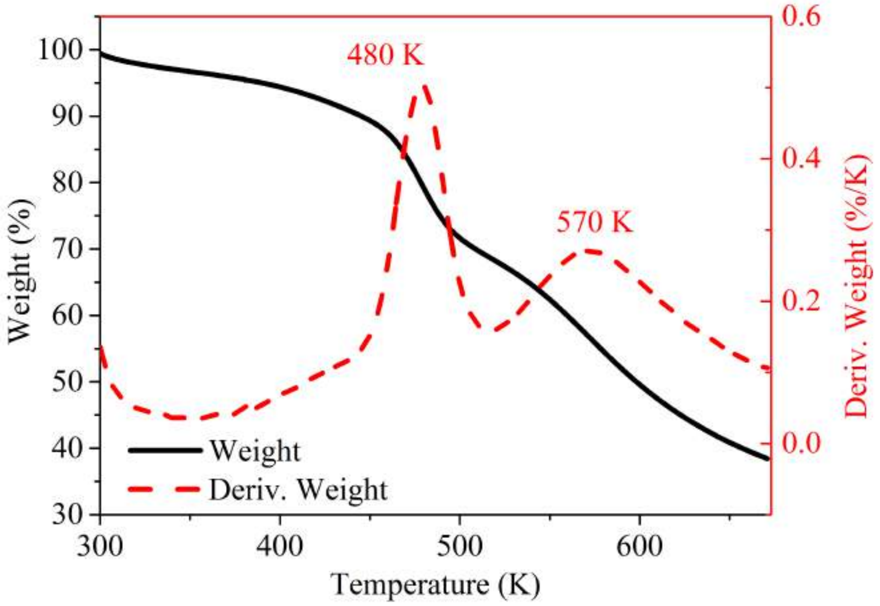

Figure 4.7: Thermogram of a GO and AA mixture that was dried before characterization. At 500 K, the total mass loss was 28.3 % and this was less than three-quarters of the expected mass loss.

products of the proposed reaction between GO and AA and these water molecules would have been removed when drying the suspension. Due to these reactions, there would be fewer oxygen functional groups available for thermally activated release and at any given temperature, the mass loss percentage in the mixture was expected to be lower than than the proportional sum.

As shown in Fig. 4.7, a second differential peak appeared at 570 K and this peak marked a further ~25 % loss in sample mass. Even so, at a temperature of 573 K, the percentage mass loss of the GO-AA mixture was 43.6 % and this was still lower than the predicted mass loss of 51.3 %.

4.3.2.2 Deposition Processes

A chemical reaction happened between GO and AA when the materials were mixed and the effects of these changes on the optoelectronic properties of the fabricated film will now be explored. It was assumed that the quality of the fabricated film depended on the fabrication technique and changes to the fabrication methods were made one step at a time. The changes were:

Step 1. Spray coating of premixed GO-AA
Step 2. Methods of improving films made by premixed GO-AA
Step 3. Dual-spray method to mix GO and AA just before deposition

Direct Mixing of GO and AA

The deposition mixture was made by adding 50 mg of AA directly to 30 ml of 5.0 mg/ml GO suspension and the contents thoroughly mixed by agitating the mixture. At this point, it was noted that adding an excess of AA to GO resulting in the quick formation of dark coloured clumps in the suspension and this was taken to mean that GO had been reduced and the clumps were made of hydrophobic reduced GO sheets. This clumping effect was also observed when the mixture was allowed to stand for a long period of time and the following experiment was devised to identify conditions that facilitated the fabrication of films with desirable optoelectronic properties.

After mixing AA into the GO suspension, the mixture was allowed to stand for either zero, one or two days at either room temperature or 353 K. In all the mixtures that were stood at 353 K, the GO flakes were no longer hydrophilic and had separated themselves from water to form a sediment at the bottom of the bottle; these mixtures could no longer be used for any depositions. The other samples that were left standing at room temperature for either one or two days also showed some sedimentation, however sufficient suspension could be taken from these mixtures to fabricate the samples.

These suspensions were deposited onto glass panels to form films and subject to thermal reduction at 573 K for 15 hours in a nitrogen environment either immediately after deposition or after thermal annealing at 353 K for three days. These processes and the corresponding optoelectronic properties of the resulting thin films are summarized in Table 4.4.

As shown, adding 50 mg of AA to 30 ml of 5 mg/ml GO suspension had little to no effect on the transmittance of the deposited films. These films exhibited a transmittance of ~70 % at 550 nm, which was similar to the 73.5±1.4 % of GO only films. However, this small reduction in transmittance was accompanied by a significant reduction in the sheet resistance of these films.

Comparing against GO only films and ignoring the effects of annealing for the moment, the sheet resistance values were observed to have fallen by up to 75 %, from 116 to 30.9 kΩ/□, and the $\sigma_{\mathrm{dc}}/\sigma_{\mathrm{op}}$ values of these films tripled, from 9.8 $\times$ 10^{-3} to 2.69 $\times$ 10^{-2}. The similar transmittance values meant that a similar quantity of GO had been deposited and the lower sheet resistance values showed that the electronic properties of the films had improved significantly.

However, the characterization results also showed that it would be difficult to fabricate TCEs reliably using this method. On one hand, the longer time between

Table 4.4: Characterization results of TCEs made from a GO-AA mixture. The solutions were allowed to stand at room temperature for between zero and two days and some of the deposited films were annealed for three days at 353 K before thermal reduction.

Time / Days	**Annealing?**	**Transmittance @ 550 nm / %**	**Sheet Resistance / kΩ $\square^{-1}$**	$\sigma_{\mathrm{dc}}/\sigma_{\mathrm{op}}$ **/ $\times 10^{-2}$**
0	No	64.4	34.2	2.69
	Yes	68.9	30.9	2.48
1	No	70.2	43.2	2.25
	Yes	72.7	64.9	1.68
2	No	72.4	28.2	3.81
	Yes	71.0	31.4	3.21

mixing and deposition, made the deposition more transparent and this was desirable. On the other hand, no trend was observable for the sheet resistance values, highlighting several shortcomings to this method:

(i) GO that had been reduced by AA had to be removed prior to deposition and this would have resulted in a GO suspension that had a concentration of less than 5.0 mg/ml

(ii) The process of separating the sediments from the aqueous GO suspension is inexact and the presence of remnant particles resulted in regular clogging of the ultrasonic spray nozzle

(iii) These problems affected the quality and reliability of the deposition process

Dual-Spray Method of Deposition

To prevent the formation of particulates in the suspension, AA had to be mixed with GO at the latest possible time. Post-deposition annealing would be introduced as some time was required for the the effects of metastability and the reaction between GO and AA to be completed before thermal reduction was performed. To achieve this, a dual-spray method of material deposition and an annealing step were introduced to the fabrication process.

AA was diluted into water at the same concentration as before, 1.67 mg/ml*, and GO was used at a concentration of 5 mg/ml. The materials were held in two separate reservoirs and fed into the nozzle via different feeding tubes. The materials were then mixed in the nozzle and in the air space while travelling from the nozzle to the substrate during the deposition process. This setup also allowed the concentration of AA to be varied by changing the volumetric flow rate of the AA solution. These deposition parameters are summarized in Table 4.5 and the effect of annealing on the optoelectronic properties of these samples was also tested.

The characterization results of these samples are summarized in Fig. 4.8 and the data showed a three- to five-fold increase in the $\sigma_{\mathrm{dc}}/\sigma_{\mathrm{op}}$ value over that of films made by the single feed method shown in Table 4.4. While the transmittance of samples that had the same concentration of AA had remained relatively constant at ~70 %, the sheet resistance of the samples had fallen greatly from over 30 kΩ/□ to 12.3 kΩ/□. The corresponding $\sigma_{\mathrm{dc}}/\sigma_{\mathrm{op}}$ value increased by about 3× from 0.027

---

[*] 50 mg of AA into 30 ml of water

Table 4.5: Parameters used to deposit each material in the dual-spray method of fabricating the TCEs.

1^{st} Feed Tube – Graphene Oxide		
Setting Number	Concentration / mg ml^{-1}	Infuse Rate / μl min^{-1}
1	*5.0*	*50*

2^{nd} Feed Tube – Ascorbic Acid		
Setting Number	Concentration / mg ml^{-1}	Infuse Rate / μl min^{-1}
1	*1.67*	*100*
2	*1.67*	*200*

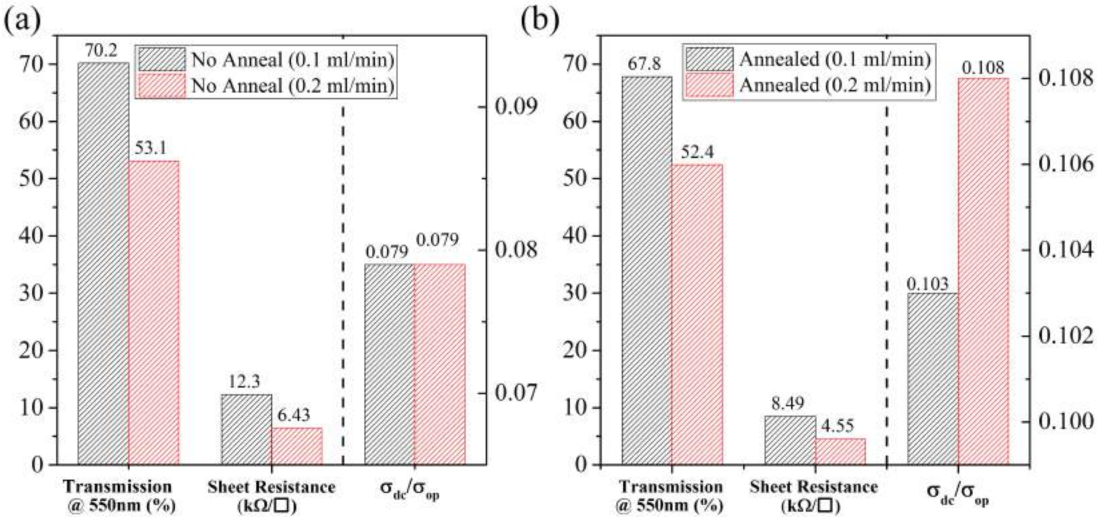

Figure 4.8: Characterization results of GO-AA thin films made by the dual-spray technique. (a) No annealing was performed and samples were thermally reduced immediately after deposition. (b) Samples were thermally annealed at 353 K in air for 72 hours before thermal reduction.

in the previous experiment to 0.079 here. As the concentration of AA in these films was kept the same, any improvement to the optoelectronic properties of this film were attributed solely to the use of the dual-spray method.

As shown in Fig. 4.8(a), increasing the concentration of AA in the film had the effect of reducing the sheet resistance from 12.3 to 6.43 kΩ/□, however the transmittance was reduced from 70.2 to 53.1 % at the same time. The film was more conductive but less transparent and the nett effect of this was no change in the average $\sigma_{\mathrm{dc}}/\sigma_{\mathrm{op}}$ values of these samples.

However, by introducing annealing, both the transmittance and sheet resistances of the TCEs decreased. The decrease in transmittance value was in-line with GO metastability[*] and overall a modest increase in the $\sigma_{\mathrm{dc}}/\sigma_{\mathrm{op}}$ values was recorded. The difference in $\sigma_{\mathrm{dc}}/\sigma_{\mathrm{op}}$ values of Figs. 4.8(a) & (b) also meant that the GO flake had changed as a result of thermal annealing.

Without annealing, the increased reduction of GO by the addition of more AA had no impact on the FOM value. Any improvements to the sheet resistance came at the cost of reduced transmittance. However, by thermal annealing, the sheet resistance of the films could be reduced further, with minimal impact on the transmittance, thereby allowing the FOM value to increase. As opposed to the situation without annealing, this represented an improvement to the quality of the deposited film. Furthermore, compared to GO only films in Table 4.3, these samples represented a hundred-fold increase in the $\sigma_{\mathrm{dc}}/\sigma_{\mathrm{op}}$ value that was achieved by improving the reduction of GO.

---

[*] Chapter 3.2

Vapour Annealing

Inspired by the quick reduction observed in the aqueous mixtures of GO and AA, a further development to the annealing step was tested by vapour annealing of the samples. Vapour annealing involves thermally annealing the samples in a high humidity environment and was accomplished by suspending the samples over a small volume of water in a sealed beaker and allowing the beaker and its contents to stand for 72 hours at 353 K.

After vapour annealing, the samples were thermally reduced in a nitrogen environment at 353 K for 15 hours, and the optoelectronic properties of the samples characterized after that. These results are shown in Fig. 4.9.

As a result of vapour annealing the transmissivity of the films was increased, the sheet resistance reduced and the corresponding $\sigma_{\rm dc}/\sigma_{\rm op}$ values increased. Comparing the $\sigma_{\rm dc}/\sigma_{\rm op}$ values of the samples in Figs. 4.8 & 4.9, it was clear that water vapour was required to improve the optoelectronic properties of the samples.

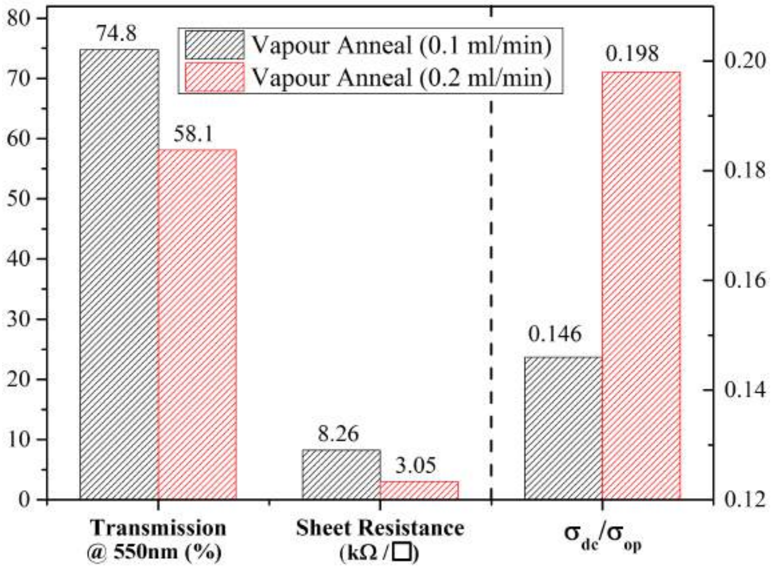

Figure 4.9: Characterization results of the GO-AA samples with annealing in a high humidity environment. A general improvement in the optoelectronic properties of all samples was observed.

Summary of Annealing Techniques

In all cases, samples that had a higher concentration of AA exhibited significantly lower transmissivity than samples with a lower concentration of AA. This reduction in transmissivity, due to the effect of a higher concentration of AA, offset any improvements to the FOM value that a decrease in the sheet resistance could give, resulting in the same $\sigma_{\mathrm{dc}}/\sigma_{\mathrm{op}}$ values. Allowing AA more time to react with GO by standing the samples at 353 K for 72 hours and the effects of GO metastability to occur on the sheet, it was observed that the sheet resistance of the films could be reduced further. In fact, the sample that had a higher concentration of AA exhibited a larger increase in the FOM than the sample that had less AA. This reduction was further improved by allowing water molecules to interact with the GO and AA mixture and the sample with more AA showed a larger improvement.

Beginning with no spread in $\sigma_{\mathrm{dc}}/\sigma_{\mathrm{op}}$ values of samples with different AA concentrations (Fig. 4.8(a)), the spread increased to 0.005 when the samples were allowed to stand for 72 hours at 353 K. By introducing a high humidity environment, the spread in FOM values was further increased to 0.052.

AA Infuse Rate

At this point, it had become clear that AA was instrumental in reducing the sheet resistance of the samples and that a good technique for its deposition had been developed. However, its presence in the film resulted in a reduction in the film's transmissivity. An experiment was thus designed to find an optimum infuse rate of AA for the fabrication of these GO based TCEs.

Keeping all other deposition parameters constant, the infuse rate of AA, with a concentration of 1.67 mg/ml, was varied between 0.05 and 0.20 ml/min and vapour annealing was conducted before the samples were thermally reduced. Three samples were made for each set of parameters and the average characterization results of these samples are displayed in Fig. 4.10.

As before, vapour annealing resulted in a higher $\sigma_{\mathrm{dc}}/\sigma_{\mathrm{op}}$ value and samples which had AA infused at a greater rate exhibited higher FOM values as well. Surprisingly, samples fabricated with AA infused at a rate of 0.15 ml/min exhibited the highest average $\sigma_{\mathrm{dc}}/\sigma_{\mathrm{op}}$ of 0.239; on average, these samples had a low sheet resistance of 2.55 k$\Omega/\square$ and a transmittance of 58.3 %. As the AA infuse rate was

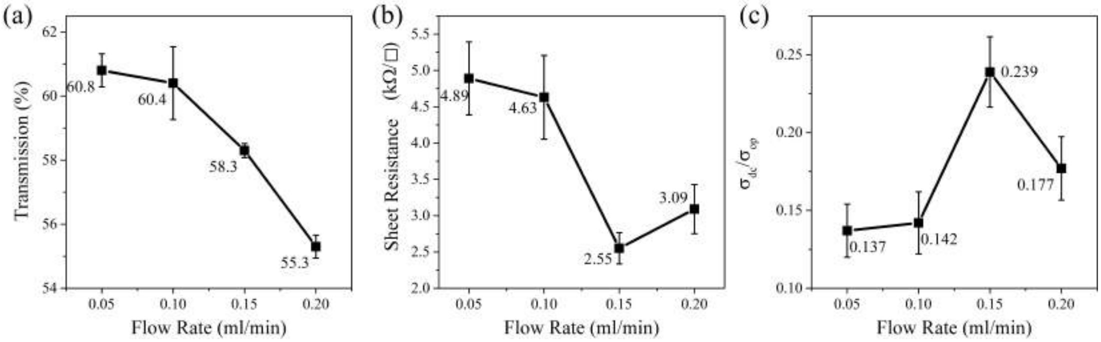

Figure 4.10: Effect of AA infuse rate on (a) the transmissivity at 550 nm, (b) the sheet resistance and (c) the calculated $\sigma_{\mathrm{dc}}/\sigma_{\mathrm{op}}$ value of the samples. The FOM value was maximized at a AA infuse rate of 0.15 ml/min.

increased from 0.05 to 0.20 ml/min, the ratio of AA to GO increased from 1:3 to 4:3 (as shown in Fig. 4.10(b)) and this increase initially resulted in an improved reduction of sheet resistance. This trend continued until the optimum AA:GO ratio of 1:1 was arrived at and beyond this, increasing the amount of AA resulted in an increase of the sheet resistance instead. This showed that besides reducing the transmissivity of the sample, an excess of AA in the sample had the effect of impeding electrical conductivity, thereby increasing the sample sheet resistance.

Effect of AA Concentration

While it had been established that the optimum GO to AA ratio was 1:1, it was not known if the AA infuse rate and if changing the volume of solution deposited had any appreciable effect on the quality of the samples. As such, the next step was designed to vary the concentration and flow rate of AA. The infuse rate of AA was reduced from 0.15 ml/min to 0.10 ml/min and the concentration of AA varied accordingly. To maintain a unity ratio of GO and AA, samples were fabricated using AA at a concentration of 2.5 mg/ml.

Other samples were also made with the same AA flow rate of 0.10 ml/min. AA with a concentration of 1.67 mg/ml was used so that these results could be compared with results from the previous batch and more samples were made with a high AA concentration of 8.35 and 12.5 mg/ml. Additionally, the time of vapour annealing was also varied in this experiment. Here, the samples were vapour annealed at 353 K for either 24 or 72 hours before thermal reduction in a nitrogen environment and two samples were made for each set of deposition parameters. A graph and a table of the characterization results of these samples is shown in Fig. 4.11 & Table 4.6 respectively.

The samples that were fabricated using an AA concentration of 1.67 mg/ml and annealed for 3 days had a $\sigma_{\rm dc}/\sigma_{\rm op}$ value of 0.144 and this was similar to the 0.142 of a sample fabricated in a similar manner in the previous experiment, Fig. 4.10(c). The highest average $\sigma_{\rm dc}/\sigma_{\rm op}$ value attained here was 0.248 for the samples that had an AA:GO ratio of 1:1 and this was slightly higher than the 0.239 of the comparable sample in the previous experiment. This showed that the optoelectronic properties of the samples were not significantly affected by the *infuse rate* of AA and the *concentration* of AA in the sample was of greater importance.

Furthermore, this experiment established that there was no advantage to having an excess of AA during fabrication. As seen from samples that used an AA concentration of 8.35 and 12.5 mg/ml, increasing the AA concentration reduced the $\sigma_{\rm dc}/\sigma_{\rm op}$ values of the films. It was also observed that a longer annealing time had the effect of raising the $\sigma_{\rm dc}/\sigma_{\rm op}$ values of the samples and improving the repeatability of the results, as evidenced by the smaller spread in the data points.

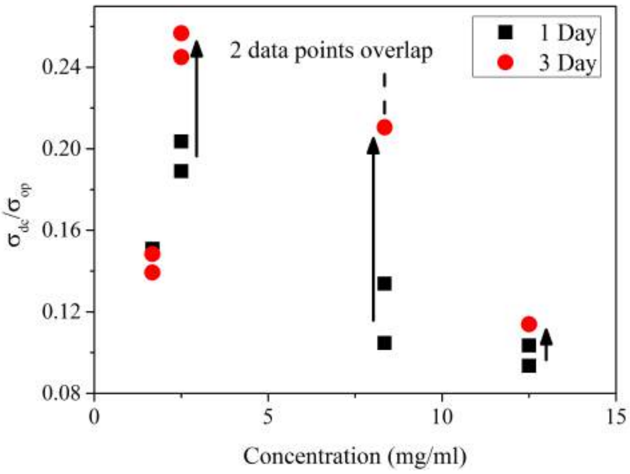

Figure 4.11: $\sigma_{\rm dc}/\sigma_{\rm op}$ values of samples that were fabricated with AA of different concentrations. The samples that were annealed for three days had a smaller variation in $\sigma_{\rm dc}/\sigma_{\rm op}$ values and showed an overall improvement over samples that were annealed for one day.

Table 4.6: Characterization results of samples that were fabricated with varying AA concentrations and annealed for either one or three days.

	1 Day Annealing		
AA Concentration / mg ml^{-}1	**Transmittance @ 550 nm / %**	**Sheet Resistance / kΩ □$^{-1}$**	$\sigma_{\mathrm{dc}}/\sigma_{\mathrm{op}}$
1.67	61.8	5.99	0.123
2.50	57.6	3.03	0.196
8.35	54.9	4.64	0.116
12.5	44.3	3.83	0.098

	3 Day Annealing		
AA Concentration / mg ml^{-}1	**Transmittance @ 550 nm / %**	**Sheet Resistance / kΩ □$^{-1}$**	$\sigma_{\mathrm{dc}}/\sigma_{\mathrm{op}}$
1.67	56.2	3.94	0.144
2.50	60.0	2.61	0.248
8.35	48.2	2.04	0.210
12.5	48.5	3.79	0.114

Summary of Optimized Deposition Parameters

Thus far, changes to the method of fabrication and associated incremental improvements to the $\sigma_{\mathrm{dc}}/\sigma_{\mathrm{op}}$ value of TCE samples fabricated by the technique of low temperature thermal reduction of GO were shown. Starting with GO only films, the method of thermal annealing, the inclusion of AA and the method of vapour annealing were progressively applied onto the depositions to improve its optoelectronic properties. The effect of these parameters on the quality of the deposition were explored and their effects on the optoelectronic properties of the deposited films characterized. These steps and the $\sigma_{\mathrm{dc}}/\sigma_{\mathrm{op}}$ values of the best samples are shown in Fig. 4.12.

While the resulting deposition could be made more transparent by fabricating thinner films, the sheet resistance would increase and the performance of the TCE would be limited by the maximum $\sigma_{\mathrm{dc}}/\sigma_{\mathrm{op}}$ achieved here. In other words, while it would be possible to fabricate a thin film of AA reduced GO with a transmittance of 90 %, based on the maximum $\sigma_{\mathrm{dc}}/\sigma_{\mathrm{op}}$ value of 0.248 shown here, this film would have an associated sheet resistance of 14 kΩ/□.

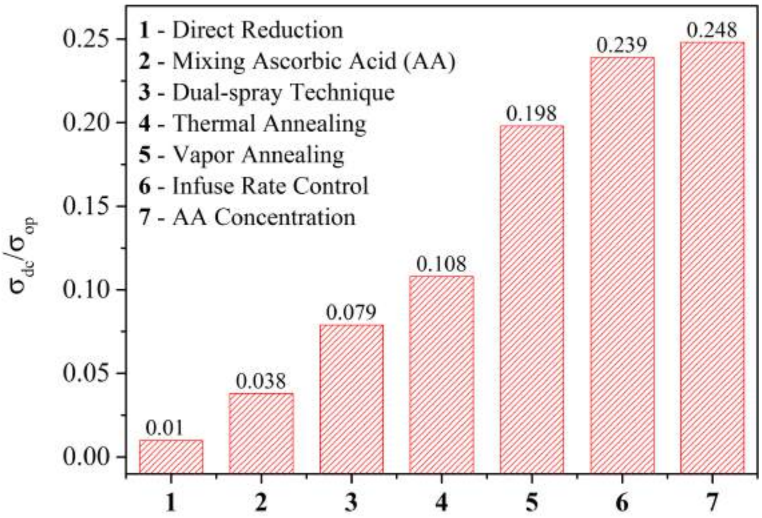

Figure 4.12: Progressive increase in the $\sigma_{\mathrm{dc}}/\sigma_{\mathrm{op}}$ value of the GO based TCEs. Starting from a minimum of 0.01 in GO only films, changes in the fabrication steps resulted in a 25-fold increase in the average $\sigma_{\mathrm{dc}}/\sigma_{\mathrm{op}}$ value of the samples.

The $\sigma_{\mathrm{dc}}/\sigma_{\mathrm{op}}$ results here set some boundary conditions on the possible uses of AA reduced GO and showed that the experiments were fast approaching a limit of how transparent and conductive reduced GO films could be made; it appeared that the experiments were reaching an upper limit for the $\sigma_{\mathrm{dc}}/\sigma_{\mathrm{op}}$ values of reduced GO. It would not be possible to improve the optoelectronic properties of the film beyond this point as the processes used in the fabrication would not reduce the GO material any further and this meant that the sheet resistance values would not be expected to decrease any further as well.

4.4 Phase 3 – Transparent Conductor using GO & Silver Nanowires

Further improvements to a TCE made using GO required that the conductivity of the film be improved significantly while keeping the impact on the transmittance at a minimum. To achieve this, silver nanowires (AgNW) were employed in the film by mixing the nanowires directly into GO. While this worked to improve the conductivity of the film, the hydrophilic nature of the GO flakes meant that the loading capacity of silver nanowires within the GO matrix was limited by the concentration of AgNW in its isopropanol solvent. Attempts were made to increased the concentration of AgNW in isopropanol before mixing with GO, however these attempts failed.

The next method involved depositing AgNW and GO in separate steps, allowing a high degree of control over the quantity of each material that was eventually deposited. From this, the optoelectronic properties of the TCEs were shown to increase dramatically and it was also observed that the application of the GO layer onto the AgNWs improved the nanowire's resistance towards thermal degradation.

A thorough study was made and it was shown that capillary instability was the root cause of thermal degradation in the AgNWs. Modelling of the time to failure of these nanowires was then studied and the calculated values compared with experimental findings. Following this attempts to improve the model are examined.

In the following sections, details on the improvements to the optoelectronic properties of GO-AgNW TCEs are shown and discussed. Following this, capillary instability in nanowires is explained and the viability of time to failure modelling from this theory discussed.

Section 4.4 is based on the publication *"Time to failure modelling of silver nanowire transparent conducting electrodes and effects of a reduced graphene oxide over layer"*[13].

4.4.1 Mixing GO, AA and AgNW

Mixing GO with AgNW

In the first experiment, AgNWs suspended in isopropanol were purchased from Sigma Aldrich and the suspension was stirred into the GO suspension. These nanowires had an expected diameter of 110 nm, lengths of between 20 and 50 μm and were suspended in isopropanol at a concentration of 0.5 %. They were fabricated by the polyol process and the nanowire surface was stabilized by a coating of polyvinylpyrrolidone, allowing the growth of very long nanowires[14–16].

Isopropanol is miscible in water and when used at low concentrations, the addition of the AgNW suspension did not appear to have any effect on the GO suspension. The main concern here was that while the AgNWs are stiff and can suspended in both water and isopropanol, GO flakes are hydrophilic and flexible and changing the solvent could inadvertently affect the dispersibility of the GO suspension[17,18].

The AgNW suspension was mixed into the GO suspension with increasing volumetric ratio and the mixture stirred to ensure a good dispersion of the AgNWs among the GO flakes. To five parts of GO suspension, one, two or three parts of the AgNW suspension were added and the mixture stirred for at least 30 minutes using a magnetic stirrer before deposition.

The dual spray method of infusing the GO suspension and ascorbic acid, at a concentration of 1.67 mg/ml, separately was by far the best method of fabricating a reduced GO TCE and the process was employed in this experiment. However, the addition of the AgNW suspension would dilute the GO suspension and this meant that there was now less GO present in the new TCEs.

Despite keeping the deposition process identical, the final effect on the optoelectronic properties of the resulting TCE was a complex interplay between the:

1. Effect of isopropanol on GO flakes
   The presence of isopropanol may affect the GO flakes in the suspension negatively as the GO sheets could curl up into ball-like structures to minimise the surface area in contact with isopropanol.
2. Dilution of the GO suspension by isopropanol
   Adding a large volume of isopropanol to the GO suspension meant diluting the suspension. Since the deposition parameters would not be changed, this should result in thinner, more transparent films. However, the presence of

AgNWs in the film has to be taken into account as well and the final effect on the transmittance can only be determined experimentally.

3. Effectiveness of AgNW dispersion among the GO flakes
   Despite the long stirring times, it is not know if and how well the nanowires would attach themselves to the GO flakes.
4. Effect of AgNWs on film conductivity
   The AgNWs are significantly more conductive than the GO flakes and this was expected to reduce the sheet resistance significantly if it is well dispersed among the GO flakes.
5. Reduction in transmittance due to presence of AgNW
   Unlike GO flakes, AgNWs are opaque, which reduces the total transmittance of the fabricated TCE and opposes the increase in transmittance mentioned in point 2.

As can be seen, there is a complex combination of, effects that finally determine the $\sigma_{\mathrm{dc}}/\sigma_{\mathrm{op}}$ value of these films. Many optimizations could have been made to maximize the FOM value of these films, but of primary importance was the need to find out how much AgNW suspension was needed to make the sheet resistance of the final TCE comparable to that of ITO.

Dispersion of AgNW within GO upon deposition

Three different mixtures of GO and AgNW were made and only the GO:AgNW suspensions that were mixed at a ratio of 4:1 and 3:2 were usable after stirring. In the suspension that had a GO:AgNW volumetric ratio of 2:3, the large volume of isopropanol caused the GO sheets to agglomerate and these agglomerations were too large to pass through the ultrasonic spray nozzle.

Of the remaining two mixtures, one sample was made using each mixture and the samples studied under optical microscope. These images are shown in Fig. 4.13 and despite the increase in AgNW suspension added to the GO suspension the increase in the quantity of nanowires present was not discernible by simple visual observation.

Moving from the mixing ratio of 4:1 to 3:2, the concentration of AgNWs was expected to have doubled and the concentration of GO reduced by 25 %. This suggested that films made using the second mixing ratio would be more transparent and conductive than films made using the first mixing ratio. Five samples were made using each mixing ratio following the optimized procedures developed in the previous section and the transmittance, sheet resistance and calculated σ_{dc}/σ_{op} ratios of these samples tabulated in Table 4.7.

Comparing the characterization data shown in Table 4.6 and 4.7, the introduction of AgNWs to GO increased the transmittance of the films from 60.0 to 75.0 % while maintaining the low sheet resistance values. This was achieved because GO had been 'displaced' from the film by the introduction of AgNWs. At the same time, the associated increase in sheet resistance that was expected with the reduction in GO concentration, was countered by the presence of the highly conductive AgNWs. The decrease in transmittance caused by these AgNWs was

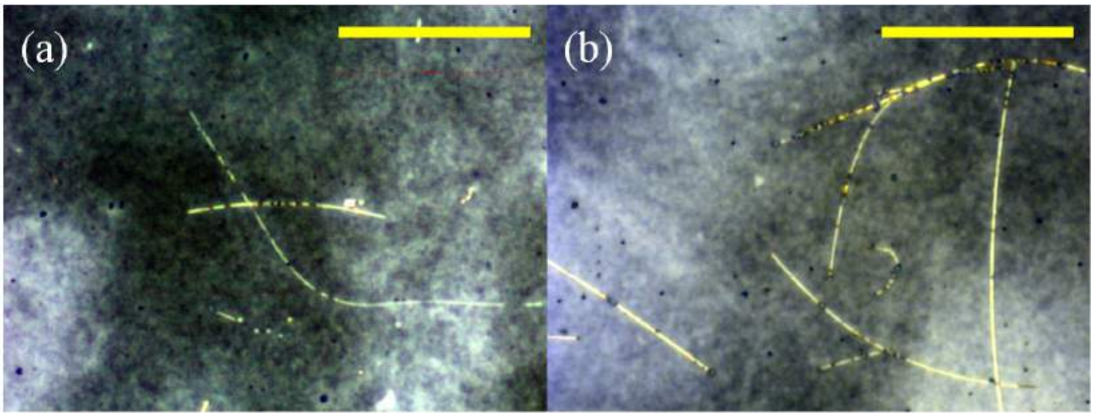

Figure 4.13: Optical images of films made from GO mixed with AgNW in volumetric ratios of (a) 4:1 and (b) 3:2. While the concentration of AgNWs in the film had doubled, this was not discernible by simple visual observation. The scale bars in the images are 20 μm long.

Table 4.7: Characterization results of films made using AA-reduced GO and AgNWs which were mixed with different volumetric ratios. %T – Transmittance at 550 nm, R_{sh} – Sheet resistance in k$\Omega/\square$.

GO:AgNW Ratio	**4:1**			**3:2**		
Sample	**%T**	**R_{sh}**	**σ_{dc}/σ_{op}**	**%T**	**R_{sh}**	**σ_{dc}/σ_{op}**
1	76.6	4.39	0.302	78.6	2.98	0.493
2	75.0	4.60	0.265	78.7	2.49	0.595
3	76.6	4.86	0.272	74.3	4.26	0.277
4	72.5	4.10	0.263	70.9	2.73	0.368
5	71.6	2.29	0.453	75.1	3.03	0.404
<Average>	*74.5*	*4.05*	*0.311*	*75.5*	*3.10*	*0.427*

less than the increase in transmittance due to the reduction of GO content in the film and this resulted in the overall nett increase in film transmittance.

The overall effect of these improvements are reflected in the $\sigma_{\mathrm{dc}}/\sigma_{\mathrm{op}}$ values, which increased from 0.248 in AA reduced GO films to 0.311 and 0.427 in the films here. However, it was also noted that the process was made less reliable when the GO and AgNW mixture was used. Of the five samples fabricated using each mixture, one sample in each set exhibited an abnormally high or low sheet resistance value, likely due to inconsistencies introduced to the deposition process when isopropanol interacted with the GO sheets.

However, as shown here, increasing the concentration of AgNWs in the GO films resulted in an overall improvement in the optoelectronic properties of these films. While it would have been desirable to increase the concentration of AgNWs in the mixture, this was not possible and an alternative method was needed. Ideally, this alternative method would increase the concentration of AgNWs in the GO films without compromising on the reliability of the deposition process.

4.4.2 GO over layer on AgNW network

The AgNW concentration in the film was increased by depositing the AgNW and GO in two separate deposition steps. AgNW would first be deposited onto the glass panel to achieve a percolating network and the AA-reduced GO would then be deposited as an over layer onto this AgNW network. With this modification, the bilayer architecture would allow full control over the optoelectronic properties of the resulting film, as long as the deposition parameters of the AgNW and GO suspensions were well controlled.

Adhesion of AgNW onto Glass Panel

As a first level test, the quality of the adhesion between the AgNWs and the glass substrate was investigated. Demonstrably good adhesion between the AgNWs and glass substrates was required as the GO over layer would be deposited onto the AgNWs in a second deposition step. The two-step deposition process would have been futile if the second deposition step caused the removal of material deposited in the first step.

To one part of the original AgNW suspension, nine parts of isopropanol was added and the diluted suspension stirred for 30 minutes before deposition was attempted. The suspension was sprayed onto a cleaned glass panel and the panel moved to an optical microscope where a picture of the AgNWs on the glass panel was taken. After this, more AgNW suspension was deposited onto the glass panel and another image of the AgNWs on the panel taken and this process was repeated a further 13 times.

In all, 15 deposition cycles were made and a selection of these optical images shown in Fig. 4.14. As shown in this series of images, neither the effect of successive deposition cycles nor the mechanical agitation of transport from the spray coater to the microscope resulted in the removal of the AgNWs once they had been deposited. The strength of the adhesion between the AgNWs and the glass substrate was sufficient to prevent the loss of the nanowires during the fabrication process and this meant that the bilayer TCE could be fabricated.

The optoelectronic properties of this AgNW network were also characterized and the UV-vis spectrum of this film shown in Fig. 4.15. In this sample, the AgNW network had a transmittance of 86.0 % at a wavelength of 550 nm and a sheet resistance of 34.4 $\Omega/\square$. This gave an estimated AgNW network density of 40 mg/m^2 and a calculated $\sigma_{\mathrm{dc}}/\sigma_{\mathrm{op}}$ value of 70.0, which was the highest $\sigma_{\mathrm{dc}}/\sigma_{\mathrm{op}}$ value achieved thus far[19]. This good result in the AgNW network meant that further improvements could be expected after the AA reduced GO over layer was incorporated.

By themselves, AgNW networks displayed very good optoelectronic properties, but it was also known that AgNW networks were not stable and would degrade when stressed[20]. Under mild operating conditions, this stress could lead to electrode failure in as little as 18 days and this did not bode well for these AgNW based electrodes. 18 days was far too short a lifetime and meant that AgNWs could not be a standalone solution for electrode replacement. However, through the application of an over layer or addition of a passivating material, the AgNWs could be protected from degradation and the lifetimes of these electrodes extended and this would be tested next[21–24].

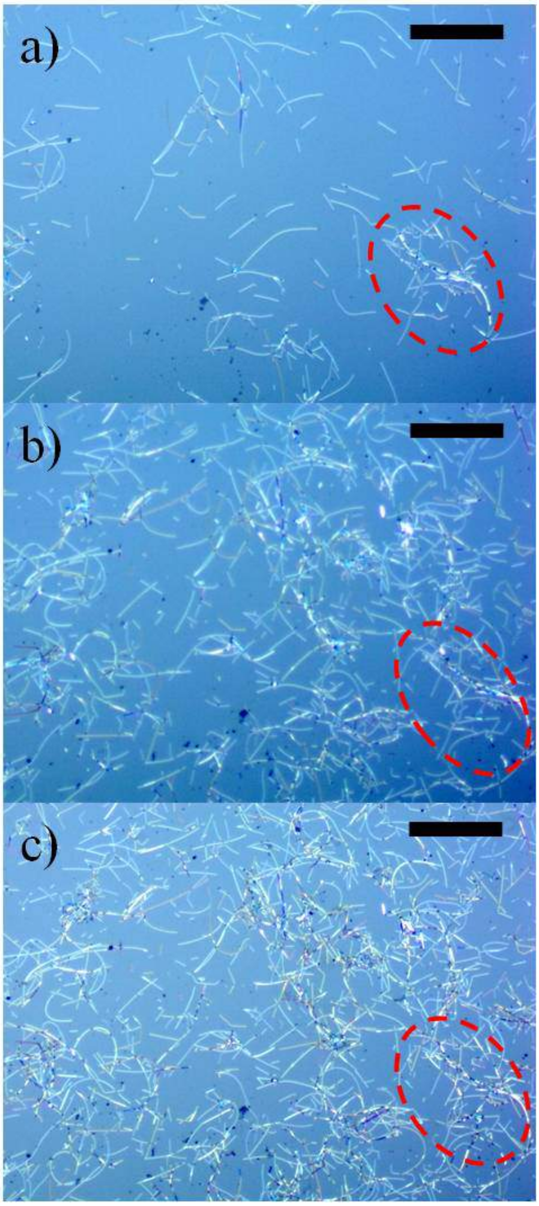

Figure 4.14: Optical microscope images of spray deposited AgNWs after multiple deposition cycles. An image was taken at approximately the same location after each deposition cycle and the images for the (a) 1st, (b) 5th and (c) 15th deposition cycles are shown here. The red-dashed circle highlights a distinct feature that was tracked across the deposition cycles and the scale bar inset is 50 μm long.

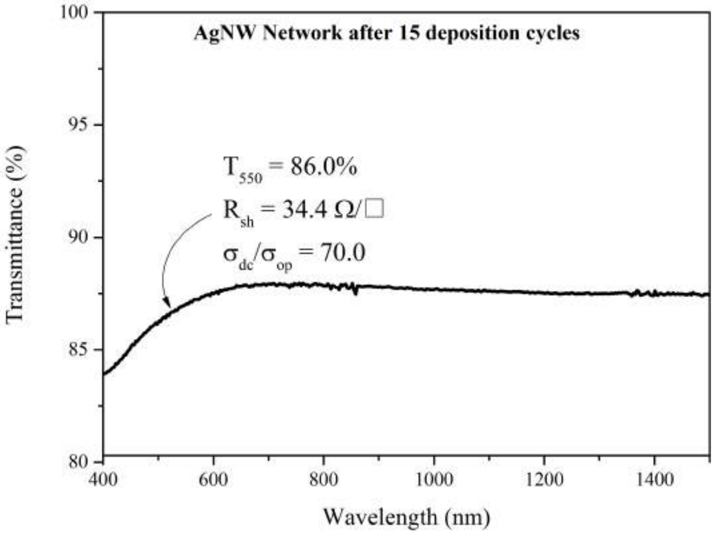

Figure 4.15: UV-vis spectrum of AgNW network. The deposited film had a transmittance of 86.0 % at 550nm, a sheet resistance of 34.4 Ω/□ and a σ_{dc}/σ_{op} value of 70.0.

Application of GO over layer

The AA reduced GO films fabricated in Chapter 4.3 would not be transparent enough for use in this application and thinner films had to be fabricated. This would increase the optical transmittance of the final film and any shortfall in electrical conductivity would be more than made up by the AgNW network underneath. Hence, very thin films of AA reduced GO were fabricated by reducing the number of passes of GO over the glass panel. Five samples were made in this manner and the samples were vapour annealed before thermal reduction. Following this, they were characterized and these details are shown in Fig. 4.16. By reducing the amount of GO deposited, the transmittance was increased from 60.0 % in the thicker samples to 87.7 % here, while the sheet resistance increased from 2.61 to 12.5 kΩ/□. Changing the deposition parameters moved the system away from optimum and caused a minor decrease in the σ_{dc}/σ_{op} values. Where a higher value of 0.248 was expected, the σ_{dc}/σ_{op} value of the thinner sample here had decreased to 0.223. Although this did not represent a drastic change in the optoelectronic properties of the final deposition, it did reiterate the sensitivity of the optoelectronic properties of a spray deposited film towards the process parameters used to fabricate it.

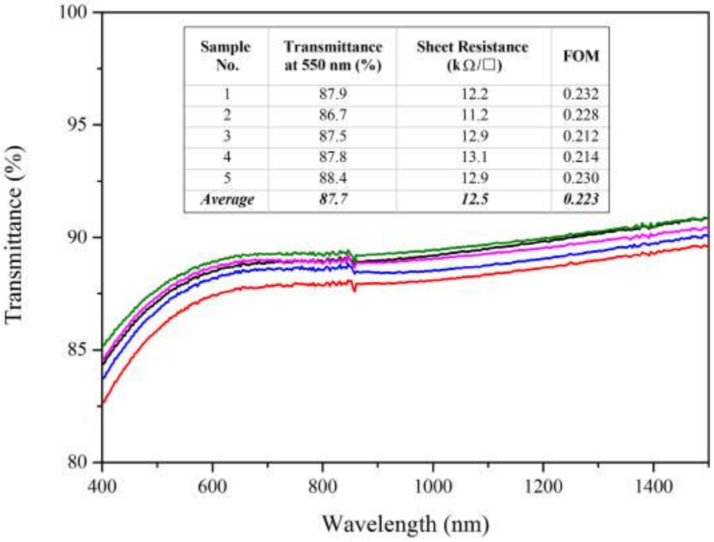

Sample No.	Transmittance at 550 nm (%)	Sheet Resistance (kΩ/☐)	FOM
1	87.9	12.2	0.232
2	86.7	11.2	0.228
3	87.5	12.9	0.212
4	87.8	13.1	0.214
5	88.4	12.9	0.230
Average	***87.7***	***12.5***	***0.223***

Figure 4.16: Optoelectronic properties of thin AA reduced GO films. Five samples were made and the deposition characteristics shown to be repeatable. Changing the deposition parameters resulted in a tolerable reduction in the $\sigma_{\mathrm{dc}}/\sigma_{\mathrm{op}}$ values of these films.

With this covered, AgNW networks were deposited onto glass panels and an AA reduced GO over layer sprayed over the AgNW network. Eight samples were made using this technique and the samples were subject to vapour annealing for three days before they were thermally annealed in a nitrogen environment for 15 hours at 573 K. Following this, characterizations of the optoelectronic properties of these films were performed and these results shown in Fig. 4.17.

The application of an AA reduced GO over layer onto the AgNW network resulted in films with an average transmittance at 550 nm of 65.7 %, an average sheet resistance of 5.1 Ω/☐ and an average $\sigma_{\mathrm{dc}}/\sigma_{\mathrm{op}}$ value of 160.0. Of these TCEs, the best performing sample had a sheet resistance of 4.7 Ω/☐ and a transmittance at 550 nm of 68.1, giving it a $\sigma_{\mathrm{dc}}/\sigma_{\mathrm{op}}$ value of 189.9. At the time of reporting the work, this was possibly the only TCE that had been fabricated using AA reduced GO[13]. Comparing the optoelectronic properties of these film against similar spray deposited films, the improvements introduced by the use of AA had increased the $\sigma_{\mathrm{dc}}/\sigma_{\mathrm{op}}$ slightly, from a previous high of 179, shown by Moon *et al.*, to the current high value of 190[22].

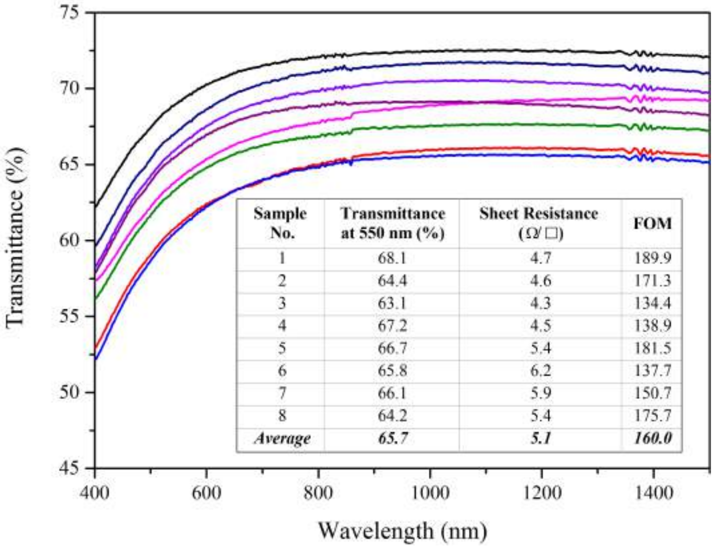

Sample No.	Transmittance at 550 nm (%)	Sheet Resistance (Ω/□)	FOM
1	68.1	4.7	189.9
2	64.4	4.6	171.3
3	63.1	4.3	134.4
4	67.2	4.5	138.9
5	66.7	5.4	181.5
6	65.8	6.2	137.7
7	66.1	5.9	150.7
8	64.2	5.4	175.7
Average	***65.7***	***5.1***	***160.0***

Figure 4.17: Characterization details of the eight AgNW with AA reduced GO over layers. The samples showed low sheet resistance values with an average value of 5.1 Ω/□.

The reasons for the observed reduction in sheet resistance of the films from the previous minimums of 12.5 kΩ/□ for AA reduced thin GO films and 34.4 Ω/□ for AgNW networks are attributed to the following effects:

(i) The addition of the AA reduced GO over layer had the effect of reducing the sheet resistance of the TCE as the flake would bridge the open spaces between nanowires. The bridging of these nanowires gave alternate pathways along which electrons could travel, thereby reducing the overall sheet resistance of the TCE[21,22,25].

(ii) Heating the nanowires during the thermal reduction step partially removed the polyol coating around the AgNWs, thereby improving inter-wire contact resistance[14,19].

(iii) The thermal reduction step also caused nanowire welding at contact points between the nanowires and this would further reduce the sheet resistance of the AgNW network[26].

While the FOM is seen to span a large range of values, this 'variation' in optoelectronic properties is caused by the way that FOM is calculated and is not indicative of a highly variable deposition process. Instead, it would be more instructive to consider the spread of transmittance values, which was 5.0 % and the spread of sheet resistance values, which was 1.9 $\Omega/\square$. These values indicated that the process was repeatable and with further automation and refinements, sample to sample variations could be reduced further and the average $\sigma_{\mathrm{dc}}/\sigma_{\mathrm{op}}$ values of the samples increased.

Summary of AA reduced GO over layer on AgNW network

The main motivation of this work was to find a method of using AgNWs with AA reduced GO in order to fabricate films with high $\sigma_{\mathrm{dc}}/\sigma_{\mathrm{op}}$ values. Due to solvent induced limitations, the benefits imbued to the electrode by the direct mixing of the GO and AgNW suspensions were limited and resulted in only modest increases in the $\sigma_{\mathrm{dc}}/\sigma_{\mathrm{op}}$ values of these films. Furthermore, while a AgNW network had both high conductivity and transmittance, the susceptibility of the nanowires to stress induced degradation mean that it could not be used as standalone electrode. The goal of a high quality TCE was achieved by using the AgNWs and the AA reduced GO in a bilayer film. At 190, the best TCE fabricated by this method had a $\sigma_{\mathrm{dc}}/\sigma_{\mathrm{op}}$ value that was moderately higher than that of a comparable film reported by Moon *et al.*[22] The improvements shown here can be attributed to the use of AA which is an exceptionally effective GO reducing agent. Additionally, the use of AA is preferred over the use of hydrazine as AA had the advantage of being an environmentally safe chemical reagent, while both chemicals were deemed equally effective at reducing GO.

Finally, the repeatability of the samples shown here was good and with further automation, the spread in transmittance and sheet resistance values were expected to become smaller, while the average $\sigma_{\mathrm{dc}}/\sigma_{\mathrm{op}}$ values are expected to increase.

From other reports, it was known that applying the GO over layer would increase the lifetime of the AgNWs in the TCEs and this would be the next topic of study.

4.5 Instability of AgNWs under Stress

AgNW percolating networks with and without an AA reduced GO over layer were tested against humidity and thermally induced degradation in different gaseous environments. After fabrication, the samples were either kept in a high humidity environment, similar to that used in vapour annealing or heated at 573 K in either air or nitrogen for an appropriate length of time.

In this section, the effects of these stresses on the nanowire are observed and discussed. The cause of the respective degradation effects are analysed and by identifying the root cause of nanowire degradation, recommendations are made to develop protocols and methods of TCE fabrication that would maximise the life time of TCEs incorporating nanowires.

4.5.1 Stress Induced AgNW Degradation

Humidity induced AgNW degradation

Samples were subject to degradation in a high humidity environment with the temperature of the system was maintained at 353 K and the relative humidity kept at 100 %. Following degradation, the nanowires were observed under a scanning electron microscope (SEM) and these images are shown in Fig. 4.18.

Comparing the images in Fig. 4.18, it is observed that the GO over layer had protected the nanowires from humidity induced degradation. When AgNWs were exposed directly to the high humidity environment, the formation of flakes and the partial erosion of the nanowire shafts were observed. The nature of nanowire degradation in the AgNW only sample was similar to the degradation observed in a report by Khaligh and Goldthorpe who also observed flaking in their degraded nanowires[20]. Degradation of these nanowires resulted in an increase in the sheet resistance of the AgNW electrode and eventually resulted in device failure.

This experiment clearly established the need for encapsulation in finished devices so that water vapour was prevented from coming into contact with the nanowires.

Section 4.5 is based on the publication *"Time to failure modelling of silver nanowire transparent conducting electrodes and effects of a reduced graphene oxide over layer"*[13].

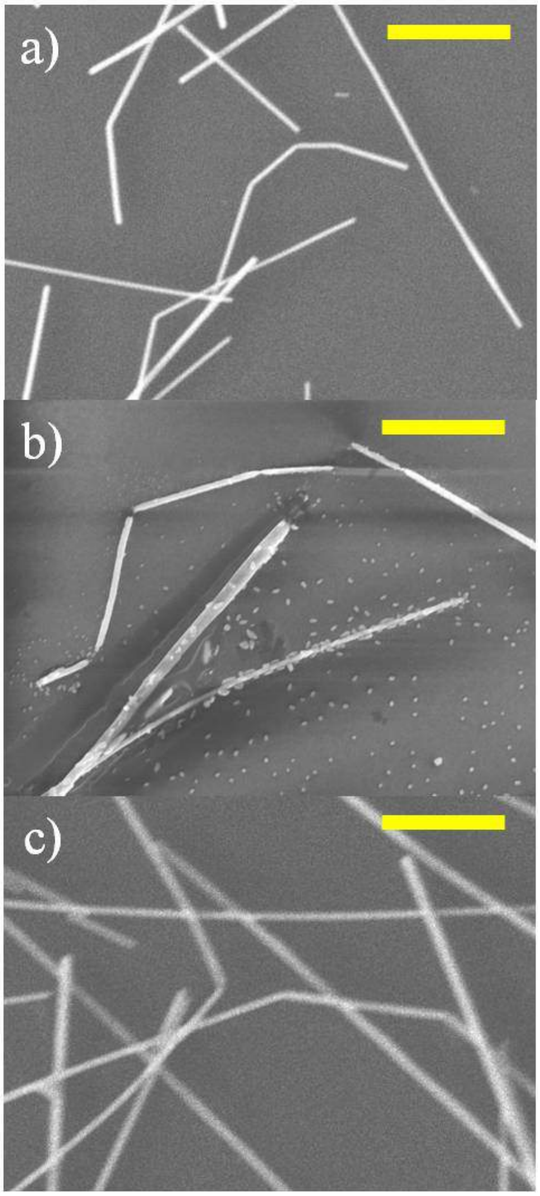

Figure 4.18: SEM images of a) as deposited AgNWs, b) AgNWs after humidity degradation and c) AgNWs with AA reduced GO over layer after humidity degradation. The formation of beads was observed on the AgNWs only sample, but no obvious change was seen in the sample that had a GO over layer. Scale bar inset is 2.0 μm long.

The exclusion of water from the sample would prevent flaking and this mode of nanowire failure could then be nipped in the bud. As shown in Fig. 4.18, simply adding an AA reduced GO over layer onto the AgNWs, the interaction of water with the nanowires could be reduced significantly or even prevented, such that no observable degradation occurred.

Thermally induced AgNW degradation

While protection from degradation due to humidity can be achieved by encapsulation, the effects of thermal degradation cannot be avoided and this is of special importance if the nanowires are to be used in devices such as solar cells or heating elements. In this test, nanowires were subject to high temperatures in either an air or nitrogen environment and the SEM images of these samples after degradation are shown in Fig. 4.19. The higher temperature was chosen so as to hasten the effects of heat induced degradation on the nanowires and minimize the effect of humidity on these samples.

As shown in Fig. 4.19(a), no obvious changes to the nanowires were observable after they had been heated for 15 hours at 573 K in a nitrogen environment. Additionally, welding of the nanowires at points of intersection could be seen and this was to be expected, while the lack of flake formation confirmed that the water free environment had prevented humidity induced degradation from occurring[26]. A second SEM image of the same location was made with higher magnification and this is shown in Fig. 4.20. Upon close inspection, it was clear that some changes had occurred to the nanowire and some undulations had begun to form along the lengths of some of the nanowires. In other locations, it appeared that long nanowires may have broken into two or more distinct pieces, suggesting that some thermally induced degradations is likely to have occurred in this sample.

On the contrary, the sample of AgNW that was heated in air, Fig. 4.19(b), did not resemble nanowires at all. The drastic difference between this sample and the sample that was degraded in nitrogen was surprising and it was only the metallic trails of silver left behind that suggested that nanowires were once present on the sample. It was deduced that the AgNWs had become the large metallic globules with diameters of ~2 μm seen here. The application of an AA reduced GO over layer served to reduce the severity of the degradation, however even in this sample, the formation of metallic globules appeared to have begun as well.

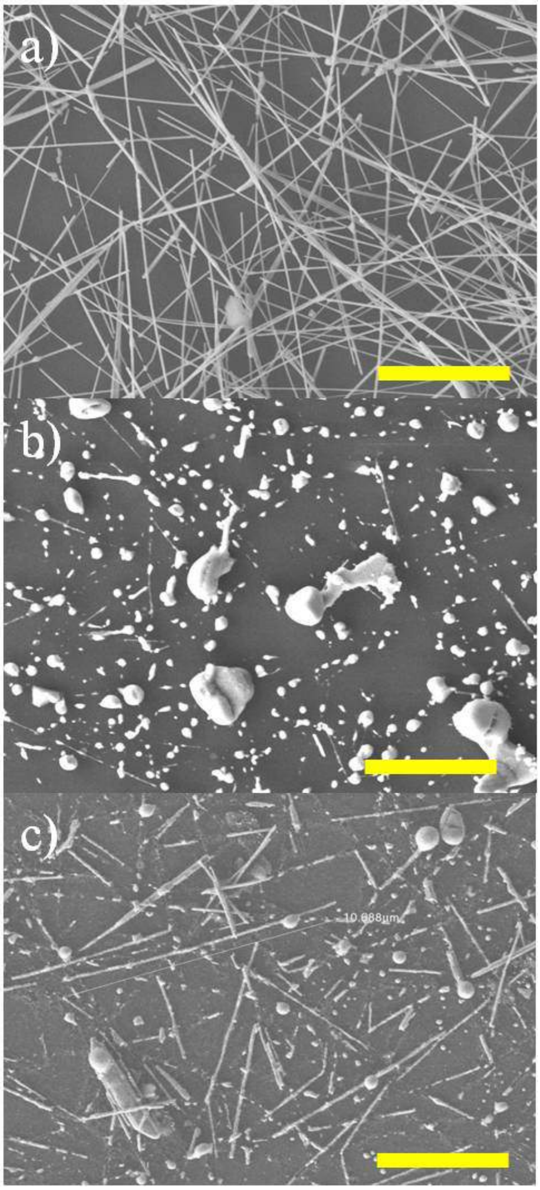

Figure 4.19: SEM images of AgNWs after high temperature degradation for 15 hours at a temperature of 573 K in (a) a nitrogen environment, (b) air and (c) air after an over layer of AA reduced GO had been applied. There were no obvious effects of thermal degradation on the AgNWs that were heated in a nitrogen environment, but when heated in air, the nanowires were destroyed and the application of the AA reduced GO over layer retarded the degradation process to some extent. Scale bar inset is 5.0 μm long.

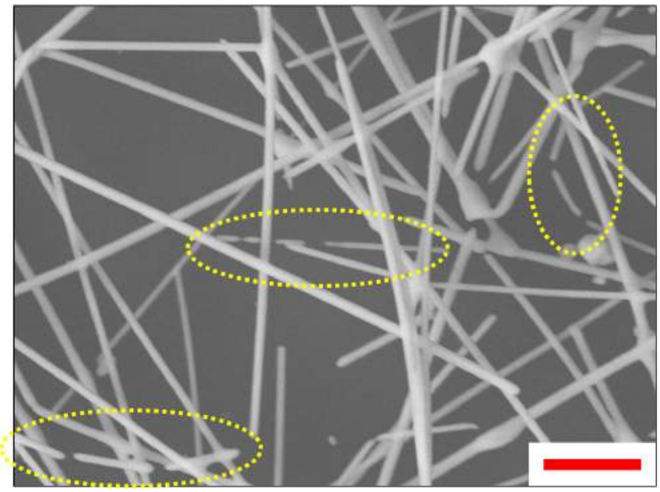

Figure 4.20: Higher magnification image of the sample in Fig. 4.19, showing changes in the shapes of the nanowires. Some of the nanowires that display signs of breakage and surface undulations are highlighted in the red-dotted ovals. Scale bar inset is 1 μm long.

These results suggested that it was the different gaseous environment that the nanowires were heated in that was causing the drastically different effects observed and this effect was understood in the following manner. By diluting the nitrogen environment with oxygen and other gases, severe degradation was observed within the same time frame and the over layer acted as a barrier to limit contact between the nanowires and the gases in the atmosphere.

4.5.2 Unsupported Hypotheses of Nanowire Instability

A search of known phenomenon that could explain the observed changes in the nanowires was performed and three possible causes were found. They are

1. Capillary instability, also known as Rayleigh-Plateau instability,
2. Geometry induced melting point depression
3. Kirkendall effect.

Close examination of these phenomenon revealed that capillary instability was the cause of the observed degradation and this will be the subject of the remainder of this chapter. Before doing so, the reasons for ruling out melting point depression and the Kirkendall effect will be discussed in this section.

Geometry induced melting point depression

It is well known that the high surface to volume ratio in nanostructures can cause the physical properties of these nanostructures to differ from that of the bulk material. According to this theory, the large surface area to volume ratio of the structure, in this case nanowires, reduces the cohesive energy in the structure and this in turn depresses the melting point of the material. Qi calculated the extent of geometry induced melting point depression in different geometric structures and using these results, it was estimated that for nanowires with a diameter of 100 nm, the melting point depression would not exceed 10 %[27].

Silver has a bulk melting temperature of 1234 K and this meant that the nanowires were expected to remain stable up to a temperature of 1110 K[28]. This geometrically depressed melting point far exceeds the temperatures attained in these experiments and cannot account for the difference seen in the samples of AgNWs that were heated in different gaseous environments. This ruled out melting as a possible explanation of the observed effects.

Kirkendall effect

The Kirkendall effect is a consequence of the different rates of diffusion of atoms through a material[29,30]. In this case, the atoms are silver from the nanowire and oxygen from air, while the layer was suspected to be silver oxide. It was possible that at the elevated temperatures used in this experiment, silver reacted with oxygen and formed a surface barrier layer of silver oxide. The different rates of diffusion of the silver and oxygen atoms through this barrier could then result in the nanowire destruction observed. Typically, the process was expected to result in the formation of hollow shelled nanoparticles, however nanowire destruction caused by the flow of atoms could not be ruled out[31].

To check this, a fresh sample of AgNW was prepared and subject to XPS characterization before thermal degradation in a nitrogen environment. The temperature used was increased to 773 K and after four hours, changes to the nanowires were observed by SEM. The XPS spectrum of silver and SEM image of the thermally degraded nanowire are shown in Figs. 4.21 & 4.22.

From the XPS spectra, it could be confirmed that only metallic silver was present on the sample prior to thermal degradation and still, breakage of the nanowire was observed[32]. The possibility that silver might form a compound with nitrogen

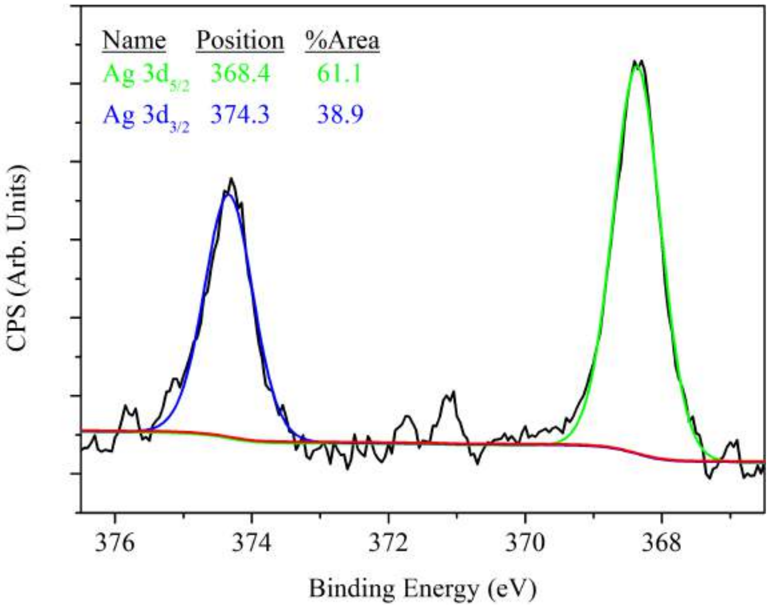

Figure 4.21: The Ag 3d XPS spectrum of AgNWs before they were subject to thermal degradation showed no signs of oxidation. Only metallic silver was present in the sample.

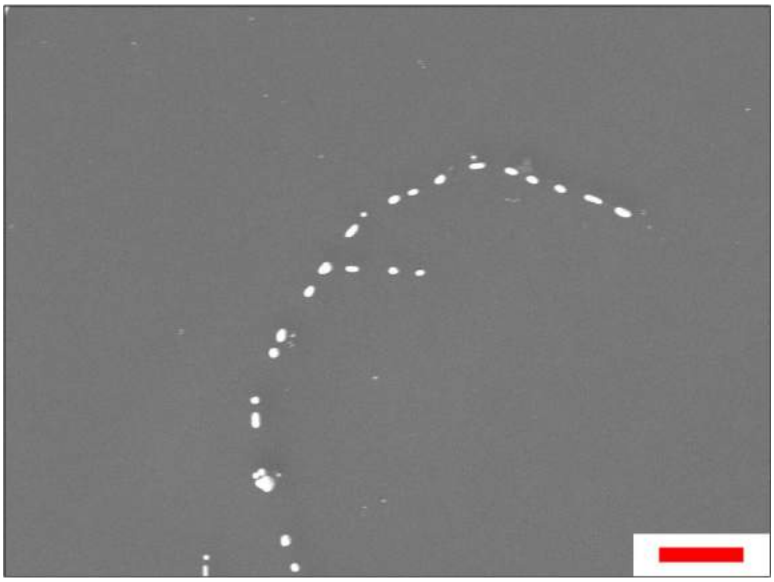

Figure 4.22: SEM image of AgNW that was thermally degraded in nitrogen for four hours at a temperature of 773 K. The formation of spheres was observed in this sample despite the exclusion of oxygen. Scale bar inset is 2.0 μm long.

was checked, but found to be extremely unlikely. While Ag_3N could be formed when silver oxide or silver nitrate and ammonia gas were brought together, this compound is unstable at temperatures greater than 438 K[33,34]. The high operation temperatures used here and the lack of proper reagents meant that the formation of a Ag_3N surface layer on the nanowire was not possible.

This ruled out the Kirkendall effect as a cause of the observed degradation. There was no boundary layer for the atoms to diffuse through meaning that no preferential diffusion gradient could be set up.

4.5.3 Capillary Instability

Capillary instability of a jet was first theorized by Lord Rayleigh in 1878 and can be summarized as the permanent relocation of surface atoms due to the occurrence of surface waves[35]. For a jet or solid of revolution, these surface waves are oriented parallel to the cylindrical axis of the body and the wavelengths of these waves determined the likelihood and speed at which capillary instability was manifested itself on the body.

Surface waves are naturally occurring perturbations which drive atoms from the troughs to the crests of these waves. While all allowed wavelengths occur at the same time, the amplitude of some wavelengths grow at a faster rate than others and the dominant wavelength is determined from the dispersion relations.

Here, the dispersion relation is given by the equation:

$$\omega^2 = \frac{\sigma}{\rho R_0^3} k R_0 \frac{I_1(kR_0)}{I_0(kR_0)} (1 - k^2 R_0^2) \tag{4.6}$$

where I_0 and I_1 are Bessel functions of the 1st kind, ω is the angular frequency, k is the wave number, ρ is the density and R_0 is the radius of the nanowire. The derivation of this dispersion relation is shown in Appendix A.

It is clear from this equation that ω is real and positive only when

$$kR_0 < 1 \Rightarrow \frac{2\pi R_0}{\lambda} < 1 \tag{4.7}$$

meaning that the wavelength of the surface wave must be greater than the circumference of the nanowire for instability to occur.

The wavelength of the fastest growing perturbation, λ_{max}, was determined using the Rayleigh's criterion. This criterion was derived from the dispersion relation and the wavelength was found to be related to the radius or diameter, D, of the nanowire by the equation

$$\lambda_{max} = 9.016 \times R_0 = 4.508 \times D \tag{4.8}$$

Inspecting the SEM image of AgNWs degraded in air and making some measurements, initial evidence was obtained to support the occurrence of capillary instability on the nanowires.

As shown in Fig. 4.23, the separation distance between some metallic globules appear to fulfil this criterion, while other globules clearly do not. For the globules that do adhere to the criterion, the diameter was estimated at ~120 while for those that did not adhere to the relationship, it was speculated to be caused by the overlapping of these nanowires, as well as the random distribution of the nanowires on the substrate.

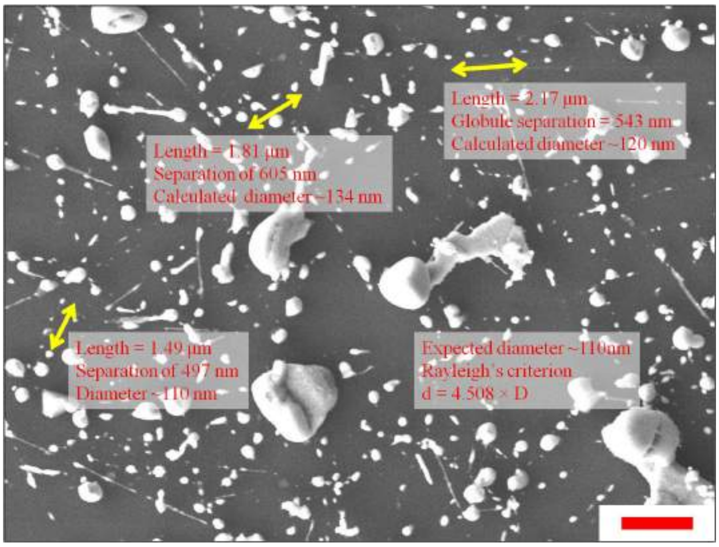

Figure 4.23: Measurements of the distance between some globules and calculations of the original nanowire diameter based on Rayleigh's criterion. The nanowires had an expected diameter of 110 nm and while the measurements here show agreement with the criterion, it is also clear that not all globule separations agree with the calculation.

This phenomenon had also been observed by other authors who worked with copper and gold nanowires which were heated to high temperatures in a vacuum[36,37]. Despite the lack of a gaseous environment, the formation of metallic globules was observed in their nanowires. This confirmed that surface waves were the cause of instability in the nanowires and confirmed the exclusion of the Kirkendall effect as an explanation for the observed phenomenon.

Furthermore, Karim *et al.* showed that Rayleigh's criterion tended to over estimate the original diameters of the nanowires and attributed this to simplifications made in the model[36]. Additionally, contact made between the nanowire and the substrate was also found to protect the nanowire from some effects of capillary instability[38]. This explained why the calculated nanowire diameters found in Fig. 4.23 were typically larger than expected.

Analysing the data that had been collected thus far, it was clear that the time taken for capillary instability to manifest in the nanowires was dependent on:

i. the gaseous environment that the nanowires were in,
ii. the temperature at which the nanowires were kept at

and possibly

iii. the mechanical contact between the nanowires and the materials around it.

While capillary instability has been identified as the cause of nanowire degradation, the analysis is developed by considering the relationship between the gaseous environment of the nanowire and the time taken for these nanowire to break apart. A calculation that takes into account these factors along with other factors such as the material that the nanowire is made of and diameter of the nanowire was shown by Nichols and Mullins and this work can be adapted to gain further insight into the results shown here[39–41].

4.5.4 Nanowire Spheroidization

A model of capillary instability in nanowires that accounted for both the effect of the gaseous environment and the temperature of the nanowires was developed by Nichols and Mullins[39–41]. They termed the process of turning nanowires into globules as spheroidization and using their model, they numerically solved the time taken for nanowire spheroidization to occur. This model takes into account the gaseous environment, material and radius of the nanowires and the temperature that the nanowires are kept at to make an estimate of the time taken for spheroidization of the nanowires to occur.

The development of this model began with Mullin's work on thermal grooving where he derived a mathematical formulation to describe the development of surface grooves[39]. Mullin's noted that the rate of growth of a groove was determined by the rate of surface diffusion of the atoms in the material, J, given by the equation:

$$J = -\frac{D_s \gamma \Omega \nu}{kT} \frac{\partial K}{\partial s} \tag{4.9}$$

where

$$K = \frac{1}{R_1} + \frac{1}{R_2} \tag{4.10}$$

and

$$D_s = D_0 \exp\left(-\frac{E_a}{kT}\right) \tag{4.11}$$

Here, R_1 [cm] and R_2 [cm] are the principal radii of the curvature, s is the arc-length of the curve formed between the intersection of a plane normal to the surface and the surface itself, D_0 is the coefficient of surface diffusion for the atomic species in a given gaseous environment [cm^2/s], E_a is the activation energy per atom [eV], γ is the surface tension [N/m], Ω is the volume of the atomic species [cm^3], ν is the number of diffusing species per unit surface area ($\nu \approx \Omega^{-2/3}$), T is the temperature [K] and k is the Boltzmann constant [J/K][39].

Together with Nichols, Mullins then successively used this formulation to model changes to the shape of a field emitter cathode using this theory[40]. The calculation and findings are summarized in the following pages.

Beginning with a finite element analysis of the surface of a solid of revolution, the normal motion of this element, n, is described by the equation:

$$\frac{\Delta n}{\Delta t} = \left(\frac{\Omega}{\bar{y}}\right)\left[\frac{\Delta(Jy)}{\Delta s}\right] \tag{4.12}$$

with $\bar{y}$ as the average distance of the surface from the cylindrical axis.

Inserting Equation (4.9) gives:

$$\frac{\partial n}{\partial t} = \frac{D_s \gamma \Omega^2 \nu}{kT}\frac{\partial^2 K}{\partial s^2} = B\,\nabla_s^2 K \tag{4.13}$$

Solving this partial differential equation numerically, the time taken for spheroidization can be found and Nichols & Mullins defined a value:

$$\tau = \frac{B\,t}{\left(\frac{\pi}{16}\,R_0\right)^4} \tag{4.14}$$

As before, R_0 is the radius of the nanowire.

Here, τ is dimensionless and spheroidization of the nanowire occurs at a τ value of 4415. By substituting the appropriate constants and experimental parameters, the time taken for spheroidization is then calculated from Equation (4.14).

Recently, the temperature dependence of the surface tension of silver was found and the relation found to follow the equation[28]:

$$\gamma = 1.134 - 0.905 \times 10^{-3} \cdot T \tag{4.15}$$

and was used in the equation.

According to this theory, the time to spheroidization of the nanowire depended on the value of B and the radius of the nanowires; smaller values of B and larger values of R_0 would mean that more time was required to achieve the same τ value. While it was obvious from this equation that larger nanowire radii increased the time taken to spheroidization, the effect of temperature was not as obvious as the temperature term appeared in both the numerator and the denominator of B. It was instructive to graph the dependence of B on temperature, shown in Fig. 4.24, which was calculated using the updated surface tension parameter in Equation (4.15).

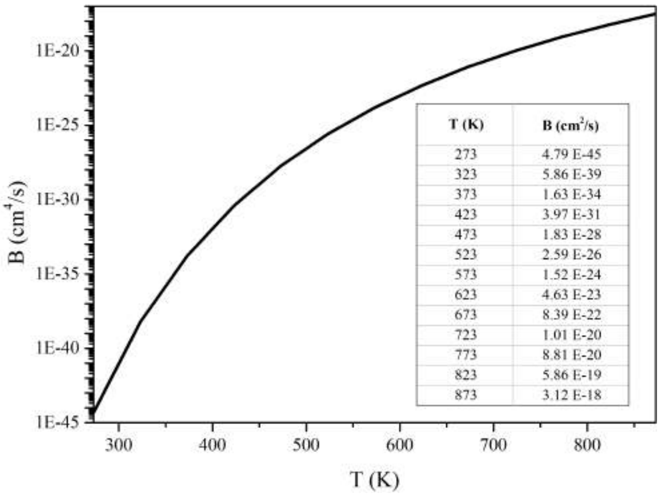

T (K)	B (cm^2/s)
273	4.79 E-45
323	5.86 E-39
373	1.63 E-34
423	3.97 E-31
473	1.83 E-28
523	2.59 E-26
573	1.52 E-24
623	4.63 E-23
673	8.39 E-22
723	1.01 E-20
773	8.81 E-20
823	5.86 E-19
873	3.12 E-18

Figure 4.24: Graph showing the change in the B parameter with respect to temperature. The self diffusion coefficient value used here was for silver in air[42], $D_0 = 2.5 \times 10^5$ cm^2/s, and $E_a = 2.16$ eV.

As can be seen, increasing the temperature increased the value of B for silver in air and this meant a reduction in the time to nanowire spheroidization. However, the value of B was dependent on the value of the surface diffusion coefficient which was in turn dependent on the gaseous atmosphere. Various authors have estimated the surface diffusion coefficient and activation energy of surface diffusion of silver in different gaseous environments. Using these values, the time to spheroidization for silver nanowires with a diameter of 110 nm at a temperature of 573 K in different gaseous environments could be estimated. Other constants were taken from a report by Ashby and the calculated time to spheroidization summarized in Table 4.8[43].

As can be seen, the introduction of environmental oxygen results in a lowering of both the surface diffusion coefficient and the activation energy of diffusion and this reduced the calculated time to spheroidization of the nanowires. It is believed that the physisorption of oxygen onto the surface of silver causes the reduction in both the surface diffusion coefficient and activation energy and clearly, it was the latter quantity that played a bigger role in determining the time to spheroidization in these nanowires.

Table 4.8: Calculated time to spheroidization, t, of a nanowire with a diameter of 110 nm at a temperature of 573 K, based on the different surface diffusion coefficients, D_0 and activation energy, E_a of the silver atoms in different gaseous atmospheres.

Gas	**D_0 / cm^2s^{-1}**	**E_a / eV**	**t / s**	**Ref.**
Air	2.5×10^5	2.16	3.94×10^3	[42]
	1×10^6	2.40 ± 0.15	1.38×10^5	[44]
Hydrogen	5.0×10^7	2.76	3.90×10^6	[45]
Nitrogen (93 %) & Hydrogen (7 %)	$1 \times 10^{14\pm2}$	4.16 ± 0.48	4.21×10^{11}	[46]

The expected time to spheroidization for these AgNWs heated at 573 K was between one and 38 hours in air and 1.17×10^8 hours in nitrogen. Referring to the SEM images shown in Fig. 4.19, calculations for AgNWs in air were accurate to within an order of magnitude and the lack of degradation on the AgNWs heated in nitrogen suggested that there was some agreement between the experiments and theory.

Additionally, Fig. 4.22 shows that spheroidization of the nanowires occurred within four hours of heating at 773 K in nitrogen. Calculating the time taken for spheroidization of the AgNWs under these conditions, it was found that spheroidization could occur on the nanowires in as little as 3 minutes under ideal conditions, giving further agreement between experiment and theory.

4.5.5 Time to Failure Modelling

Time to spheroidization modelling was an important step in determining the validity of the Nichols & Mullins model in the previous section. However, nanowire spheroidization was not a good indicator of device failure as the device was expected to fail before full spheroidization occurs. To check this, the τ values for silver nanowires that had failed under different stress conditions were considered. Surveying experimental data available, time to nanowire electrode breakdown could be broadly classified under one of two categories:

1) Thermally induced degradation
2) Thermal and humidity induced degradation

In the first case, the temperatures used were high and experiment time spans short meaning that capillary instability was the only cause of degradation in the nanowires. While in the second case, the temperatures used were low and nanowire the effects of humidity played an equally, if not more important, role in the degradation process of the nanowires.

Considering AgNW electrodes that were only subject to thermally induced degradation and using the appropriate data from these reports, τ values of the nanowires were calculated and tabulated in Table 4.9. The τ values calculated here were separated into either conditions for which the electrodes remained stable or conditions for which the electrode had failed.

This data shows that the lifetime of the nanowires are well behaved and that the τ value can be used to estimate the actual lifetime of the AgNW electrodes. The electrodes are seen to be stable up to a τ value of ~1000, while electrode breakdown was first observed at a τ value of 1.35×10^3. Using a τ value of 1000 as the limit of AgNW electrode stability, the lifetime of a AgNW electrode made from nanowires of radius 20 nm was estimated to be on the order of 5.61×10^5 years when heated at 353 K, a typical temperature condition that solar energy conversion devices would face.

Table 4.9: Calculated τ values based on various experimental conditions. The τ values are split into two categories, the first being the maximum values at which the AgNW electrode was observed to remain stable, while the second category was the minimum value for which the AgNW electrode was known to have failed.

Conditions				τ		**Ref.**
Gas	**Temperature / K**	**Radius / nm**	**Time / min**	**Stable**	**Fail**	
Air	523	30	20	258	–	[47]
	573	55	20	–	1.35×10^3	
N_2	673	55	20	2.89	–	
	773	55	20	–	2.65×10^4	
Air	573	50	10	980		[48]
	653	50	10	–	1.80×10^5	
	503*	13	60*	–	3.47×10^3	
	523*	30	140*	–	1.81×10^3	
	553*	60	155*	–	1.53×10^3	

*Estimated values

Even under the harshest naturally occurring temperature conditions, failure of nanowire electrodes in these solar panels would not be due to capillary instability. This finding is an important step towards the development of stable nanowire based TCEs and allays fears that the nanowires would not be sufficiently robust. Instead, these results point to the presence of gaseous water as the main culprit in nanowire degradation. Depending on the substrate that the nanowires were deposited onto, the sheet resistance tripled within eight to 30 days[21–23,47]. This meant that a good encapsulation technique and the use of oxygen and water getters are extremely important when using nanowires as electrodes.

4.6 Summary of Findings

‘ In this chapter, the development of a spray coated TCE based on reduced GO was shown. Using AA as a reducing agent and under optimum spray coating conditions, a TCE with a transmittance of 60% at a wavelength of 550 nm and sheet resistance of 2.61 kΩ/□ was fabricated, giving the TCE a $\sigma_{\mathrm{dc}}/\sigma_{\mathrm{op}}$ value of 0.248.

By itself, AA reduced GO did not have sufficient conductivity or transparency to function as a TCE. To improve the optoelectronic properties of these films, AgNWs were incorporated into the films and the combination proved to be very effective. Using these materials together, a TCE with a transmittance of 68.1 % at a wavelength of 550 nm and sheet resistance value of 4.7 Ω/□ was fabricated. The incorporation of AA reduced GO with AgNW films enabled the fabrication of TCEs with improved high temperature stability under ambient conditions and high $\sigma_{\mathrm{dc}}/\sigma_{\mathrm{op}}$ values of about 190[13].

Studying the effect of thermal degradation on the AgNWs led to the use of a model that could estimate the lifetime of the nanowires under different thermal conditions. This model was accurate in predicting the time to degradation of the nanowires to within one order of magnitude and allowed the estimation of a lifetime of these nanowires when used in electrodes[13]. Through this analysis, it was found that nanowire degradation due to capillary instability was not the main cause of electrode failure. Instead, humidity induced degradation played the leading role of electrode degradation, establishing the need for good encapsulation techniques when using nanowires as electrodes.

References

[1] Sukanta De and Jonathan N. Coleman. **Are there fundamental limitations on the sheet resistance and transmittance of thin graphene films?** *ACS Nano*, **4**:2713–2720, 2010, `DOI:10.1021/nn100343f`. 140

[2] Junbo Wu, Mukul Agrawal, Hector A. Becerril, Zhenan Bao, Zunfeng Liu, Yongsheng Chen, and Peter Peumans. **Organic Light-emitting diodes on solution-processed graphene transparent electrodes**. *ACS Nano*, **4**:43–48, 2010, `DOI:10.1021/nn900728d`.

[3] K. F. Mak, M. Y. Sfeir, Y. Wu, C. H. Lui, J. A. Misewich, and T. F. Heinz. **Measurement of the optical conductivity of graphene**. *Phys. Rev. Lett.*, **101**(19):196405, 2008, `DOI:10.1103/PhysRevLett.101.196405`.

[4] R.R. Nair, P. Blake, A.N. Grigorenko, K.S. Novoselov, T.J. Booth, T. Stauber, N.M.R. Peres, and A.K. Geim. **Fine structure constant defines visual transparency of graphene**. *Science*, **320**:1308, 2008, `DOI:10.1126/science.1156965`. 140

[5] Yanwu Zhu, Shanthi Murali, Weiwei Cai, Xuesong Li, Ji Won Suk, Jeffrey R. Potts, and Rodney S. Ruoff. **Graphene and Graphene Oxide: Synthesis, Properties, and Applications**. *Adv. Mater.*, **22**:3906–3924, 2010, `DOI:10.1002/adma.201001068`. 144

[6] Xuan Wang, Linjie Zhi, and Klaus Mllen. **Transparent, Conductive Graphene Electrodes for Dye-Sensitized Solar Cells**. *Nano Lett.*, **8**:323–327, 2008, `DOI:10.1021/nl072838r`. 149

[7] Dongxing Yang, Aruna Velamakanni, Ulay Bozoklu, Sungjin Park, Meryl Stoller, Richard D. Piner, Sasha Stankovich, Inhwa Jung, Daniel A. Field, Carl A. Ventrice Jr., and Rodney S. Ruoff. **Chemical analysis of graphene oxide films after heat and chemical treatments by x-ray photoelectron and micro-raman spectroscopy**. *Carbon*, **47**:145–152, 2009, `DOI:10.1016/j.carbon.2008.09.045`. 149

[8] Akshay Mathkar, Dylan Tozier, Paris Cox, Peijie Ong, Charudatta Galande, Kaushik Balakrishnan, Arava Leela Mohana Reddy, and Pulickel M. Ajayan. **Controlled, Stepwise Reduction and Band Gap Manipulation of Graphene Oxide**. *J. Phys. Chem. Lett.*, **3**(8):986–991, 2012, `DOI:10.1021/jz300096t`. 149

[9] ACROS Organics. **Material Safety Data Sheet - Hydrazine hydrate**, One Reagent Lane, Fair Lawn, NJ 07410, U.S.A., 20th July 2009. 149

[10] Jian Gao, Fang Liu, Yiliu Liu, Ning Ma, Zhiqiang Wang, and Xi Zhang. **Environment-Friendly Method To Produce Graphene That Employs Vitamin C and Amino Acid**. *Chem. Mater.*, **22**:2213–2218, 2010, `DOI:10.1021/cm902635j`. 149, 150

[11] Jiali Zhang, Haijun Yang, Guangxia Shen, Ping Cheng, Jingyan Zhang, and Shouwu Guo. **Reduction of graphene oxide vial-ascorbic acid**. *Chem. Commun.*, **46**:1112–1114, 2010, `DOI:10.1039/B917705A`. 149, 150

[12] M. J. Fernández-Merino, L. Guardia, J. I. Paredes, S. Villar-Rodil, P. Soliís-Fernández, A. Martínez-Alonso, and J. M. D. Tascón. **Vitamin C Is an Ideal Substitute for Hydrazine in the Reduction of Graphene Oxide Suspensions**. *J. Phys. Chem. C*, **114**:6426–6432, 2010, `DOI:10.1021/jp100603h`. 151

[13] Kwan Yue Chau Garen, Le Quan Luan, and Huan Cheng Hon Alfred. **Time to failure modeling of silver nanowire transparent conducting electrodes and effects of a reduced graphene oxide over layer**. *Sol. Energ. Mat. Sol. Cells*, **144**:102–8, 2016, `DOI:10.1016/j.solmat.2015.08.005`. 164, 172, 175, 191

[14] Y. Sun and Y. Xia. **Large-Scale Synthesis of Uniform Silver Nanowires Through a Soft, Self-Seeding, Polyol Process**. *Adv. Mater.*, **14**:833–837, 2002,

DOI:10.1002/1521-4095(20020605)14:11<833::AID-ADMA833>3.0.CO;2-K. 165, 173

[15] Yugang Sun, Byron Gates, Brian Mayers, and Younan Xia. **Crystalline Silver Nanowires by Soft Solution Processing**. *Nano Lett.*, **2**:165–168, 2002, DOI:10.1021/nl010093y.

[16] Yugang Sun, Brian Mayers, Thurston Herricks, and Younan Xia. **Polyol Synthesis of Uniform Silver Nanowires: A Plausible Growth Mechanism and the Supporting Evidence**. *Nano Lett.*, **3**:955–960, 2003, DOI:10.1021/nl034312m. 165

[17] K. K. Caswell, Christopher M. Bender, and Catherine J. Murphy. **Seedless, Surfactantless Wet Chemical Synthesis of Silver Nanowires**. *Nano Lett.*, **3**:667–669, 2003, DOI:10.1021/nl0341178. 165

[18] Stephen M. Bergin, Yu-Hui Chen, Aaron R. Rathmell, Patrick Charbonneau, Zhi-Yuan Li, and Benjamin J. Wiley. **The effect of nanowire length and diameter on the properties of transparent, conducting nanowire films**. *Nanoscale*, **4**:1996–2004, 2012, DOI:10.1039/C2NR30126A. 165

[19] D.P. Langley, G. Giusti, M. Lagrange, R. Collins, C. Jimnez, Y. Brchet, and D. Bellet. **Silver nanowire networks: Physical properties and potential integration in solar cells**. *Sol. Energ. Mat. Sol. Cells*, **125**:318–324, 2014, DOI:10.1016/j.solmat.2013.09.015. 169, 173

[20] Hadi Hosseinzadeh Khaligh and Irene A. Goldthorpe. **Failure of silver nanowire transparent electrodes under current flow**. *Nanoscale Res. Lett.*, **8**:235, 2013, DOI:10.1186/1556-276X-8-235. 169, 175

[21] Yumi Ahn, Youngjun Jeong, and Youngu Lee. **Improved Thermal Oxidation Stability of Solution-Processable Silver Nanowire Transparent Electrode by Reduced Graphene Oxide**. *ACS Appl. Mater. Interfaces*, **4**:6410–6414, 2012, DOI:10.1021/am301913w. 169, 173, 190

[22] In Kyu Moon, Jae Il Kim, Hanleem Lee, Kangheon Hur, Woon Chun Kim, and Hyoyoung Lee. **2D Graphene Oxide Nanosheets as an Adhesive Over-Coating Layer for Flexible Transparent Conductive Electrodes**. *Sci. Rep.*, **3**:1112, 2012, DOI:10.1038/srep01112. 172, 173, 174

[23] Donghwa Lee, Hyungjin Lee, Yumi Ahn, Youngjun Jeong, Dae-Young Lee, and Youngu Lee. **Highly stable and flexible silver nanowire-graphene hybrid transparent conducting electrodes for emerging optoelectronic devices**. *Nanoscale*, **5**:7750–7755, 2013, DOI:10.1039/c3nr02320f. 190

[24] Bo-Tau Liu and Shao-Xian Huang. **Transparent conductive silver nanowire electrodes with high resistance to oxidation and thermal shock**. *RSC Adv.*, **4**:59226–59232, 2014, DOI:10.1039/c4ra11660g. 169

[25] P. Meenakshi, R. Karthick, M. Selvaraj, and S. Ramu. **Investigations on reduced graphene oxide film embedded with silver nanowire as a transparent conducting electrode**. *Sol. Energ. Mat. Sol. Cells*, **128**:264–269, 2014, DOI:10.1016/j.solmat.2014.05.013. 173

[26] Jaemin Lee, Inhwa Lee, Taek-Soo Kim, and Jung-Yong Lee. **Efficient Welding of Silver Nanowire Networks without Post-Processing**. *Small*, **9**:2887–2894, 2012, DOI:10.1002/smll.201203142. 173, 177

[27] W.H. Qi. **Size effect on melting temperature of nanosolids**. *Phys. B: Cond. Matt.*, **368**:46–50, 2005, DOI:10.1016/j.physb.2005.06.035. 180

[28] W. Gasior, J. Pstru, Z. Moser, A. Krzyak, and K. Fitzner. **Surface tension and thermodynamic properties of liquid Ag-Bi solutions**. *J. Phase. Equilib.*, **24**:40–49, 2003, DOI:10.1007/s11669-003-0005-5. 180, 186

[29] E.O. Kirkendall. **Diffusion of Zinc in Alpha Brass**. *Trans. AIME*, **147**:104–110, 1942. 180

[30] A.D. Smigelskas and E.O. Kirkendall. **Diffusion of Zinc in Alpha Brass**. *Trans. AIME*, **171**:130–142, 1947. 180

[31] Hong Jin Fan, Ulrich Gsele, and Margit Zacharias. **Formation of Nanotubes and Hollow Nanoparticles Based on Kirkendall and Diffusion Processes: A Review**. *Small*, **3**:1660–1671, 2007, DOI:10.1002/smll.200700382. 180

[32] A.M. Ferraria, A.P. Carapeto, and A.M. Botelho do Rogo. **X-ray photoelectron spectroscopy: Silver salts revisited**. *Vacuum*, **86**:1988–1991, 2012, DOI:10.1016/j.vacuum.2012.05.031. 180

[33] John L. Ennis and Edward S. Shanley. **On hazardous silver compounds**. *J. Chem. Educ.*, **68**:A6, 1991, DOI:10.1021/ed068pA6. 182

[34] Dietrich Breitinger, Wolfgang A. Herrmann, and Wolfgang Hiller. **Synthetic Methods of Organometallic and Inorganic Chemistry, Volume 5, 1999: Volume 5: Copper, Silver, Gold, Zinc, Cadmium and Mercury**. Georg Thieme Verlag, 2014, 1999. Page 38. 182

[35] Lord Rayleigh. **On the instability of jets**. *Proc. Lond. Math. Soc.*, **10**:4–13, 1878, DOI:10.1112/plms/s1-10.1.4. 182

[36] S. Karim, M. E. Toimil-Molares, A. G. Balogh, W. Ensinger, T. W. Cornelius, E. U. Khan, and R. Neumann. **Morphological evolution of Au nanowires controlled by Rayleigh instability**. *Nanotechnology*, **17**:5954, 2006, DOI:10.1088/0957-4484/17/24/009. 184

[37] M. E. Toimil Molares, A. G. Balogh, T. W. Cornelius, R. Neumann, and C. Trautmann. **Fragmentation of nanowires driven by Rayleigh instability**. *Appl. Phys. Lett.*, **85**:5337–5339, 2004, DOI:10.1063/1.1826237. 184

[38] K. F. Gurski, G. B. McFadden, and M. J. Miksis. **The Effect of Contact Lines on the Rayleigh Instability with Anisotropic Surface Energy**. *SIAM J. Appl. Math.*, **66**:1163–1187, 2006, DOI:10.1137/050626946. 184

[39] W. W. Mullins. **Theory of Thermal Grooving**. *J. Appl. Phys.*, **28**:333–339, 1957, DOI:10.1063/1.1722742. 184, 185

[40] F.A. Nichols and W. W. Mullins. **Morphological Changes of a Surface of Revolution due to CapillarityInduced Surface Diffusion**. *J. Appl. Phys.*, **36**:1826, 1965, DOI:10.1063/1.1714360. 185

[41] F.A. Nichols. **On the spheroidization of rod-shaped particles of finite length**. *J. Mater. Sci.*, **11**:1077–1082, 1976, DOI:10.1007/BF00553115. 184, 185

[42] F.A. Nichols. **Theory of sintering of wires by surface diffusion**. *Acta Metall. Mater.*, **16**:103–113, 1968, DOI:10.1016/0001-6160(68)90079-5. xxi, 187, 188

[43] M.F. Ashby. **A first report on sintering diagrams**. *Acta Metall. Mater.*, **2**:275–289, 1974, DOI:10.1016/0001-6160(74)90167-9. 187

[44] G. E. Rhead. **Surface self-diffusion and faceting on silver**. *Acta Metall. Mater.*, **11**:1035–1042, 1963, DOI:10.1016/0001-6160(63)90191-3. 188

[45] R.R. Hough. **An investigation of the surface self-diffusion coefficients of pure copper and silver by the grain boundary grooving technique**. *Scr. Metall. Mater.*, **4**:559–561, 1970, DOI:10.1016/0036-9748(70)90147-X. 188

[46] G. E. Rhead. **Surface self-diffusion of silver in various atmospheres**. *Acta Metall. Mater.*, **13**:223–226, 1965, DOI:10.1016/0001-6160(65)090199-9. 188

[47] Bo-Tau Liu and Shao-Xian Huang. **Transparent conductive silver nanowire electrodes with high resistance to oxidation and thermal shock**. *RSC Adv.*, **4**:59226–59232, 2014, DOI:10.1039/c4ra11660g. 189, 190

[48] D. P. Langley, M. Lagrange, G. Giusti, C. Jimenez, Y. Brechet, N. D. Nguyen, and D. Bellet. **Metallic nanowire networks: effects of thermal annealing on electrical resistance**. *Nanoscale*, **6**:13535–13543, 2014, DOI:10.1039/C4NR04151H. 189

5

Graphene Oxide in Phthalocyanine Gas Sensors

Besides use in transparent conducting electrodes, other potential applications of GO make use of either its large surface area to volume ratio or its unique electronic structure to achieve a desired outcome. As mentioned in Chapter 1.3.2, GO is not selective towards any analyte and most gas sensors make use of its large surface area to volume ratio to improve the capabilities of a second material that is both sensitive and selective towards an analyte gas[1–5].

This chapter begins by an analysis of a new operating principle that combines two materials in a chemiresistor setup for a gas sensing device. This is followed by a demonstration of the sensing characteristics of monolayers of Zinc Phthalocyanine (ZnPC) and GO with respect to a nitrogen dioxide (NO_2) analyte. The sensing material and analyte was chosen with foreknowledge that the reaction between ZnPC and NO_2 was well researched, thereby allowing the work to focus on demonstrating the operating principle and analysing the device design[6–12].

The bilayer device was analysed by comparing experimental results against the theoretical model developed and with this understanding, a new sensing layer was chosen. This new sensing layer was expected to improve the performance characteristics of the bilayer device and the results from this test validated the accuracy of the theoretical model.

This chapter is based on work in patent application with filing number: PCT/2015/050210.

5.1 ZnPC/GO Bilayer for Gas Sensing

5.1.1 Gas Sensing Principles

Gas Sensing Capabilities of Phthalocyanines

The sensitivity of MPc materials towards NO_2 was established in the early 1990s and its electrical conductivity made it and ideal sensing layer material in a chemiresistor setup[9,13]. The high selectivity towards NO_2, a pollutant that has adverse effects on the human body, and low cross-sensitivity of ZnPC towards other analyte gases, with the exception of chlorine, makes ZnPC an ideal starting point for this work[9,14].

When compared against metal oxide gas sensors, phthalocyanines have the advantage of low working temperatures. While the former was operated at temperatures in the range of hundreds of Celsius, the operating temperature for phthalocyanines was typically less than 100 °C and this greatly reduced the energy used during device operation[15–17]. Reducing the energy consumption of the gas sensing device is important as modern electronic equipments are typically powered by a built-in secondary battery and the lower operating temperature potentially allows the incorporation of the phthalocyanine based device into these devices with limited energy sources.

Besides this, phthalocyanine layers consists of small molecules with mobile $\pi-$electrons meaning that, unlike metal oxides, crystallinity is not required for conductivity. This allows flexibility in phthalocyanines based sensors and could increase the possible uses of phthalocyanines gas sensors significantly.

Despite the superior sensing properties of ZnPC, and other phthalocyanines, potential uses of the material were limited by the low electrical conductivity of the material[18,19]. As shown in the schematic of ZnPC in Fig. 5.1, only 18 π-electrons per phthalocyanine molecule are available to provides the material with its electrical conductivity when deposited as a film[11,12,19]. As a result, phthalocyanine films have typical resistivity values of ~1×10^9 Ω/m and, when operated at voltages of <5 V, the finished devices would have typical operating currents on the order of nanoamps[11,12,19]. These exceptionally low operating currents and large drifts in the baseline current and higher device currents would be beneficial towards improving device accuracy and ease of signal processing.

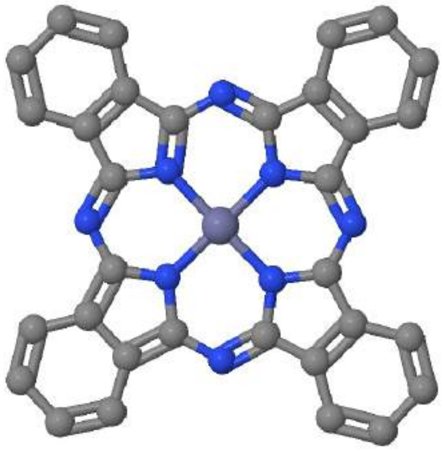

Figure 5.1: Schematic of ZnPC molecule showing the macrocycles surrounding the zinc center of the molecule.

Gas Sensing Capabilities of Graphenic Material

On the other hand, graphene and GO have large surface area to volume ratios making them ideal platforms for gas sensing. Reduced GO could be made exceptionally sensitive to the presence of even a single analyte molecule, however the film still lacked analyte selectivity[20]. Just like reduced GO, GO is not a selective sensing material and this made it a poor gas sensing layers as well[20–23].

Graphene is different from GO in the sense that it is poorly reactive to a majority of analyte molecules. To utilize the large surface area to volume ratio of graphene for gas sensing, it has to be functionalized by attaching sensing molecules onto the carbon basal plane[4]. Though promising, this method runs into the problem that the density of sensing sites was limited by the density of sensing molecules that could be arranged onto the carbon basal plane.

Despite these drawbacks, graphene based materials have better conductivities than phthalocyanine materials and this advantage could be harnessed to improve phthalocyanine based sensors for integration with ASICs. By combining the materials in a properly designed device, the strengths of one material could be used to overcome the limitations of the other.

Typically, this is achieved by dispersing the sensing material as particles on a conductive graphene based platform, and the change in current detected when the analyte molecule interacts with the sensing material[3,4].

Concurrent use of ZnPC and GO in a Device

While ZnPC and GO have individually demonstrated their potential for gas sensing, the combination of these materials for a gas sensing application has yet to be studied. A search through online databases revealed that these materials have only been used together in a broadband optical limiter and the experiments reported in this chapter are the first to report on the gas-sensing properties of these materials when used together[24].

5.1.2 Bilayer Device Fundamentals

Device Background

In mixed material devices, the device resistance is changed when the analyte physisorbs onto the sensing molecules of a first material and, in a doping like reaction, changes the carrier density or mobility in the conductive matrix made of a second material. While this concept is excellent in improving particular aspects of the sensing device, it is not without its drawbacks.

These drawbacks include:

(i) The non-selective conductive layer is exposed to the analyte and this increases the likelihood of false positives due to cross-sensitivities

(ii) Due to the lower concentration of sensing sites, sensitivity of the device to the analyte is reduced

The embodiment of this design is shown in Fig. 5.2 and differs from others in the way that the phthalocyanine materials were expected to interact with the conductive film. Instead of using a doping technique to change the carrier density, this design utilized a change in the external applied field to modulate the Fermi level in the conductive layer to change the resistance of the layer. Changing this Fermi level then changes the resistance of the layer by modifying the concentration of carriers in the conducting layer.

Device Principles

Instead of depending on a doping like interaction in the form of a physical connection between the analyte, sensing material and conducting layer, interaction in the bilayer gas sensor device is in the form of an electric field coupling between the analyte and sensing material.

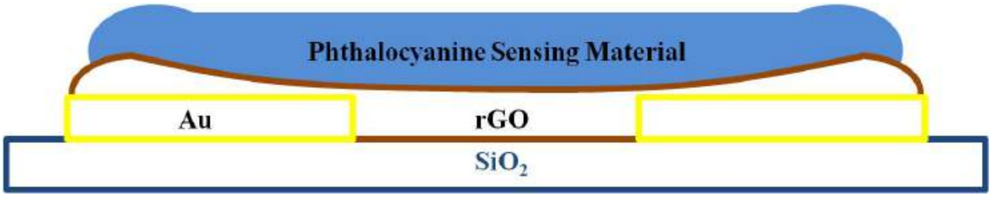

Figure 5.2: Schematic of the bilayer device for gas sensing showing the deposition of a sensing layer onto a conductive reduced GO layer with variable sensing layer and conductive layer thicknesses.

This design offers the following advantages:

(i) Errors due to cross sensitivity can be eliminated if the sensing layer used encapsulates the conductive material

(ii) Sensing sites density is higher in the bilayer device than a device that decorates the GO flake with sensing material

Graphene and reduced GO are candidate materials for the conductive layers as the application of an external electric field is known to change the conductivity of a reduced GO layer and open band gaps in bilayer graphene[25–28]. The goal of this work was to prove and collect data on the concept of the bilayer device by characterizing the performance of this novel device. After that, the specific requirements of the device design, conductive layer and sensing layer can be defined and optimum materials chosen.

In this design, the electric field was provided by the ZnPC sensing material when it reacted with the analyte molecule. In layers consisting of only ZnPC, the material acted as a p-type semiconductor and holes would be injected into the layer when it interacted with an oxidising gas such as NO_2[8,10,12].

ZnPC is sensitive to sub-ppm concentrations of NO_2 and responses were observed within seconds of NO_2 exposure[6,7,9]. This response comes from the physisorption of NO_2 onto the ZnPC molecule and results in an exchange of electrons, creating a microscopic dipole that spans the two molecules. This is represented as a change in the contact potential difference (CPD) at the ZnPC/environment interface when the film is exposed to NO_2, shown in Fig. 5.3.

However it is not known if the dipoles created from the individual ZnPC-NO_2 interactions result in the formation of a field. Even if a field was created, it was also not known if this field would be sufficiently large to cause a change in the resistivity of the conducting layer.

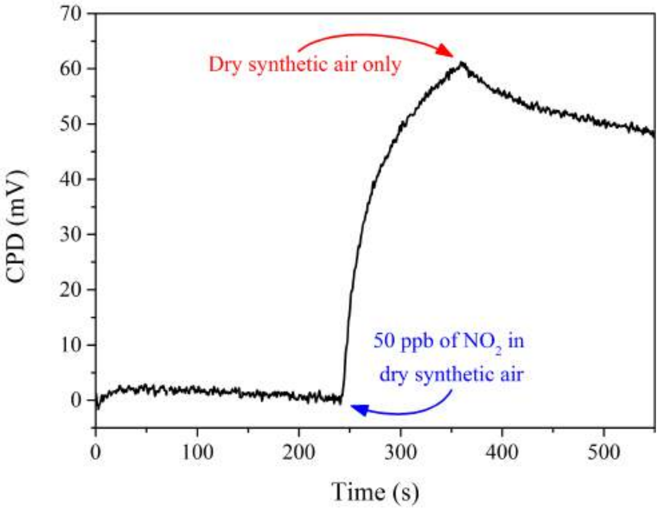

Figure 5.3: Contact potential difference measured by Kelvin Probe at the ZnPC/environment interface when 50 ppb of NO_2 is introduced.

Device Design

The device is fabricated by depositing a layer of sensing material onto a layer of conductive material in a bilayer device as shown in Fig. 5.2. On a silicon substrate, gold interdigitated electrodes were deposited in a finger like structure as was shown in Fig. 2.7 and on to these electrodes, varying thicknesses of GO and ZnPC were deposited. As phthalocyanines are not stable at the higher temperatures used to reduce GO, the sensing layer was deposited onto conductive layer only after thermal reduction of GO had been performed.

After fabrication, the devices were pre-conditioned by exposure to ambient conditions for at least two days before any sensing measurements were made. This practice was carried over from ZnPC only devices which required the pre-conditioning step to allow oxygen doping to occur. In these samples, oxygen doping helped to reduce the resistance of the finished ZnPC only device but was not expected to affect the bilayer device. In this case, the pre-conditioning step was retained to stabilize the sensing material and minimize changes to the ZnPC layer used.

5.2 Expected Response of the Bilayer Device

5.2.1 Theoretical Model of a Bilayer Device

Before coming to the results from the bilayer devices, the expected outcome from the experiment was studied by considering the effect of an electric field from a sensing layer on the resistance of the conductive layer underneath. A simplified schematic of the bilayer device is shown in Fig. 5.4, which assumes that the source and drain electrodes are of the same height, h, as the conductive layer, while the sensing layer forms neatly over the conductive layer only.

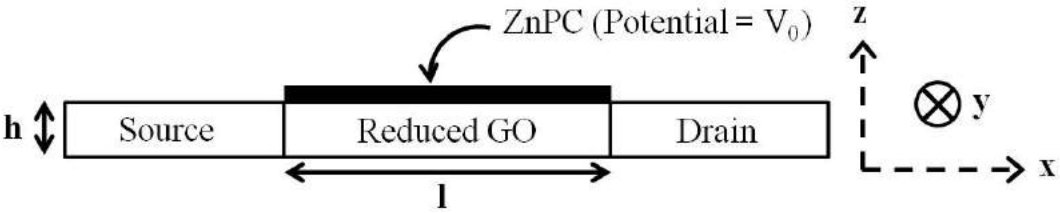

Figure 5.4: Simplified schematic of the bilayer gas sensor used in deriving the expected response. The thickness of the conductive layer, source and drain are exaggerated for visual clarity.

Setup of Model

The resistance, R, of the conductive layer is given by:

$$R = \frac{\rho\, l}{A} = \frac{\rho\, l}{b \cdot h} \tag{5.1}$$

where ρ is the resistivity of the conductive layer and b is the breadth of the electrode in the y-direction of the schematic in Fig. 5.4.

Making the simplification that electrons are responsible for conductivity and neglecting the conductivity of the ZnPC layer, ρ is rewritten as:

$$\rho = \frac{1}{n\, e\, \mu} \tag{5.2}$$

where n is the carrier concentration, e the electron charge and μ the mobility of the carrier.

Treating the reduced conductive layer as a semiconductor, the carrier concentration varies as a function of the external applied voltage, V, according to:

$$n(V) \;=\; n_i \exp\left(\frac{V + E_f - E_i}{kT}\right) \tag{5.3a}$$

with

$$n(0) \;=\; n_i \exp\left(\frac{E_f - E_i}{kT}\right) \;=\; n_0 \tag{5.3b}$$

Here n_i is the intrinsic carrier concentration, E_f & E_i are the Fermi and intrinsic energy levels respectively, k is the Boltzmann constant and T is the temperature. The sensing layer provides the external applied voltage and, like a parallel plate capacitor, was assumed to change linearly through the conductive material:

$$V \;=\; V_0\left(\frac{z}{h}\right),\; 0 \;<\; z \;<\; h \tag{5.4}$$

5.2.2 Effect of Analyte Sensing Event

Dependence of Layer Resistance on V_0

Using this model, the conductive layer can be treated as a stack of parallel resistors and the total sheet resistance found by summing the resistance of these resistors. This is done in the form of an integration by using Equations (5.1) through (5.4) as shown in the following calculation.

$$\begin{aligned}
\frac{1}{R} = \int_0^h \frac{b}{\rho l}dz \;&= \int_0^h \frac{bne\mu}{l}dz \\
&= \frac{be\mu}{l}\int_0^h n_i \exp\left(\frac{V + E_f - E_i}{kT}\right)dz \\
&= \frac{be\mu n_0}{l}\int_0^h \exp\left(\frac{\frac{z}{h}V_0}{kT}\right)dz \\
&= \frac{be\mu n_0}{l}\frac{hkT}{V_0}\left[\exp\left(\frac{V_0}{hkT}\,z\right)\right]_0^h \\
&= \frac{be\mu n_0}{l}\frac{hkT}{V_0}\left[\exp\left(\frac{V_0}{kT}\right) - 1\right] \\
&= \frac{A}{\rho l}\frac{kT}{V_0}\left[\exp\left(\frac{V_0}{kT}\right) - 1\right]
\end{aligned}$$

Taking the inverse of this gives the relationship between the resistance of the conductive layer and the external applied voltage from the sensing layer. The previous equation then becomes:

$$R = \frac{\rho l}{A} \frac{V_0}{kT \left[\exp\left(\frac{V_0}{kT} - 1\right)\right]} \tag{5.5}$$

This modified equation has the familiar resistance term that was shown in Equation (5.1) and a second voltage dependent term. Taking the limit of this second term as $V_0 \to 0$:

$$\lim_{V_0 \to 0} \frac{V_0}{kT \left[\exp\left(\frac{V_0}{kT} - 1\right)\right]} = 1 \tag{5.6}$$

which is the expected behaviour of the device. That is to say, the resistance of the conductive layer is not changed when no external voltage is applied.

Equation (5.5) is plot in Fig. 5.5 and shows the relationship between the resistance of the conductive layer and the magnitude of the applied voltage. The graph shows that the magnitude and direction of the change in resistance of the conductive layer depends on the voltage applied to the system.

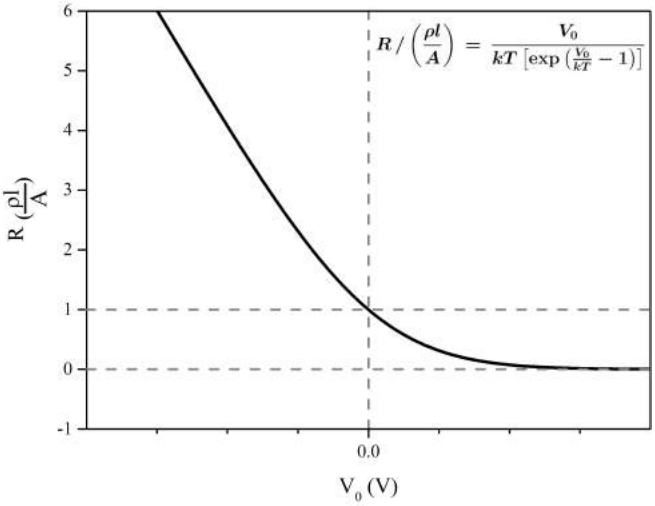

Figure 5.5: Plot of the resistance, R, of a semiconducting layer against an arbitrary applied voltage, V_0 at room temperature. Resistance values are shown as a multiple of the resistance of the layer without an applied voltage.

Taking derivatives with respect to V_0

This analysis is further developed by taking the first and second derivatives of Equation (5.5). These derivatives are:

$$\frac{dR}{dV_0} = \frac{\rho l}{A} \frac{kT\left[\exp\left(\frac{V_0}{kT}\right) - 1\right] - V_0 \exp\left(\frac{V_0}{kT}\right)}{(kT)^2\left[\exp\left(\frac{V_0}{kT}\right) - 1\right]^2} \tag{5.7a}$$

$$\frac{d^2R}{dV_0^2} = \frac{\rho l}{A} \frac{\exp\left(\frac{V_0}{kT}\right)\left[-2\,kT\exp\left(\frac{V_0}{kT}\right) + V_0\exp\left(\frac{V_0}{kT}\right) + 2\,kT + V_0\right]}{(kT)^3\left[\exp\left(\frac{V_0}{kT}\right) - 1\right]^3} \tag{5.7b}$$

At room temperature, kT ≈ 25 meV and letting $\frac{\rho l}{A} = 1$, the above equations are plot for arbitrary values of V_0 in Fig. 5.6. The graphs show that maximum gradient change occurs at high negative voltage values, while the maximum rate of gradient change occurs when the external applied voltage is equal to zero. Borrowing naming conventions from field effect transistors, the external voltage can be affected by the application of a gate voltage, V_g, which affects the system by replacing all instances of V_0 with $V_0 + V_g$ in the equations.

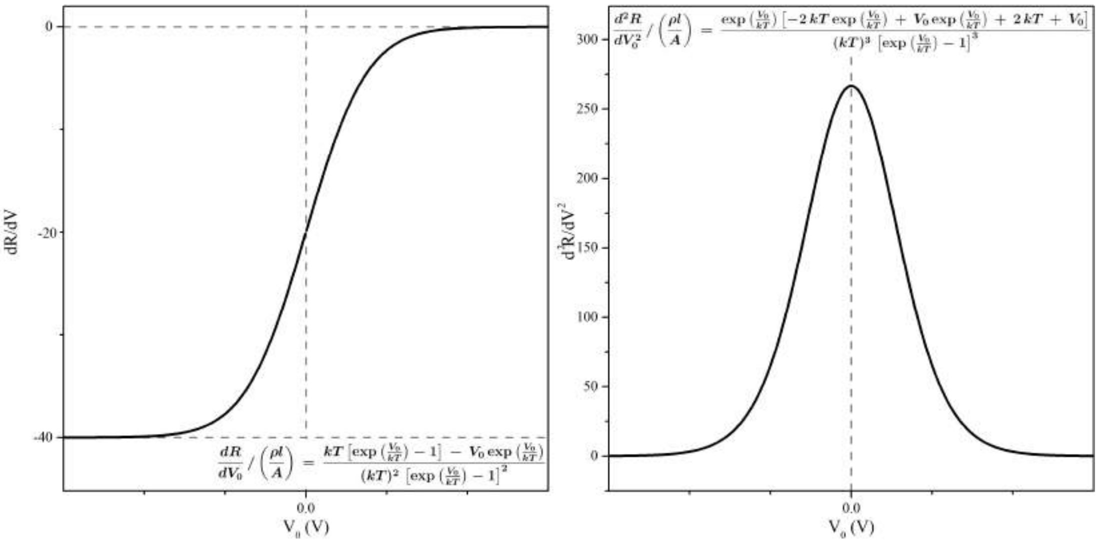

Figure 5.6: (a) First derivative and (b) second derivative of resistance with respect to applied external voltage. kT at room temperature is taken as 25 meV and $\frac{\rho l}{A}$ is taken to be unity.

This point is important as different Fermi energies in the conductive and sensing layers means that a contact potential, V_c exists along the interface region of these materials. Depending on the depth of the depletion region formed, the contact potential could change the carrier concentration within the conductive layer, may have an effect on the sensitivity of the device and can be removed or enhanced by the $V_0 + V_g$ term. For $V_0 + V_g \neq 0$, either a larger or smaller $\dfrac{dR}{dV_0}$ value can be attained, but the $\dfrac{d^2R}{dV_0^2}$ will always be made smaller.

This has implications on the device depending on the signal processing method utilised for detection. For example, if the signalling method used is an absolute change in the resistance of the device, it is desirable that the contact potential and applied gate voltage work in tandem to put the device in a region where the magnitude of $\dfrac{dR}{dV_0}$ is large. This ensures that any change in V_0 due to a sensing event would result in a large change in the resistance of the device.

Similarly, if the signalling method used in detection is the instantaneous change in the gradient of the resistance graph, then it would be ideal to apply a voltage by means of a bottom gate design to counteract the contact potential ($V_g - V_c = 0$), so that the change in gradient due to analyte detection event is maximised.

Effect of Changing Layer Thicknesses

Conductive Layer Thickness

The relationship between the resistance of the device and its dependence on the external applied voltage can be found from Equation (5.5) by expansion of the A term ($A = b \times h$). Changing the thickness of the conducting layer will causes its resistance to change according to $\frac{1}{h}$.

Using the theoretical model, the magnitude of the change in device current due to a sensing event is expected to scale linearly with h. This is shown in Equation (5.5), where the device resistance is a product of $\dfrac{\rho\, l}{b \cdot h}$ and a function of V_0. For the same V_0 value, a larger h will give a larger change in R and hence a larger change in the device current.

Sensing Layer Thickness

In principal, modifying the thickness of the sensing layer should not affect the performance of this bilayer device as the applied voltage from the sensing layer depends on the concentration of bound analytes in the sensing layer and not the quantity of these bound analytes. Treating the analyte-sensing layer combination as a bound charge, the potential experienced at a given distance, **r**, from the surface of the sensing layer depends on:

$$V(\mathbf{r}) = \frac{1}{4\pi\epsilon_0} \oint_{\mathcal{S}} \frac{\sigma_d}{r} da' + \int_{\mathcal{V}} \frac{\rho_d}{r} d\tau' \tag{5.8}$$

where the unit surface charge is integrated across the surface, $\mathcal{S}$, and the unit charge density integrated for the volume, $\mathcal{V}$, of the layer.

While this may be true for a steady state solution, it oversimplifies the model. Besides considering the dynamic nature of analyte bonding onto the sensing molecules, one will need to take into account the rate of diffusion of the analyte through the sensing layer as well.

In the short term, it is likely that a majority of sensing events occurs at the sensing layer/environment interface and not within the bulk of the sensing material. This effect would weaken the field in the sensing material and could reduced the change in device current observed.

Discussions on the Model

In these calculations, some assumptions were made which will be discussed here. It was assumed that

1. the sensing layer was infinitesimally thin,
2. the sensing layer did not contribute to resistivity,
3. the conductive layer was not affected by the analyte gas,
4. the sheet resistance in the conductive layer was much greater than the contact resistance between the conductive material and the metal electrode.
5. and the external applied voltage from the sensing layer, V_0 changes according to the concentration of analyte physisorbed onto the sensing layer.

The first assumption was made to simplify the calculation and remains true for ultra-thin sensing layers on a reduced-GO conducting layer. The model can be improved to include the real thickness of the sensing layer, however this would introduce a time dependent factor to the equation and require one to have knowledge on the rate of diffusion of the analyte through the sensing material.

The second assumption may not hold true all the time. As shall be shown later, a typical ZnPC sensing layer deposited on the finger electrode setup exhibits a device resistance in the order of gigaohms, while the GO layer has a sheet resistance on the order of kilohms. Since the layers act as resistors in parallel, it is easy to see that the overall resistance of the system is not affected significantly by the addition of a high resistance sensing layer onto the lower resistance conduction layer. Additionally, it was noted that the model does not account for instances when the sensing and conductive layers have similar conductivities.

The third assumption is not true for reduced GO as its resistivity does change when introduced to NO_2 and this must be taken into account during data analysis[29,30]. However, this point may be ignored if the ZnPC turns out to be a good encapsulant and can be engineered to prevent interaction between reduced GO and NO_2.

The fourth assumption can be assumed to be true as the contact resistance between reduced GO and a metal electrode is typically in the order of kilohms which is much lower than the sheet resistance of the reduced GO conductive layer[31].

The fifth assumption is arrived at by taking account of the fact that the rate of absorption and desorption on the sensing layer depends on the proportion of available sensing sites available in the layer. It is expected that the voltage derived from the sensing layer depends on the concentration of filled sensing sites in the sensing layer and at a given analyte concentration, the rate of analyte physisorption onto the sensing layer will gradually decrease over time while the rate of analyte desorption will gradually increase.

Given enough time, an equilibrium will be reached such that the rate of desorption will match the rate of physisorption and there is a constant number of occupied sensing sites in the sensing layer. These occupied sensing sites then provide a net electric field whose strength depends on the concentration of these dipoles.

Finally, although these assumptions affect the accuracy of the quantitative data, they are not expected to affect the qualitative data described and future work will improve on the model to address these assumptions.

5.3 Characterization of Monolayer Devices

Due to the low device currents inherent in the phthalocyanine only devices, there was a need to increase currents in the device so as to reduce data acquisition time and to improve the systems response speed to changes in external stimuli. A typical ZnPC sensing layer in the gas sensor device is 60 nm thick, however device currents rarely exceeded one nanoamp. As a result of these low device currents, data sampling rates on a Keithley 2636A did not exceed 1 Hz and this limited the responsiveness of the system.

Sampling rates could be increased dramatically as device currents were increased and these higher currents would reduce the challenges involved in integrating the device into an ASIC as well. Ideally, the modified device should display significantly increased conductivity values while retaining the same sensitivity towards the analyte.

In this section, the sensing capabilities of a ZnPC layer and reduced GO layers are first explored. In the following section, the performance characteristics of the bilayer devices with various combinations of layer thicknesses are shown. Finally, the results shown in these sections and the effectiveness of the approach towards achieving the desired goal are discussed.

5.3.1 Characterization Parameters

Experiment

In a standard experiment, the finished device is prepared for testing by first mounting it into a closed testing chamber, shown in Fig. 2.15, after the sample had been subject to two days of oxygen doping. After mounting, a stream of synthetic dry air is blown into the chamber and the electrodes held at a bias of 5 V for two minutes before the testing phase was conducted. This was done to stabilize the device and to get a baseline current of the device.

The testing phase consisted of running a stream of synthetic dry air which has a controlled concentration of the analyte gas mixed into it and recording the change in device current. The analyte gas was mixed with the synthetic dry air at concentrations of 50, 60, 80, 100, 120, 200 and 500 ppb and for each given concentration, the mixture was pumped into the chamber for one minute. After each minute of testing, the chamber was purged with synthetic air for two minutes before the next concentration of the mixed gases was pumped into the chamber.

Device

The devices were made using ZnPC and/or reduced GO layers of varying thicknesses and a list of all samples used is shown in Table 5.1. For the reference device, only ZnPC at a thickness of 60 nm is shown as it was a thickness optimized for maximum sensitivity and device current[32]. For the reduced GO reference devices, two thicknesses were used so that the responsiveness of thin and thick layers of reduced GO towards the presence of NO_2 can be shown.

5.3.2 ZnPC Sensing Layer

The response of the ZnPC sensing layer to increasing concentrations of NO_2 is shown in Fig. 5.7 along with a plot of the sensitivity of the device towards changes in analyte concentration. Here, the sensitivity of the device is determined by the slope of the relative gradient change (RGC) graph and the RGC graph is a plot of the change in the gradient of the current time graph against the concentration

Table 5.1: List of all ZnPC and GO thicknesses used in the gas sensing devices in this chapter. All thicknesses in nanometres.

Experiment	**Thicknesses**		**Sample Reference**
	ZnPC	**GO**	
Reference	60	0	60/0
	0	5	0/5
	0	44	0/44
Constant ZnPC Thickness	1	5	1/5
	1	11	1/11
	1	22	1/22
	1	33	1/33
	1	44	1/44
Constant Reduced GO Thickness	1	44	1/44
	10	44	10/44
	60	44	60/44
Equal Thicknesses	5	5	5/5

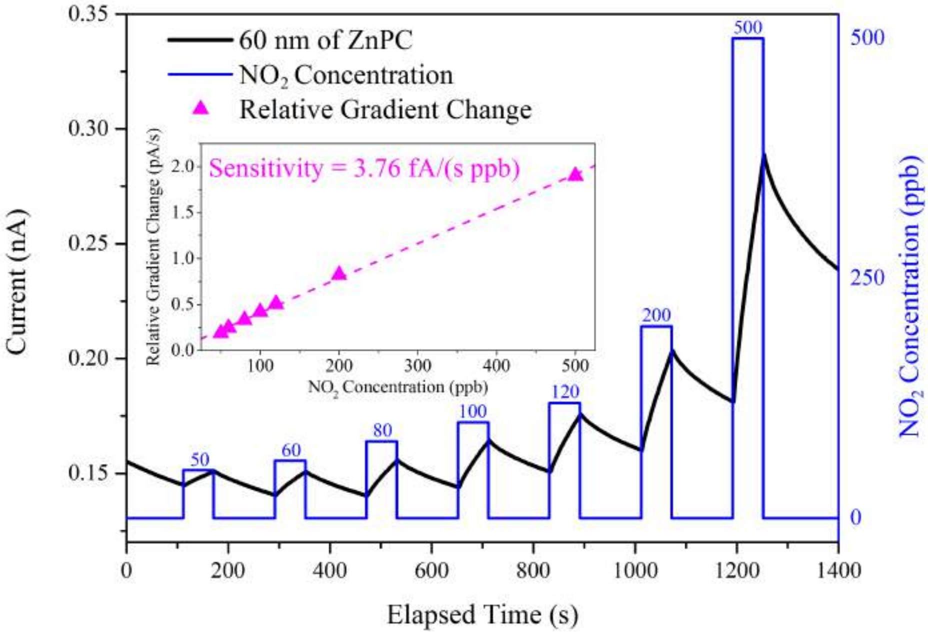

Figure 5.7: Characterization results of the ZnPC gas sensing device. The black line represents the device current and the blue line represents the NO_2 concentration. (Inset) A plot of the RGC at different NO_2 concentrations; the device sensitivity is given by the gradient of the RGC against NO_2 concentration graph.

of NO_2 introduced into the chamber. As a point of clarification, the change in the gradient was calculated at the point in time when NO_2 was introduced into the chamber and is calculated by subtracting the gradient after NO_2 introduction from the gradient before NO_2 was introduced.

As shown in Fig. 5.7, the typical gas sensor device with a ZnPC layer has a device current on the order of 0.1 nA and the RGC of the device changed almost linearly with respect to NO_2 concentration. From this graph, the sensitivity of the device was calculated to be 3.76 fA(s ppb)$^{-1}$.

While the linearity of the RGC towards NO_2 concentration is important, the low device current needs to be overcome while keeping operating voltages unchanged so that the sensor can be easily integrated into hand-held consumer devices which have typically have low operating voltages and significant limitations in terms of operating power available. Besides low device currents, the characterization results also showed other problems that were inherent to the ZnPC based gas sensor device.

These problems noted are as follows:

(i) Baseline drift

The current levels of the ZnPC device falls over time and this is most visible just before the 50 ppb measurement, where the device current is falling steadily. The cause of this drift is as yet undetermined and poses issues to the reliability of the device.

(ii) Long saturation times

In all cases, the time taken for saturation was longer than one minute and and no saturation was observed. This was also why the RGC, and not the absolute change in current, was used to characterize sensitivity of the device towards the presence of NO_2.

Due to this, the sensitivity of the device to the concentration of NO_2 present was determined by means of RGC and not the gradient as it was recognized that the two minute recovery interval was not sufficient for full removal of the absorbed NO_2. By using RGC, the effects of desorption and absorption are accounted for without having to fully remove all NO_2 from the sensing layer and this speeds up the process of characterization. However, use of this technique comes with the following issues:

(i) It is easy to envision circumstances under which the RGC technique will give an erroneous result. For example, if the device were first exposed to a NO_2 concentration of 100 ppb and this was increased to 200 ppb, the RGC method would not show a NO_2 concentration of 200 ppb. Based on the RGC shown in Fig. 5.8, it is likely that the device will reflect a NO_2 concentration of less than 50 ppb instead. While this may be a real problem for a consumer device, the controlled experiment conditions ensures that this does not occur here.

(ii) This method may lead to an artificial improvement of the device sensitivity as shown in Fig. 5.8. The slope of the graph increases slightly from 3.62 to 3.76 fA/(s ppb) when the method of RGC is used. However, because it would not be feasible to fully remove all NO_2 before the next sensing event, taking the actual gradient is not a robust method especially if the sample has a lower proportion of sensing sites available. Furthermore, the same error will be carried throughout the experiment and is not expected to affect the final result when comparing among devices.

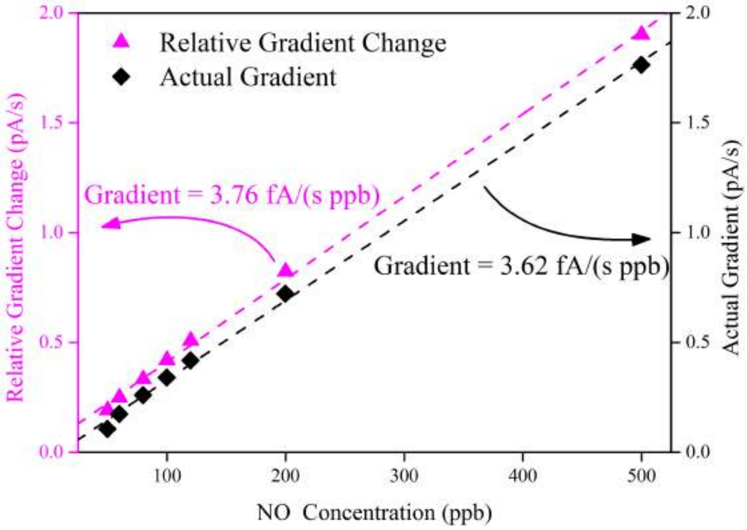

Figure 5.8: Graph showing the sensitivity of the ZnPC gas sensor device towards NO_2 and two methods of finding the sensitivity are shown.

5.3.3 Reduced GO Sensing Layer

Reduced GO layers of 5 and 44 nm were tested for sensitivity towards the presence of NO_2 and these characterization results are shown in Fig. 5.9. Despite being thinner than the ZnPC layer, these devices have measured current values on the order of milliamps and this is six orders of magnitude greater than the current values in ZnPC layers.

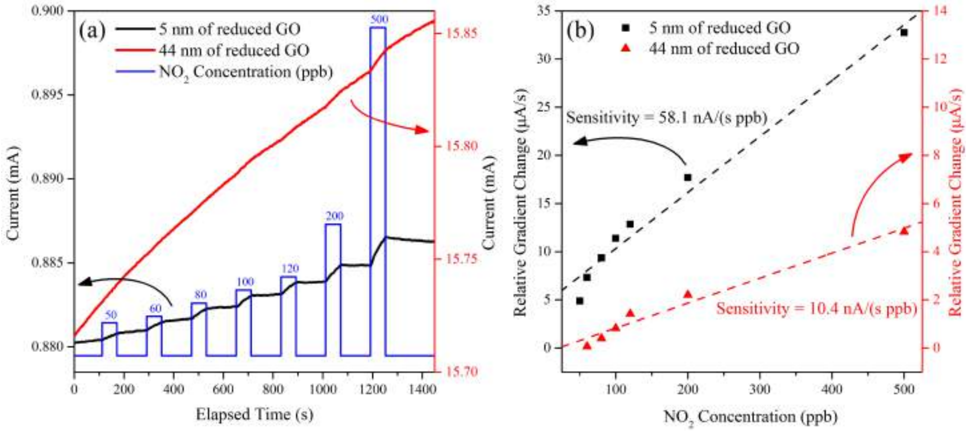

Figure 5.9: (a) Response of 5 and 44 nm thick reduced GO layers to increasing concentration of NO_2. (b) Sensitivity graph of the layers.

With a slope of 58.1 nA/(s ppb), the RGC graph shows that the device made using 5 nm of reduced GO was almost 6× more sensitive to changes in the NO_2 concentration the the device made using 44 nm of reduced GO. However the latter device had the advantage of having a device current that was almost 20 times higher than the device made using the thinner layer of reduced GO.

These results suggest that the rate of NO_2 diffusion through reduced GO is low. Although the devices were made of the same material and should have the same reactivity towards NO_2, the thicker device had a higher current and lower sensitivity towards the presence of NO_2. This observation also meant that the ZnPC layer could sufficiently encapsulate the reduced GO layer such that NO_2 could be prevented from reacting with the bulk of the conductive layer.

5.3.4 Comparing Sensitivities of Monolayer Devices

Due to the large differences in current values, the data had to be normalized before comparison. Normalization was done by dividing each data point by the range of the experimental data after shifting the first data point as '0'.

In terms of an equation, the current, I, was normalized using the equation

$$I_i^{\text{Norm}} = \frac{I_i - I_1}{I_{\text{Max}} - I_{\text{Min}}} \tag{5.9}$$

where I_i^{Norm} is the normalized current, i is the index of the data point and I_{Min} and I_{Max} are the minimum and maximum current points respectively.

Using this method, the effect of device current on the value of the sensitivity can be removed and the normalized RGC used to compare the devices. A graph of the data after normalization and the normalized RGC of these devices are shown in Fig. 5.10(a) & (b) respectively. Despite the marked improvement in device currents when using reduced GO, the slope of the normalized RGC graph confirms that reduced GO was less sensitive to NO_2 than ZnPC. Additionally, it is well known that reduced GO is an unselective gas sensor, making it an unattractive material for use in the sensing layer.

Comparing the 5 & 44 nm thick reduced GO layers, the lower normalized sensitivity of the device with a thicker reduced GO layer confirms that NO_2 diffusion through the layer is slow. Being made of the same material, the rate of physisorp-

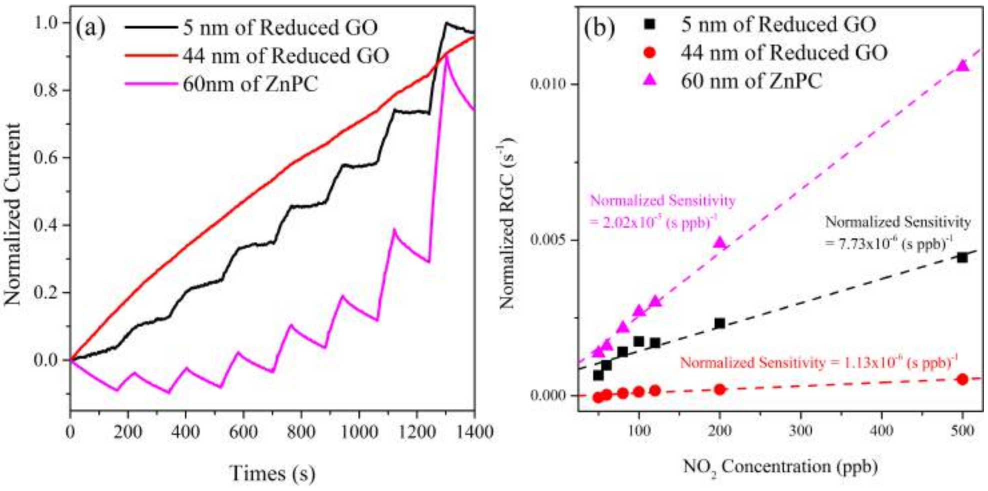

Figure 5.10: (a) Experimental data of ZnPC and reduced GO layers after normalization. (b) Normalized RGC graphs of the monolayer devices.

tion of NO_2 onto the reduced GO flakes should be the same in both devices and assuming that the NO_2 was uniformly distributed through the reduced GO layer the films should have had the same normalized sensitivities.
Instead, a lower normalized sensitivity was observed and this could only be understood if the NO_2 penetrated the reduced GO layer slowly. Table 5.2 collates the values of the ZnPC and GO layers and it appeared that sensitivity and normalized sensitivity were inversely related to device in monolayer devices. These characteristics of the ZnPC and reduced GO layers will be used later in the chapter to prove the validity of the bilayer concept.

Table 5.2: Summary of the important performance characteristics of the monolayer gas sensor devices.

Material	**ZnPC**	**Reduced GO**	
Thickness	60 nm	5 nm	44 nm
Current	0.20 nA	0.89 mA	15.8 mA
Sensitivity	3.76 fA(s ppb)$^{-1}$	58.1 nA(s ppb)$^{-1}$	10.4 nA(s ppb)$^{-1}$
Normalized Sensitivity	2.02×10^{-5} (s ppb)$^{-1}$	7.73×10^{-6} (s ppb)$^{-1}$	1.13×10^{-6} (s ppb)$^{-1}$

5.4 Characterization of Bilayer Devices

This section will consider the sensitivity of the bilayer device to the presence of varying concentrations of NO_2. The first part of this section will focus on the effect of varying the thickness of reduced GO with a thin layer of ZnPC, while the second part of the section will vary the thickness of ZnPC on a layer of reduced GO. To complete the characterization, a device with equal thicknesses of GO and ZnPC was fabricated and characterized.

5.4.1 Changing Reduced GO Thickness

In the first series of experiments, a 1 nm thick layer of ZnPC was deposited onto reduced GO with thicknesses from 5 to 44 nm. After oxygen doping for two days, the devices were tested for sensitivity towards NO_2 and the experiment results are shown in Fig. 5.11. Set in each results graph is the normalized RGC when the device was exposed to different NO_2 concentrations and the corresponding normalized sensitivity value of the device.

From these results and those shown in Table 5.2, adding 1 nm of ZnPC onto 5 nm of reduced GO almost tripled the normalized sensitivity of the sensor based on reduced GO from 7.73×10^{-6} to 2.01×10^{-5} (s ppb)$^{-1}$. However, increasing the thickness of the reduced GO layer decreased the normalized sensitivity of the bilayer device and all of the devices that followed had normalized sensitivity values lower than the 0/5 device.

At the same time, the results also showed that device currents increased with increasing reduced GO thickness. The current levels in the device increased from ~14.5 μA in the 1/5 device to ~18 mA in the 1/44 device and this is a marked improvement over the 0.1 nA device currents observed in the devices made using ZnPC only. Furthermore, the graph of the device current against reduced GO layer thickness, shown in Fig. 5.12, confirms that a linear relationship exists between these parameters and the slope of the graph was used to derive a physical property of the gas sensor device.

The device current and reduced GO thickness are related by Ohm's law and Equation (5.1) to give:

$$I = V \cdot \frac{b}{\rho l} \cdot h \tag{5.10}$$

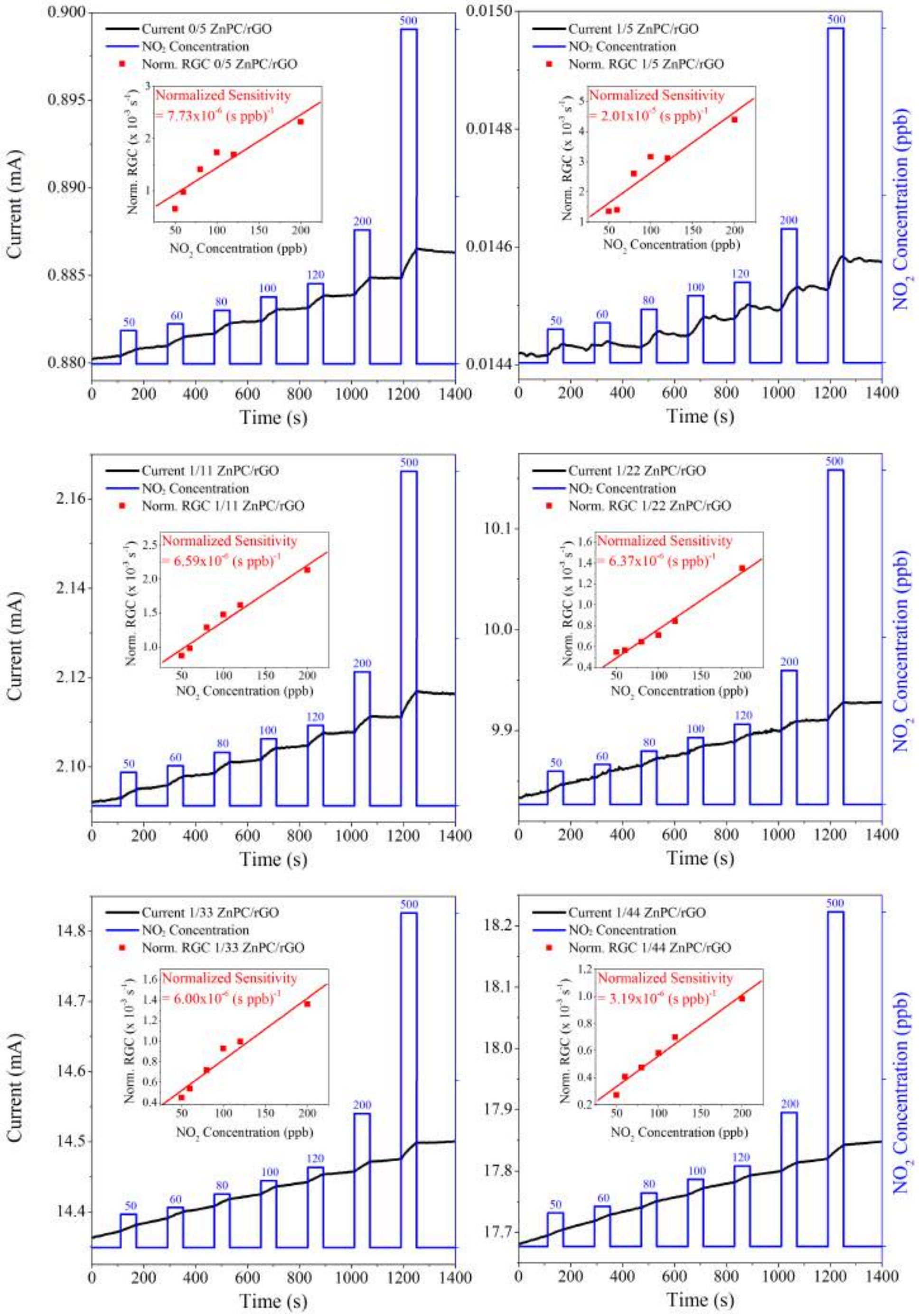

Figure 5.11: Response of bilayer sensor device consisting of 1 nm of ZnPC on 5, 11, 22, 33 & 44 nm of reduced GO as compared to a device consisting of only 5 nm of reduced GO. Inset graphs are the normalized RGC values and the device consisting of 5 nm of reduced GO is included as a point of reference.

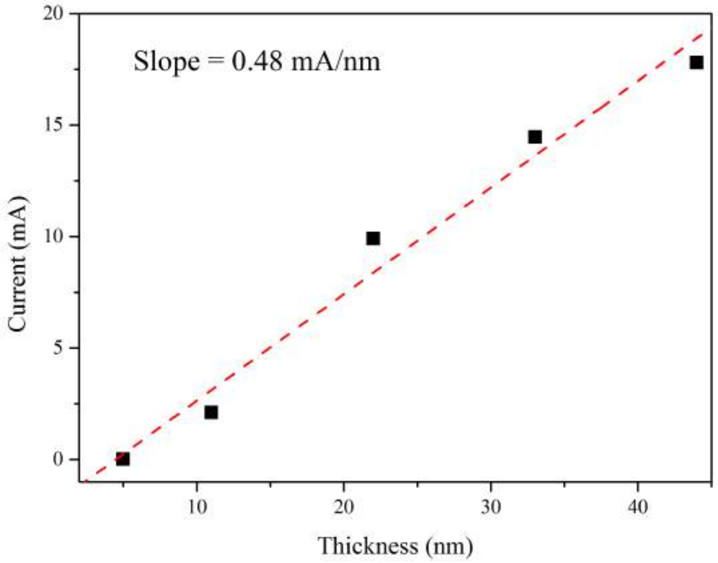

Figure 5.12: Graph showing the linear increase in device current with respect to reduced GO thickness.

The device current changed linearly with respect to the thickness of the reduced GO layer and since the bias applied was 5 V, $\frac{b}{\rho l}$ was found to be equal to 0.096. This value depends on the design of the electrode and has implications on the design of the inter-digitated finger electrodes.

5.4.2 Changing ZnPC Thickness

In this series of experiments, the thickness of the reduced GO layer is kept constant at 44 nm, while the thickness of the ZnPC layer is increased from 1 to 60 nm. As before, the devices are oxygen doped prior to the characterization measurement and the results are shown in Fig. 5.13.

The device current was high, in the order of tens of milliamps and the samples with 1 and 10 nm of ZnPC recorded an increase in normalized sensitivity. With the addition of 1 nm of ZnPC, the normalized sensitivity was almost tripled from 1.13×10^{-6} (s ppb)$^{-1}$ in the 0/44 device to 3.19×10^{-6} (s ppb)$^{-1}$ in the 1/44 device. On the other hand, the addition of 10 nm of ZnPC onto 44 nm of reduced GO resulted in a modest 18 % increase in the value of the device's normalized sensitivity and the device with 60 nm of ZnPC on 44 nm of reduced GO exhibited a 33 % decrease.

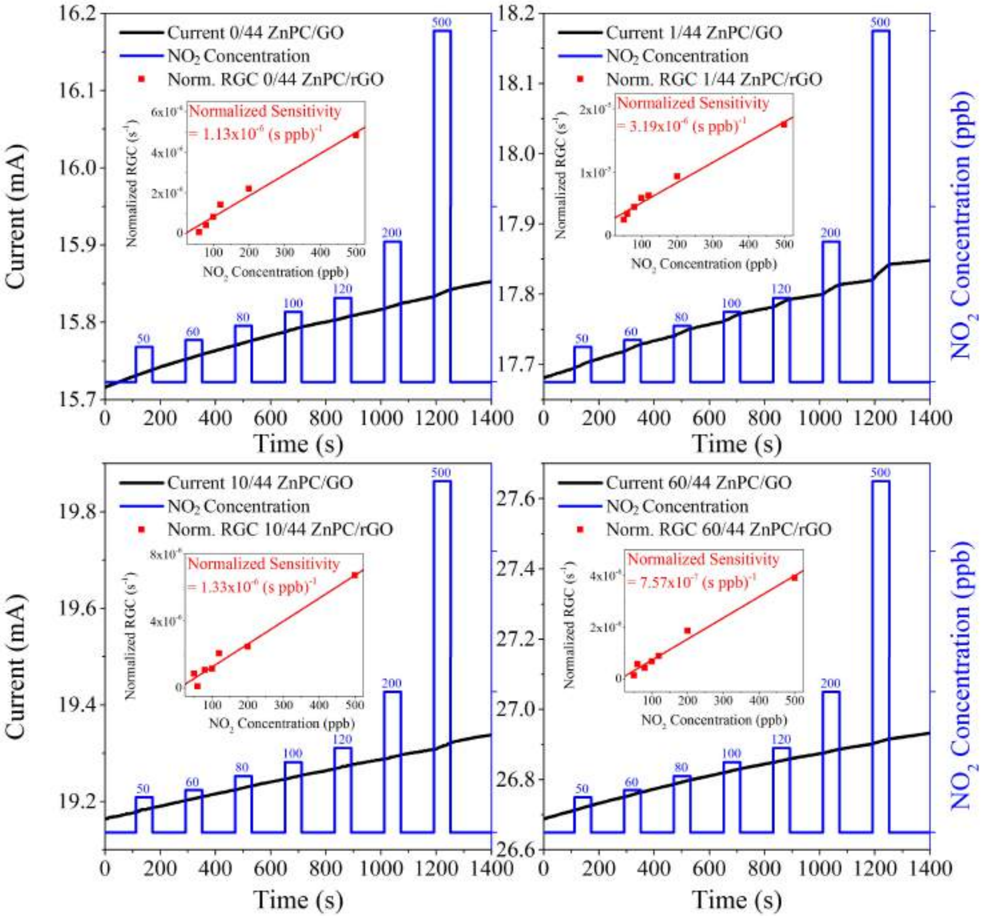

Figure 5.13: Response of bilayer sensor device consisting of ZnPC with thicknesses of 1, 10, & 60 nm on a 44 nm thick layer of reduced GO. Inset graphs are the normalized RGC values and the device consisting of 44 nm of GO only is shown for reference.

These results show three things about the bilayer devices. Firstly, the maximal effective thickness of the interaction between ZnPC and reduced GO was more than 54 nm, but less than 104 nm. Secondly, the decrease in normalized sensitivity values with increasing device thickness that was observed in the previous section was also seen here. Finally, the device current increases with increasing thickness of the ZnPC layer.

5.4.3 Discussions on Bilayer Device Concept

Relative Gradient Change of Bilayer Device

The measurement of device sensitivity shown thus far is the second time derivative of the current time graph of a device under test and by using Equation (5.5), the expected change in device sensitivity to a change in conducting layer thickness can be predicted.

The current and resistance of the device are related by Ohm's law, $I = \frac{V_A}{R}$, where V_A, the applied bias, is a constant. Taking the derivative with respect to R gives:

$$\frac{dI}{dR} = -\frac{V_A}{R^2} \tag{5.11}$$

The RGC at the point of NO_2 introduction is the change in gradient and is related to the change in current as follows:

$$\begin{aligned}
\text{RGC} &= \frac{d^2I}{dt^2} \\
&= \frac{d}{dt}\left(\frac{dI}{dR}\cdot\frac{dR}{dt}\right) \\
&= \frac{d}{dt}\left(-\frac{V_A}{R^2}\cdot\frac{dR}{dt}\right) \\
&= -V_A\left[\left(-2\frac{\frac{dR}{dt}}{R^3}\cdot\frac{dR}{dt}\right) + \frac{1}{R^2}\cdot\frac{d^2R}{dt^2}\right] \\
&= 2V_A\frac{\left(\frac{dR}{dt}\right)^2 - R\cdot\frac{d^2R}{dt^2}}{R^3}
\end{aligned} \tag{5.12}$$

The resistance of the bilayer device was shown in Equation 5.5 and is composed of two component; a time independent component, comprising of physical dimensions, and a time dependent component that depends on the concentration of analyte in the gaseous environment in the form $V_0(t)$.

With this, the equation can be rewritten as:

$$R = \frac{\rho l}{bh}\frac{V_0(t)}{kT\left[\exp\left(\frac{V_0(t)}{kT}-1\right)\right]} = \frac{\rho l}{bh}f(V_0(t)) \tag{5.13}$$

The first and second differentials of this equation are simply:

$$\frac{dR}{dt} = \frac{\rho l}{bh} \cdot \frac{d\,f(V_0(t))}{dt} \tag{5.14a}$$

$$\frac{d^2R}{dt^2} = \frac{\rho l}{bh} \cdot \frac{d^2 f(V_0(t))}{dt^2} \tag{5.14b}$$

This simplifies Equation 5.12 to become

$$\begin{aligned}\mathrm{RGC} &= 2V_A \frac{\left(\frac{\rho l}{bh} \cdot \frac{d\,f(V_0(t))}{dt}\right)^2 - \left(\frac{\rho l}{bh} \cdot f(V_0(t)) \cdot \frac{\rho l}{bh} \cdot \frac{d^2V_0(t)}{dt^2}\right)}{\left(\frac{\rho l}{bh} \cdot f(V_0(t))\right)^3} \\ &= 2V_A \cdot \frac{bh}{\rho l} \cdot \frac{\left(\frac{d\,f(V_0(t))}{dt}\right)^2 - \left(f(V_0(t)) \cdot \frac{d^2V_0(t)}{dt^2}\right)}{f(V_0(t))} \end{aligned} \tag{5.15}$$

According to this equation, the RGC of the device is expected to change linearly with respect to the thickness of the conductive layer.

To check if the calculations match the experimental results, the relative gradient change and sensitivity graphs of bilayer devices consisting of 1 nm of ZnPC on various thicknesses of reduced GO are shown in Fig. 5.14.

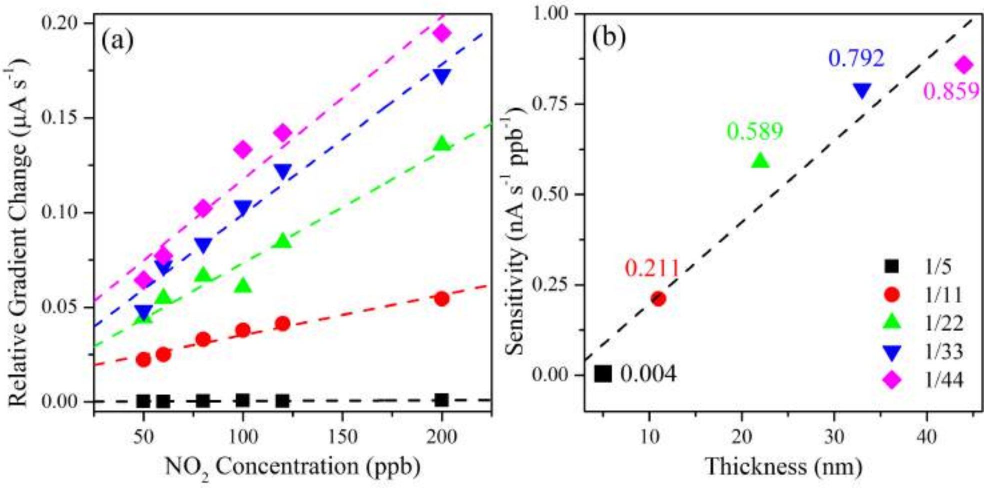

Figure 5.14: Graphs of the (a) RGC values at different concentrations of NO_2 and (b) sensitivity of bilayer devices with 1 nm of ZnPC on various thickness of reduced GO.

The values of the RGCs shown in Fig. 5.14(a) are not normalized values from the current versus time graphs in Fig. 5.11 and this is not the same as the normalized RGC values that are shown in the inset of the graphs in Figs. 5.11 & 5.13. For a given NO_2 concentration, the graphs show that the RGC values increases with increasing conductive layer thickness.

However, the sensitivity values of these devices are lower than the sensitivity values of reduced GO only devices, as shown in Table 5.3. In the case of the device with 5 nm of reduced GO, the addition of 1 nm of ZnPC caused the sensitivity to fall by over 12,000×, while the current decreased by 61×.

It is believed that the difference in device currents observed here is caused by a lack of environmental dopants in the thinner reduced GO layer. The concentration of oxygen and water molecules from the environment that is present within the the layer is expected to change the conductivity of graphene, carbon nanotubes and reduced GO and the height of the electrode walls and presence of the ZnPC layer would have prevented this doping interaction from occurring in the thinner 1/5 device but not in the thicker 1/44 device[33–35].

The cause of this decrease in sensitivity values becomes clearer when comparing devices with 44 nm of reduced GO. Here the device current did not change significantly, but the sensitivity still fell by 12× and indicates that the addition of the ZnPC layer imparts analyte selectivity to the devices. Instead of reacting with all the gases present, the ZnPC layer selective binds with the NO_2 molecules and prevents a significant proportion of the other gases from binding with the

Table 5.3: Device current and sensitivities of devices made from either 5 or 44 nm of reduced GO with and without 1 nm of ZnPC. While the sensitivity is reduced, the normalized sensitivity is improved by the addition of 1 nm of ZnPC. *Abbreviations: Sens. – Sensitivity & N. Sens. – Normalized Sensitivity.*

Thickness of / nm	**0**	**1**	**ZnPC**
5	885	14.5	*Current / μA*
	58.1	0.004	*Sens. / nA* $(s\ ppb)^{-1}$
	0.773	2.01	*N. Sens. /* $\times 10^{-5} (s\ ppb)^{-1}$
44	15.8	17.8	*Current / mA*
	10.4	0.859	*Sens. / nA* $(s\ ppb)^{-1}$
	1.13	3.19	*N. Sens. /* $\times 10^{-6} (s\ ppb)^{-1}$
Reduced GO			

reduced GO layer. While this reduces the sensitivity in real terms, the normalized sensitivities of the devices are shown to benefit from the addition of ZnPC and this normalized sensitivity is more important for the gas sensing device.

Furthermore, comparing sensitivities instead of RGC at a given NO_2 concentration has the added advantage of reducing data noise as each sensitivity data point is the gradient of the RGC against NO_2 concentration graph. Furthermore, Fig. 5.14(a) shows that the RGC changes linearly with respect to NO_2 concentration and Equation 5.15 shows a linear relationship between RGC and h. This means that the sensitivity is expected to change linearly with thickness and this is shown in Fig. 5.14(b). By comparing device sensitivities, the accuracy of the analysis is improved and confidence in the reliability of the conclusions increased.

Normalized Sensitivity of Bilayer Device

The normalized sensitivity values of these bilayer devices towards the presence of NO_2 are tabulated in Table 5.4 and plot against layer thickness in Fig. 5.15. The results indicate that normalized sensitivities decrease predictably as the overall thickness of the device increased.

Considering first the samples with 1 nm of ZnPC on reduced GO, increasing the reduced GO layer thickness decreased the normalized sensitivity of the device. However, as shown in Figs. 5.11 and 5.14(a), this decrease also came with an increase in both device conductivity and RGC.

On the other hand, adding 1 nm of ZnPC onto 5 or 44 nm of reduced GO resulted in a two and half to three time increase in the normalized sensitivity of the reduced GO layer. The sensitivities increased from 7.73×10^{-6} and 1.13×10^{-6} (s ppb)$^{-1}$ in the 0/5 and 0/44 samples respectively to 2.01×10^{-5} and 3.19 $\times$ 10^{-6} (s ppb)$^{-1}$ in the 1/5 and 1/44 samples respectively

Similarly, increasing the thickness of the ZnPC layer reduced the normalized sensitivity of the device as well. For the devices made using 44 nm of reduced GO, the normalized sensitivity fell from 3.07×10^{-6} to 7.57×10^{-7}(s ppb)$^{-1}$ as the thickness of the ZnPC layer was increased from 1 to 60 nm. This clearly indicated that enhancements in sensitivity were due to changes occurring at the surface of the ZnPC/environment interface and not within the sensing layers.

Taken together, it can be deduced that the increase in normalized sensitivity towards NO_2 must have come from the addition of the ZnPC layer.

Table 5.4: Tabulation of the normalized sensitivity values of the different devices towards the presence of NO_2. Norm. Sens. refers to the normalized sensitivity value.

	Sample	**Norm. Sens.**		**Sample**	**Norm. Sens.**		**Sample**	**Norm. Sens.**
rGO Thickness	1/5	20.1	**ZnPC Thickness**	1/44	3.07	**Reference**	0/5	7.73
	1/11	6.59		10/44	1.33		0/44	1.13
	1/22	6.37		60/44	0.757		60/0	20.3
	1/33	6.00						
	1/44	3.19						
Normalized sensitivity values have the suffix "$\times 10^{-6}$ (s ppb)$^{-1}$"								

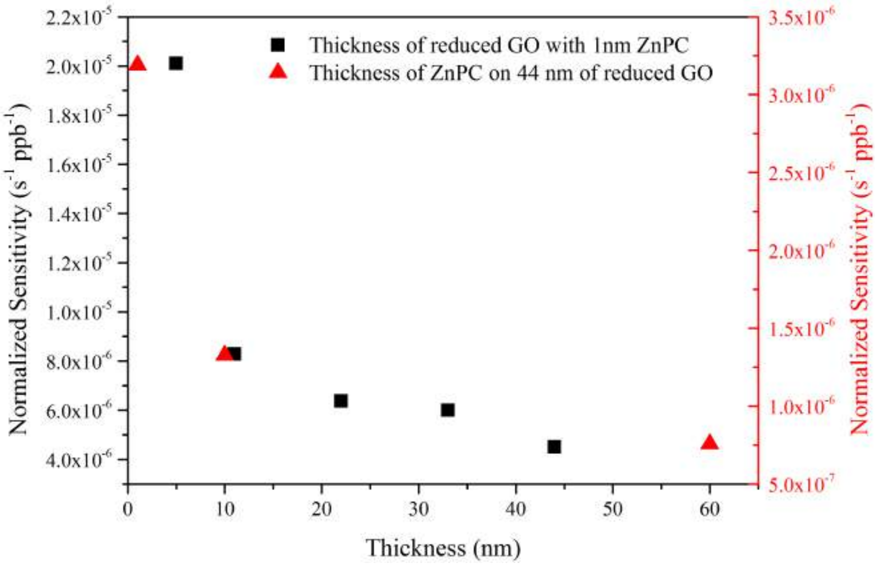

Figure 5.15: Normalized ensitivity of device plot against changes in the thickness of the variable layer. Left axis: Normalized sensitivity of device with 1 nm of ZnPC on a variable thickness of reduced GO (black squares). Right axis: Normalized sensitivity of devices with a variable thickness of ZnPC on a 44 nm thick layer of reduced GO (red triangles).

As mentioned earlier in Section 5.1.1, the sensitivity of reduced GO towards the presence of an analyte is typically enhanced by the direct dispersal of sensing particles onto the reduced GO flakes[1–4]. However, barring effects of analyte diffusion rate through the sensing layer, these devices sensitivities are expected to be independent of thickness and cannot these observations.

Taking the following points into consideration,

1. The same two and half to three fold increase in normalized sensitivity observed in both the 5 and 44 nm thick reduced GO samples, indicates that the effect responsible for the improvements observed in both the samples is independent of thickness within this thickness range.
2. Whether the thickness of reduced GO or ZnPC was change, the same trend of decreasing normalized sensitivity was observed as shown in Fig. 5.15
3. Based on the fabrication method, one can be sure that ZnPC forms a thin layer on top of the conductive reduced GO layer.

The evidence points towards an electric field as the cause of these improvements.

5.4.4 Equal Thicknesses of ZnPC and reduced GO

To further verify these effects, a device with equal thicknesses of ZnPC and GO was fabricated and 5 nm of each material was used to make the layers in this 5/5 device. Based on the results shown in Fig. 5.15, the analyte-ZnPC interaction appeared to occur at the ZnPC/environment interface only and increasing the thickness of ZnPC was expected to reduce the device's normalized sensitivity.

In fact, the sensitivity and normalized sensitivity of this device would be expected to be between that of the 1/5 and 1/11 devices i.e. a sensitivity of between 4 & 211 pA(s ppb)$^{-1}$and a normalized sensitivity of between 6.59×10^{-6} & 2.01×10^{-5} (s ppb)$^{-1}$. The experimental data of this 5/5 bilayer device along with the device sensitivity values are shown in Fig. 5.16 and Table 5.5 respectively.

As predicted, the 5/5 device had sensitivity and normalized sensitivity values closer to the 1/5 device than the 1/11 device, had a device current of about 0.1 mA and the a normalized RGC that changed linearly with respect to NO_2 concentration. With this result, it was confirmed that the electric field from the ZnPC layer had cause the improvements in normalized sensitivities seen here.

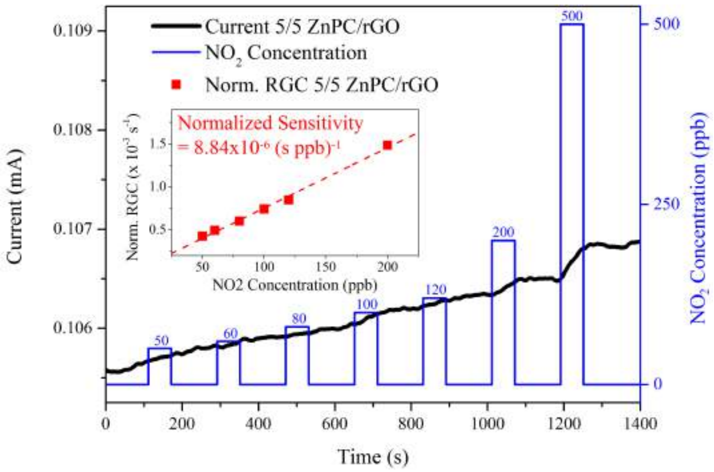

Figure 5.16: Change in the device current over time when the 5/5 device was exposed to NO$_2$. Inset: Normalized RGC at different concentrations of NO$_2$ and the normalized sensitivity of the device.

Table 5.5: RGC and normalized RGC values of the 5/5 device.

NO$_2$ Conc. / ppb	**RGC / nA s^{-1}**	**Norm. RGC / $\times$ 10^{-4} s^{-1}**
50	0.252	4.26
60	0.656	4.92
80	0.535	6.00
100	1.18	7.43
120	1.13	8.45
200	1.98	14.8
500	5.82	43.6
Slope	12.1 pA (s ppb)$^{-1}$	8.84×10^{-6} (s ppb)$^{-1}$

Most significantly, this result confirms the validity of the model developed. The change in the current of the conductive layer depended on the applied voltage from the sensing layer, the diffusion of NO$_2$ through ZnPC was slow, keeping a majority of the physisorbed molecules at the top of the sensing layer and the magnitude of this applied voltage from the sensing layer was modulated by the thickness of the device.

5.5 NiPC(OBu)$_8$ on GO Bilayer Device

5.5.1 Choice of Sensing Layer

Besides predicting the relationship between layer thickness and device sensitivity, the model also predicted that the sensitivity of the device depended on the magnitude of the applied voltage from the sensing layer. The device response and sensitivity were expected to increase if the sensing layer used could generate a larger applied voltage when bound to an analyte molecule. This meant changing the sensing layer to increase the strength of the field from the dipole formed when NO_2 binds with the sensing molecule.

NO_2 is an oxidising gas and by increasing the availability of electrons in the sensing molecule, the net electron transfer for a single sensing event could be higher. In turn, this would increase the strength of the dipole and the electric field into the conductive layer. Chemically, this can be achieved by attaching electron donating groups as side chains to the phthalocyanine material.

Bohrer *et al.* showed that the binding energy between NO_2 and nickel phthalocyanine (NiPC) was greater than the binding energy between ZnPC and NO_2[36]. NiPC could be a good alternative sensing material as the stronger binding between NO_2 and itself could form a dipole with a stronger field.

By attaching 8 side chains consisting of $-OCH_2CH_2CH_2CH_3$ to NiPC as shown in Fig. 5.17, Nickel(II) 1,4,8,11,15,18,22,25-octabutoxy-29H,31H-phthalocyanine (NiPC(OBu)$_8$) is formed. The addition of the side chains around the phthalocyanine would increase the availability of electrons in the NiPC layer.

Due to this effect, the peak absorption wavelength of NiPC(OBu)$_8$ was 740 nm and this was longer than the peak absorption wavelength of 670 nm of NiPC. This meant that the highest occupied molecular orbital (HOMO) was now closer to the lowest unoccupied molecular orbital (LUMO) in the modified material[37].

5.5.2 NiPC and NiPC(OBu)$_8$ Sensors

Before use in bilayer devices, layers of of NiPC and NiPC(OBu)$_8$ were deposited onto interdigitated electrodes and the devices tested for sensitivity to NO_2. Unlike NiPC which was was deposited by PVD, NiPC(OBu)$_8$ was deposited onto the electrodes by spin coating. Layers with a thickness of 60 nm were fabricated

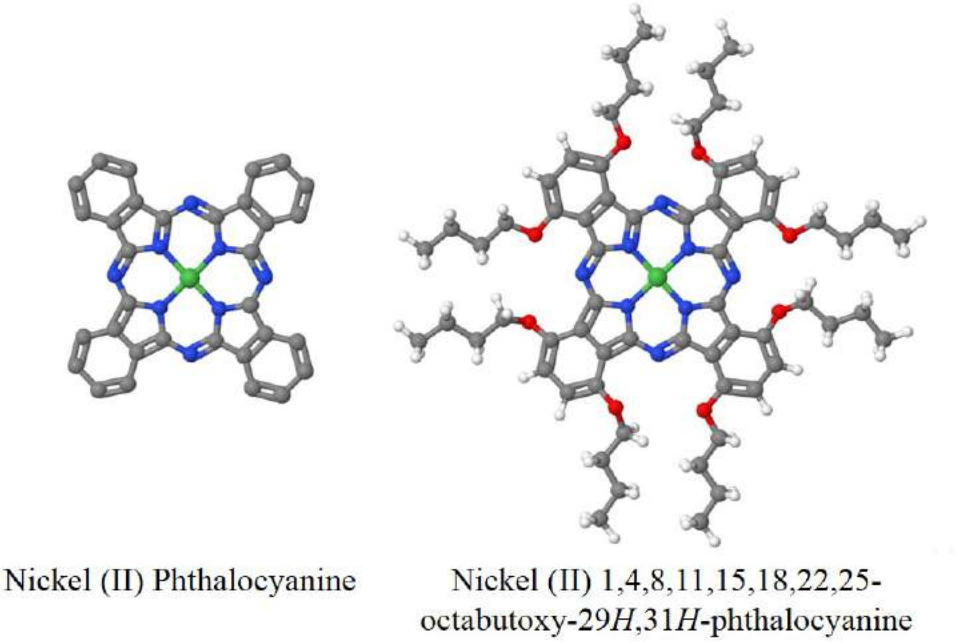

Figure 5.17: Molecular structures of nickel phthalocyanine and Nickel(II) 1,4,8,11,15,18,22,25-octabutoxy-29H,31H-phthalocyanine

using these materials and the completed devices tested for sensitivity towards different concentrations of NO_2; the results of these tests are shown in Fig. 5.18.

The device currents were found to be on the order of nanoamps and this was close to the device current of the ZnPC device (Fig. 5.7). However, the addition of the alkyl side chains to the phthalocyanine molecule reduced the device current by two orders of magnitude from 47 nA in NiPC to 0.7 nA in NiPC(OBu)$_8$.

The key performance indicators of the three phthalocyanine only devices in this chapter are collated in Table 5.6. Comparing the NiPC and NiPC-OR layers against the ZnPC layer, the former layers gave higher device currents but surprisingly had lower normalized sensitivities. This was surprising as the stronger binding between the analyte and sensing molecule did not result in greater monolayer sensitivities[36]. However, these results also showed that the NiPC(OBu)$_8$ layer was the more suitable substitute to ZnPC for the reasons that follow.

Firstly, the normalized sensitivity of the NiPC(OBu)$_8$ layer was closer to that of the ZnPC layer. This reduced the likelihood of sensitivity induced differences that would have to be considered if NiPC were used as the substitute.

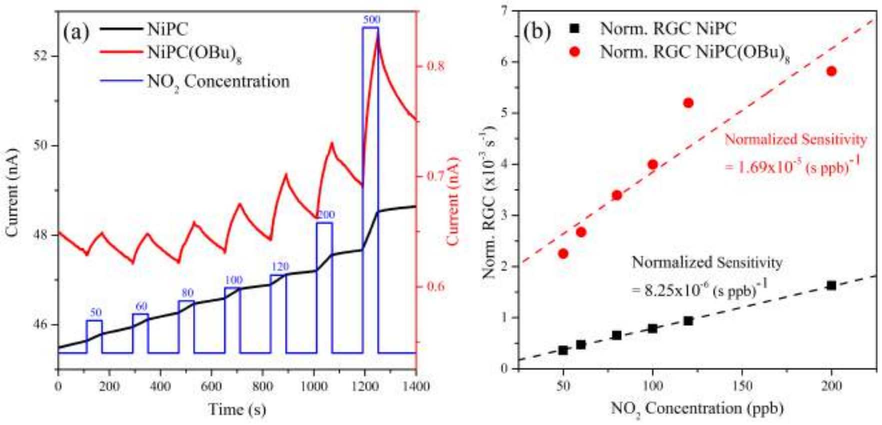

Figure 5.18: (a) Characterization results of NiPC and NiPC(OBu)$_8$ gas sensing devices. (b) Normalized RGC and normalized sensitivity values of the devices at different concentrations of NO$_2$.

Table 5.6: Key performance indicators of the phthalocyanine layers in NO$_2$ gas sensing devices.

Material	**Normalized Sensitivity / (s ppb)$^{-1}$**	**Operating Current / nA**
NiPC	8.25×10^{-6}	47
NiPC(OBu)$_8$	5.63×10^{-6}	0.7
ZnPC	2.60×10^{-5}	0.2

Secondly, the absorption peak of NiPC(OBu)$_8$ occurred at 740 nm and this was lower in energy than the 688 nm absorption peak of ZnPC and 630 nm absorption peak of NiPC, suggesting that the HOMO-LUMO separation was smaller in NiPC(OBu)$_8$[38,39]. This also meant that the likelihood of electron donation from the material to an oxidizing analyte was greater in NiPC(OBu)$_8$.

Finally, the device currents were more similar and this would avoid any unwanted effects on the normalized sensitivity of the device due to the different current levels in the new sensing layer.

For these reasons, NiPC(OBu)$_8$ was the more appropriate material to use to test the hypothesis described in Section 5.5.1. Any differences in the performance of the bilayer device to a comparable ZnPC/rGO device could be attributed immediately to changes in the strength of the field from the dipole formed between the analyte and sensing layer.

5.5.3 NiPC(OBu)$_8$ on reduced GO Sensor

While NiPC(OBu)$_8$ films with thicknesses of 60 nm could be fabricated consistently, the minimum thickness that could be reliably fabricated was 30 nm. Although this was thicker than desired, a reliably consistent process was more important as it would not be possible to determine the thickness of NiPC(OBu)$_8$ in a non-destructive manner in the finished device.

The characterization results of the finished device are shown in Fig. 5.19; as before, the inclusion of 5 nm of reduced increased the conductivity of the device significantly. The device currents was ~0.38 mA and this value was lower than the 0.89 mA of the 0/5 device, but higher than the 0.015 mA of the 1/5 device. As was discussed earlier in Section 5.4.4, the sensitivity of a given bilayer device increased with higher operating currents. Unsurprisingly, the higher device current in NiPC(OBu)$_8$/rGO gave a device with a higher sensitivity of 82.4 pA(s ppb)$^{-1}$ than the 1/5 device. However, the thickness of the NiPC(OBu)$_8$ layer in this device meant that the normalized sensitivity of the device had to be compared against that of the 1/33 device.

The normalized sensitivity of the NiPC(OBu)$_8$/rGO device was more than one and a half times greater than that of the 1/33 device and this can be attributed to the presence of a stronger field from the sensing layer. As shown in Fig. 5.15 and by the example of the 5/5 device, the normalized sensitivity depends on the total thickness of the layers in the device. These values are shown in Table 5.7.

According to the model, improvements in the normalized sensitivity of devices of similar thicknesses had to come from an increase in the magnitude of V_0, the applied voltage from the sensing layer. Corroborating evidence from other fundamental studies point towards NO_2 forming stronger dipoles with NiPC(OBu)$_8$ than ZnPC and the facts converge to the conclusion that the improved normalized sensitivity observed in the NiPC(OBu)$_8$/rGO device was due to a stronger electric field from the sensing layer[36] .

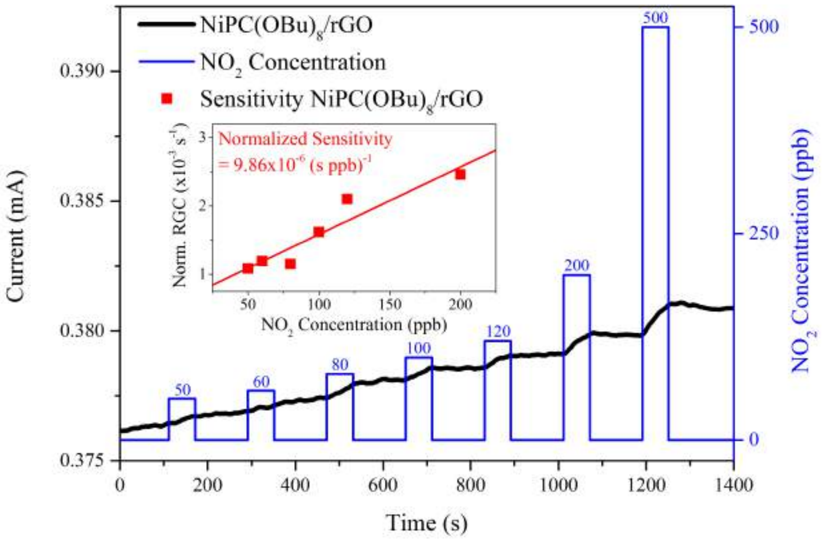

Figure 5.19: Characterization data of the device made from 30 nm of NiPC(OBu)$_8$ on 5 nm of reduced GO.

Table 5.7: Sensitivity and normalized sensitivity values of the NiPC(OBu)$_8$/rGO device compared against the 1/5 and 1/33 ZnPC on reduced GO devices respectively.

Sample	NiPC(OBu)$_8$/rGO	ZnPC/rGO
Thickness (nm)	30 / 5	1/5
Sensitivity (pA s^{-1} ppb^{-1})	82.4	4.0
Thickness (nm)	30 / 5	1/33
Normalized Sensitivity ($\times10^{-6}$ s^{-1} ppb^{-1})	9.86	6.00

5.6 Concluding Gas Sensor Device

In summary, the work shown in this chapter covers the following points:

(i) Testing of a bilayer device to improve current levels in phthalocyanine based gas sensor devices
(ii) Proof that a bilayer device could be made with higher device currents while maintaining little to no loss in normalized device sensitivity
(iii) Development of a theoretical model to describe the bilayer device
(iv) Proof of the theoretical model by testing prediction from the model against experimental results

A summary of the sensitivity values of all the devices discussed in this chapter is shown in Fig. 5.20. Fig. 5.20(a) shows that there is a relationship between the normalized sensitivity value and the total thickness of the bilayer device while Fig. 5.20(b) shows that devices with higher operating currents generally have higher sensitivities.

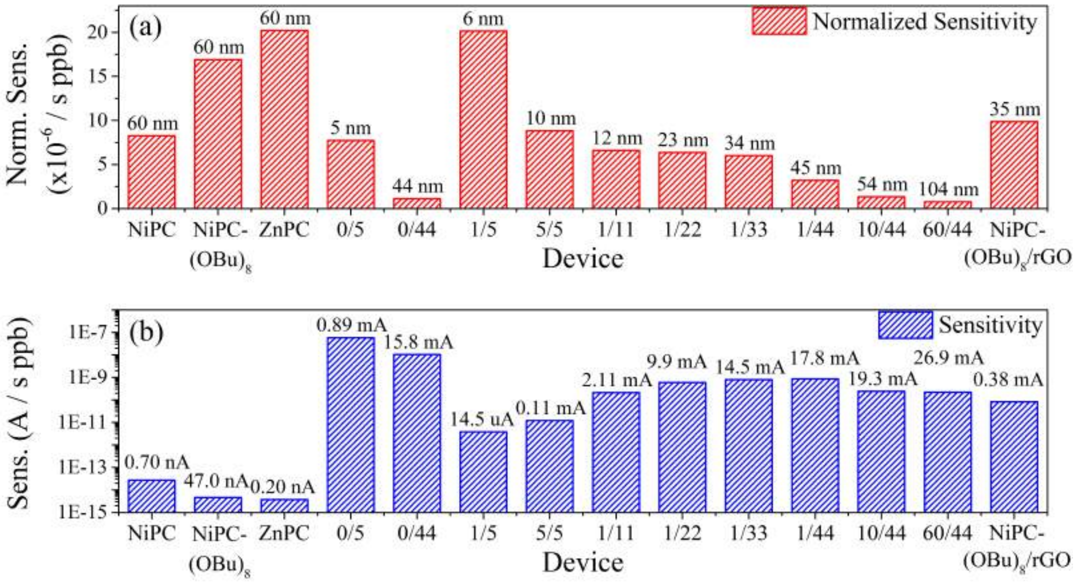

Figure 5.20: Summary of (a) normalized sensitivity and device thickness and (b) sensitivity values and device currents of the monolayer and bilayer gas sensing devices. The data shows that the normalized sensitivity and sensitivity values in the bilayer devices are respectively dependent on the total thickness of the device and the thickness of the conductive layer.

Comparing the ZnPC device against the 1/5 device shows that good control over the thicknesses of the sensing and conducting layer allows the normalized sensitivity of the device to be maintained while the sensitivity and device currents are improved dramatically. Additionally, increasing the thickness of either the conducting or sensing layer typically resulted in improved device currents and sensitivities, but had the side effect of reducing the associated normalized sensitivity of the device.

The theoretical model developed treated an analyte bound to a sensing molecule as a dipole which would emit an electric field. The field from the dipole would interact with the conductive layer by changing the conductive layer's carrier concentration, thereby modulating the device current and producing a measurable response. Consequently, the thickness of the conducting layer was also expected to affect the sensitivity of the device and the model was validated by the experimental results summarized in Fig. 5.20(b).

This model also predicted that the strength of the signal could be increased by increasing the strength of the field from the dipole. This was tested by using NiPC(OBu)$_8$ to replace ZnPC in the sensing layer as it was expected to form a stronger bond with NO_2 than with ZnPC. Due to limitations in the fabrication phase, the resulting NiPC(OBu)$_8$ on reduced GO device had layer thicknesses of 30 and 5 nm respectively and could not be directly compared against any device fabricated earlier.

However with the device characterization results, a firm confirmation could be made regarding the effect of the dipole field on the bilayer gas sensing device. The bilayer samples in Fig. 5.20(a) shows that the normalized sensitivity of a bilayer device falls with increasing device thickness. The NiPC(OBu)$_8$/rGO device bucked the trend and had a normalized sensitivity greater than that of the 1/33 device while having sensitivity values similar to that of bilayer device with 5 nm of reduced GO.

According to the theoretical model, this meant that the dipole formed between NO_2 and NiPC(OBu)$_8$ gave a stronger electric field than the dipole formed between NO_2 and ZnPC.

The result shows that the reduced GO conducting layer can be used as a platform for a multitude of sensing materials which form strong dipoles when bound to an analyte molecule. While the sensitivity of the bilayer device is controlled by the thickness of the conducting layer and thicker conducting layers are more sensitive than thinner ones, the normalized sensitivity depends strength of this dipole and the total thickness of the bilayer device.

As shown, the bilayer gas sensor device improves device operating currents and sensitivity towards analyte gases. With good control on layer thicknesses, these improvements can be made with little to no change in the normalized sensitivity values and the platform also allows new tunable dimensions in the device so that a device with the exact attributes desired can be fabricated .

References

[1] Sen Liu, Bo Yu, Hao Zhang, Teng Fei, and Tong Zhang. **Enhancing NO2 gas sensing performances at room temperature based on reduced graphene oxide-ZnO nanoparticles hybrids**. *Sens. Actuators B: Chem.*, **202**:272–278, 2014, DOI:10.1016/j.snb.2014.05.086. 195, 224

[2] Giovanni Neri, Salvatore Gianluca Leonardi, Mariangela Latino, Nicola Donato, Seunghwan Baek, Donato E. Conte, Patrcia A. Russo, and Nicola Pinna. **Sensing behavior of SnO2/reduced graphene oxide nanocomposites toward NO2**. *Sens. Actuators B: Chem.*, **179**:61–68, 2013, DOI:10.1016/j.snb.2012.10.031.

[3] Xiaoqing Zhou, Xiaolin Wang, Bin Wang, Zhimin Chen, Chunying He, and Yiqun Wu. **Preparation, characterization and NH3-sensing properties of reduced graphene oxide/copper phthalocyanine hybrid material**. *Sens. Actuators B: Chem.*, **193**:340–348, 2014, DOI:10.1016/j.snb.2013.11.090. 197

[4] Z. Tehrani, G. Burwell, M. A. Mohd Azmi, A. Castaing, R. Rickman, J. Almarashi, P. Dunstan, A. Miran Beigi, S. H. Doak, and O. J. Guy. **Generic epitaxial graphene biosensors for ultrasensitive detection of cancer risk biomarker**. *2D Mater.*, **1**:025004, 2014, DOI:10.1088/2053-1583/1/2/025004. 197, 224

[5] Zuquan Wu, Xiangdong Chen, Shibu Zhu, Zuowan Zhou, Yao Yao, Wei Quan, and Bin Liu. **Enhanced sensitivity of ammonia sensor using graphene/polyaniline nanocomposite**. *Sens. Actuators B: Chem.*, **178**:485–493, 2013, DOI:10.1016/j.snb.2013.01.014. 195

[6] J. P. Germain, A. Pauly, C. Maleysson, J. P. Blanc, and B. Schllhorn. **Influence of peripheral electron-withdrawing substituents on the conductivity of zinc phthalocyanine in the presence of gases. Part 2: oxidizing gases**. *Thin Solid Films*, **333**:235–239, 1998, DOI:10.1016/S0040-6090(98)00830-X. 195, 199

[7] Jiawei Shi, Liqiang Luan, Wenjuan Fang, Tianyu Zhao, Wei Liu, and Deliang Cui. **High-sensitive low-temperature NO2 sensor based on Zn (II) phthalocyanine with liquid crystalline properties**. *Sens. Actuators B: Chem.*, **204**:218–223, 2014, DOI:10.1016/j.snb.2014.07.070. 199

[8] Harald R. Kerp and E. E. van Faassen. **Oxygen doping in zinc phthalocyanine layers for photovoltaic applications**. *Proc. SPIE, Org. Photovolt.*, **4108**:62–75, 2001, DOI:10.1117/12.416933. 199

[9] B. Bott and T. A. Jones. **A highly sensitive NO2 sensor based on electrical conductivity changes in phthalocyanine films**. *Sens. Actuators*, **5**:43–53, 1984, DOI:10.1016/0250-6874(84)87005-5. 196, 199

[10] Forest I. Bohrer, Corneliu N. Colesniuc, Jeongwon Park, Manuel E. Ruidiaz, Ivan K. Schuller, Andrew C. Kummel, and William C. Trogler. **Comparative Gas Sensing in Cobalt, Nickel, Copper, Zinc, and Metal-Free Phthalocyanine Chemiresistors**. *J. Am. Chem. Soc.*, **131**:478–485, 2009, DOI:10.1021/ja803531r. 199

[11] Marcel Bouvet. **Phthalocyanine-based field-effect transistors as gas sensors**. *Anal. Bioanal. Chem.*, **384**:366–373, 2006, DOI:10.1007/s00216-005-3257-6. 196

[12] Mohammad Javad Jafari, Mohammad Esmaeil Azim-Araghi, Samira Barhemat, and Sobhenaz Riyazi. **Effect of post-deposition annealing on surface morphology and gas sensing properties of palladium phthalocyanine thin films**. *Surf. Interface Anal.*, **44**:601–608, 2012, DOI:10.1002/sia.4831. 195, 196, 199

[13] T. A. Jones and B. Bott. **Gas-induced electrical conductivity changes in metal phthalocyanines**. *Sens. Actuators*, **9**:27–37, 1986, DOI:10.1016/0250-6874(86)80004-X. 196

[14] Debbie J. Jarvis, Gary Adamkiewicz, Marie-Eve Heroux, Regula Rapp, and Frank J.

Kelly. **Nitrogen dioxide**. WHO Guidelines for Indoor Air Quality: Selected Pollutants. World Health Organization, Geneva, 2010. 196

[15] Jiri Janata and Mira Josowicz. **Organic semiconductors in potentiometric gas sensors**. *J. Solid State Electrochem.*, **13**:41–49, 2008, `DOI:10.1007/s10008-008-0597-0`. 196

[16] J. Brunet, A. Pauly, L. Mazet, J. P. Germain, M. Bouvet, and B. Malezieux. **Improvement in real time detection and selectivity of phthalocyanine gas sensors dedicated to oxidizing pollutants evaluation**. *Thin Solid Films*, **490**:28–35, 2005, `DOI:10.1016/j.tsf.2005.04.015`.

[17] N. Padma, Aditee Joshi, Ajay Singh, S. K. Deshpande, D. K. Aswal, S. K. Gupta, and J. V. Yakhmi. **NO2 sensors with room temperature operation and long term stability using copper phthalocyanine thin films**. *Sens. Actuators B: Chem.*, **143**:246–252, 2009, `DOI:10.1016/j.snb.2009.07.044`. 196

[18] Josef Náhlík, Irena Kašpárková, and Přemysl Fitl. **Methodology of evaluating the influence of the resistance of contact regions in the measurements of sheet resistance on stripes of ultrathin high-resistance materials**. *Rev. Sci. Instrum.*, **83**:074701, 2012, `DOI:10.1063/1.4731654`. 196

[19] Darya M. Sedlovets, Maksim V. Shuvalov, Yury V. Vishnevskiy, Vladimir T. Volkov, Igor I. Khodos, Oleg V. Trofimov, and Vitaly I. Korepanov. **Synthesis and structure of high-quality films of copper polyphthalocyanine 2D conductive polymer**. *Mater. Res. Bull.*, **48**:3955–3960, 2013, `DOI:10.1016/j.materresbull.2013.06.015`. 196

[20] J. T. Robinson, F. K. Perkins, E. S. Snow, Z. Wei, and P. E. Sheehan. **Reduced graphene oxide molecular sensors**. *Nano Lett.*, **8**:3137–40, 2008, `DOI:10.1021/nl8013007`. 197

[21] Yong Jung Kwon, Hong Yeon Cho, Han Gil Na, Byung Cheol Lee, Sang Sub Kim, and Hyoun Woo Kim. **Improvement of gas sensing behavior in reduced graphene oxides by electron-beam irradiation**. *Sens. Actuators B: Chem.*, **203**:143–149, 2014, `DOI:10.1016/j.snb.2014.06.025`.

[22] Pi-Guey Su and Hung-Chiang Shieh. **Flexible NO2 sensors fabricated by layer-by-layer covalent anchoring and in situ reduction of graphene oxide**. *Sens. Actuators B: Chem.*, **190**:865–872, 2014, `DOI:10.1016/j.snb.2013.09.078`.

[23] Yong Zhou, Yadong Jiang, Tao Xie, Huiling Tai, and Guangzhong Xie. **A novel sensing mechanism for resistive gas sensors based on layered reduced graphene oxide thin films at room temperature**. *Sens. Actuators B: Chem.*, **203**:135–142, 2014, `DOI:10.1016/j.snb.2014.06.105`. 197

[24] Jinhui Zhu, Yongxi Li, Yu Chen, Jun Wang, Bin Zhang, Jinjuan Zhang, and Werner J. Blau. **Graphene oxide covalently functionalized with zinc phthalocyanine for broadband optical limiting**. *Carbon*, **49**:1900–1905, 2011, `DOI:10.1016/j.carbon.2011.01.014`. 198

[25] Fei Liu, Yo Han Kim, Doo Sung Cheon, and Tae Seok Seo. **Micropatterned reduced graphene oxide based field-effect transistor for real-time virus detection**. *Sens. Actuators B: Chem.*, **186**:252–257, 2013, `DOI:10.1016/j.snb.2013.05.097`. 199

[26] K. S. Vasu, Biswanath Chakraborty, S. Sampath, and A. K. Sood. **Probing top-gated field effect transistor of reduced graphene oxide monolayer made by dielectrophoresis**. *Solid State Commun.*, **150**:1295–1298, 2010, `DOI:10.1016/j.ssc.2010.05.018`.

[27] Eduardo V. Castro, K. S. Novoselov, S. V. Morozov, N. M. R. Peres, J. M. B. Lopes dos Santos, Johan Nilsson, F. Guinea, A. K. Geim, and A. H. Castro Neto. **Biased Bilayer Graphene: Semiconductor with a Gap Tunable by the Electric Field Effect**. *Phys. Rev. Lett.*, **99**:216802, 2007, `DOI:10.1103/PhysRevLett.99.216802`.

[28] Jeroen B. Oostinga, Hubert B. Heersche, Xinglan Liu, Alberto F. Morpurgo, and Lieven M. K. Vandersypen. **Gate-induced**

insulating state in bilayer graphene devices. *Nat. Mater.*, **7**:151–157, 2008, `DOI:10.1038/nmat2082`. 199

[29] Jukka Hassinen, Jussi Kauppila, Jarkko Leiro, Anni M´a´att´anen, Petri Ihalainen, Jouko Peltonen, and Jukka Lukkari. **Low-cost reduced graphene oxide-based conductometric nitrogen dioxide-sensitive sensor on paper**. *Anal. Bioanal. Chem.*, **405**:3611–3617, 2013, `DOI:10.1007/s00216-013-6805-5`. 207

[30] Wenjing Yuan, Liang Huang, Qinqin Zhou, and Gaoquan Shi. **Ultrasensitive and Selective Nitrogen Dioxide Sensor Based on Self-Assembled Graphene/Polymer Composite Nanofibers**. *ACS Appl. Mater. Interfaces*, **16**:17003–17008, 2014, `DOI:10.1021/am504616c`. 207

[31] Christian Punckt, Franziska Muckel, Svenja Wolff, Ilhan A. Aksay, Carlos A. Chavarin, Gerd Bacher, and Wolfgang Mertin. **The effect of degree of reduction on the electrical properties of functionalized graphene sheets**. *Appl. Phys. Lett.*, **102**:023114, 2013, `DOI:10.1063/1.4775582`. 207

[32] Based on work already conducted at Corporate Research, Robert Bosch (SEA) Pte Ltd. 209

[33] K. S. Novosolev, A. K. Geim, S. V. Morozov, D. Jiang, Y. Zhang, S. V. Dubonos, I. V. Grigorieva, and A. A. Firsov. **Electric Field Effect in Atomically Thin Carbon Films**. *Science*, **306**:666–669, 2004, `DOI:10.1126/science.1102896`. 221

[34] R. Martel, V. Derycke, C. Lavoie, J. Appenzeller, K.K. Chan, J. Tersoff, and Ph. Avouris. **Ambipolar Electrical Transport in Semiconducting Single-Wall Carbon Nanotubes**. *Phys. Rev. Lett.*, **87**:256805, 2001, `DOI:10.1103/PhysRevLett.87.256805`.

[35] Cristina Gómez-Navarro, R. Thomas Weitz, Alexander M. Bittner, Matteo Scolari, Alf Mews, Marko Burghard, and Klaus Kern. **Electronic Transport Properties of Individual Chemically Reduced Graphene Oxide Sheets**. *Nano Lett.*, **7**:3499–3503, 2007, `DOI:10.1021/nl072090c`. 221

[36] Forest I. Bohrer, Corneliu N. Colesniuc, Jeongwon Park, Manuel E. Ruidiaz, Ivan K. Schuller, Andrew C. Kummel, and William C. Trogler. **Comparative Gas Sensing in Cobalt, Nickel, Copper, Zinc, and Metal-Free Phthalocyanine Chemiresistors**. *J. Am. Chem. Soc.*, **131**:478–485, 2009, `DOI:10.1021/ja803531r`. 226, 227, 229

[37] Alexandra V. Soldatova, Junhwan Kim, Xinzhang Peng, Angela Rosa, Giampaolo Ricciardi, Malcolm E. Kenney, and Michael A. J. Rodgers. **Effects of Benzoannulation and -Octabutoxy Substitution on the Photophysical Behavior of Nickel Phthalocyanines: A Combined Experimental and DFT/TDDFT Study**. *Inorg. Chem.*, **46**:2080–2093, 2007, `DOI:10.1021/ic061524o`. 226

[38] Dhrubojyoti Roy, Nayan Mani Das, Nanda Shakti, and P.S. Gupta. **Comparative study of optical, structural and electrical properties of inc phthalocyanine Langmuir-Blodgett thin film on annealing**. *RSC Adv.*, **4**:42514, 2014, `DOI:10.1039/c4ra05417b`. 228

[39] K.N. Narayanan Unni and C.S. Menon. **Electrical, optical and structural studies on nickel phthalocyanine thin films**. *Mater. Lett.*, **45**:326–330, 2000, `DOI:10.1016/S0167-577X(00)00127-0`. 228

6

Conclusions & Future Work

6.1 X-ray Photoelectron Spectroscopy of GO

Summary

The oxygen functional groups on GO were identified by means of the O $1s_{1/2}$ electron binding and four distinct peaks were identified. For the first time, the binding energy of these electrons in the carbonyl (530.9 eV), carboxyl (532.3 eV), hydroxyl (533.1 eV) and the epoxy (534.4 eV) functional groups on GO are identified and these peaks verified by means of chemical and mathematical analysis. The identification and assignment of these peaks will aid in overcoming future challenges when using GO with high C/O ratios.

O $1s_{1/2}$ electrons in oxygen atoms that were singly bound to the graphene basal plane were easily distinguished from electrons that were doubly bound to carbon atoms, the peaks were identified pair wise. The analysis was done such that carbonyls and carboxyls were identified in one set of experiments (Chapters 3.1.3.1 & 3.1.3.2) while hydroxyls and epoxies were identified in a different set of experiments (Chapters 3.1.3.1 & 3.1.3.3).

To do so, irregularities introduced to the data by the presence of OD and the effects of vacancies on the binding energies of hydroxyls and epoxies in GO were studied and accounted for in the experiment setup and during analysis. During characterization, OD was removed from the material and by accounting for the effect of vacancies on O $1s_{1/2}$ electron binding energies, the findings harmonized conflicting accounts in literature.

As it turned out, GO with vacancies caused a separation in the peaks of the hydroxyl and epoxy groups and was historically interpreted as a shift in the position of the peak due to the changing chemical environment on GO during reduction. However, computational results showed that while electrons from the O $1s_{1/2}$ orbital in the epoxy and hydroxyl functional groups on GO had the same binding energy, the presence of a neighbouring carbon vacancy separated these peaks. By taking into account the C/O ratio in GO, the expected concentration of carbonyl groups present, it was concluded that a large number of vacancies existed in GO and confirmed the computation findings.

By identifying these functional groups on GO, it was observed that carboxylation occurred at a thermal reduction temperature of about 543 K. It was therefore recommended that techniques of GO reduction employing thermal reduction not exceed this critical temperature and that alternative chemical means be employed to suppress the temperatures required.

With these findings, metastability in aqueous GO was also studied and found to be a rearrangement of the oxygen functional groups on GO (Chapter 3.2). This rearrangement resulted in the formation of domains of high oxygen concentration on GO and is verified by spectroscopic techniques. Computational results also showed that this configuration was preferred as the configuration minimized the energy of the GO flake. However, this had implications on the thermal reduction process of GO and the formation of domains in aged-GO meant that the material would form carboxyls more readily.

The identification of these O $1s_{1/2}$ peaks meant also meant that the chemical composition of edge functionalized graphene oxide could be characterized (Chapter 3.3). The high C/O ratio in the material meant that the proportion of the C $1s_{1/2}$ spectra taken up by oxygen bound carbon atoms was so small that the peaks had to be combined so as to give a meaningful interpretation of the spectrum. By using the O $1s_{1/2}$ spectrum, the individual functional groups could be identified and the relative proportions of the groups were found. In the second case,

The spectroscopic work was then extended to analyse a mixture of thermally reduced $FeCl_3$and GO. From the O $1s_{1/2}$ spectra, the presence of metal bound oxygen was observed and its identity found by analysis of the Fe $2p_{3/2}$ spectra. While $FeCl_3$ worked as a good chemical reagent to remove oxygen functional groups from GO, it resulted in the formation of difficult to remove FeO.

Future Work

Having identified that oxygen functional groups were readily removed in a thermally reduced mixture of $FeCl_3$ and GO, much effort was spent in identifying a suitable method of removing the FeO by product. Despite reducing the sheet resistance of the fabricated film significantly, the by product left behind reduced the optical transmission of the film substantially and this affected the performance of the film as a TCE. While some effort was initially spent in trying to remove this by product, no further progress was made on this front. As it turned out, FeO was a persistent material that would resist effort spent in removing in. It would be interesting to develop a method where the by product is easily washed away by a solvent and if so, the effort may lend itself to an industrial application.

On top of this, the oxygen functional groups were identified for O $1s_{1/2}$ peaks from GO produced by the Hummer's technique and these assignments are expected to be robust for GO produced by the other methods as well. Successful characterization of GO produced by the Staudenmaier and Brodie methods would further verify the validity of the O $1s_{1/2}$ assignments described here and further development of the canonical GO model mooted for in this thesis.

6.2 GO in Transparent Conducting Electrodes

Summary

Films of GO were fabricated by depositing GO onto heated glass panels by the method of ultrasonic spray coating. By changing deposition parameters such as nozzle move rate and suspension infuse volume, the thickness of the film could be varied and the method was reliable in producing films of the desired thickness. After deposition, these films were thermally reduced at 573 K in a nitrogen environment to form TCEs. By optimising the deposition process, TCEs with an average sheet resistance of 106 k$\Omega/\Box$ and transmittance of 72.9 % at 550 nm were produced and these TCEs had an average FOM of 10.4×10^{-3}.

The next step involved improving the reduction of GO at the low thermal reduction temperatures. This was achieved by the optimal use of AA in a dual spray process. The dual spray process involved spraying GO through one nozzle and AA through a second nozzle during the ultrasonic spray coating step. After deposition, vapour annealing was performed at 353 K to allow the chemical reaction between AA and GO to occur before the samples were thermally reduced at 573 K. This method gave optimized TCEs with an average sheet resistance of 2.55 k$\Omega/\Box$, transmittance of 58.3 % at 550 nm and a FOM value of 0.239.

Further improvements to the GO based TCE required the sheet resistance to be reduced further while increasing the transmittance of the film. This was done by adding a second material with high conductivity to a thinner GO film. The second material would reduce the sheet resistance while the thinner GO film would improve the transmittance of the film. By using a bilayer consisting of AgNWs in one and AA reduced GO in another, TCEs with an average sheet resistance of 5.1 $\Omega/\Box$ and transmittance of 65.7 % at 550 nm were fabricated. The average FOM of these samples was 160 and the best sample produced by this method had an FOM of 189.9 with sheet resistance and transmittance values of 4.7 $\Omega/\Box$& 68.1 respectively.

It was also found that the GO over layer protected the AgNWs from degradation due to capillary instability by limiting the amount of oxygen present near the nanowires and damping surface waves on the nanowires. Excluding oxygen decreases the rate of surface diffusion of silver atoms on the cylindrical surface of the AgNWs, while damping the surface waves slows the mechanical motion of the nanowire surface and these effects increase the time taken for spheroidization significantly. The time taken for spheroidization was calculated using equations developed by Nichols and Muller and the experimental and theoretical times were found to be agree to within an order of magnitude.

Future Work

While silver nanowires were used in this work, the methods are potentially can be extended for use with other nanowires and this would improve the device in several ways:

(i) Although AgNWs are highly conductive, the material cost is of silver is high and can be reduced cheaper metals were used to fabricate the nanowire. The spray deposition process could be kept unchanged while metals such as copper or even aluminium could be considered as substitutes for silver to bring down material costs.

(ii) Different metals have different coefficient and activations energies of surface diffusion and this has implications on the time take for spheroidization to occur in these nanowires. In this way, new material may increase the lifetime of the conductive nanowire network.

(iii) Understanding on the damping effect of substrates and over layers on the time taken for spheroidization in nanowires is new and more effort can be spent towards improving understanding in this area so that the model of Nichols & Mullins can be improved further.

By working on these points, understanding of the spheroidization process in nanowires can be increased and the model will be useful for predicting the lifetime of nanowires under different conditions. The effect of water vapour and should be included in this model and with this understanding, new methods of passivating the effect of spheroidization can be developed so that the nanowires can be kept stable for the desired lifetime.

6.3 GO in Gas Sensing Devices

Summary

Some issues faced in the use of phthalocyanine or GO only sensing layers for chemiresistive gas sensors were shown and the relative merits and flaws of these monolayer devices were demonstrated and discussed. While more sensitive and selective towards a particular analyte gas, phthalocyanine sensing layers have the problem of high device resistivities. This resulted in devices which have extremely small currents when operated at low voltages and proved to be a barrier towards ASIC integration.

GO films on the other had were significantly more conductive and device currents were typically three to six orders of magnitude higher in these devices. Compared to devices built with phthalocyanine sensing layers, devices built with a reduced GO layer recorded a large change in device current when the NO_2 analyte was introduced, but the reduced GO layer lacked analyte selectivity, making it a poor gas sensing layer.

A design for a bilayer device was proposed and the method of fabrication proposed and tested in this chapter. By adding a thin layer of phthalocyanine onto a thin layer of reduced GO, the electric field emanating from the dipole that forms when an analyte pairs with a sensing molecule in the phthalocyanine layer was expected to modulate the carrier concentration in the GO device, thereby modulating the device currents. This bilayer device was tested by varying the thicknesses of ZnPC and reduced GO used and confirmed by replacing the ZnPC sensing layer with a $NiPC(OBu)_8$ layer.

A theoretical model to describe the sample was shown and the calculations and predictions of the model shown. Following that, the results from the experiments were compared against the theoretical model and the two were found to be in good agreement. The bilayer model was supported by experimental results and the stronger electric field from the reaction of NO_2 with $NiPC(OBu)_8$ resulted in a larger change in a larger device normalized sensitivity.

Most importantly, a bilayer device would increase the device currents by at least five orders of magnitude with no change in the normalized sensitivity of the device. This improvement removed the challenge of low device currents that was typically faced when integrating phthalocyanine devices into ASICs.

Future Work

It was noted in the discussion that the bilayer model was did not take into account the effect of sensing layer current in the calculation of device current. While this does not seem to have affected the results, the model would benefit from a development in this aspect. Besides improving confidence in the findings of these experiments, the inclusion of sensing layer currents may also serve to explain the increase in device currents observed when the thickness of the phthalocyanine sensor was increased for a given thickness of reduced GO.

Furthermore, the model also makes a crucial assumption that analyte diffusion through the sensing layer was minimal within the given time period. While this assumption is in line with the method of RGC, it does not paint a complete picture of the sensing mechanism in phthalocyanines and the model can be improved by taking this point into consideration.

A value of 0.096 for $\frac{b}{\rho l}$ was found and this value is understood to depend greatly on the design of the fingers in the electrodes. This value is affected by changing the electrode width, length and separation and larger magnitudes give devices with greater device currents levels. This information can be utilized in the design process and greater understanding will allow electrode design to be optimized for the desired use.

Besides device performance, device cycle durability and sensing material reliability are important aspect of sensor design. On one hand, the impact of the bilayer gas sensor on the cycle durability of the ZnPC layer has not been looked into and it is also not known if any interactions occur between the reduced GO and phthalocyanine layers. On the other hand, some initial work done has indicated the reliability of the ZnPC material and more work is being done to verify this point. These are important steps that will have to be looked into carefully when developing the bilayer gas sensor device.

Appendices

Appendix A

Derivation of Dispersion Relation in Capillary Instability

Perturbation of an infinitely long nanowire

Assuming a AgNW of infinite length, with a radius of R_0, density of ρ and surface tension of σ in free space, the pressure within the nanowire p_0 is:

$$p_0 = \sigma \nabla \cdot \mathbf{n} = \frac{\sigma}{R_0} \tag{A.1}$$

where it is assumed that there is no external pressure.

Applying a perturbation to the surface, the perturbed radius of the nanowire is:

$$\mathbf{R^{(1)}} = R_0 + \varepsilon e^{\omega t + ikz} \tag{A.2}$$

where $\varepsilon \ll R_0$, ω & k and t have their usual meanings and z is the distance along the axis of the nanowire.

Considering the radial, $\mathbf{u_r^{(1)}}$, and axial, $\mathbf{u_z^{(1)}}$, components of the perturbation velocity and using the Navier-Stokes equations to first order approximation gives:

$$\frac{\partial \mathbf{u_r^{(1)}}}{\partial t} = -\frac{1}{\rho}\frac{\partial p^{(1)}}{\partial r} \tag{A.3a}$$

$$\frac{\partial \mathbf{u_z^{(1)}}}{\partial t} = -\frac{1}{\rho}\frac{\partial p^{(1)}}{\partial z} \tag{A.3b}$$

where $p^{(1)}$ is the perturbation pressure.

Applying the Continuity and Navier-Stokes equations

The continuity equation becomes:

$$\begin{aligned} \rho A_1 V_1 = &\quad \rho A_2 V_2 \\ \frac{\partial \mathbf{u_r^{(1)}}}{\partial r} + \frac{\mathbf{u_r^{(1)}}}{r} + \frac{\partial \mathbf{u_z^{(1)}}}{\partial z} = &\quad 0 \end{aligned} \tag{A.4}$$

For simplicity, it is assumed that the perturbations have the same form:

$$\mathbf{u_r^{(1)}} = R(r)e^{\omega t + ikz} \tag{A.5a}$$

$$\mathbf{u_z^{(1)}} = Z(r)e^{\omega t + ikz} \tag{A.5b}$$

$$\mathbf{p_r^{(1)}} = P(r)e^{\omega t + ikz} \tag{A.5c}$$

These perturbation equations are substituted into the Navier-Stokes and continuity equations to give:

Navier-Stokes equations

$$\omega R = -\frac{1}{\rho}\frac{dP}{dr} \tag{A.6a}$$

$$\omega Z = -\frac{ik}{\rho}P \tag{A.6b}$$

Continuity equation

$$\frac{dR}{dr} + \frac{R}{r} + ikZ = 0 \tag{A.7}$$

Combining them yields:

$$r^2\frac{d^2R}{dr^2} + r\frac{dR}{dr} - (1 + (kr)^2)R = 0 \tag{A.8}$$

which is a modified Bessel equation. For the solution to be well behaved, the first kind of these solutions requires that

$$R(r) = CI_1(kr) \tag{A.9}$$

where C is a constant.

Determining pressure and normal force on surface

The pressure on the cylindrical surface, P(r), can then be found by using the Bessel function identity $I_0'(\zeta) = I_1(\zeta)$, the Navier-Stokes equation and the condition for stability in Equation (A.9):

$$P(r) = -\frac{\omega\rho C}{k} I_0(kr) \tag{A.10}$$

To determine the normal force on the surface of the nanowire, the boundary conditions for this nanowire are considered. This is given by:

$$\frac{\partial \mathbf{R^{(1)}}}{\partial t} \approx \mathbf{u_r^{(1)}} \tag{A.11}$$

Substituting this into Equations (A.5a) & (A.9) gives:

$$C = \frac{\varepsilon\omega}{I_1(kR_0)} \tag{A.12}$$

and Equation (A.10) becomes:

$$P(r) = -\frac{\omega^2\rho\varepsilon}{k}\frac{I_0(kr)}{I_1(kR_0)} = -\frac{\omega^2\rho\varepsilon}{k}\frac{I_0(kR_0)}{I_1(kR_0)} \tag{A.13}$$

Here, the Bessel equation identity

$$I_v(\lambda z) = \lambda^v \sum j = 0 \frac{((\lambda^2-1)\frac{z}{2})^j}{j!} I_{v+j}(z) \tag{A.14}$$

was used, where $\lambda = 1 + \varepsilon$ and z = kR_0.

The curvature of the surface is calculated from the principal radii of the surface, R_1 and R_2, and the normal force on the surface of the nanowire is balanced when

$$p_0 + \mathbf{p_r^{(1)}} = \left(\frac{1}{R_1} + \frac{1}{R_2}\right) \tag{A.15}$$

where

$$\frac{1}{R_1} = \frac{1}{R_0} + \varepsilon e^{\omega t + ikz} \approx \frac{1}{R_0} + \frac{\varepsilon}{R_0^2} e^{\omega t + ikz} \tag{A.16a}$$

$$\frac{1}{R_2} = \varepsilon k^2 e^{\omega t + ikz} \tag{A.16b}$$

Using these expressions for R_1 and R_2 in Equation (A.15) gives:

$$p_0 + \mathbf{p_r^{(1)}} = \frac{\sigma}{R_0} - \frac{\varepsilon\sigma}{R_0^2}\left(1 - k^2 R_0^2\right) e^{\omega t + ikz} \tag{A.17}$$

Since it was established in Equation (A.1) that $p_0 = \frac{\sigma}{R_0}$, Equation (A.17) becomes

$$\mathbf{p_r^{(1)}} = -\frac{\varepsilon\sigma}{R_0^2}\left(1 - k^2 R_0^2\right) e^{\omega t + ikz} \tag{A.18}$$

Dispersion Relation

Taking the relationship in Equation (A.5c), the equation for P(r) in Equation (A.13) and making these substitutions into Equation (A.18), the dispersion relation is written as

$$\boxed{\omega^2 = \frac{\sigma}{\rho R_0^2} k \frac{I_1(kR_0)}{I_0(kR_0)}\left(1 - k^2 R_0^2\right)} \tag{A.19}$$

*Calculations based on derivation shown in "**On the instability of jets.**, Proc. London Math. Soc., 10:4-13, 1878." with annotations.*

Appendix B

Rights and Permissions

Chapter 1

- Fig. 1.4 – License Number: 3632941270096
- Fig. 1.9(b) – License Number: 3633391246763
- Fig. 1.10 – License Number: 3633521137014
- Fig. 1.12 – License Number: 3633470204851
- Fig. 1.13 – License Number: 3633470999643

Chapter 2

- Fig. 2.2 – License Number: 3633570689539

Chapter 3

- Fig. 3.25(a) – License Number: 3633560375745
- Fig. 3.25(b) – License Number: 3633560845357

B. RIGHTS AND PERMISSIONS

Rightslink Printable License https://s100.copyright.com/App/PrintableLicenseFrame.jsp?publisher...

American Physical Society
License Details

May 20, 2015

This is an Agreement between Yue Chau Kwan ("You") and American Physical Society ("Publisher"). It consists of your order details, the terms and conditions provided by American Physical Society, and the payment instructions.

License Number	3632941270096
License date	May 20, 2015
Licensed content publisher	American Physical Society
Licensed content publication	Physical Review Letters
Licensed content title	Raman Spectrum of Graphene and Graphene Layers
Licensed copyright line	Copyright © 2006, American Physical Society
Licensed content author	A. C. Ferrari et al.
Licensed content date	Oct 30, 2006
Volume number	97
Type of Use	Thesis/Dissertation
Requestor type	Student
Format	Print, Electronic
Portion	image/photo
Number of images/photos requested	1
Portion description	Figure 2
Rights for	Main product
Duration of use	Life of current edition
Creation of copies for the disabled	no
With minor editing privileges	no
For distribution to	U.K. and Commonwealth (excluding Canada)
In the following language(s)	Original language of publication
With incidental promotional use	no
The lifetime unit quantity of new product	0 to 499
The requesting person/organization is:	Kwan Yue Chau
Order reference number	None
Title of your thesis / dissertation	Graphene, Nanotube and Organic Materials Composites for Transparent Conductor and Electrical Device Applications
Expected completion date	Dec 2015
Expected size (number of pages)	300
Total	0.00 USD

Terms and Conditions

1 of 3 20/05/2015 15:50

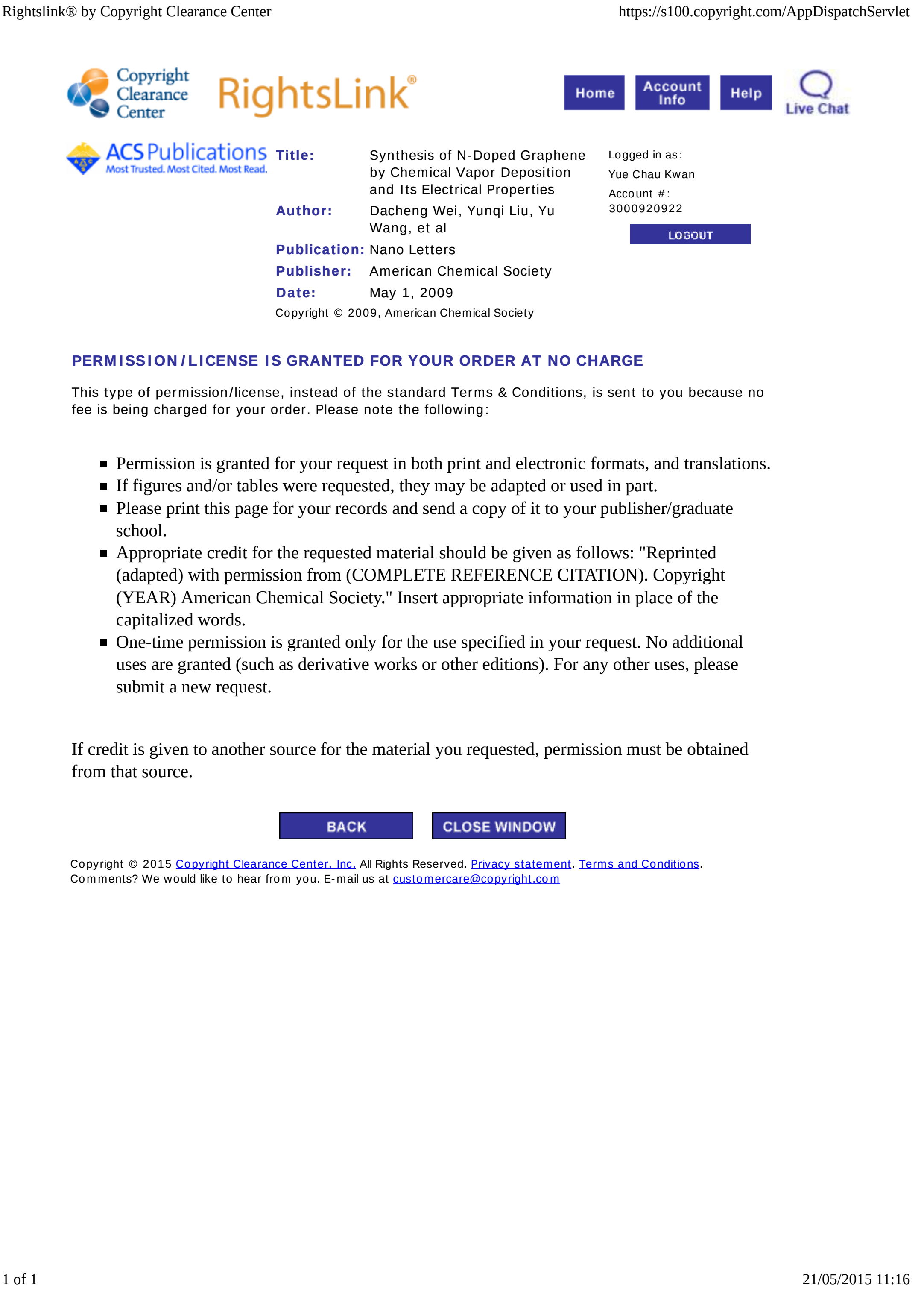

Rightslink® by Copyright Clearance Center https://s100.copyright.com/AppDispatchServlet

Title: Synthesis of N-Doped Graphene by Chemical Vapor Deposition and Its Electrical Properties

Author: Dacheng Wei, Yunqi Liu, Yu Wang, et al

Publication: Nano Letters

Publisher: American Chemical Society

Date: May 1, 2009

Copyright © 2009, American Chemical Society

Logged in as:
Yue Chau Kwan
Account #:
3000920922

PERMISSION/LICENSE IS GRANTED FOR YOUR ORDER AT NO CHARGE

This type of permission/license, instead of the standard Terms & Conditions, is sent to you because no fee is being charged for your order. Please note the following:

- Permission is granted for your request in both print and electronic formats, and translations.
- If figures and/or tables were requested, they may be adapted or used in part.
- Please print this page for your records and send a copy of it to your publisher/graduate school.
- Appropriate credit for the requested material should be given as follows: "Reprinted (adapted) with permission from (COMPLETE REFERENCE CITATION). Copyright (YEAR) American Chemical Society." Insert appropriate information in place of the capitalized words.
- One-time permission is granted only for the use specified in your request. No additional uses are granted (such as derivative works or other editions). For any other uses, please submit a new request.

If credit is given to another source for the material you requested, permission must be obtained from that source.

1 of 1 21/05/2015 11:16

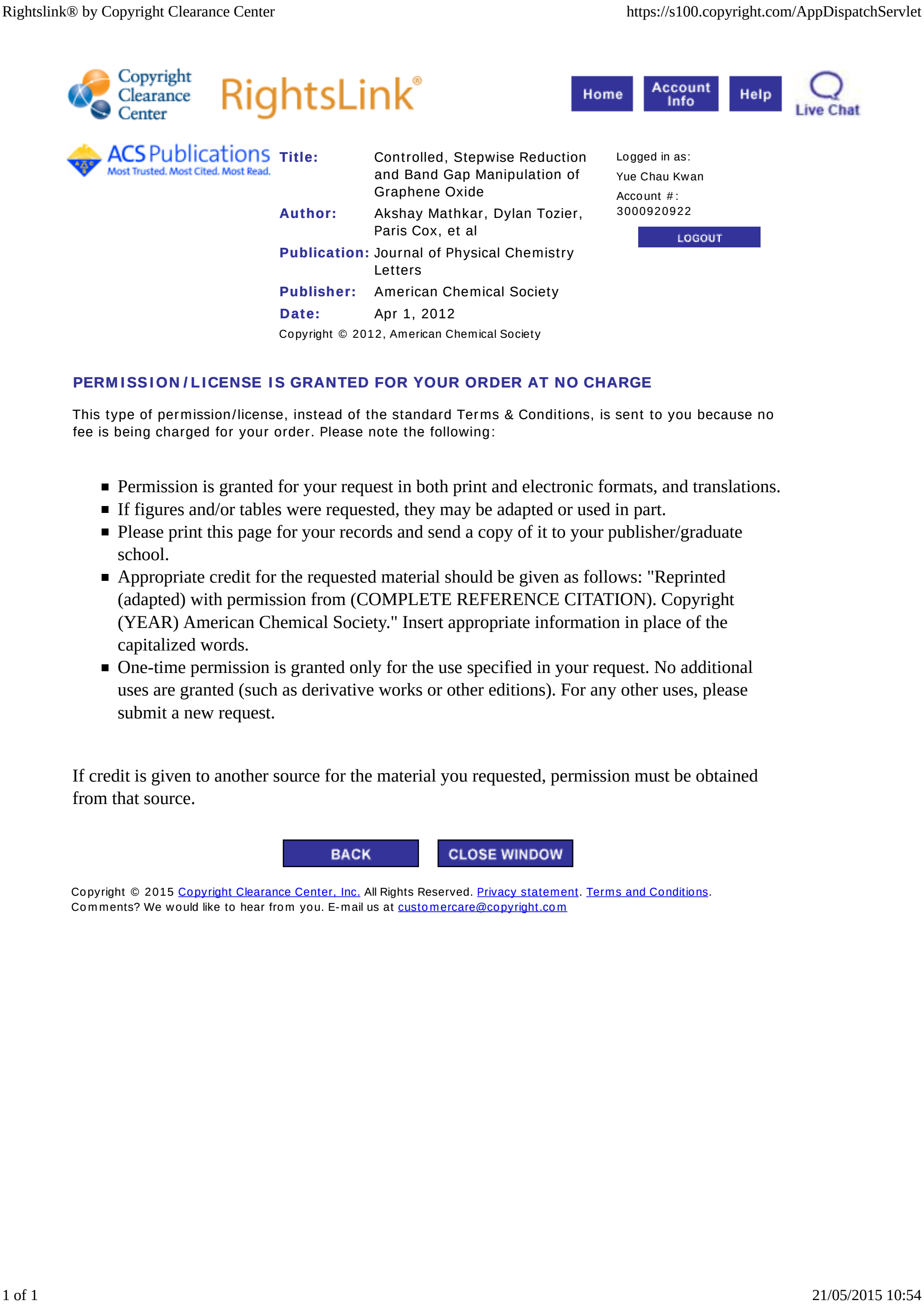

Rightslink® by Copyright Clearance Center https://s100.copyright.com/AppDispatchServlet

Title:	Controlled, Stepwise Reduction and Band Gap Manipulation of Graphene Oxide
Author:	Akshay Mathkar, Dylan Tozier, Paris Cox, et al
Publication:	Journal of Physical Chemistry Letters
Publisher:	American Chemical Society
Date:	Apr 1, 2012

Copyright © 2012, American Chemical Society

Logged in as:
Yue Chau Kwan
Account #:
3000920922

PERMISSION/LICENSE IS GRANTED FOR YOUR ORDER AT NO CHARGE

This type of permission/license, instead of the standard Terms & Conditions, is sent to you because no fee is being charged for your order. Please note the following:

- Permission is granted for your request in both print and electronic formats, and translations.
- If figures and/or tables were requested, they may be adapted or used in part.
- Please print this page for your records and send a copy of it to your publisher/graduate school.
- Appropriate credit for the requested material should be given as follows: "Reprinted (adapted) with permission from (COMPLETE REFERENCE CITATION). Copyright (YEAR) American Chemical Society." Insert appropriate information in place of the capitalized words.
- One-time permission is granted only for the use specified in your request. No additional uses are granted (such as derivative works or other editions). For any other uses, please submit a new request.

If credit is given to another source for the material you requested, permission must be obtained from that source.

Copyright © 2015 Copyright Clearance Center, Inc. All Rights Reserved. Privacy statement. Terms and Conditions.
Comments? We would like to hear from you. E-mail us at customercare@copyright.com

1 of 1 21/05/2015 10:54

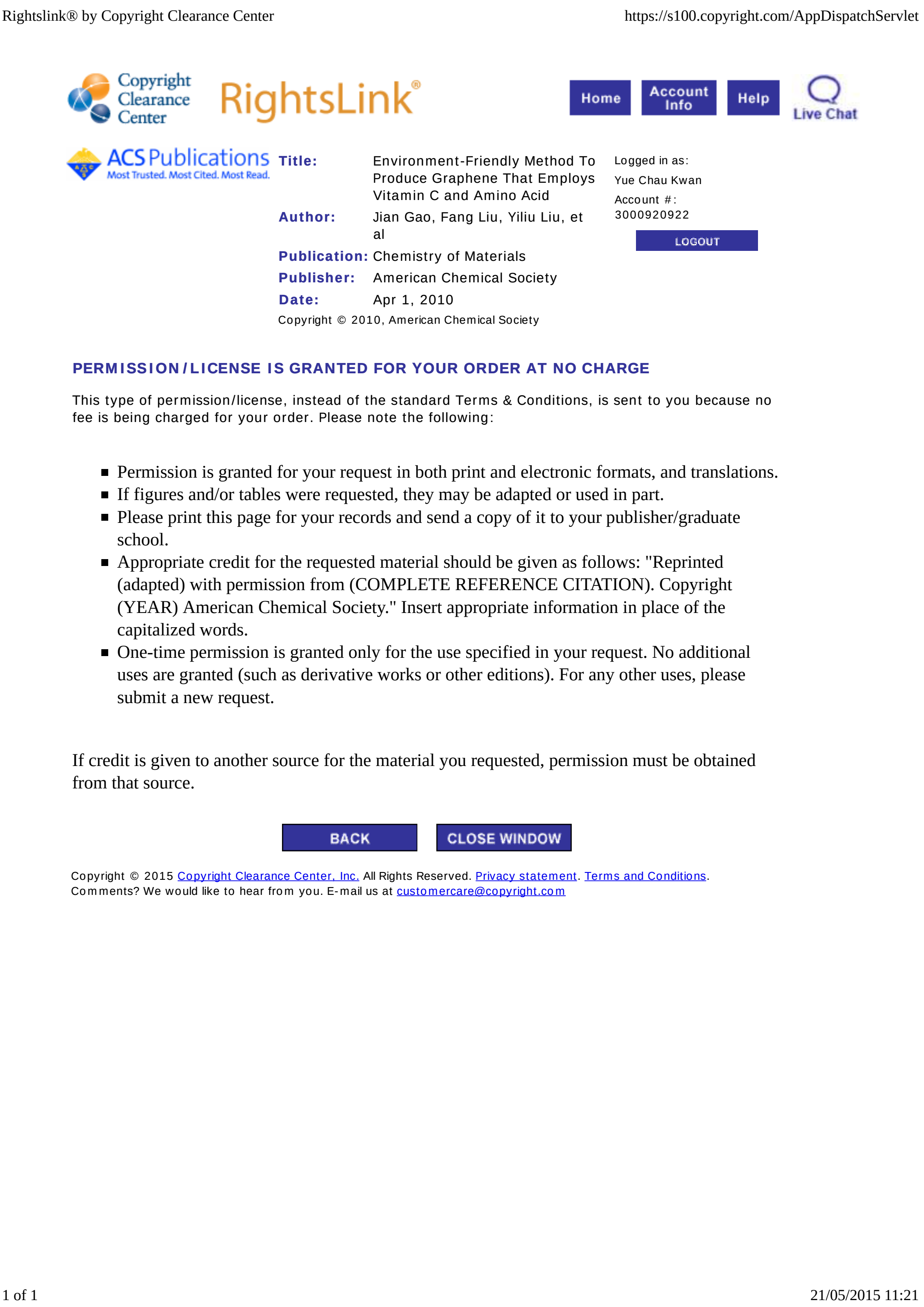

Rightslink® by Copyright Clearance Center https://s100.copyright.com/AppDispatchServlet

Title:	Environment-Friendly Method To Produce Graphene That Employs Vitamin C and Amino Acid
Author:	Jian Gao, Fang Liu, Yiliu Liu, et al
Publication:	Chemistry of Materials
Publisher:	American Chemical Society
Date:	Apr 1, 2010

Copyright © 2010, American Chemical Society

Logged in as:
Yue Chau Kwan
Account #:
3000920922

PERMISSION/LICENSE IS GRANTED FOR YOUR ORDER AT NO CHARGE

This type of permission/license, instead of the standard Terms & Conditions, is sent to you because no fee is being charged for your order. Please note the following:

- Permission is granted for your request in both print and electronic formats, and translations.
- If figures and/or tables were requested, they may be adapted or used in part.
- Please print this page for your records and send a copy of it to your publisher/graduate school.
- Appropriate credit for the requested material should be given as follows: "Reprinted (adapted) with permission from (COMPLETE REFERENCE CITATION). Copyright (YEAR) American Chemical Society." Insert appropriate information in place of the capitalized words.
- One-time permission is granted only for the use specified in your request. No additional uses are granted (such as derivative works or other editions). For any other uses, please submit a new request.

If credit is given to another source for the material you requested, permission must be obtained from that source.

1 of 1 21/05/2015 11:21

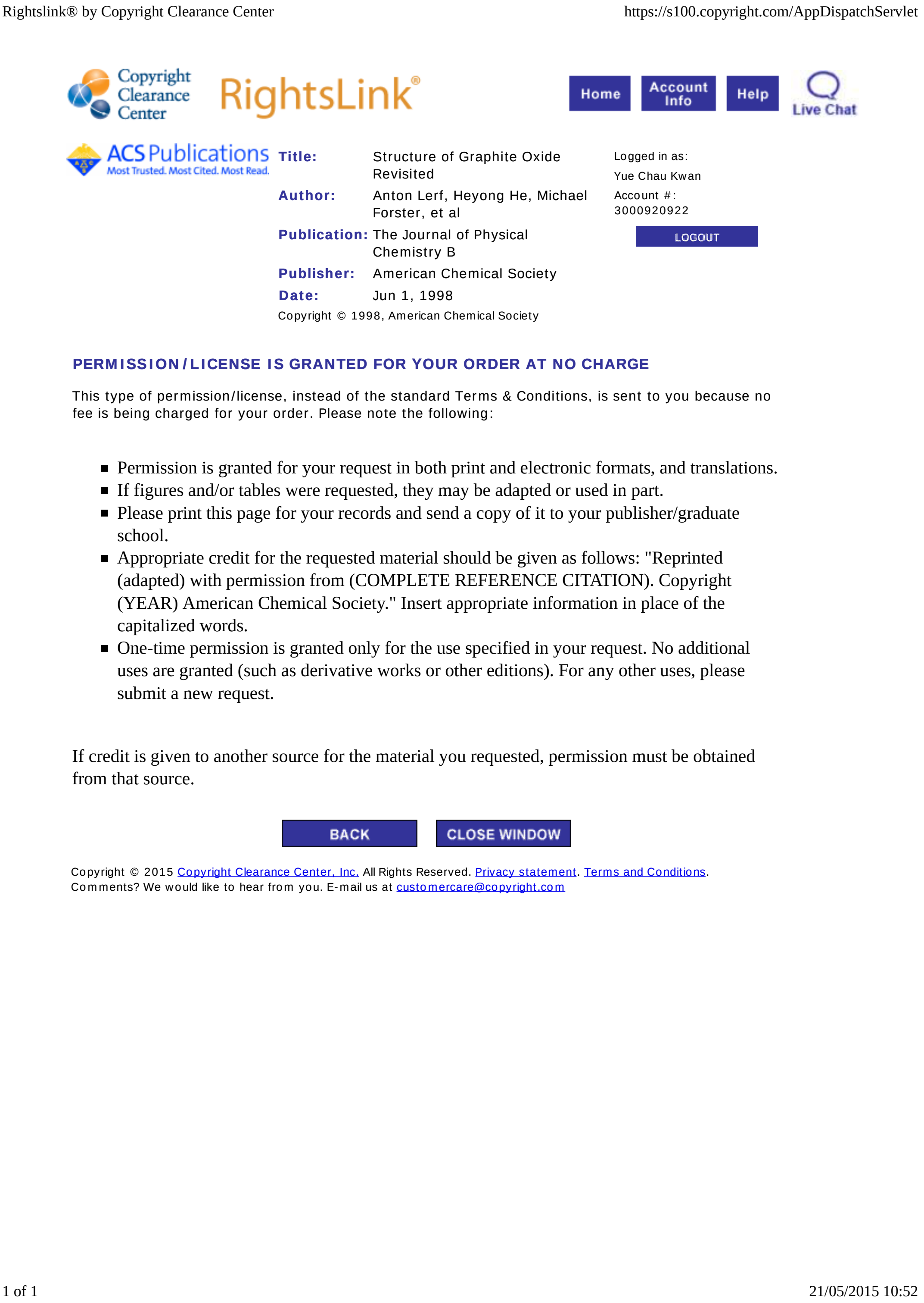

Title:	Structure of Graphite Oxide Revisited
Author:	Anton Lerf, Heyong He, Michael Forster, et al
Publication:	The Journal of Physical Chemistry B
Publisher:	American Chemical Society
Date:	Jun 1, 1998

Copyright © 1998, American Chemical Society

Logged in as:
Yue Chau Kwan
Account #:
3000920922

PERMISSION/LICENSE IS GRANTED FOR YOUR ORDER AT NO CHARGE

This type of permission/license, instead of the standard Terms & Conditions, is sent to you because no fee is being charged for your order. Please note the following:

- Permission is granted for your request in both print and electronic formats, and translations.
- If figures and/or tables were requested, they may be adapted or used in part.
- Please print this page for your records and send a copy of it to your publisher/graduate school.
- Appropriate credit for the requested material should be given as follows: "Reprinted (adapted) with permission from (COMPLETE REFERENCE CITATION). Copyright (YEAR) American Chemical Society." Insert appropriate information in place of the capitalized words.
- One-time permission is granted only for the use specified in your request. No additional uses are granted (such as derivative works or other editions). For any other uses, please submit a new request.

If credit is given to another source for the material you requested, permission must be obtained from that source.

Copyright © 2015 Copyright Clearance Center, Inc. All Rights Reserved. Privacy statement. Terms and Conditions.
Comments? We would like to hear from you. E-mail us at customercare@copyright.com

1 of 1

21/05/2015 10:52

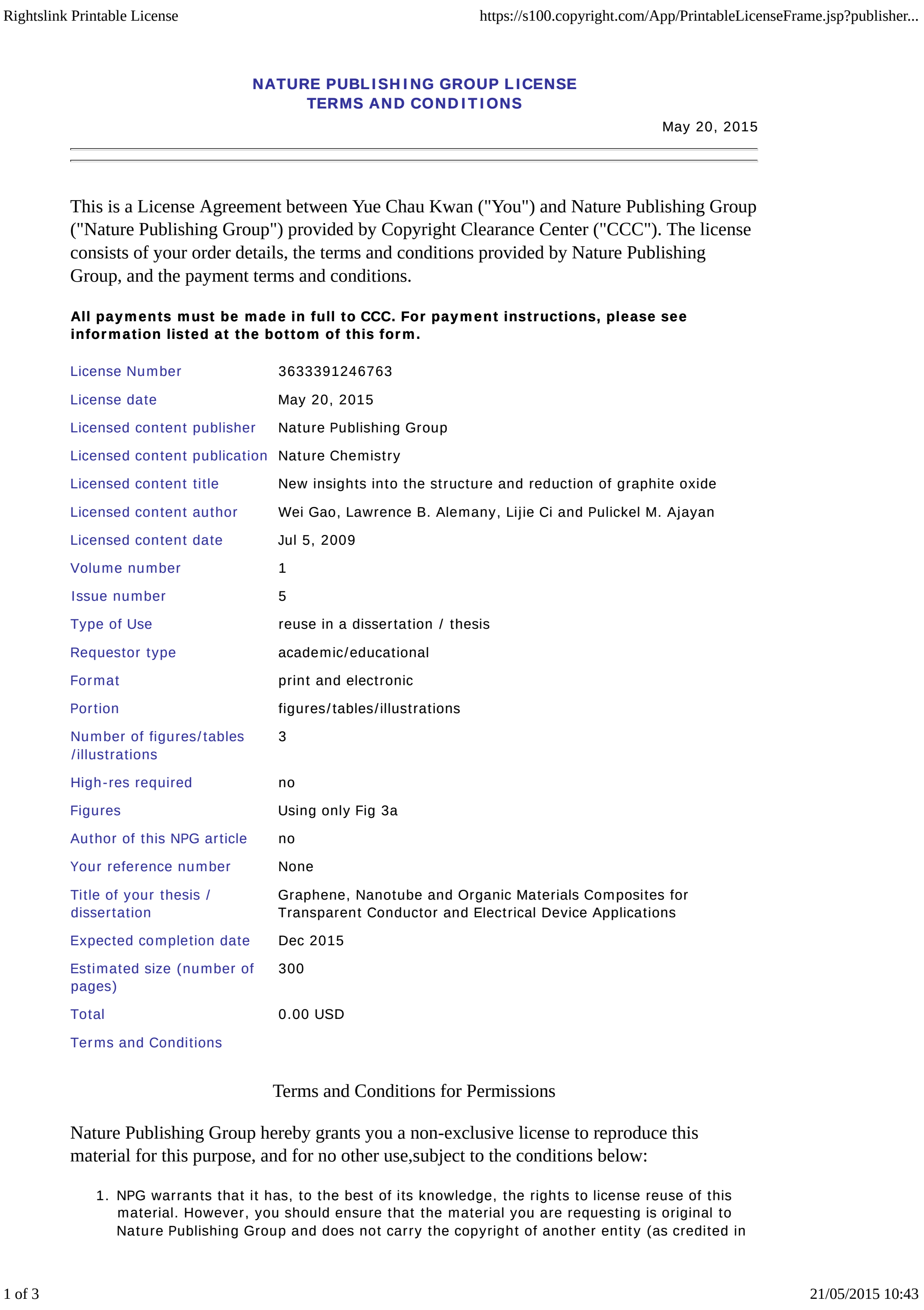

NATURE PUBLISHING GROUP LICENSE
TERMS AND CONDITIONS

May 20, 2015

This is a License Agreement between Yue Chau Kwan ("You") and Nature Publishing Group ("Nature Publishing Group") provided by Copyright Clearance Center ("CCC"). The license consists of your order details, the terms and conditions provided by Nature Publishing Group, and the payment terms and conditions.

All payments must be made in full to CCC. For payment instructions, please see information listed at the bottom of this form.

License Number	3633391246763
License date	May 20, 2015
Licensed content publisher	Nature Publishing Group
Licensed content publication	Nature Chemistry
Licensed content title	New insights into the structure and reduction of graphite oxide
Licensed content author	Wei Gao, Lawrence B. Alemany, Lijie Ci and Pulickel M. Ajayan
Licensed content date	Jul 5, 2009
Volume number	1
Issue number	5
Type of Use	reuse in a dissertation / thesis
Requestor type	academic/educational
Format	print and electronic
Portion	figures/tables/illustrations
Number of figures/tables /illustrations	3
High-res required	no
Figures	Using only Fig 3a
Author of this NPG article	no
Your reference number	None
Title of your thesis / dissertation	Graphene, Nanotube and Organic Materials Composites for Transparent Conductor and Electrical Device Applications
Expected completion date	Dec 2015
Estimated size (number of pages)	300
Total	0.00 USD
Terms and Conditions	

Terms and Conditions for Permissions

Nature Publishing Group hereby grants you a non-exclusive license to reproduce this material for this purpose, and for no other use,subject to the conditions below:

1. NPG warrants that it has, to the best of its knowledge, the rights to license reuse of this material. However, you should ensure that the material you are requesting is original to Nature Publishing Group and does not carry the copyright of another entity (as credited in

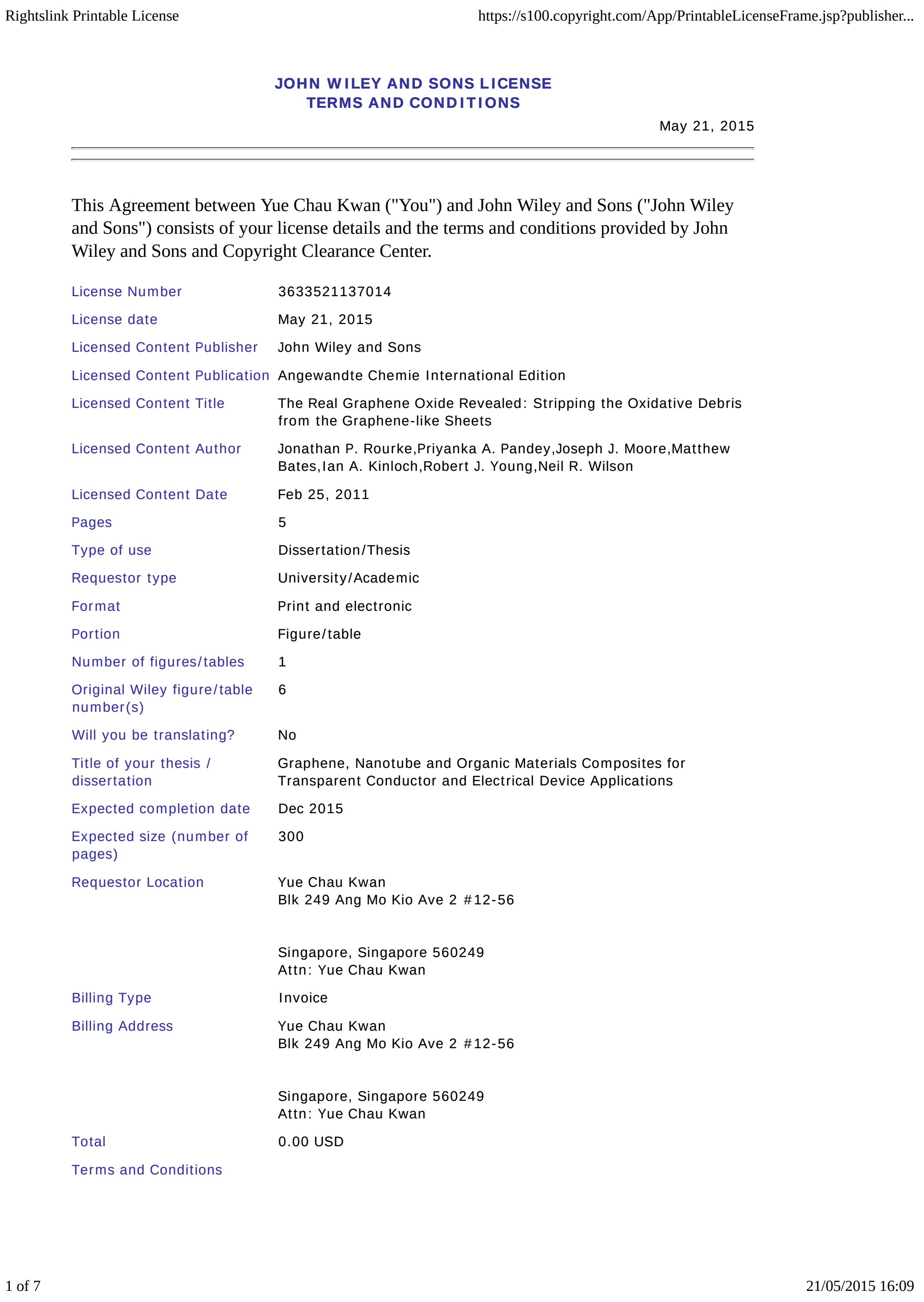

JOHN WILEY AND SONS LICENSE
TERMS AND CONDITIONS

May 21, 2015

This Agreement between Yue Chau Kwan ("You") and John Wiley and Sons ("John Wiley and Sons") consists of your license details and the terms and conditions provided by John Wiley and Sons and Copyright Clearance Center.

License Number	3633521137014
License date	May 21, 2015
Licensed Content Publisher	John Wiley and Sons
Licensed Content Publication	Angewandte Chemie International Edition
Licensed Content Title	The Real Graphene Oxide Revealed: Stripping the Oxidative Debris from the Graphene-like Sheets
Licensed Content Author	Jonathan P. Rourke,Priyanka A. Pandey,Joseph J. Moore,Matthew Bates,Ian A. Kinloch,Robert J. Young,Neil R. Wilson
Licensed Content Date	Feb 25, 2011
Pages	5
Type of use	Dissertation/Thesis
Requestor type	University/Academic
Format	Print and electronic
Portion	Figure/table
Number of figures/tables	1
Original Wiley figure/table number(s)	6
Will you be translating?	No
Title of your thesis / dissertation	Graphene, Nanotube and Organic Materials Composites for Transparent Conductor and Electrical Device Applications
Expected completion date	Dec 2015
Expected size (number of pages)	300
Requestor Location	Yue Chau Kwan Blk 249 Ang Mo Kio Ave 2 #12-56 Singapore, Singapore 560249 Attn: Yue Chau Kwan
Billing Type	Invoice
Billing Address	Yue Chau Kwan Blk 249 Ang Mo Kio Ave 2 #12-56 Singapore, Singapore 560249 Attn: Yue Chau Kwan
Total	0.00 USD
Terms and Conditions	

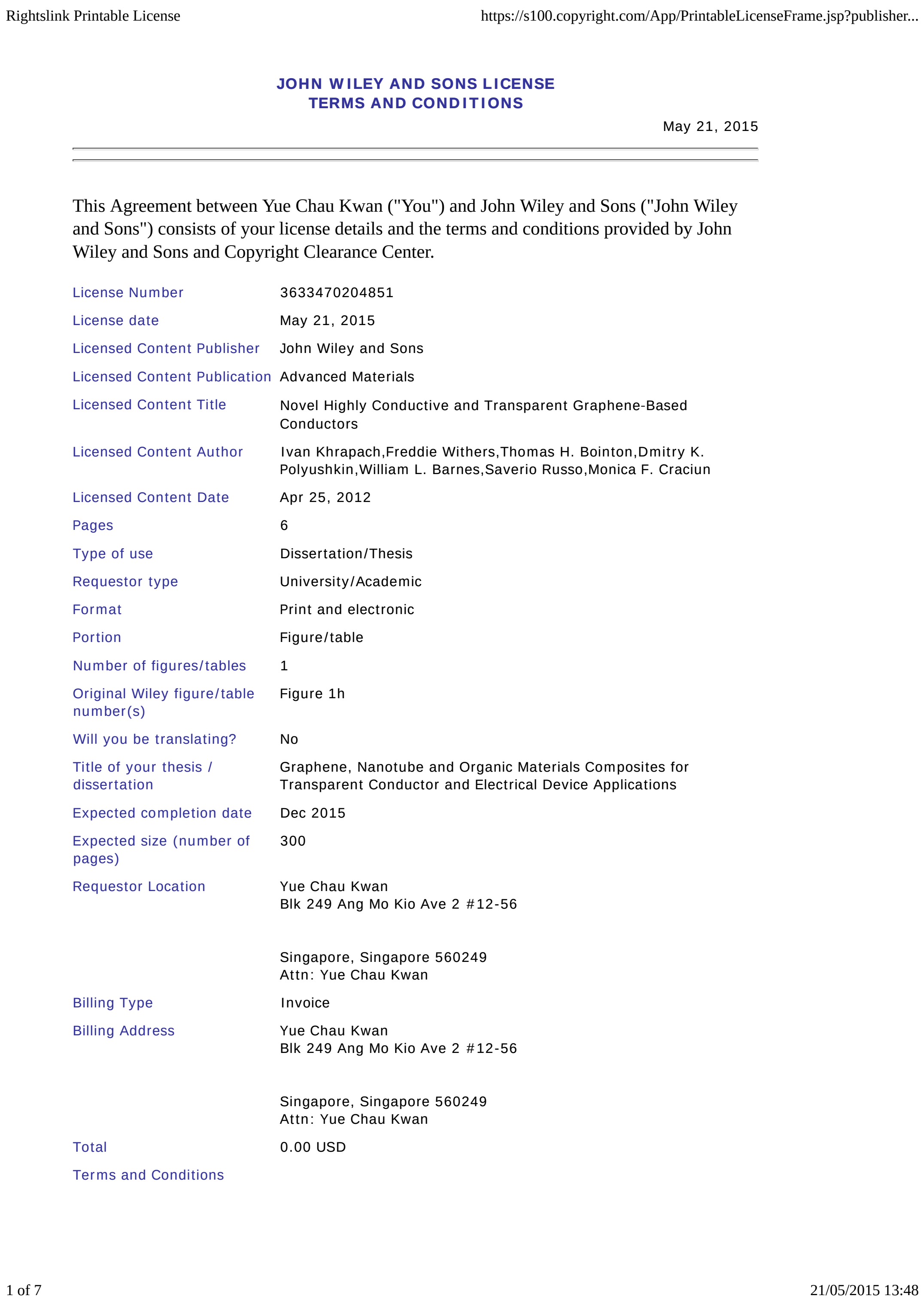

JOHN WILEY AND SONS LICENSE
TERMS AND CONDITIONS

May 21, 2015

This Agreement between Yue Chau Kwan ("You") and John Wiley and Sons ("John Wiley and Sons") consists of your license details and the terms and conditions provided by John Wiley and Sons and Copyright Clearance Center.

License Number	3633470204851
License date	May 21, 2015
Licensed Content Publisher	John Wiley and Sons
Licensed Content Publication	Advanced Materials
Licensed Content Title	Novel Highly Conductive and Transparent Graphene-Based Conductors
Licensed Content Author	Ivan Khrapach,Freddie Withers,Thomas H. Bointon,Dmitry K. Polyushkin,William L. Barnes,Saverio Russo,Monica F. Craciun
Licensed Content Date	Apr 25, 2012
Pages	6
Type of use	Dissertation/Thesis
Requestor type	University/Academic
Format	Print and electronic
Portion	Figure/table
Number of figures/tables	1
Original Wiley figure/table number(s)	Figure 1h
Will you be translating?	No
Title of your thesis / dissertation	Graphene, Nanotube and Organic Materials Composites for Transparent Conductor and Electrical Device Applications
Expected completion date	Dec 2015
Expected size (number of pages)	300
Requestor Location	Yue Chau Kwan Blk 249 Ang Mo Kio Ave 2 #12-56 Singapore, Singapore 560249 Attn: Yue Chau Kwan
Billing Type	Invoice
Billing Address	Yue Chau Kwan Blk 249 Ang Mo Kio Ave 2 #12-56 Singapore, Singapore 560249 Attn: Yue Chau Kwan
Total	0.00 USD
Terms and Conditions	

B. RIGHTS AND PERMISSIONS

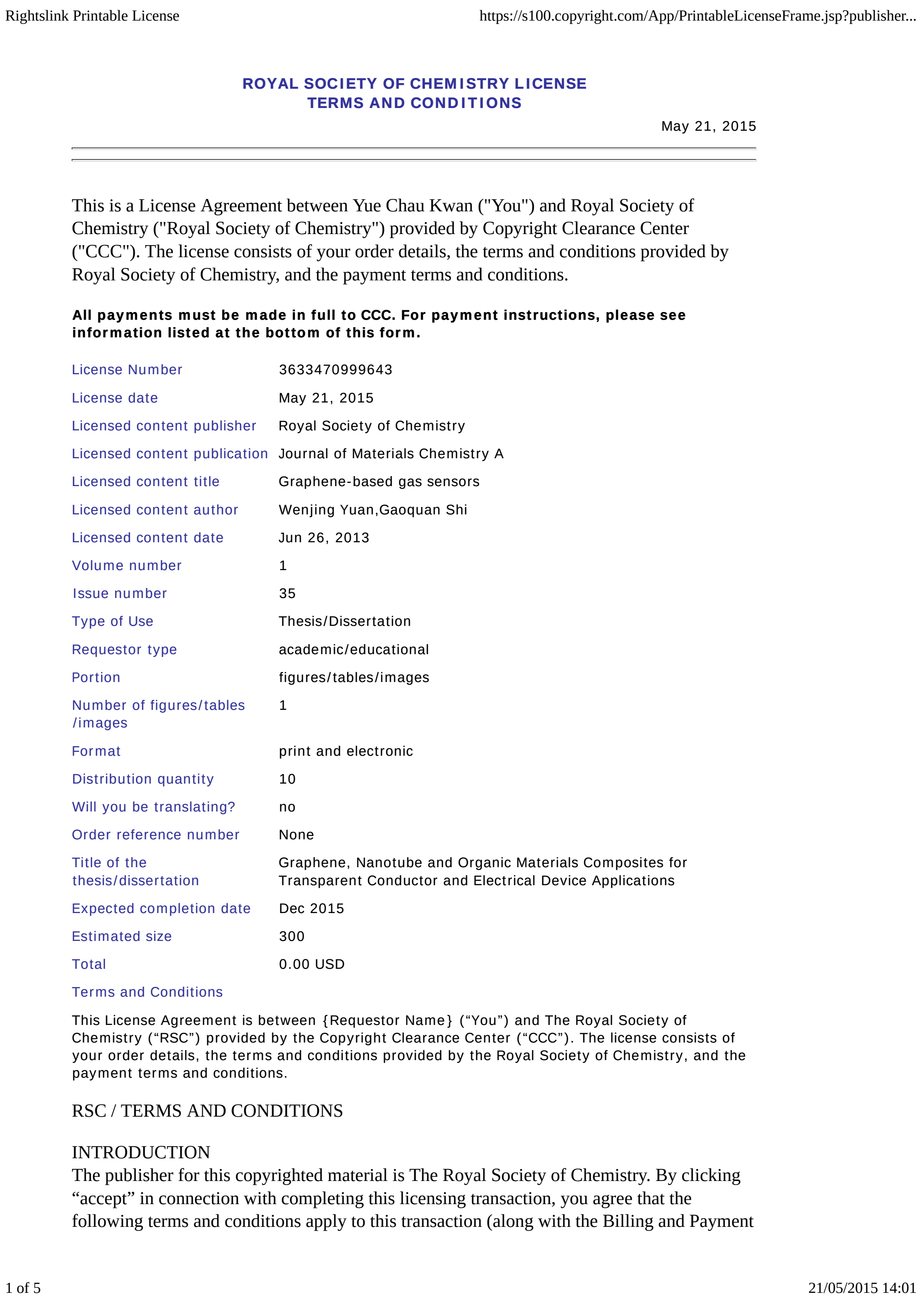

Rightslink Printable License https://s100.copyright.com/App/PrintableLicenseFrame.jsp?publisher...

ROYAL SOCIETY OF CHEMISTRY LICENSE
TERMS AND CONDITIONS

May 21, 2015

This is a License Agreement between Yue Chau Kwan ("You") and Royal Society of Chemistry ("Royal Society of Chemistry") provided by Copyright Clearance Center ("CCC"). The license consists of your order details, the terms and conditions provided by Royal Society of Chemistry, and the payment terms and conditions.

All payments must be made in full to CCC. For payment instructions, please see information listed at the bottom of this form.

License Number	3633470999643
License date	May 21, 2015
Licensed content publisher	Royal Society of Chemistry
Licensed content publication	Journal of Materials Chemistry A
Licensed content title	Graphene-based gas sensors
Licensed content author	Wenjing Yuan,Gaoquan Shi
Licensed content date	Jun 26, 2013
Volume number	1
Issue number	35
Type of Use	Thesis/Dissertation
Requestor type	academic/educational
Portion	figures/tables/images
Number of figures/tables /images	1
Format	print and electronic
Distribution quantity	10
Will you be translating?	no
Order reference number	None
Title of the thesis/dissertation	Graphene, Nanotube and Organic Materials Composites for Transparent Conductor and Electrical Device Applications
Expected completion date	Dec 2015
Estimated size	300
Total	0.00 USD

Terms and Conditions

This License Agreement is between {Requestor Name} ("You") and The Royal Society of Chemistry ("RSC") provided by the Copyright Clearance Center ("CCC"). The license consists of your order details, the terms and conditions provided by the Royal Society of Chemistry, and the payment terms and conditions.

RSC / TERMS AND CONDITIONS

INTRODUCTION
The publisher for this copyrighted material is The Royal Society of Chemistry. By clicking "accept" in connection with completing this licensing transaction, you agree that the following terms and conditions apply to this transaction (along with the Billing and Payment

1 of 5 21/05/2015 14:01

Title: A Graphene Field-Effect Device
Author: Lemme, Max C.; Echtermeyer, T.J.; Baus, M.; Kurz, H.
Publication: IEEE Electron Device Letters
Publisher: IEEE
Date: April 2007
Copyright © 2007, IEEE

Logged in as:
Yue Chau Kwan
Account #:
3000920922

Thesis / Dissertation Reuse

The IEEE does not require individuals working on a thesis to obtain a formal reuse license, however, you may print out this statement to be used as a permission grant:

Requirements to be followed when using any portion (e.g., figure, graph, table, or textual material) of an IEEE copyrighted paper in a thesis:

1) In the case of textual material (e.g., using short quotes or referring to the work within these papers) users must give full credit to the original source (author, paper, publication) followed by the IEEE copyright line © 2011 IEEE.
2) In the case of illustrations or tabular material, we require that the copyright line © [Year of original publication] IEEE appear prominently with each reprinted figure and/or table.
3) If a substantial portion of the original paper is to be used, and if you are not the senior author, also obtain the senior author's approval.

Requirements to be followed when using an entire IEEE copyrighted paper in a thesis:

1) The following IEEE copyright/ credit notice should be placed prominently in the references: © [year of original publication] IEEE. Reprinted, with permission, from [author names, paper title, IEEE publication title, and month/year of publication]
2) Only the accepted version of an IEEE copyrighted paper can be used when posting the paper or your thesis on-line.
3) In placing the thesis on the author's university website, please display the following message in a prominent place on the website: In reference to IEEE copyrighted material which is used with permission in this thesis, the IEEE does not endorse any of [university/educational entity's name goes here]'s products or services. Internal or personal use of this material is permitted. If interested in reprinting/republishing IEEE copyrighted material for advertising or promotional purposes or for creating new collective works for resale or redistribution, please go to http://www.ieee.org/publications_standards/publications/rights/rights_link.html to learn how to obtain a License from RightsLink.

If applicable, University Microfilms and/or ProQuest Library, or the Archives of Canada may supply single copies of the dissertation.

B. RIGHTS AND PERMISSIONS

JOHN WILEY AND SONS LICENSE TERMS AND CONDITIONS

May 21, 2015

This Agreement between Yue Chau Kwan ("You") and John Wiley and Sons ("John Wiley and Sons") consists of your license details and the terms and conditions provided by John Wiley and Sons and Copyright Clearance Center.

License Number	3633570689539
License date	May 21, 2015
Licensed Content Publisher	John Wiley and Sons
Licensed Content Publication	Surface & Interface Analysis
Licensed Content Title	Quantitative electron spectroscopy of surfaces: A standard data base for electron inelastic mean free paths in solids
Licensed Content Author	M. P. Seah,W. A. Dench
Licensed Content Date	Sep 15, 2004
Pages	10
Type of use	Dissertation/Thesis
Requestor type	University/Academic
Format	Print and electronic
Portion	Figure/table
Number of figures/tables	1
Original Wiley figure/table number(s)	Fig. 1
Will you be translating?	No
Title of your thesis / dissertation	Graphene, Nanotube and Organic Materials Composites for Transparent Conductor and Electrical Device Applications
Expected completion date	Dec 2015
Expected size (number of pages)	300
Requestor Location	Yue Chau Kwan Blk 249 Ang Mo Kio Ave 2 #12-56 Singapore, Singapore 560249 Attn: Yue Chau Kwan
Billing Type	Invoice
Billing Address	Yue Chau Kwan Blk 249 Ang Mo Kio Ave 2 #12-56 Singapore, Singapore 560249 Attn: Yue Chau Kwan
Total	0.00 USD
Terms and Conditions	

TERMS AND CONDITIONS

JOHN WILEY AND SONS LICENSE
TERMS AND CONDITIONS

May 21, 2015

This Agreement between Yue Chau Kwan ("You") and John Wiley and Sons ("John Wiley and Sons") consists of your license details and the terms and conditions provided by John Wiley and Sons and Copyright Clearance Center.

License Number	3633560845357
License date	May 21, 2015
Licensed Content Publisher	John Wiley and Sons
Licensed Content Publication	Surface & Interface Analysis
Licensed Content Title	Investigation of multiplet splitting of Fe 2p XPS spectra and bonding in iron compounds
Licensed Content Author	A. P. Grosvenor,B. A. Kobe,M. C. Biesinger,N. S. McIntyre
Licensed Content Date	Oct 7, 2004
Pages	11
Type of use	Dissertation/Thesis
Requestor type	University/Academic
Format	Print and electronic
Portion	Figure/table
Number of figures/tables	1
Original Wiley figure/table number(s)	1
Will you be translating?	No
Title of your thesis / dissertation	Graphene, Nanotube and Organic Materials Composites for Transparent Conductor and Electrical Device Applications
Expected completion date	Dec 2015
Expected size (number of pages)	300
Requestor Location	Yue Chau Kwan Blk 249 Ang Mo Kio Ave 2 #12-56 Singapore, Singapore 560249 Attn: Yue Chau Kwan
Billing Type	Invoice
Billing Address	Yue Chau Kwan Blk 249 Ang Mo Kio Ave 2 #12-56 Singapore, Singapore 560249 Attn: Yue Chau Kwan
Total	0.00 USD
Terms and Conditions	

TERMS AND CONDITIONS

B. RIGHTS AND PERMISSIONS

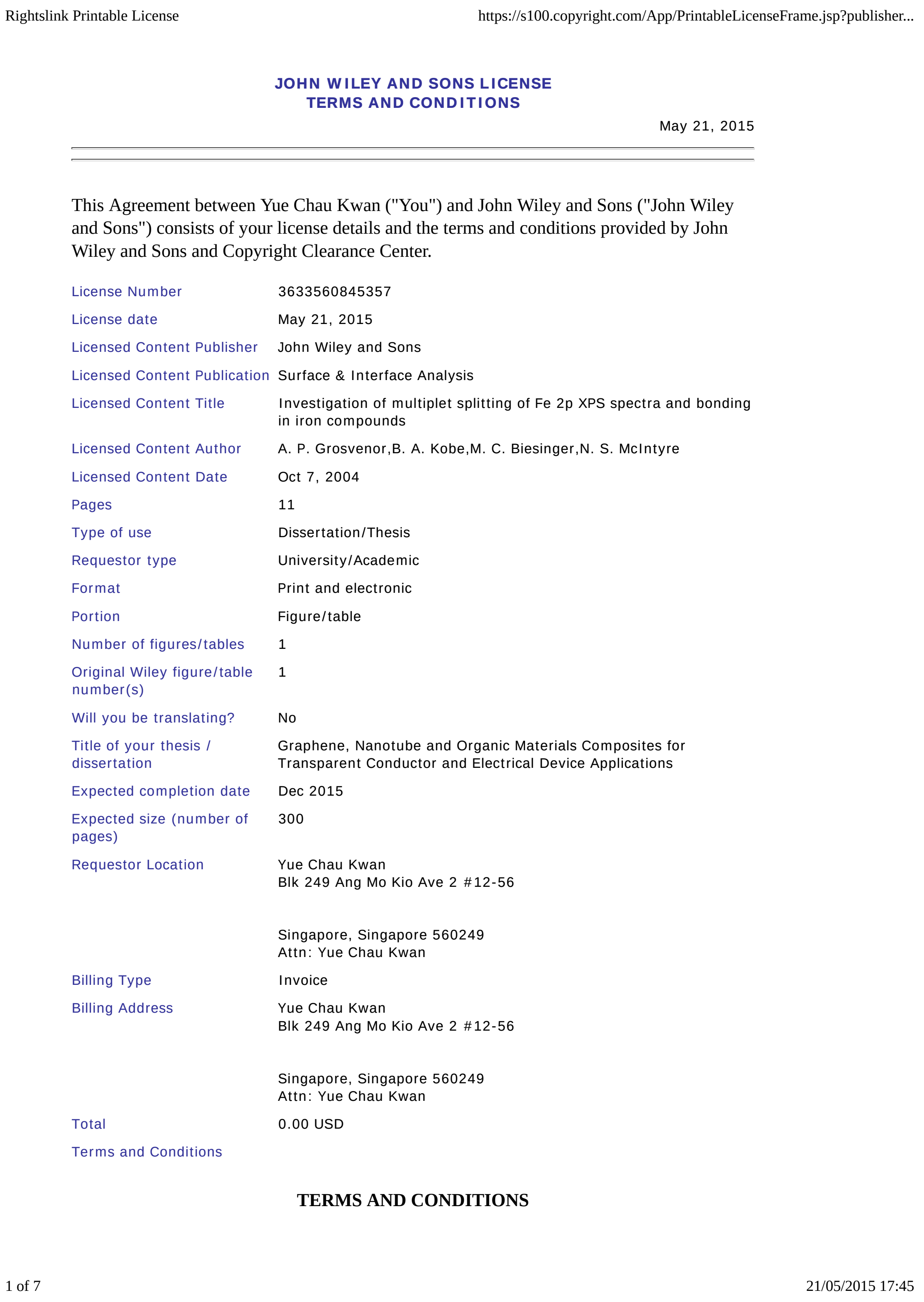

JOHN WILEY AND SONS LICENSE
TERMS AND CONDITIONS

May 21, 2015

This Agreement between Yue Chau Kwan ("You") and John Wiley and Sons ("John Wiley and Sons") consists of your license details and the terms and conditions provided by John Wiley and Sons and Copyright Clearance Center.

License Number	3633560845357
License date	May 21, 2015
Licensed Content Publisher	John Wiley and Sons
Licensed Content Publication	Surface & Interface Analysis
Licensed Content Title	Investigation of multiplet splitting of Fe 2p XPS spectra and bonding in iron compounds
Licensed Content Author	A. P. Grosvenor,B. A. Kobe,M. C. Biesinger,N. S. McIntyre
Licensed Content Date	Oct 7, 2004
Pages	11
Type of use	Dissertation/Thesis
Requestor type	University/Academic
Format	Print and electronic
Portion	Figure/table
Number of figures/tables	1
Original Wiley figure/table number(s)	1
Will you be translating?	No
Title of your thesis / dissertation	Graphene, Nanotube and Organic Materials Composites for Transparent Conductor and Electrical Device Applications
Expected completion date	Dec 2015
Expected size (number of pages)	300
Requestor Location	Yue Chau Kwan Blk 249 Ang Mo Kio Ave 2 #12-56 Singapore, Singapore 560249 Attn: Yue Chau Kwan
Billing Type	Invoice
Billing Address	Yue Chau Kwan Blk 249 Ang Mo Kio Ave 2 #12-56 Singapore, Singapore 560249 Attn: Yue Chau Kwan
Total	0.00 USD
Terms and Conditions	

TERMS AND CONDITIONS

Rightslink® by Copyright Clearance Center https://s100.copyright.com/AppDispatchServlet

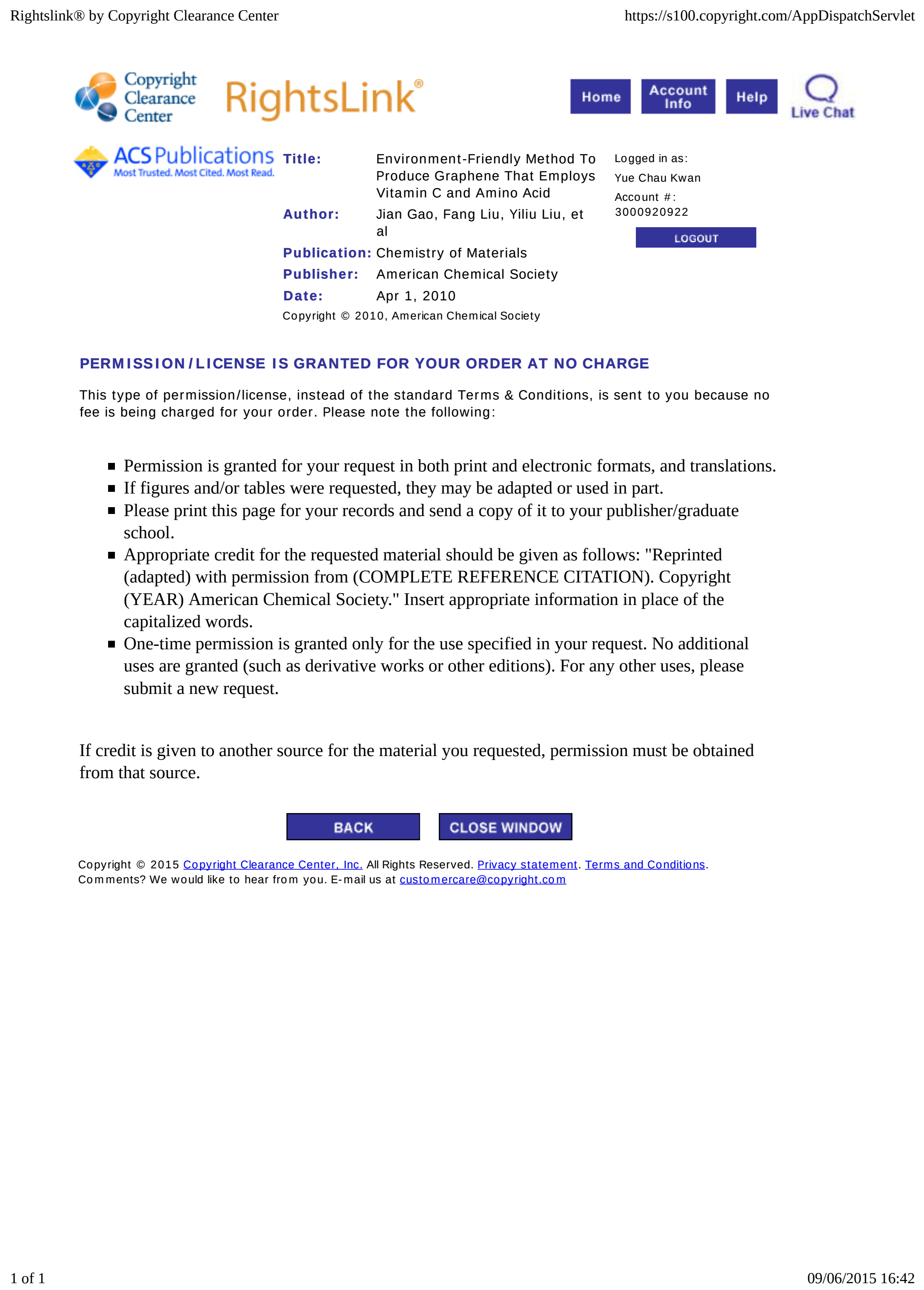

Title:	Environment-Friendly Method To Produce Graphene That Employs Vitamin C and Amino Acid
Author:	Jian Gao, Fang Liu, Yiliu Liu, et al
Publication:	Chemistry of Materials
Publisher:	American Chemical Society
Date:	Apr 1, 2010

Copyright © 2010, American Chemical Society

Logged in as:
Yue Chau Kwan
Account #:
3000920922

PERMISSION/LICENSE IS GRANTED FOR YOUR ORDER AT NO CHARGE

This type of permission/license, instead of the standard Terms & Conditions, is sent to you because no fee is being charged for your order. Please note the following:

- Permission is granted for your request in both print and electronic formats, and translations.
- If figures and/or tables were requested, they may be adapted or used in part.
- Please print this page for your records and send a copy of it to your publisher/graduate school.
- Appropriate credit for the requested material should be given as follows: "Reprinted (adapted) with permission from (COMPLETE REFERENCE CITATION). Copyright (YEAR) American Chemical Society." Insert appropriate information in place of the capitalized words.
- One-time permission is granted only for the use specified in your request. No additional uses are granted (such as derivative works or other editions). For any other uses, please submit a new request.

If credit is given to another source for the material you requested, permission must be obtained from that source.

1 of 1 09/06/2015 16:42